Title

THE STRUCTURE, ORDERING. AND CHEMISTRY OF MOLECULAR OVERLAYERS ON RH(111) AND RH(100) SINGLE CRYSTAL SURFACES: A VIBRATIONAL SPECTROSCOPIC AND LEED CRYSTALLOGRAPHIC STUDY

Author

Kao, C.T.

Publication Date

1988-10-01

LBL-26346 c.2

Center for Advanced Materials

CAM

The Structure, Ordering, and Chemistry of Molecular Overlayers on Rh(111) and Rh(100) Single Crystal Surfaces: A Vibrational Spectroscopic and LEED Crystallographic Study

C.-T. Kao
(Ph.D. Thesis)

October 1988

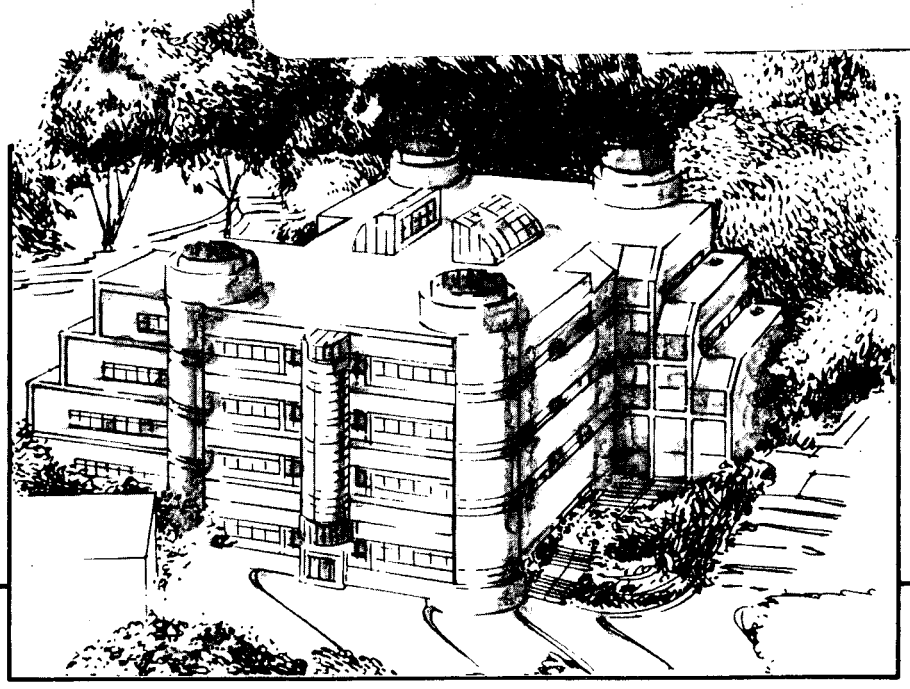

Materials and Chemical Sciences Division

Lawrence Berkeley Laboratory • University of California

ONE CYCLOTRON ROAD, BERKELEY, CA 94720 • (415) 486-4755

Prepared for the U.S. Department of Energy under Contract DE-AC03-76SF00098

DISCLAIMER

LBL-26346

THE STRUCTURE, ORDERING AND CHEMISTRY OF MOLECULAR OVERLAYERS ON Rh(111) and Rh(100) SINGLE CRYSTAL SURFACES: A VIBRATIONAL SPECTROSCOPIC AND LEED CRYSTALLOGRAPHIC STUDY

Chi-Tzu Kao
Ph.D. Thesis

Department of Chemistry
University of California at Berkeley
and
Center for Advanced Materials
Materials and Chemical Sciences Division
Lawrence Berkeley Laboratory
1 Cyclotron Road
Berkeley, California 94720

October 1988

This work was supported by the Director, Office of Energy Research, Office of Basic Energy Sciences, Chemical Sciences Division, of the U.S. Department of Energy under Contract No. DE-AC03-76SF00098.

The Structure, Ordering and Chemistry of Molecular Overlayers on Rh(111) and Rh(100) Single Crystal Surfaces: A Vibrational Spectroscopic and LEED Crystallographic Study.

Chi-Tzu Kao

Department of Chemistry

University of California

and

Materials and Chemical Sciences Division

Lawrence Berkeley Laboratory

Berkeley, California, 94720

Abstract

In order to understand the mechanism of adsorbate-substrate and adsorbate-ad sorbate interactions on catalytically important surfaces, the surface structures and thermal chemistry of molecular overlayers on Rh(111) and Rh(100) single crystal surfaces have been studied under ultra-high vacuum conditions.

For C-H and C-C bond activations the bonding and reactivity of unsaturated hydrocarbons, acetylene, ethylene, and benzene, chemisorbed on Rh(100) at 100-800 K were analyzed by using high-resolution electron energy loss spectroscopy (HREELS), low-energy electron diffraction (LEED) and thermal desorption spectroscopy (TDS). The observed bond strengths of both acetylene and ethylene, as indicated by the shifts of ν(CC) and ν(CH) relative to gas phase values, are stronger on Rh(100) than on Rh(111). Similar surface fragments, CCH (acetylide) and CCH_3 (ethylidyne), were observed from thermal activated decomposition of both chemicals. The formation of a highly dehydrogenated CCH species below half monolayer coverages suggests Rh(100) is a more active surface for C-H bond breaking than the Rh(111) surface. Contrary to the case of acetylene and ethylene, the chemical bond between benzene and Rh(100) is weaker than the bond to Rh(111); nevertheless,

the thermal decomposition of benzene is insensitive to a change of crystallographic orientation from (111) to (100) surface.

For N-O bond activation, the surface ordering, structure and activity of the (2x2)-3NO and c(4x2)-CCH_3+NO monolayers on Rh(111) have been studied by dynamical LEED analysis and HREELS. It was observed that a pure NO overlayer prefers bridge and top site adsorption; while when coadsorbed with ethylidyne the NO is pushed into a three fold hollow site. The sensitivity of molecular bonding geometries toward surface coverages, temperature and presence of coadsorbates has a potential for the development of site selective chemistry. The coadsorbed Rh(111)/c(4x2)-CCH_3+NO monolayer film was demonstrated to have high thermal and pressure stability due to the attractive interaction between NO and ethylidyne.

Elucidation of adsorbate-adsorbate interactions was made possible by monitoring HREELS and work function changes upon coadsorption on Rh(111) and Rh(100) surfaces. By coadsorbing antiparallel dipole adsorbates, such as CO + hydrocarbons or CO + alkali metals, a new ordered, intermixed structure, can be formed. However, the coadsorption of parallel dipoles, such as CO+NO or Na+hydrocarbons, causes the disordering and separation of both adsorbates. The stabilization energies between coadsorbates of antiparallel dipoles ranges from -0.12 eV for c(4x2)-CO+CCH_3 to -0.70 eV for c(4x2)-CO+Na on Rh(111) as determined by a simple model calculation from work function measurement data. The general applicability of this "coadsorbate induced ordering" model to other transition metal surfaces is promising.

Contents

Acknowledgement

I would like to express my acknowledgement to all the people involved in the research projects described in the thesis. First of all, I am most grateful to Professor Gabor Somorjai, for introducing me to the exciting field of surface science. Gabor's enthusiasm, knowledge, and enlighting ideas in science always encourage me. I am most proud to be a member of Gabor's group and to have the opportunity to work together with the best surface chemists and physicists from all around the world.

I would also like to share my accomplishments in science to the following people. In particular, the people of the surface structure group: Greg Blackman, who first patiently taught me how to play with various pieces of ultra-high vacuum equipment, and who was my coworker for the video LEED experiments; and Dr. Michel Van Hove, who is no doubt the world's expert in LEED crystallography, was in charge of the LEED calculation work for all the surface structures mentioned in this thesis. I particularly enjoyed collaborating with Dr. Brian Bent and Professor Al Slavin for the work on hydrocarbons on Rh(100). I have learned a great deal of surface vibrational spectroscopy and organometallic chemistry from Brian Bent. I would also like to thank Dr. Mathew Mate (a physicist with no fear of playing with large hydrocarbon molecules), who has made significant contributions to the coadsorption studies. I am grateful to Dr. Ian Harrison, who made my last year's stay in Berkeley become the most fruitful and colorful year. Special acknowledgement goes to Dr. Ian Harrison and Peter McAnally, who provide a great deal of help in proofreading the thesis.

The support staff of LBL provided enormous assistance to my experimental work. Dan Columb helped me out of with all kinds of trouble with my chambers. Joe Katz and James Severns' expertise in electronics saved me much time, especially when everything was ready except the HREELS power supply. Special thanks to Gabor's secretary, Brigid Tung, for taking care of all kinds of things

that I could not be able to list in detail.

I am indebted to my family for their continuous support in the past few years. My parents have provided tremendous love and care to me, which I could never possibly return. I am particularly grateful to my wife, Mei Lee, who always encouraged me when I was depressed. Without her help and assistance, I would not have been able to finish my work in four years. Particular credit goes to my son, Joseph Kao, who has been a great source of pride and delight for the past 16 months.

Finally, I would like to thank Prof. Yu Wang, my former research advisor in National Taiwan University, for her help in recommending me to Berkeley, the place I will never forget for the rest of my life.

This work was supported by the Director, Office of Energy Research, Office of Basic Energy Sciences, Materials Sciences Division of the U.S. Department of Energy under Contract No. DE-AC03-76SF00098. The author is also grateful for a fellowship support from B.P.-America Corp.

List of Figures

List of Tables

Chapter 1

Introduction and Overview

1.1 Preface

The surfaces and interfaces of various materials play an important role in nature. For instance, the economic production of industrial chemicals relies on catalytic conversion from various starting materials such as petroleum, coal, or natural gases. In particular, transition metals, such as rhodium, are good catalysts for reactions like alkene hydrogenation [1]. Furthermore, rhodium is used as a major catalyst for NO reduction, which is now becoming an important process for atmospheric pollution control [1]. The catalytic processes of these chemical reactions involve C-H, C-C, or N-O bond activation at the surface of the heterogeneous catalyst. Studies of the bonding and reactivity of molecular adsorbates on transition metal surfaces are important for a molecular-level understanding of these heterogeneous catalytic reactions.

In order to obtain details of surface structural information, single crystal surfaces with regular atomic arrays have been used as model substrates of heterogeneous reaction processes. Rhodium, a group VIIIB metal, was chosen for its unique catalytic activity toward hydrogenation of unsaturated hydrocarbons and

reduction of nitric oxide. Two low-Miller-index surfaces, Rh(111) and Rh(100), have been selected to study the structure sensitivity of surface bonding and reaction. The hexagonal close packed Rh(111) surface has three major high-symmetry sites, top, bridge, and threefold hollow, with coordination numbers of 9 [2,3]; while the square Rh(100) surface consists of top, bridge, and fourfold hollow sites with 8 atoms surrounding each surface atom [2,4]. Rh(100) is more open than Rh(111) by about 15%, as judged by the relative surface area per unit cell.

The surface science experiments were performed under ultra-high vacuum conditions to insure a well-characterized surface. Catalytically interesting molecules have been used as adsorbed reagents to study surface bonding and chemical reactivity on the model Rh(111) and Rh(100) single-crystal surfaces. Also, a combination of various surface science techniques was used to characterize the surface structure of different chemical species. The major techniques applied include surface vibrational analysis by high-resolution electron energy loss spectroscopy (HREELS), structural determination by dynamical low-energy electron diffraction (LEED), thermal desorption spectroscopy (TDS) for desorption product analysis, work function measurements for determination of surface dipole orientation, and Auger electron spectroscopy (AES) for analysis of surface composition.

In order to have a fundamental insight into chemical interactions at surfaces, a model of chemisorption and catalytic reaction processes will be given in the following section to describe the details of specific research topics.

1.2 A Model of Heterogeneous Reaction Processes

The fundamental principle of a catalytic reaction can be explained by a simple

catalytic reaction: A+B $\longrightarrow$ C+D, as shown in figure 1.1. The mechanism of surface activation can be subdivided into three major steps discussed in the following subsections.

1.2.1 The First Step: Chemisorption

The first step shown in figure 1.1 is the chemisorption of reactants A and B onto the surface. In general, chemisorption on transition metals involves strong surface chemical bonds, with enthalpies of adsorption (ΔH_{ads}) in the range of 10-200 Kcal/mole [1,5]. Typical examples studied in this thesis include the adsorption of prototypical unsaturated hydrocarbons such as acetylene, ethylene, and benzene, and inorganic adsorbates such as CO and NO. The formation of new adsorbate-surface bonds is usually accompanied by a redistribution of the electron density within the adsorbed molecules. In order to investigate the nature of the surface chemical bond, surface vibrational spectroscopy by HREELS has been utilized. This technique is based on inelastic low-energy electron scattering, due to vibrational excitation, from metal surfaces [6]. Since its first successful demonstration in 1975 [7], HREELS is becoming the most versatile spectroscopic tool for obtaining vibrational spectra from submonolayer molecules.

To accurately assign the observed spectra, several steps have been taken during this study. These include (1) isotopic substitution, mainly to distinguish the difference between C-C and C-H vibrational modes [8], and (2) an extensive literature search for spectral information of model compounds. One striking observation from HREELS is that the surface chemical bond is "cluster like",-i.e., similar vibrational fingerprints exist for molecular species adsorbed on specific surface sites and bonded to multinuclear organometallic clusters [9,10,11,12,13,14,15]. In fact,

Model Heterogeneous Reaction Process:

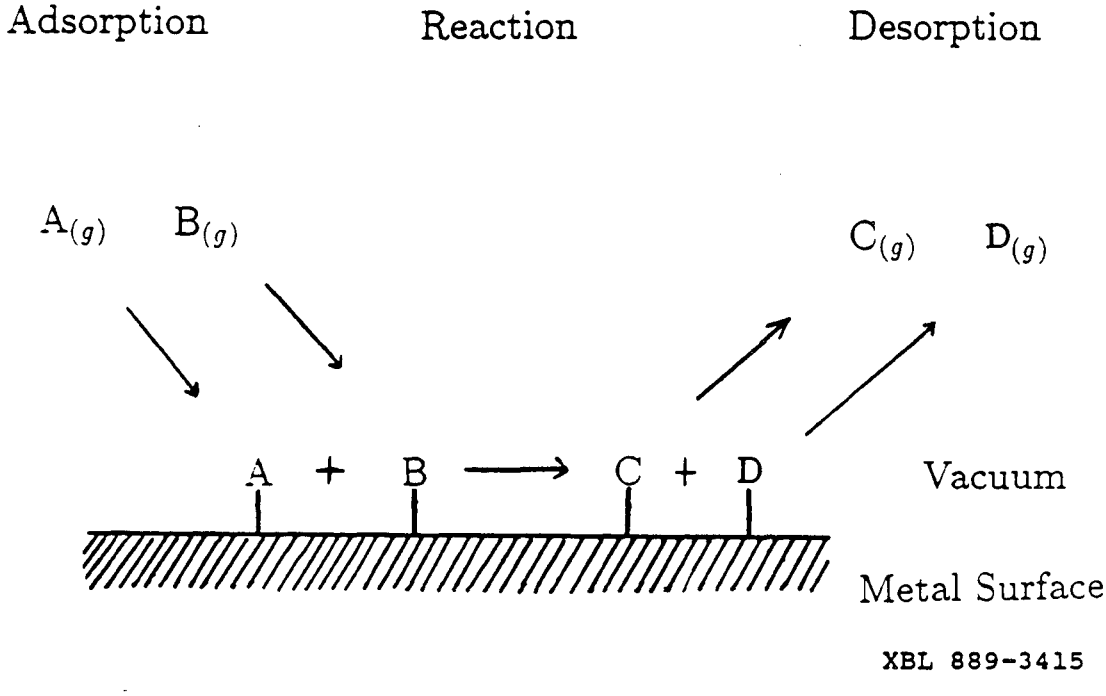

Figure 1.1: Three major steps–adsorption, reaction, and desorption–are shown to describe the fundamental processes happening at the vacuum-metal interface.

for virtually every surface species observed so far there is a cluster equivalent that was synthesized by organometallic chemists [13,15]. For example, acetylene adsorbed at the top, bridge, and fourfold sites on Rh(100) can be modeled by analogous acetylene bonding to mono-, bi-, or tetra-metallic cluster compounds [15]. This cluster-surface analogy links together the inorganic coordination chemistry to surface chemisorption [14]. Each adsorbate-substrate interaction can be viewed as a chemical complex with the adsorbate behaving as a ligand.

The surface chemical properties of transition metals toward molecular adsorbates can be characterized by either the trend toward C-C and C-H distortion of hydrocarbons or N-O and C-O weakening of inorganic adsorbates. The real-space structure of these strongly perturbed adsorbates can be further determined by LEED [16,17].

It is worth mentioning that the surface structure of an adsorbate depends strongly on parameters such as the surface coverage, temperature, pressure [18], and the presence of coadsorbates [19,20,21]. This implies that complicated adsorbate -substrate and adsorbate-adsorbate interactions are coupled to form the stable bonding geometries observed by static surface science techniques. The adsorbate-adsorbate interaction within a coadsorbed monolayer is of particular importance in modeling the effects of surface modifiers in catalytic reactions. Furthermore, this result can be correlated to coordination chemistry with analogous co-ligand effects [14]. In fact, one of the distinct features of coordination and cluster chemistry is the interaction between different ligands. In clusters, the substitution of one ligand by one that is electronically dissimilar may lead to different modes of binding for some ligands. For example, the substitution of carbonyl ligands in $Ir_4(CO)_{12}$ by a strong donor ligand like phosphine effects a shift of three terminal carbonyl ligands to bridge sites in a common face [14]. A similar site-shift effect of

either CO or NO induced by an electron donor coadsorbate has also been studied to substantiate the validity of the surface-cluster analogy [20,22,23]. The details of adsorbate-adsorbate interactions have been explored by work function measurements and vibrational spectroscopy. In fact, the data reported in the thesis show a universal shift of CO or NO toward higher coordination sites by coadsorption of an electron donor, such as Na or unsaturated hydrocarbons.

1.2.2 Surface Chemical Reaction by Thermal Activation

As shown in figure 1.1, after the formation of chemisorbed species, the coadsorbates, "A" and "B," could further react by thermal activation, and lead to products "C" and "D" adsorbed on surfaces. This surface reaction is one of the central issue in heterogeneous catalysis, as the primary effect of a catalyst on a chemical reaction is to enhance the rate by surface activation [1,24,25]. This also means the rate coefficient of the chemical reaction is increased by the presence of a catalyst surface. The consequential effect can be analyzed in terms of absolute rate theory, and the rate coefficient K is then given by

$$K = \frac{k_B T}{h} exp(-\Delta G_a / RT), \tag{1.1}$$

where k_B is the Boltzmann constant, ΔG_a is the Gibbs free energy of activation, and h is Planck's constant, and so the effect of a catalyst must be to decrease the free energy of activation. This in turn is composed of an entropy and an enthalpy of activation ($\Delta G_a = \Delta H_a - T\Delta S_a$). The entropic part of the activation energy in a surface-catalyzed reaction is usually less than that for an uncatalyzed reaction, because the transition state is immobilized on surfaces, resulting in loss of some translational freedom. Therefore, the enthalpy of surface activation must

be decreased relative to the uncatalyzed reaction to compensate for the entropic factor.

A typical potential energy surface of a catalyzed reaction relative to an uncatalyzed reaction is shown in figure 1.2 to demonstrate the effect [26]. The potential energy of adsorbed reactants and products are lower than in the gas phase due to the exothermic chemisorption process. A surface-catalyzed reaction can be seen by the lowering of the activation energy from E_{hom} (homogeneous uncatalyzed) to E_{het} (heterogeneous catalyzed). This lowering of the activation energy is a fundamental principle of catalysis.

The major surface reaction studied in this thesis is unimolecular decomposition as a function of temperature. Thermal fragmentation of acetylene, ethylene, and benzene on the Rh(100) surface has been studied over the temperature range of 200-800 K. In this case, unsaturated hydrocarbons were adsorbed below 200 K to form molecular adsorbates, and the rearrangement of the C-H and C-C bonds was detected by HREELS as a function of temperature and coverage. Due to strong distortions toward sp^3 hybridization of the molecular species, facile C-H and C-C bond dissociation was generally observed. A typical surface-activation example is the dehydrogenation reaction from acetylene (C_2H_2) to acetylide (C_2H):

$$C_2H_{2_{(a)}} \longrightarrow C_2H_{(a)} + H_{(a)}, \tag{1.2}$$

which happens at around 200-300 K on transition metals [21] even though a molecular beam study indicates that the bond dissociation energy is as high as 132±2 Kcal/mole [27].

In some cases, the catalytic industry uses CO to modify surface reactions. For instance, the selectivity of acetylene hydrogenation on supported palladium catalysts can be enhanced by adding CO [28,29]. This implies that coadsorbates

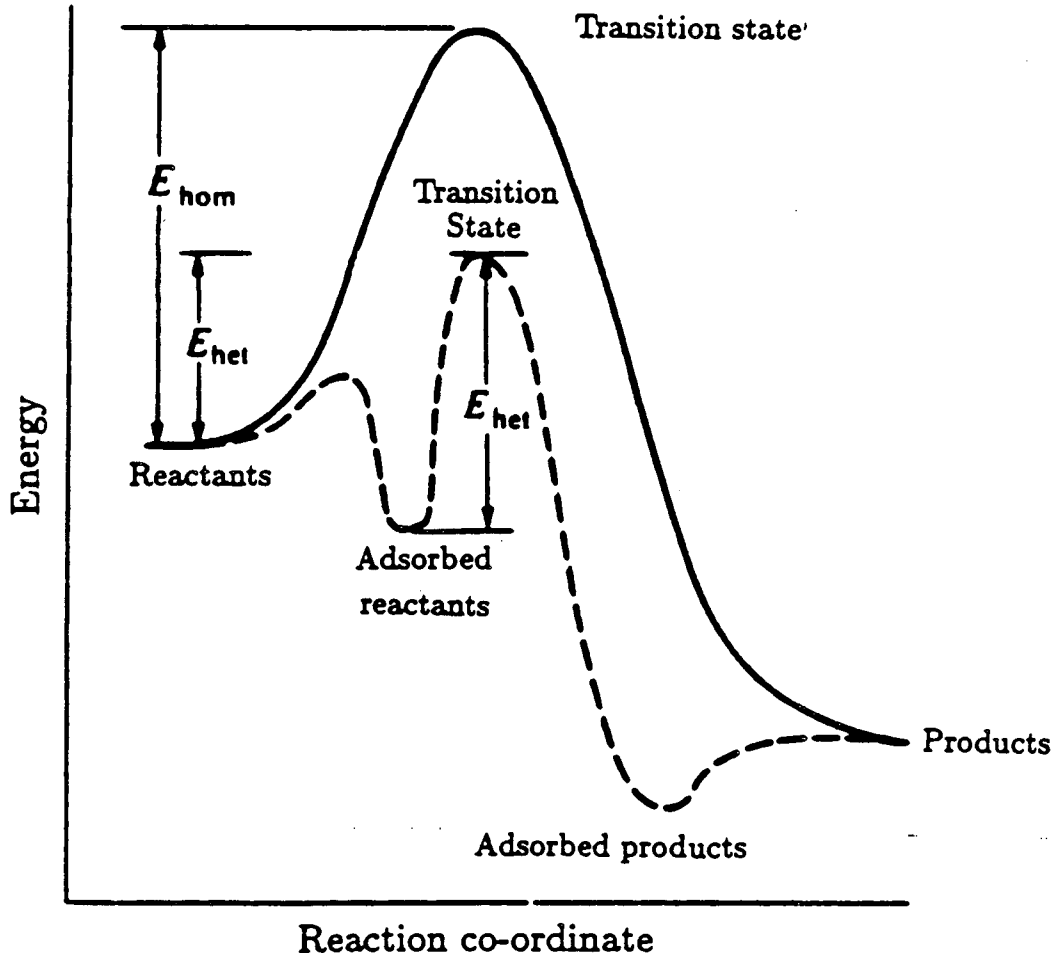

Figure 1.2: A one-dimensional potential energy surface is drawn to show the effect of surface interaction on the lowering of activation energy. E_{het} and E_{hom} represent the activation energies of catalyzed (heterogeneous surface reaction) and uncatalyzed (homogeneous gas-phase reaction) processes, respectively.

could have significant effects on surface chemistry. In order to pursue this topic, CO was adsorbed together with hydrocarbons to modify thermal decomposition pathways by coadsorption.

1.2.3 Thermally Activated Desorption of Products

The third step depicted in figure 1.1 is the desorption of products "C" and "D" by thermal activation. This then completes the total reaction from "A" plus "B" to form "C" and "D" through surface activation. There are an enormous number of heterogeneous catalytic reactions that follow the three-step sequence. For instance, ethylene hydrogenation involves a reaction between ethylene and hydrogen at surfaces to produce ethane, which then desorbs as gas-phase products. As can be seen in figure 1.2, the stronger the surface bond energy of the adsorbed product the higher the activation energy for desorption. One surface science technique, thermal desorption spectroscopy (TDS), is based on this fundamental idea [26,30]. This technique was applied in the thesis to study the surface dehydrogenation reaction of unsaturated hydrocarbons on Rh(100). A sequential hydrogen desorption is generally observed during the fragmentation process.

1.3 Overview

In this thesis, I will focus on the surface chemical bonding of prototype organic (acetylene, benzene, ethylene, ...) and inorganic (NO, CO, ...) compounds on Rh(111) and Rh(100) surfaces. The interaction between adsorbate and the thermal chemistry of different adsorbed species will also be addressed. The flow chart shown in figure 1.3 describes the route undertaken to achieve my research goals.

The major goal was to demonstrate the importance of surface science for the development of a fundamental understanding of surface structure and thermal chemistry. The long-term goal of this project would be the design of next-generation catalytic materials.

The abbreviated contents of the following chapters are given below:

- Chapter 2 introduces the experimental apparatus and various techniques used in this work.

- Chapter 3 concerns high-resolution electron energy loss spectroscopy, which is the major characterization technique used in this thesis. I discuss the basic instrumentation and the data-reduction process, including spectral analysis and surface symmetry analysis of the adsorbed species.

- Chapter 4 starts with a discussion of acetylene, benzene, and ethylene bonding and reactivity on the Rh(100) surface. The surface geometry, ordering, and thermal chemistry are extensively discussed by comparison with other metal surfaces. The trend of surface chemistry for these unsaturated hydrocarbons is reviewed and discussed.

- In chapter 5, the HREELS and dynamical LEED analysis results of (2x2)-3NO and c(4x2)-CCH_3(ethylidyne)+NO on the Rh(111) surface in the temperature range of 120-480 K is presented. It was found that the bonding geometry of NO is strongly dependent on coverage, surface temperature, and coadsorbed ethylidyne. These results are compared with similar findings of (2x2)-3CO and c(4x2)-CCH_3+CO on the Rh(111) surface and NO chemisorption on other transition metal surfaces.

- Chapter 6 focuses on the effect of CO and NO on surface ordering and the

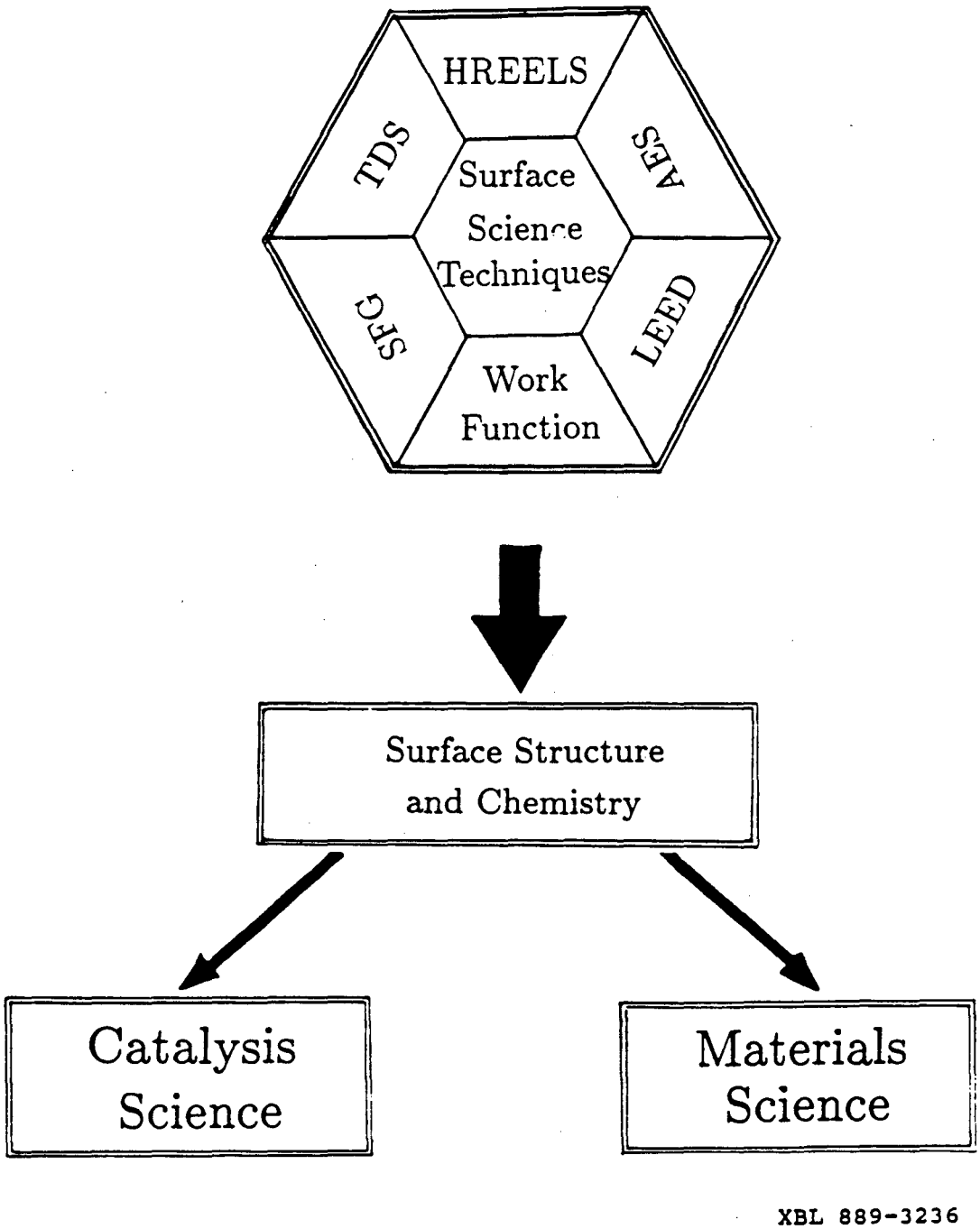

Figure 1.3: Flow chart of my research goals.

structure of coadsorbates on Rh(111) and Rh(100) surfaces. A generalized model based on surface dipole-dipole interaction between coadsorbates is proposed to explain the "coadsorbate-induced ordering" phenomenon. Similar coadsorbate-induced effects on other metal surfaces are compared and reviewed.

Chapter 2

Experimental Methods

2.1 Apparatus: The Design Consideration of Ul tra-High Vacuum Chambers

The experiments were carried out in three different ultra-high vacuum (UHV) chambers with base pressures of 2 x 10^{-10} torr. Each chamber was equipped with various surface analytical techniques such as low-energy electron diffraction (LEED), Auger Electron Spectroscopy (AES), and a mass spectrometer for thermal desorption spectroscopy (TDS). These systems also have an ion sputter gun for sample cleaning and a gas manifold and several leak valves for introducing gas onto the crystal surface.

Two of the chambers, which have high-resolution electron energy loss (HREEL) spectrometers, were used for vibrational analysis. The third chamber is equipped with a video LEED system for quantitative structural analysis and is called the "video LEED chamber" (as shown in figure 2.1). One of the HREELS chambers (as shown in figure 2.2) has a high-pressure (HP) cell, which is also capable of running surface reactions at 1 atmosphere ambient pressure within the cell, while still maintaining UHV in the rest of the chamber. As the major part of the thesis

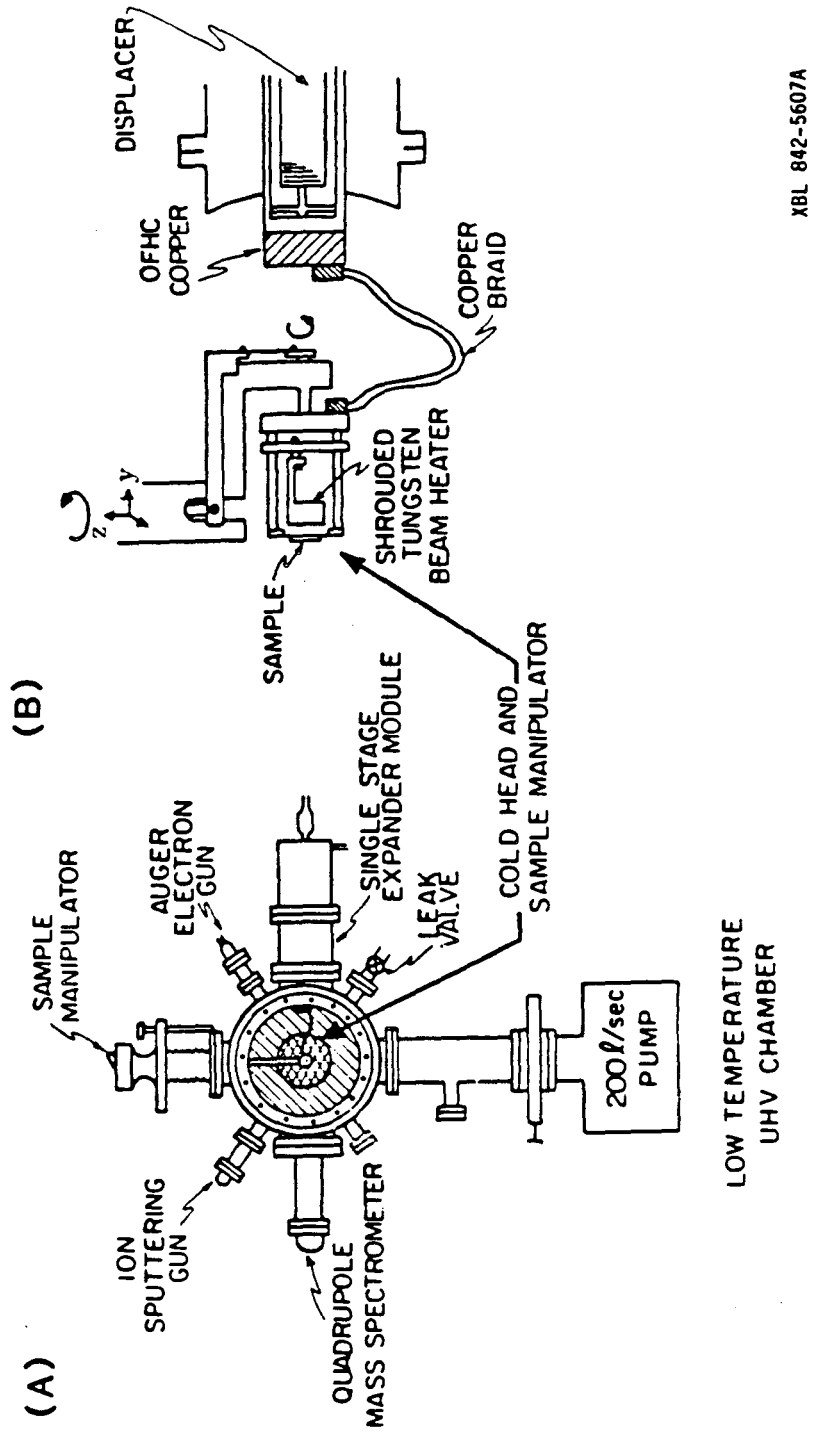

Figure 2.1: (A). Front view of LEED apparatus showing various surface science techniques attached to the system. (B). The details of cooling and heating connections to the sample are shown.

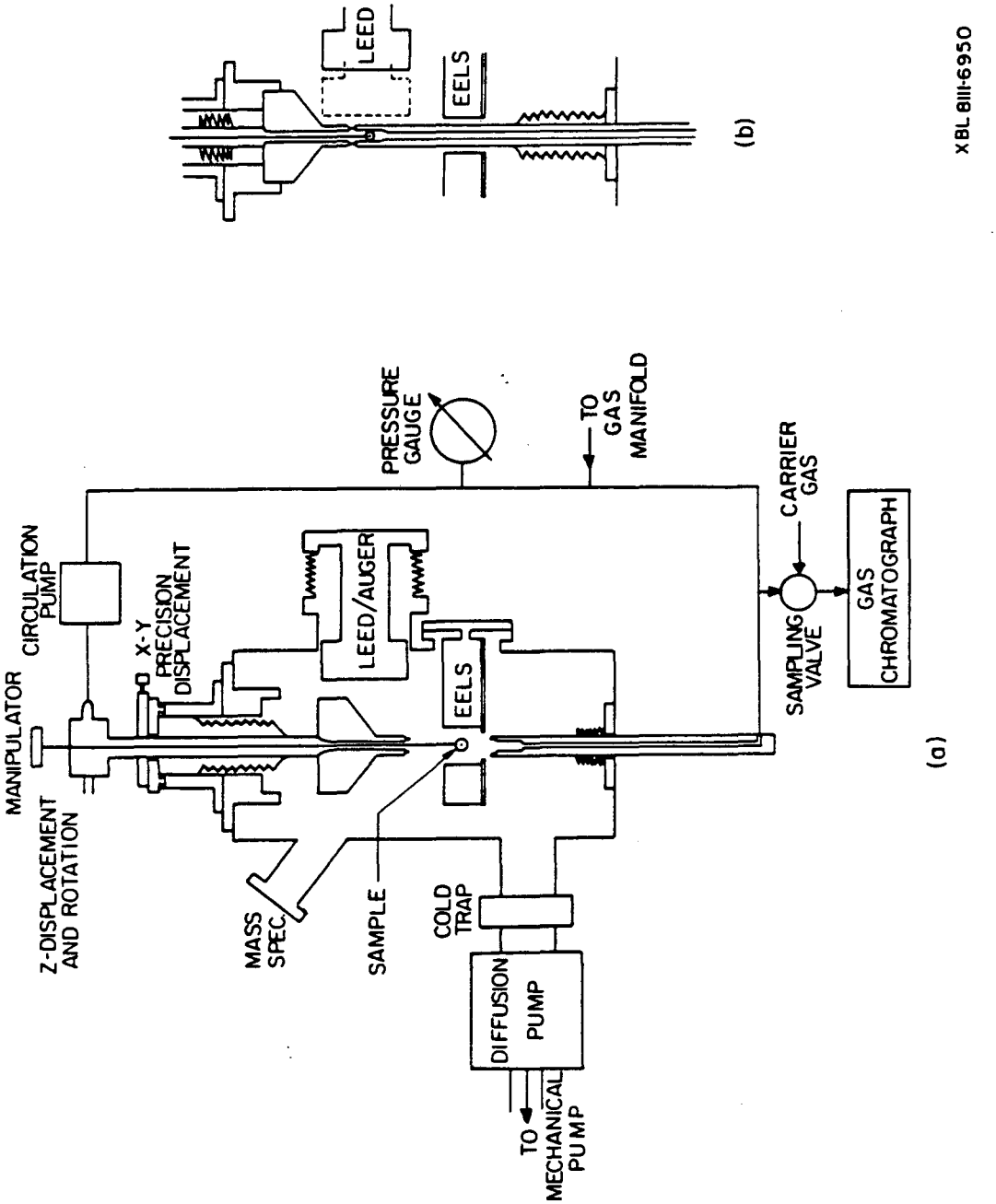

Figure 2.2: In (a), the side view of the chamber and external reaction loop of the high-pressure reactor are shown. The crystal is positioned at the lower level for vibrational analysis. In (b), the sample was positioned at the top of system and enclosed in a HP cell tube. The LEED/AES optics were retracted during positioning of the sample in both cases.

work was done in this HREELS chamber and the video LEED chamber, only these two systems will be described. The other HREELS system was used mainly for work function measurements and will be discussed only when necessary.

Figure 2.2 a is a side view of the HREELS chamber with high pressure/UHV surface analysis capabilities. Details of the design have been reported and improved by several previous workers [13,31]. This UHV chamber is pumped mainly by a 6-in. oil diffusion pump (DP) (Varian VHS-6) with a liquid nitrogen cryotrap. Another two backup pumps (omitted in figure 2.2 for clarity), an ion pump with 400 l/sec pumping speed and a water cooled titanium sublimator (Varian Ti-ball), were used either to reduce pumpdown time or for major overnight pumping to avoid oil back-streaming from the DP. Viton O-ring sealed gate valves were used to isolate these pumps from the main chamber. Routine operating pressures of 10^{-10} torr can be obtained by baking the chamber for 24-48 hr. at 400-420 K after exposure to high-pressure conditions. The temperature was monitored carefully by chromel-alumel thermocouples attached to the crystal sample, HREEL spectrometer, or chamber wall. Periodically, an overnight baking was necessary after the high-pressure cell was exposed to reacting gas. The system was baked internally using a tungsten halogen lamp (GE quartz line Q1500T3/CL), which efficiently heated up the high-pressure cell and HREEL spectrometer. In order to ensure a homogeneous thermal distribution around the system, an external baking by heating tapes covered with aluminum foil was also used to assist the baking.

The sample manipulators were used to translate and rotate the sample to specified positions for surface science studies. In the HREELS chamber, a 20-cm translation along the central axis of the chamber (defined as z direction) was made possible by welded bellow seals [figure 2.2 a]. This motion is extremely important for a two-level system. The other two axes (x and y) can also move by ± 1 cm.

For rotation, 360 degrees around the z axis was the only degree of freedom in the HREELS chamber, while two extra motions, namely "azimuthal" and "tilted" rotations, were possible within the video LEED chamber for more accurate sample alignment.

As shown in figure 2.3, the major part of the manipulator consists of two meter-long copper tubes attached to a tubular ceramic feedthrough at the top. Inside these tubes, thin stainless steel tubes were used to flow liquid nitrogen to a reservoir close to the sample. The liquid nitrogen was sucked by the "house" vacuum line. Several insulated Cu-Be fittings were tied along the tubes to reduce stresses on the samples caused by uneven thermal contraction or expansion. The UHV seal of this manipulator was made by two differentially pumped o-rings. Rotational motion along the z-axis was facilitated by a Kaydon slim-line bearing.

The crystal in the HREELS chamber was mounted on the manipulator by spot-welding 0.020-in.-diameter tantalum wire between the crystal edge and 1/8-in. tantalum rods that were fastened to copper tubes by set screws. The crystal temperature was monitored by spot-welding 0.005-in.-diameter chromel-alumel thermocouple wires to the top edge of the crystal. An ice/water bath was used as a reference junction for thermocouple voltages. The single crystals were resistively heated by passing currents through the connection between the crystal and supported Ta wire. Cooling was provided by flowing liquid nitrogen within the copper tubes, which were in thermal contact with the sample [32]. Sample temperatures of 85-1250 K could be readily obtained by these methods.

The crystal in the video LEED chamber was mounted by spot-welding the back side of the crystal onto two stainless steel plates that were attached to the copper stand at the bottom of the manipulator and connected to the cold head through the copper braid. Different cooling and heating systems were used, and the setup

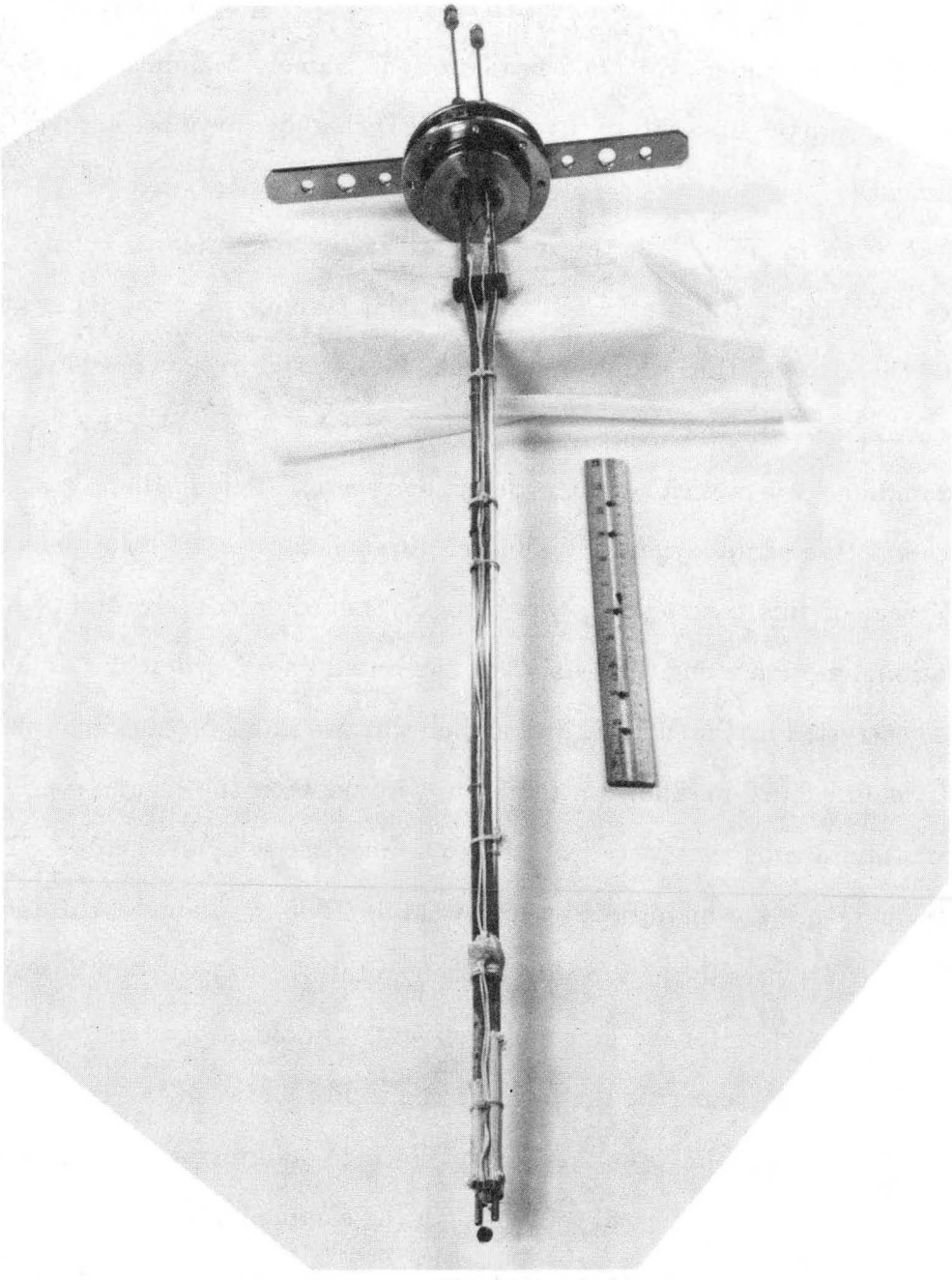

XBB 889-10130

Figure 2.3: The mounted disc-shaped Rh(100) single crystal is shown at the bottom of this meter-long manipulator before insertion into the chamber.

is shown in figure 2.1B. A single-stage Displex closed-cycle refrigeration system (Air Products, Displex OSP) was used to cool the sample down to 30 K. The heat was conducted through copper braid connections (10 cm long x 0.8 cm wide) between the expander module of the cold head and the manipulator, which in turn was connected to the crystal. A shrouded tungsten beam heater was enclosed in a tantalum box and was isolated from the cooling system by quartz spacers. An electron beam generated by thermionic emission from the filament was accelerated toward the sample's back side by a -1.0 to -2.0 keV bias voltage relative to the crystal. By the combination of electron-bombardment heating and He refrigerator cooling, the crystal can be flashed to $T \geq 1200$ K in 60 sec and recooled back down to 30 K in another 90 sec.

The sample preparation and analysis were done on two separate levels in the HREELS chamber, as shown in figure 2.2 a. The upper level is equipped with :

- a conventional four grid LEED optics (Retarding Field Analyzer, Varian 981-0127) for both LEED and AES measurements
- a glancing-incidence electron gun (Varian 981-2454) for Auger excitation
- a quadruple mass spectrometer (UTI-100C) for TDS and residual gas analysis (RGA)
- an ion sputter gun (PHI, 4-161) for crystal cleaning
- a nude ion gauge (Varian 971-5008) for pressure monitoring
- a metal deposition source for dosing of alkali metals(SAES), titanium, or other metallic materials onto the surface
- three precision leak valves (Varian 951-5106) for controlling gas dosage onto the sample surface.

The lower level had a HREEL spectrometer (McAllister Technical Services) for surface vibrational analysis. This spectrometer is enclosed in a μ metal shielding to reduce magnetic fields. Due to the bulky shaft around the manipulator (necessary to disperse the sealing force, about 2200 psi, when closing the high-pressure cell), the retarding field analyzer (RFA) of the LEED/AES optics is mounted on retractable bellows. In the video LEED chamber, all the surface analytical equipments was located on one level, as shown in figure 2.1A.

The sealing of the HP cell around the sample within the HP/UHV HREELS chamber is shown in figure 2.2 b. The manipulator bellows are contracted and the sample is moved to the very top of the chamber. A hydraulic piston is pumped to pressurize knife-edge seals into a copper gasket between the stainless steel HP cell tube and the manipulator shaft to 2200 psi. Stainless steel tubings of 3/8 in. diameter is used to connect both the top of manipulator and the bottom of HP cell. This closed loop can serve as a batch reactor for studying catalytic reaction on model single-crystal surfaces. The pressure in the reactor is monitored by a Heise gauge (Temp. Comp., C-58992). The gases are circulated by a bellows pump, and 0.5 ml gas samples can be taken through an high-pressure gas chromatograph (Hewlett Packard 5720A) in series with an integrator for product analysis.

The HP cell was used extensively in this work for transferring the sample in and out of the vacuum chamber while still maintaining UHV inside the main chamber. The stability of the coadsorbed monolayer CCH_3+NO on Rh(111) in air was studied by flowing room air through the HP cell. This result will be discussed in chapter 5.

2.2 Sample Preparation and Cleaning Procedure

Three Rh(111) and one Rh(100) single crystals were used over the course of the experiments; all four were 0.5-1.0 cm^2 disks, 2 mm thick and cut by spark erosion from a single-crystal rod of $\geq$ 99.996% purity (Materials Research Corperation). They were prepared by Winnie Hepler of the LBL staff. The surface orientations were within 1° of the ideal fcc(111) or (100) planes, as judged by Laue x-ray diffraction. Periodically, the crystals were repolished using 0.25-6 micron diamond paste and a 0.05-micron alumina slurry to regain a microscopically flat surface [33,34].

Although a high-purity single crystal was obtained commercially, extensive surface cleaning was necessary to remove the original bulk impurities and surface contaminants introduced during crystal cutting and polishing. This is a very crucial step in surface science research, as a lot of surface chemical properties are extremely sensitive to minor residual impurities at surface concentrations of 1-5% of a monolayer. For a new rhodium sample, the major contaminants are boron, sulfur, phosphorus, silicon, and hydrocarbons, as determined by AES and HREELS. Both physical (argon ion sputtering) and chemical (oxidation or reduction reaction) treatments were combined to remove these contaminants from the near-surface region. Cleaning procedures for various materials have been reviewed in a recent publication [35].

For Rh(111) surfaces, a three-step cycle was used as a routine cleaning procedure:

- Oxygen treatment in 1-8x10^{-7} torr O_2 pressure at 1000-1100 K for 5-30 minutes. Most of the impurities could be driven to the near-surface region by formation of the low surface-free-energy oxide. Carbon, and some of sulfur and boron, could be eliminated by forming volatile oxides at the surface temperature indicated above. The rest of the oxides and some elemental species could only be removed by physical sputtering.

- Argon ion sputtering using 1-keV Ar^+ beams with about 5 μA crystal current to ground ($5x10^{-5}$ to $1x10^{-4}$ torr of argon) at room temperature for 10-30 minutes. This process would sputter away the oxides or other contaminants that could not be eliminated by chemical treatment. Occasionally, sputtering at high surface temperature (800-1000 K) or with some additional oxygen partial pressure ($1x10^{-7}$ to $1x10^{-6}$ torr) was found to enhance surface segregation and the cleaning of impurities. A successful sputtering would generate a rough, disordered surface as judged by the appearance of fuzzy LEED patterns.

- Three to five minutes of annealing at 1250 K (The melting point of rhodium is 2230 K) to produce LEED patterns representative of a smooth and well-ordered crystal surface. This process removed the physical damage caused by high-energy ion sputtering.

The most persistent contaminant for rhodium was boron, which can only be reduced by prolonged cycles of oxygen treatment and Ar^+ sputtering. It has also been suggested that chemical treatment with 1 atm of hydrogen at 1300 K for 3-4 days could also be helpful [36]. The effect of residual boron on the enhancement of surface reactivity toward NO and CO_2 dissociation on Rh(111) has been reported recently [37].

After first obtaining a clean Rh(111) surface, one cycle of cleaning is sufficient to maintain surface cleanliness even after exposure to air. Small amounts of surface carbon can be dissolved into the bulk by heating above 1100 K [13].

Extra care is necessary in cleaning a Rh(100) surface. This is because surface hydroxyl or water species form easily after oxygen treatment from background reactions [38,39]. The best recipe for cleaning a Rh(100) surface was Ar^+ sputtering

at 1100 K, and oxygen treatment and flashing to 1100 K, immediately followed by a saturation dosage of CO (7-10 L) at 320 K to scavenge residual O_2 [38], and to passivate the surface from any background gas adsorption. A sharp (4 $\sqrt{2}$ x2 $\sqrt{2}$) R45° LEED pattern caused by saturated CO adsorption guaranteed a successful surface cleaning [40]. The crystal sample was then cooled to experimental temperature, and a clean surface was obtained by flashing to 1000 K to desorb CO. Unlike Rh(111), the carbon deposit from hydrocarbon fragmentation cannot be removed simply by dissolution into the bulk, so that oxygen treatment (10-15 minutes) was always necessary to remove carbon and traces of boron after every experimental run.

During the sample-cleaning process, the surface cleanliness was regularly checked by AES until the contaminant level was less than 1% of a monolayer. This was then followed by HREELS analysis, which provided more surface sensitivity and less electron-beam-induced surface segregation than the 1.5-2.0 keV electron beam used for AES excitation. A clean surface should have a sharp, well-ordered (1x1) LEED pattern with low background intensity. The HREEL spectra of such a surface should have no energy-loss peaks caused by contaminants except for a to a fractional coverage of CO (less than 0.1 %) from background adsorption. On the other hand, a dirty sample with adsorbed hydrocarbons could have peaks in the range of 700-900, 1300-1400, and 2850-3050 cm^{-1}. Intense energy-loss peaks within 600-1450 cm^{-1} are indicative of surface oxides like PO_x, BO_x, and SiO_x [13]. Several LEED patterns caused by these contaminants were also reported on dirty Rh(111) or Rh(100) samples [13,39].

Table 2.1: Summary of reagents used in this thesis.

Reagent	Source	Purity (wt %)	Contaminants
Ar (argon)	LBL-Matheson	≥99.998	H_2O
CO (carbon monoxide)	LBL-Matheson	≥99.5	—
C_2H_2 (acetylene)	LBL-Matheson	~99.5	acetone
C_2D_2 (acetylene-d_2)	MSD Isotopes	≥98 at% D	—
C_2H_4 (ethylene)	LBL-Matheson	CP, ~99.5	—
C_2H_4 (ethylene)	LBL-Matheson	Research, 99.98	—
C_2D_4 (ethylene-d_4)	MSD Isotopes	≥99 at% D	C_2D_3H
C_4H_6 (1,3-butadiene)	LBL-Matheson	CP, ~99	—
C_6H_6 (benzene)	Fisher	~99.9	—
C_6D_6 (benzene-d_6)	Norell Chemical	≥99 at% D	C_6D_5H
D_2 (deuterium)	LBL-Matheson	~99.5 at% D	HD, H_2
H_2 (hydrogen)	LBL-Matheson	~99.9	CO
NO (nitric oxide)	LBL-Matheson	≥99.5	—
O_2 (oxygen)	LBL-Matheson	≥99.9	H_2O

2.3 Gas Dosing and Surface Coverage Calibration

2.3.1 Reagent Preparation

Table 2.1 lists the chemical reagents used in this thesis. Most of the gases were obtained from lecture bottles ordered through the LBL cylinder shop. The deuterated gases (MSD isotope) were stored in break-seal flasks fitted with O-ring sealed teflon stopcocks. Cajon ultra-torr fittings were used between glass tubing and the stainless steel tubing of gas manifolds.

The liquid chemicals (C_6 hydrocarbons) were stored in glass vials fitted with teflon stopcocks. Benzene was stored either over CaH_2 or 3Å molecular sieve to facilitate dehydration.

For liquid chemicals, several freeze-pump-thaw cycles were used to outgas air in the sampling vial. All gases except acetylene, O_2, and Ar were used as received.

Acetylene was passed through a dry ice/acetone molecular-sieve trap to remove acetone, while liquid-nitrogen-cooled u-tubes were utilized to remove water vapor in the O_2 and Ar gases.

The purity of the reagents was carefully checked by gas chromatography and mass spectrometry. The most definitive test was done by adsorbing gas at low surface temperatures (85-100 K), where multilayer molecular species could be formed. The surface vibrational fingerprint of these physisorbed molecules could be checked by comparison to infrared spectra reported in the literature for gas or liquid samples.

2.3.2 Gas Dosing

After checking for purity, gases were admitted to the chamber through a manifold connected to two variable-leak valves. Manifold lines were connected to the top and bottom leak valves and the high-pressure cell. These were pumped by both mechanical and sorption pumps to less than 1 mtorr. The manifold was flushed with reagent gases several times before filling the lines. The top leak valve produced a diffuse spray of gas that backfilled the chamber with a uniform pressure distribution before adsorption. The bottom leak valve was attached to a microchannel array doser positioned about 4 cm from the surface (at the z position about 8 cm from the top of the manipulator). A doser enhancement in the molecular flux at the surface of five (calibrated for CO by TDS) over the measured chamber pressure was obtained for the bottom doser.

All gas exposures were reported in langmuirs (L). 1.0 L corresponds to an exposure of 10^{-6} torr-sec. The reported exposures have been corrected for background pressure and doser enhancement, but they are not corrected for the ion-gauge

sensitivities of different gases. The definition of one-monolayer (1-ML) coverage of adsorbates is "a coverage with one adsorbate per surface atom." For instance, θ_{CO}=0.33 on Rh(111) means 0.33 monolayer coverage with one CO molecule for every three rhodium atoms. The surface atomic densities of Rh(111) and Rh(100) are 1.6×10^{15} and 1.4×10^{15} atoms/cm^2, respectively. These numbers were used to calculate the absolute surface coverages of adsorbates. The term saturation coverage is also used to represent the maximum coverage attainable at the adsorption temperature. Typical saturation coverages were 0.25-0.75 for small molecular adsorbates like CO or NO, and about 0.1-0.33 monolayer for the hydrocarbons studied in this thesis. The surface coverages of adsorbates were calibrated by LEED, AES, and TDS. These characterization methods will be discussed in the following sections.

2.4 Surface Characterization Techniques

2.4.1 Introduction

In this thesis, a combination of surface science techniques has been used to characterize the bonding geometry, surface coverage, desorption kinetics, ionization energies, and chemical reactivity of adsorbed molecular overlayers. Among these, energy-resolved electron spectroscopies are major diagnostic tools for surface analysis. Typical example of an electron spectrum is shown in figure 2.4. In this case, a Rh(111) surface covered with (2x2)-ethylidyne was bombarded by an electron beam of energy E_p, and the intensities of the scattered primary (solid line) and secondary (dashed curve) electrons are shown as a function of their kinetic energy. The important features of this curve include:

Energy Distribution of Scattered Electrons from a
(2x2)-CCH_3 (ethylidyne) Overlayer on Rh(111) at 220 K.

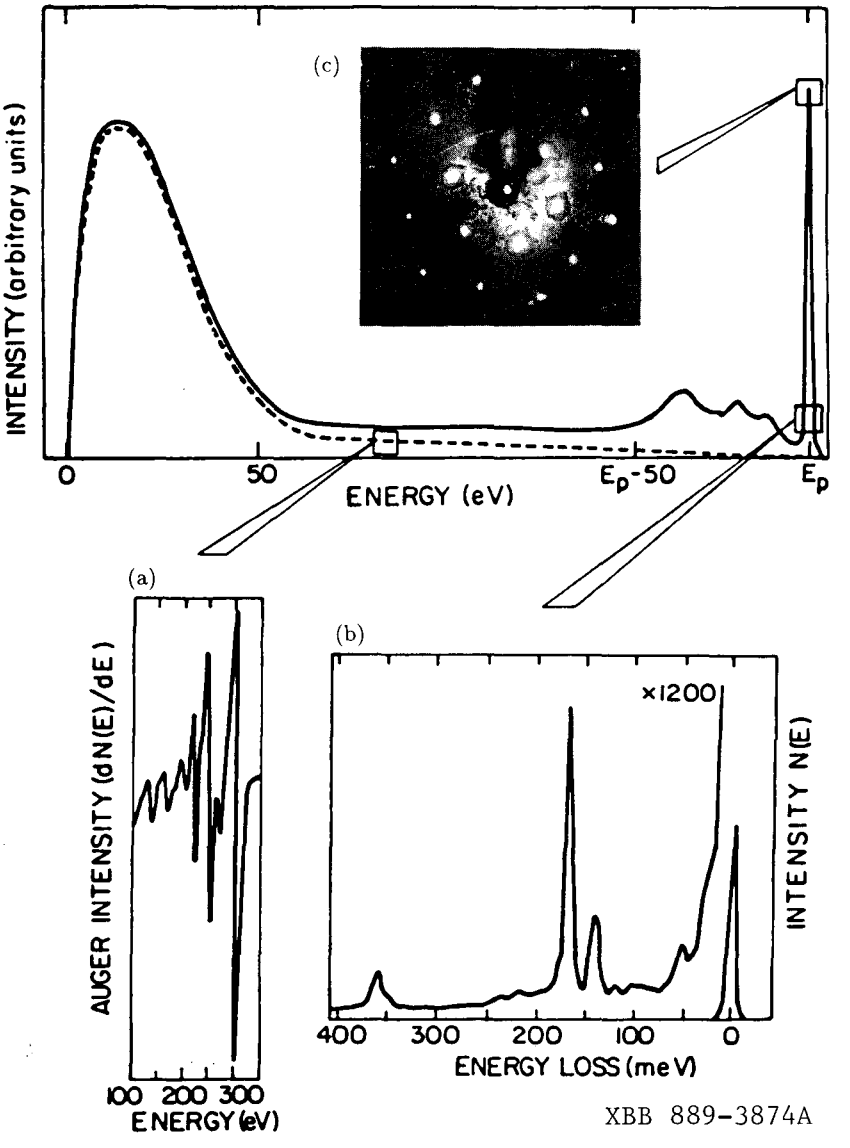

Figure 2.4: A typical example of an electron-distribution [N(E)] curve after a sample is struck by a monoenergetic electron beam of energy E_p. The AES, HREELS, and LEED patterns are shown in inserts (a), (b), and (c), respectively.

- The broad and intense peak on the left side is from low-energy secondary electrons generated from inelastic scattering between primary electrons and electrons in the solid. These can be used to measure the work function.

- The small peaks in the medium-energy range are caused by secondary Auger emission processes. The derivative collection mode for Auger electrons generated from a Rh(111) surface covered with ethylidyne is shown in insert (a).

- The elastic primary electrons at E_p are caused by electron diffraction from the Rh(111) surface, a (2x2)-ethylidyne pattern is shown in insert (c). The analysis of scattering intensity as a function of energy can provide detailed structural information concerning adsorption sites, bond lengths, and bond angles.

- The inelastic electrons with energy losses in the range of 10-500 meV to the left of E_p can be resolved by a high-resolution spectrometer. The vibrational excitation energies of adsorbates and surface phonon modes can be obtained by monitoring electron intensity versus energy loss as shown in insert (b).

- At higher energy losses, up to 50 eV below E_p, electronic excitations and plasmon losses can also be detected. This is called electronic EELS, in order to distinguish it from vibrational HREELS.

Both primary and secondary electrons with kinetic energies of 2-1000 eV are involved in the processes mentioned above. The mean free path of electrons within this energy range is about 5-10 $\AA$ [1]. This makes the electron spectroscopic techniques extremely surface sensitive in comparison to conventional optical techniques.

In the following sections, a brief discussion of the principles and applications of LEED, AES, work function measurement, and thermal desorption spectroscopy (TDS) will be presented. The major technique, HREELS, will be discussed at length in chapter 3.

2.4.2 Low-Energy Electron Diffraction (LEED)

In 1924, the possibility of electron diffraction was proposed by de Broglie (as a graduate student!) based on a theoretical description of wave mechanics [16,41]. De Broglie postulated that the wavelength λ of an electron with linear momentum p is given by

$$\lambda = h/p, \tag{2.1}$$

where h is Planck's constant. We know the momentum p of an electron can also be related to kinetic energy E :

$$p = mv = [(\frac{1}{2}mv^2)(2m)]^{\frac{1}{2}} = (2mE)^{\frac{1}{2}}. \tag{2.2}$$

Combining Eqs. 2.1 and 2.2,

$$\lambda(\mathring{A}) = h/p = h/(2mE)^{\frac{1}{2}} = [150/E(eV)]^{\frac{1}{2}}. \tag{2.3}$$

In order to observe electron diffraction, the incident beam has to satisfy the condition $\lambda \leq$ d, where d is the interatomic distance within the surface lattice. Thus, in the energy range 20-200 eV the wavelength of electrons varies from 2.7 to 0.9 $\mathring{A}$, smaller than or equal to most of the interatomic distances in materials. This is why these low-energy electrons were used during LEED measurements.

Compared to x-ray diffraction, which is an optical scattering technique applied extensively to solve bulk crystal structures [42], LEED has a scattering cross

section six orders of magnitude larger. The mean free path of an electron beam with 20-200 eV energy is around 5-10 $\AA$, or about 2-3 atomic layer thicknesses. Therefore, LEED has enough surface sensitivity to probe the structure of the topmost layers. On the other hand, a simpler kinematical single-scattering calculation is sufficient for modeling x-ray diffraction, while for LEED, dynamical multiple-scattering calculations are needed to model the electron scattering with comparable accuracy. Such an involved theoretical model also prohibits LEED from becoming a routine structural analysis like x-ray diffraction.

The first experimental observation of LEED was made by Davisson and Germer at Bell Laboratories in 1925 [43]. The electron diffraction from a (111) face of a nickel sample was reported after an accidental high-temperature recrystallization of polycrystalline nickel. Since then, tremendous experimental progress has been made to obtain both qualitative and quantitative pictures of the surface structural information.

The most commonly used electron optics for LEED measurements is based on a "post-accelerated" four-grid LEED optics. A schematical LEED experiment is shown in figure 2.5. In this setup, a monoenergetic electron beam (20-300 eV) is directed onto a single crystal that backscatters a portion of the incoming electrons. A set of hemispherical grids is used to filter out the inelastically backscattered electrons, while the elastically backscattered electrons are post-accelerated onto a phosphorous screen for viewing of the diffraction pattern. The diffraction pattern can then be viewed and photographed outside the UHV chamber. A Polaroid camera is commonly used for photographing the diffraction pattern, and most published LEED patterns are obtained in this way. This provides a qualitative observation of the surface ordering and phase transitions as a function of surface temperature and coverage.

(A)

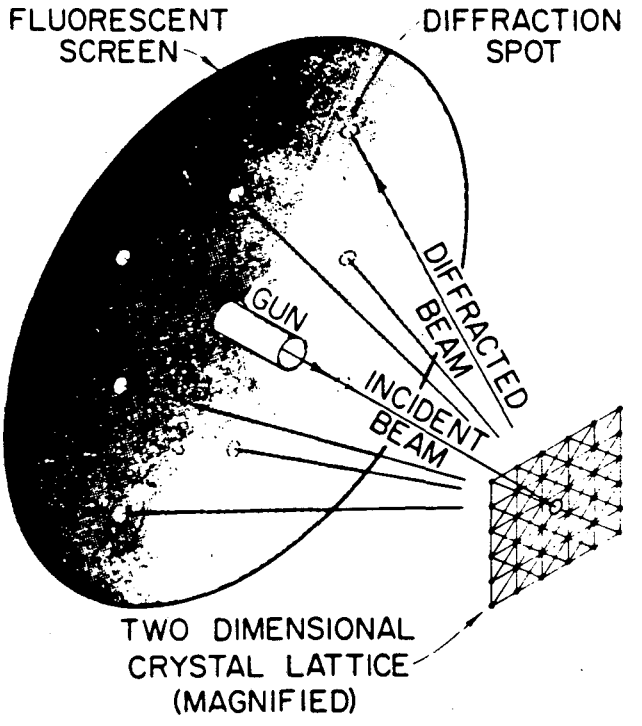

(B)

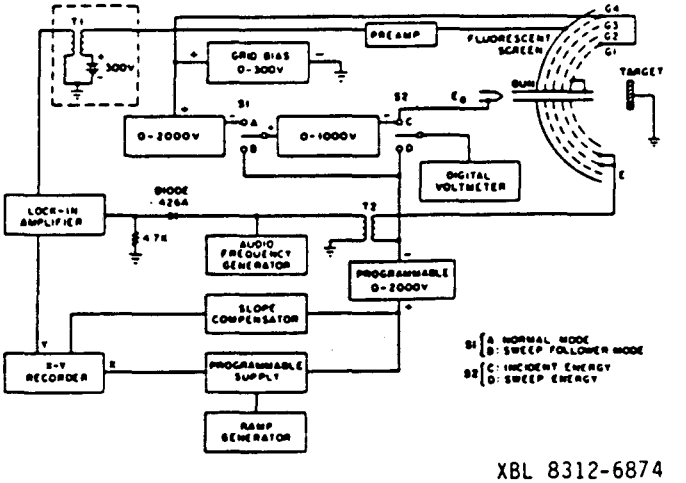

XBL 8312-6874

Figure 2.5: (A). Simple picture of electron scattering experiment from a 2-dimensional square lattice. (B) A schematic diagram of a four-grid retarding field analyzer used for LEED and AES. In the LEED mode, a DC bias is applied across G2 and G3 to suppress inelastic electrons. In AES, an extra, small AC modulation voltage is also connected to use these grids as a high-pass energy filter. G1 and G4 are grounded in both cases.

In order to perform quantitative measurements, a video LEED system was used to monitor diffraction intensities as a function of electron-beam energy or crystal orientation. This system was developed and built by Dr. D.F. Ogletree and LBL supporting staff before the author arrived [44,45]. The experimental setup of such a video LEED UHV chamber and the details of data-reduction procedures are shown in figure 2.6 (A) and (B), respectively. An LSI-11/23 computer was interfaced with both electron gun power supply and video system. The Varian (Model 981-2145) LEED power supply was modified to allow external voltage programming by computer. A video camera (Panasonic, Model WV-1550) with fast lens and high-sensitivity vidicon tube (18-mm Newvicon type S4075 vidicon tube with a CdZnTe target) was used to image the LEED pattern on the phosphorous screen of a conventional LEED optics. This camera was enclosed in a light-tight box attached to the view port of the vacuum chamber. A video cassette recorder (Panasonic, Model NV8050) was used to record the video signal by using the standard cassettes (Fuji HG VHS), and the images were simultaneously displayed on a black-and-white monitor. A typical data collection time was about 3 seconds per incident beam energy, and about 5 minutes for a full scan (20-200 eV with 2-eV increments). These data were stored on the video cassette for later data analysis.

During the data-analysis procedures shown in figure 2.6B, a videotape of the LEED experiment was sent to the video processer. The image was digitized with 8-bit accuracy, i.e., 256 gray levels. The output is a two-dimensional digital intensity map with resolution of 512 x 480 pixels of the original LEED pattern. As shown in figure 2.6B, for each diffracted beam in the LEED pattern (step 1), the digital intensity map is used by a program to calculate the integrated intensity of each spot (step 2). lining up the intensity (I) as a function of beam voltage (V), an

(A) Video LEED System

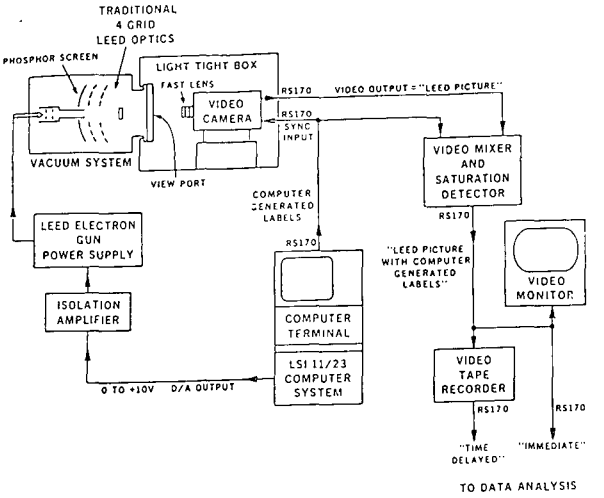

(B) Data Reduction Procedure

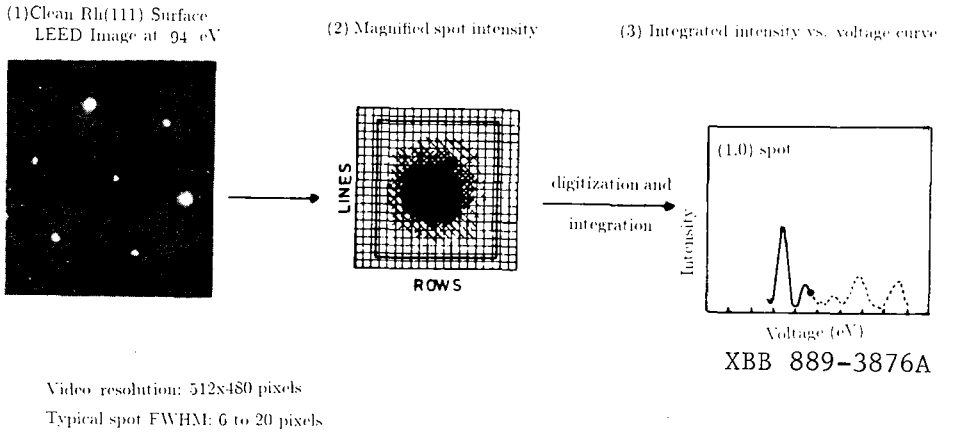

Figure 2.6: (A) Block diagram of a video LEED data-acquisition system, showing video signal and synchronization connections. (B) Simplified flow chart of data-reduction procedures for a clean Rh(111) surface, involving three major steps.

experimental I-V curve can be generated (step 3).

The normal incidence was obtained by visual comparison of symmetric equivalent spots. Rotational motion of the crystal along the manipulator axis (θ angle) was used for off-normal LEED data collection. The azimuthal angle was adjusted by rotation around the surface normal (axis perpendicular to surface, ϕ angle).

Typical I-V curves for each symmetry group (groups of spots that are symmetrically equivalent) can be deduced by averaging over the spots belonging to each group. Normal incidence was also confirmed by similarities in various features of the electron diffraction for spots of equivalent symmetry. After data averaging of these spot intensities, an I-V curve for each symmetry group with enhanced signal-to-noise could be obtained.

Following the generation of experimental I-V curves for each symmetry group of a diffraction pattern, a theoretical model calculation is started. A simplified picture of the procedure is shown in figure 2.7, for an example of Rh(111)/($\sqrt{3}$ x $\sqrt{3}$)R30° -CO. In this case, a LEED pattern of CO adsorption on Rh(111) is obtained at 0.33 monolayer coverage. The experimental I-V curve of the (1,0) symmetry group is shown in the middle of the figure. A series of theoretical models based on other experimental techniques such as HREELS are proposed. The preferred adsorption site is top-site CO, with ν(C-O) of 2010 cm^{-1} from vibrational analyses [31].

By changing the C-O bond length from 0.9 to 1.2 $\AA$, four theoretical I-V curves can be obtained from multiple-scattering calculations of the assumed structure. Several "goodness of fit" schemes, labeled R-factor analyses, were used to compare the experimental and theoretical I-V curves [16,17]. These are mainly based on the relative intensities and peak positions of these two curves. An average of five different R-factors was generally used in this thesis.

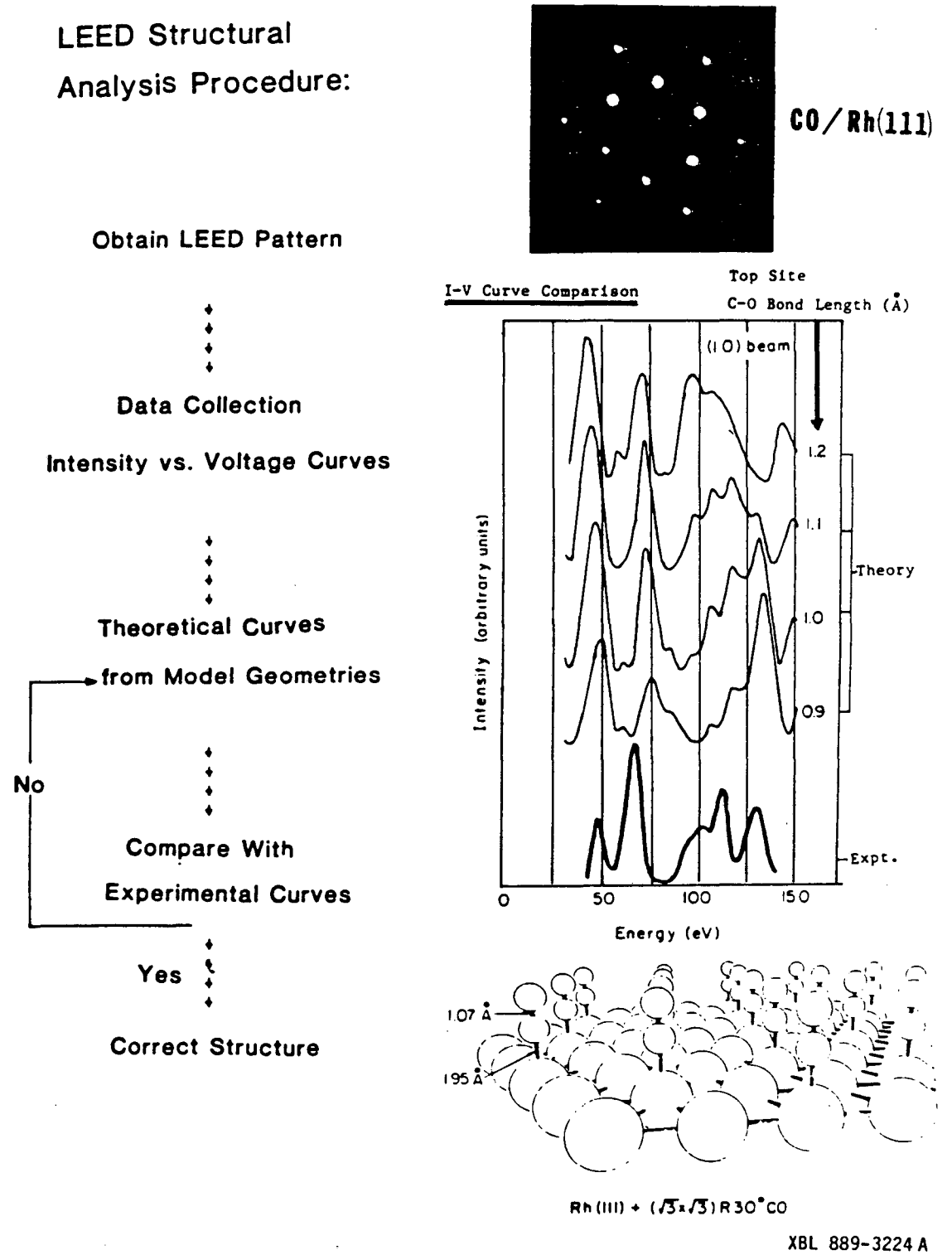

Figure 2.7: Structural analysis shown for Rh(111)/($\sqrt{3}$ x $\sqrt{3}$)R30°-CO at 0.33 monolayer coverage. The pattern, I-V curve comparison, and solved surface structure are shown at top, middle, and bottom of the figure, respectively.

The process mentioned above is iterated by systematic variation of bonding geometries until the best R factor (smallest) can be found. A real-space structure of CO on Rh(111) can be resolved by this dynamical LEED analysis, and it is shown at the bottom of the figure.

In this thesis, LEED was used to monitor :

- long-range ordering as a function of surface coverage
- size and shape of surface unit cell
- real-space structure by dynamical LEED analysis.

To describe the ordered overlayers, both matrix and Wood's notation can be used [16,17]. Wood's notation is most suitable to describe the simple commensurate lattice and will be used throughout this thesis. In this notation, the overlayer is described by the relative size and orientation of adsorbate unit cell to substrate, which is defined as (1x1). A ($\sqrt{3}$ x $\sqrt{3}$)R30° pattern means that the overlayer has $\sqrt{3}$ times the substrate unit cell dimensions for both axes and is rotated 30° from the substrate lattice. The prefix "c" in front of left bracket, such as c(4x2), means the unit cell has an extra adsorbate at the center of the (4x2) lattice.

In chapter 5, the complete LEED structural analysis of Rh(111) /(2x2)-3NO and c(4x2)-CCH_3+NO (or CO) will be discussed. The detail of the structural information obtained from such an analysis can be best appreciated then.

2.4.3 Auger Electron Spectroscopy (AES)

Auger electron spectroscopy is the most commonly used technique for surface compositional analysis. The detection limit is about 1 % of a monolayer, and the experimental setup is relatively simple. The emission of an Auger electron occurs

in the following manner and is shown schematically in figure 2.8. An electron or x-ray beam of 1000-5000 eV is first directed at the surface (usually at glancing incidence in order to enhance the surface sensitivity). As the normal binding energy of electrons in the core level of an atom (10-500 eV) is less than the beam energy, an inner-shell electron can be ejected and an electron vacancy created. Two processes are possible at this moment.

The first de-excitation mechanism is x-ray fluorescence. As shown in figure 2.8c, an electron in the outer shell can drop into the vacancy and release one photon with energy change ΔE of

$$\Delta E = h\nu = E_{outer} - E_{inner}, \tag{2.4}$$

where E_{outer} and E_{inner} represent the energy level of the outer and inner shell, respectively, and ν is frequency of the released x-ray.

The second process is Auger electron generation and is shown in figure 2.8b. The ΔE can also be transferred to another electron (same or different atoms) with a binding energy (E_b) less than the de-excitation energy ΔE, and the electron can be ejected to vacuum with a kinetic energy of

$$\frac{1}{2}mv^2 = E_{outer} - E_{inner} - E_b, \tag{2.5}$$

This secondary electron is called the Auger electron in memory of the French scientist who first observed such a process, in materials, based on the equation above. The Auger electron has a characteristic kinetic energy depending on the energy-level separation in the ion, which varies from one element to another. Therefore the energy analysis of emitted electrons provides an elemental analysis of the near-surface region of materials.

The escape depth of the Auger electron is a function of the final energy, and it ranges from one to seven atomic layers. In principle, the energy (or energy shift)

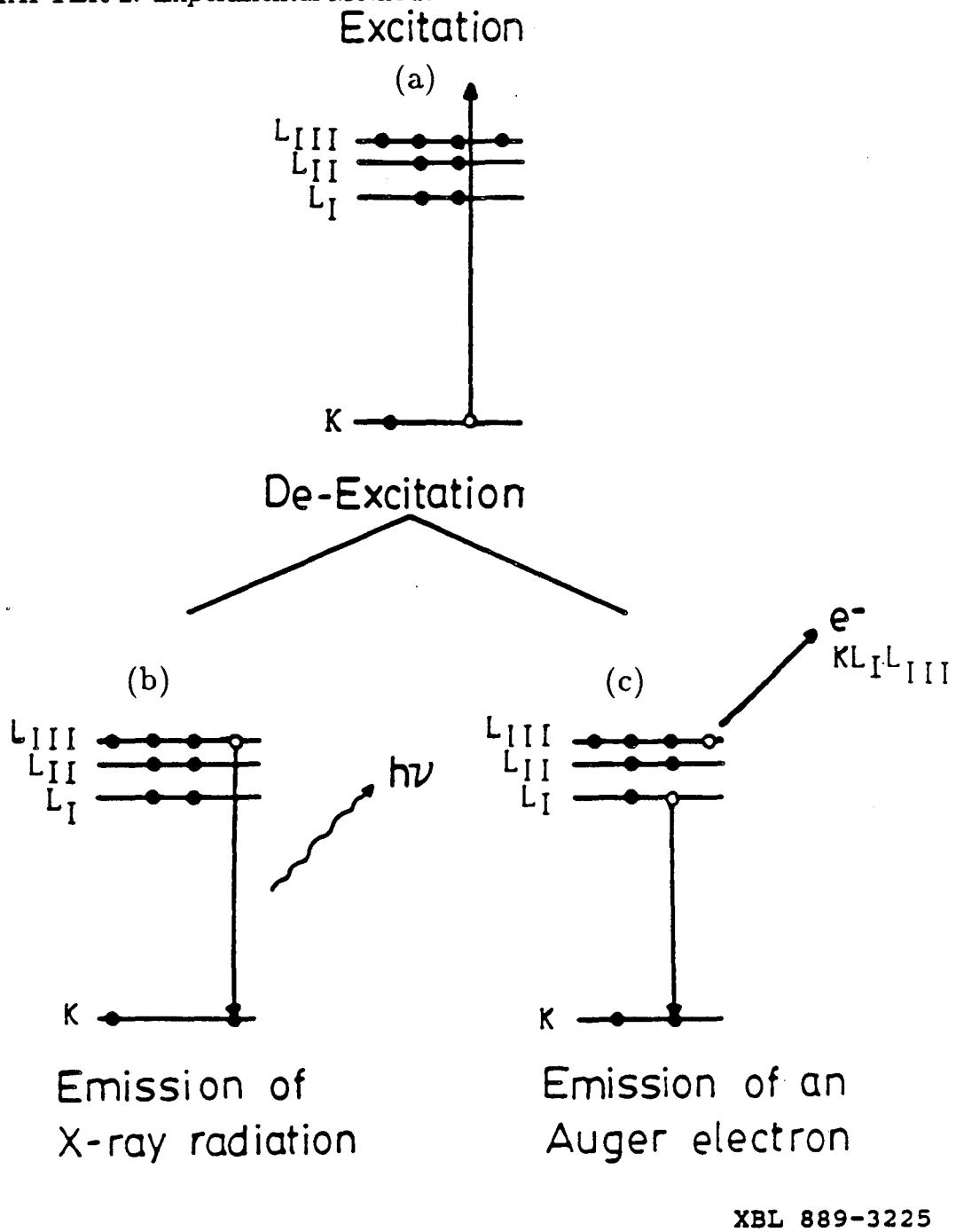

Figure 2.8: Energy-level diagram of (a) excitation by an electron or x-ray beam, (b) de-excitation by Auger emission processes, and (c) de-excitation by x-ray fluorescence of an excited ion.

and the line shape (intensity vs. electron-energy curve) can provide elemental analysis and electronic information about the environment of atoms. As with other electron spectroscopies, the observation depth is about 10-30 $\AA$ and is determined by the escape depth of Auger electron energy.

The nomenclature of Auger spectroscopy is also shown in figure 2.8. For a typical example of atomic energy levels, one type of Auger transition, KL_IL_{III}, is described. The first vacancy is generated in the K shell, and an outer L_I subshell electron fills the hole. The energy released can be given to another electron in the L_{III} shell, which is then ejected from the atom. Then the energy (E) of the outgoing electron is

$$E = E_k - E_{L_I} - E_{L_{III}}. \tag{2.6}$$

This process is a KL_IL_{III} Auger transition, and the final electronic configuration would find the 2S shell with one electron and the 2P shell with five electrons. Since electron-electron interactions are strongest between electrons whose orbitals are closest together the strongest Auger transitions are of the type KLL or LMM.

The AES experiments were done by using the retarding field analyzer of the LEED/AES optics shown in figure 2.5B. The Auger emission was initiated by a glancing-incidence electron beam (about 70-80° from surface normal) with 1500-2000 eV energy. The beam current impinging on the surface relative to ground was 5-10 μA. Grids 2 and 3 were tied together and a DC ramp coupled to an AC modulation voltage (10 V, 2000-3000 Hz). A 300-V positive bias was applied at the fluorescent screen, which acts as a electron collector. The second harmonic of the modulated signal was monitored by a phase-sensitive lock-in amplifier. The output was plotted against the DC ramp voltage on a chart recorder (HP 7044B), which gives the derivative spectrum for the Auger electrons. A typical AES for a Rh(111)/(2x2)-CCH_3 overlayer is shown in figure 2.4a.

In this thesis, AES was used mainly for qualitative compositional analysis. Occasionally, the surface coverages of adsorbates, such as NO and acetylene, were calibrated by AES. This was done by plotting the carbon (272 eV) or nitrogen (392 eV) Auger signal relative to the rhodium signal (302 eV) against dosage. The absolute coverage was then calibrated by ordered LEED patterns observed at several different coverages.

2.4.4 Work Function Measurement

The definition of the work function of a material is the threshold energy needed to excite an electron into the vacuum, or the energy difference between vacuum and Fermi levels. The work function of a material depends on its surface crystallographic orientation and the presence of adsorbed species [46,47]. In order to measure this threshold ionization phenomenon, a monochromatic photon or electron beam was used as the primary excitation source.

In our research, we are mainly concerned about the work function change upon adsorption or coadsorption. The monochromator of the HREEL spectrometer was used to provide a monoenergetic source of electrons (~2-10 eV) with 10^{-10} A current. This can be focused onto the Rh(111) sample oriented perpendicular to the beam, as shown in figure 2.9b. The current to the sample was measured by a floating picoammeter connected in series with a bias voltage supplied by a DC ramp. As shown in figure 2.9a, when the bias voltage becomes sufficiently negative, the current to the sample drops to zero as the vacuum level of the sample is raised above the energy of the incident electrons. The changes in work function are also equal to the changes in the position of the relative energy between the vacuum level and the Fermi level. We can then determine the work function change by

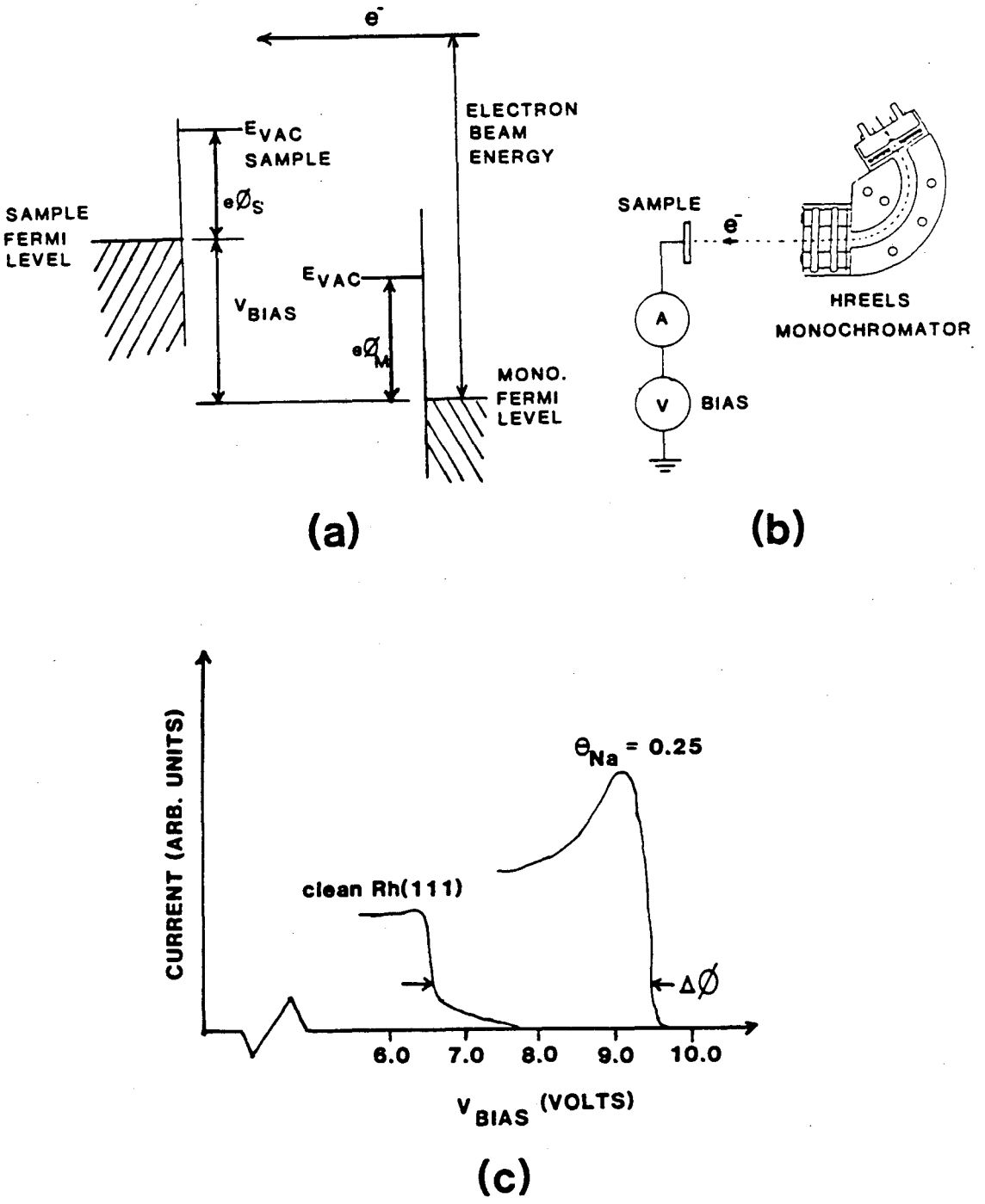

Figure 2.9: (a) Energy-level diagram of sample and HREELS monochromator used for work function measurements. (b) Simplified diagram of experimental setup. (c) An example of observed current vs. bias voltage curves for clean and 0.25-monolayer Na-covered Rh(111) surface. The shift in threshold voltage gives the work function change.

measuring the shift in cutoff voltage from a plot of current vs. bias voltage.

Figure 2.9c shows two such plots for the clean Rh(111) surface and for Rh(111) covered with an 0.25-monolayer of sodium. Since the energy resolution (FWHM of elastic beam) of the monochromator is small (about 0.005 eV), the main inaccuracy comes from the shape of the current vs. voltage plot. The high-energy tail in figure 2.9c for the clean Rh(111) surface is probably a result of electrons hitting the sample supports, because this tail is sensitive to the position of the sample but does not change during adsorption or desorption. By using the method described, it was possible to measure work function changes with an accuracy of 0.01 eV.

2.4.5 Thermal Desorption Spectroscopy (TDS)

The fundamental idea of desorption spectroscopy is quite simple. By ramping the surface temperature at a certain heating rate, which is supplied by direct thermal heating or indirect laser heating, the surface-bound species can desorb into the gas phase and be detected by a mass spectrometer. In principle, such a measurement can provide quantitative thermodynamic information on the binding energy of adsorbates, and different kinetics aspects of surface fragmentation and desorption processes.

We used a simplified one-dimensional potential energy surface (PES) to describe the adsorption-desorption process at a crystal surface. In figure 2.10a, point A_1 is considered to be a physisorbed precursor state, while point B_1 is a chemisorbed state without a barrier. Usually, binding energies $E \leq 15$ kcal, are considered appropriate for physisorbed molecules. A higher binding energy corresponds to a chemisorbed state. This potential energy surface is used to describe the nondissociative chemisorption process. For instance, CO adsorption on Rh(111)

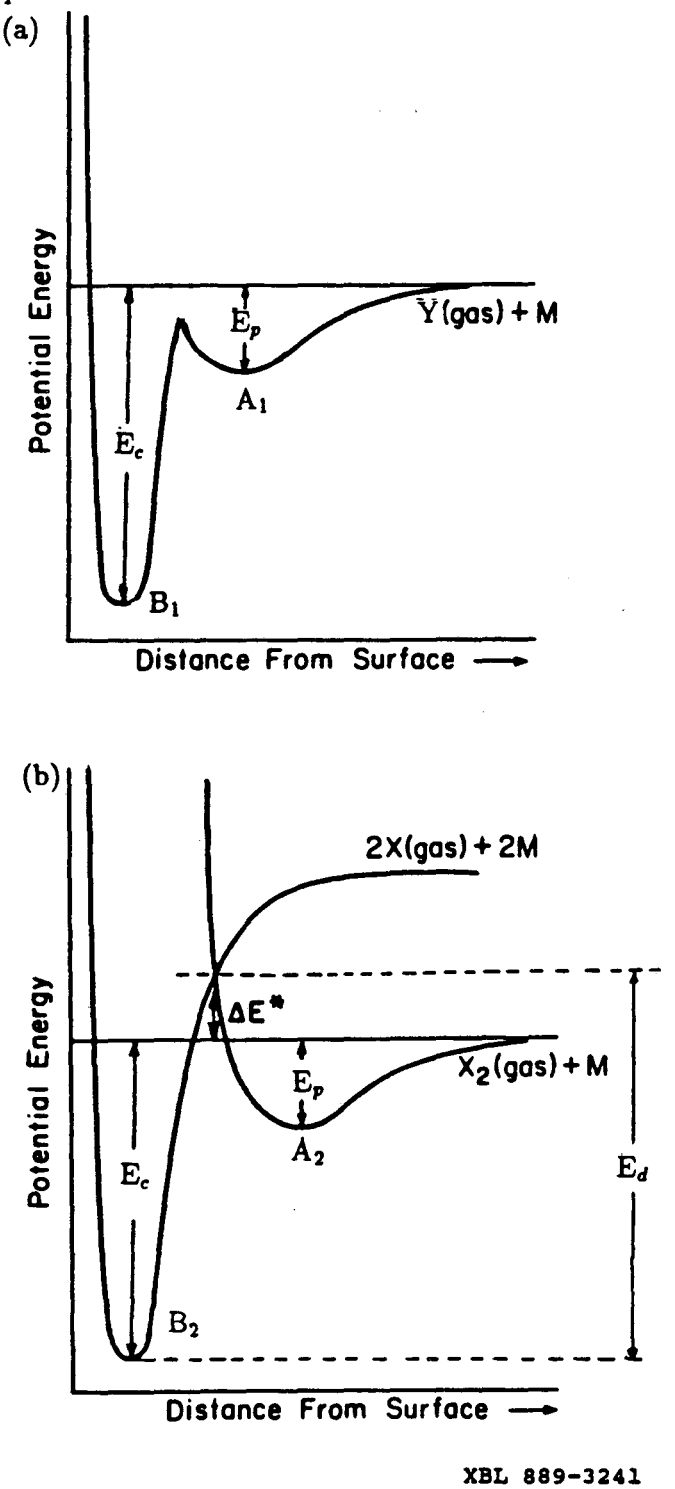

Figure 2.10: (a) Adsorption into a chemisorbed state with no activation energy; (b) activated chemisorption with activation energy ΔE^*. A physisorbed precursor state exists for both cases.

can be classified into this category.

A typical PES is shown in figure 2.10b for dissociative chemisorption with a barrier of bond dissociation near the surface. H_2 adsorption on Rh(111) with the formation of atomic hydrogen from molecular hydrogen can be classified into this category. In this case, the difference between the activation energy of desorption (E_d) and the heat of chemisorption (E_c) equals the activation energy for dissociative chemisorption (ΔE^*).

By using simple rate equations to describe each step shown above, the desorption rate (R) of a nth-order process can be expressed in the Arrhenius form:

$$R = \frac{d\theta}{dt} = \nu\theta^n exp(-E_d/RT), \tag{2.7}$$

where E_d is the activation energy of desorption, ν is the pre-exponential factor, and θ is surface coverage of the adsorbate.

In practice, we measure the partial-pressure change of certain molecular species as a function of surface temperature (or time). This pressure change is proportional to the rate of desorption, under the condition that the pumping speed is fast compared to the characteristic time for desorption (this is generally true for most UHV systems). Therefore, for a linear heating rate, the surface temperature T can be expressed as a function of time t, and

$$T = T_0 + \beta t, \tag{2.8}$$

In this formula, the heating rate is β = dT/dt, and T_0 represents the initial surface temperature. In the approximation that ν and E_d are coverage independent (ignore adsorbate-adsorbate interaction), we can solve our equation to find the temperature (T_p) of the maximum desorption rate. For first-order desorption,

$$E_d/RT_p^2 = (\nu_1/\beta)exp(-E_d/RT_p); \tag{2.9}$$

for second-order desorption,

$$E_d/RT_p^2 = (\nu_2\theta_0/\beta)exp(-E_d/RT_p); \tag{2.10}$$

and for zeroth-order desorption,

$$E_d/R = (\nu_0/\theta_0\beta)exp(-E_d/RT_p), \tag{2.11}$$

where θ_0 is the initial surface coverage of adsorbates. For a first-order desorption, the peak position T_p should be independent of surface coverage, and this is the general case for physisorption and associative chemisorption. For second-order desorption, the peak temperature should decrease with increasing coverage. The dissociative chemisorption of molecules is of this type. A typical example of hydrogen TDS on Rh(111) is shown in figure 2.11. The observed peak temperature decreases from 390 to 275 K from low to saturation coverage. For zeroth-order kinetics, the peak temperature increases as the coverage increases. The desorption kinetics of metal and metal oxide multilayers show this kind of behavior. Alternatively, expressions have been derived by Edwards [48] and Chan et al. [49], where E_d can be calculated independently of ν_n by using not only T_p but also information from the shape of the desorption peak.

It is also possible for one type of adsorbate like CO to occupy adsorption sites on the surface, which then give rise to several desorption peaks. In truth, one will find both E_d and ν to be coverage dependent, and the presence of precursor states can also modify the desorption kinetics.

In principle, if one can vary the heating rate over a wide range (two orders of magnitude), the activation barrier of desorption and the pre-exponential factor can be obtained by fitting the experimental thermal desorption spectrum. This is particularly useful in the low-coverage regime, where adsorbate-adsorbate interactions could be ignored. However, this variation of heating rate is nontrivial

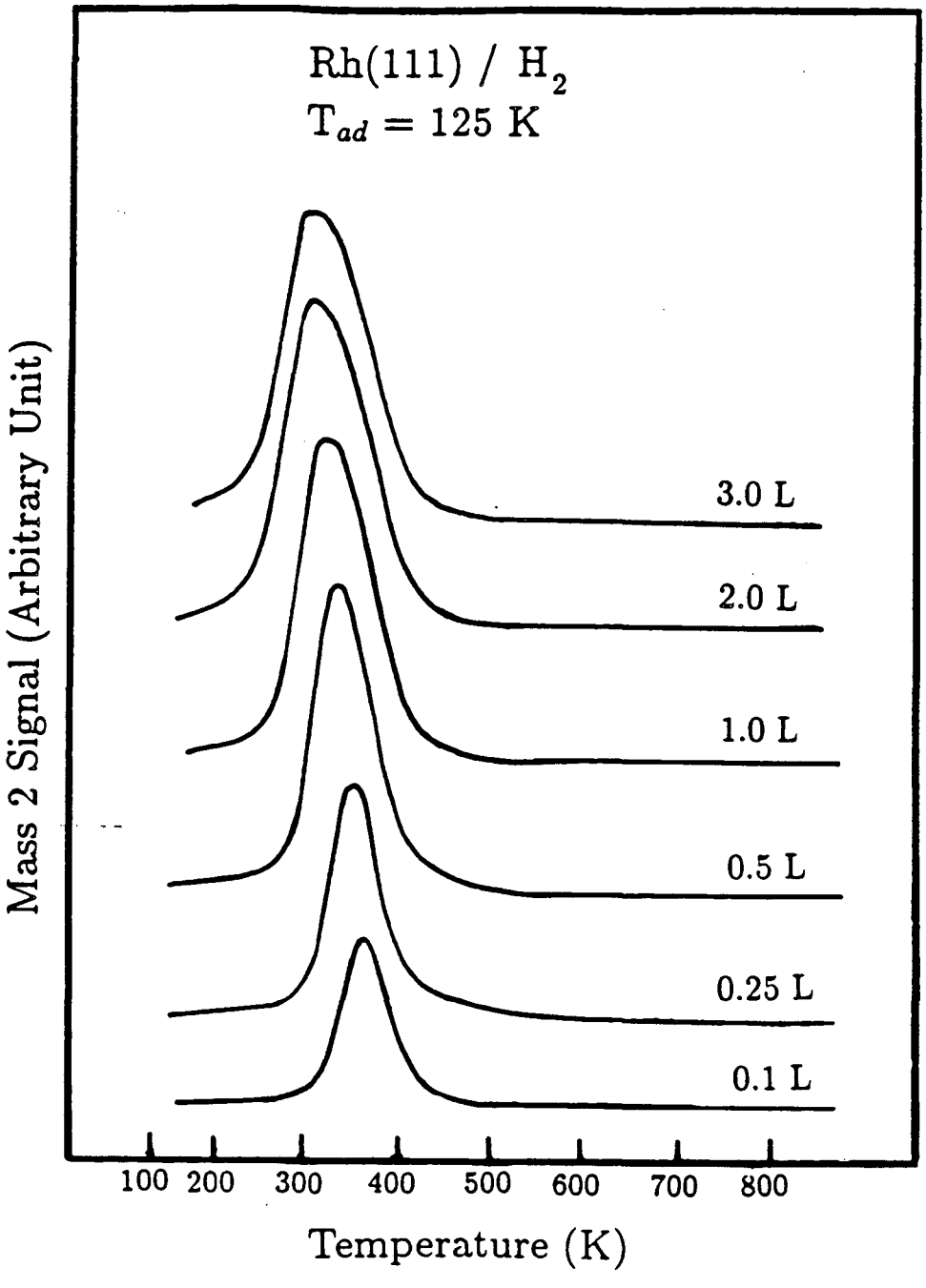

Figure 2.11: Mass-2 signals from hydrogen desorption plotted against temperature with different dosages at 150 K. The peak temperature shifts to lower values at higher dosages for this type of second-order desorption. The heating rate was 25 K/sec.

experimentally. Assumptions are made for the value of the pre-exponential factor as 10^{13} sec^{-1} and 10^{-2} cm^2sec^{-1} for first and second-order desorption, respectively. The barrier of desorption can then be determined based on the observed peak temperature, heating rate, and the derived Eqs. 2.9-2.11.

TDS also provides a convenient way to calibrate the relative coverage of adsorbates. For example, the relative coverage of nondissociative chemisorbed CO on Rh(111) can be calculated based on the relative areas under the mass-28 desorption peak. The absolute coverage can then be calibrated against LEED patterns at particular dosages. For CO, two ordered LEED structures, $(\sqrt{3} \times \sqrt{3})R30°$ and (2x2) at 0.33 and 0.75 monolayer coverage, respectively, can be used as calibration points.

For dissociative chemisorbed organic adsorbates, the relative coverages can be calibrated by the hydrogen TDS peak area. Then the absolute coverage can be calibrated against the TDS of H_2 adsorption or other organic adsorbates with known surface coverages.

Thermal desorption spectra presented in this thesis were recorded by plotting selected mass signals from the mass spectrometer vs. surface temperature monitored by the thermocouple reading. Typical spectra are shown in figure 2.11. The sample was facing the ionizer of a mass spectrometer at a distance of 5 cm. The heating rate was recorded simultaneously by a temperature vs. time plot. A linear ramp of 15-25 K/sec could be normally achieved by flowing constant current through the sample. Most of the obtained TDS data will be discussed in chapter 4 for hydrocarbon adsorption on the Rh(100) surface.

Chapter 3

Surface Vibrational Analysis by High-Resolution Electron Energy Loss Spectroscopy

3.1 Introduction

Surface vibrational spectroscopy is regarded as one of the most powerful techniques for identifying adsorbed surface species. Extensive structural information, including surface symmetry, adsorption site, molecular orientation, or even the mechanism of adsorbate-substrate and adsorbate-adsorbate interactions can be obtained by vibrational analysis [6]. In principle, it is also possible to extract bond lengths, bond angles, bond dissociation energies, and force constants of various vibrational modes by normal coordinate analysis [50] and empirical correlation models [6,51,52,53].

In order to obtain high-sensitivity and high-resolution vibrational spectroscopy of submonolayer adsorbates on surfaces or at interfaces, various spectroscopic tools have been developed to probe vibrational signals from 10^{13} to 10^{15} molecules/cm^2 within 3-10 $\AA$ thickness. Optical, electron, and neutron spectroscopies have been used for vibrational analysis. Among the optical spectroscopic techniques, infrared

transmission absorption spectroscopy (ITAS) has been used extensively to study high-surface-area materials, such as supported catalysts of finely divided metals [54,55,56]. Surface-enhanced Raman spectroscopy (SERS) has been utilized to study corrugated surfaces like silver electrodes. A factor of 10^3 enhancement in surface vibrational signal is generally observed [56,57]. In order to study low-surface-area single crystals (a surface density of 1 cm^2/g, compared to 100-1000 cm^2/g on supported catalysts), enormous efforts have been focused on the improvement of light sources, dynamic range of detector sensitivity, accurate alignment of beams to enhance surface sensitivity, etc. The details of these developments have been reviewed by Chabal in a recent publication [58].

Recently, it has been demonstrated that both reflection-absorption infrared spectroscopy (RAIRS) [58,59] and nonenhanced Raman spectroscopy [56,58] can have submonolayer sensitivity on metal single-crystal surfaces. A recent publication of ethylidyne on Pt(111) by RAIRS shows a rather interesting result. An instrumentally limited 1.45 cm^{-1} linewidth of the $\delta(CH_3)$ mode of surface ethylidyne species was reported [60]. It is believed that the true line-width of such vibrations could be even narrower. In the future, both IR and Raman have the potential to study submonolayer absorbates at 0.5 cm^{-1} resolution over the range of 200-4000 cm^{-1}. These techniques may become important competitors with the presently widely used HREELS. However, at this moment, it is still nontrivial to set up surface IR or Raman spectrometers for routine analysis.

It is worthwhile to mention that an exciting development in surface laser spectroscopy was achieved last year by Ron Shen's group in the Physics Department of the University of California at Berkeley. A visible-infrared sum-frequency generation (SFG) has been successfully developed to probe the vibrational structure of various interfaces [61,62,63,64]. This technique also has the potential to monitor

the dynamics of surface processes in real time by using a pulsed picosecond laser source. Moreover, due to the properties of nonlinear optics, the predominant signal will originate from interfacial species once the bulk phase is centrosymmetric (this is generally the case for gas, liquid, and solid-state materials). There is little doubt that this could open a new era in studying different interfacial phenomena. In particular, it will be extremely powerful for probing liquid-liquid, solid-solid, solid-air, and air-liquid interfaces, where almost no other spectroscopic tool has sufficient sensitivity.

Electron spectroscopic techniques like inelastic electron tunneling spectroscopy (IETS) has been applied to study adsorption at the interface of metal and metal-oxide materials [56,65]. This is particularly important for understanding catalytic and lubrication processes. On the other hand, this technique has restricted applications because of the difficulties in sample preparation.

Another analogous technique based on electron tunneling is scanning tunneling spectroscopy, which has proved successful in mapping surface electronic states by electron tunneling between a pointed tip and surface [66]. In principle, it also has the potential to map out the vibrational state of each separate molecular adsorbate [67]. However, liquid helium temperature is generally needed to improve spectral resolution ($\sim$kT). The general application of this method in probing interface vibrational structure is also limited by this constraint.

Moreover, vibrational spectroscopic techniques, such as inelastic atom and neutron scattering [56,68], infrared emission spectroscopy [56,69], and photoacoustic spectroscopy [70,71,72], have also been demonstrated to have limited applicability to surface vibrational structure. At this stage, high-resolution electron energy loss spectroscopy (HREELS) is still the most widely used technique for low-surface-area materials. This is due to the fact that HREELS has high surface sensitivity

(10^{-2} to 10^{-3} of a monolayer), wide spectral range (200-5000 cm^{-1}), and commercial availability. The major drawbacks of it are similar to those of other electron spectroscopic tools, limited pressure range ($\leq 10^{-7}$ torr) and poor spectral resolution (30-80 cm^{-1}). However, HREELS is still the recommended spectroscopic tool for studying simple molecular adsorbates at vacuum-solid interfaces.

In this chapter, different aspects of HREELS, including instrumentation, spectral assignment and surface species identification, surface symmetry, and structural information, will be discussed. A typical working example, the (2x2) CCH_3 (ethylidyne) overlayer on the Rh(111) surface is shown in figure 3.1 and will be used throughout the rest of this chapter to demonstrate the electron scattering mechanism, observed HREEL spectrum, and the assignment of the spectrum.

3.2 Instrumentation

The use of low-energy electron beams to excite surface vibrational mode was first presented by Probst and Piper in 1967 [73]. Although poor spectral resolution (400 cm^{-1}) and various problems were reported at that time, the potential applicability of the method had long been recognized. In 1974-1975, Fritzheim, Ibach, and Lehwald designed a spectrometer which refined the HREELS technique to its current status in surface science [7,74]. Since then, instruments of different designs have been developed and some have been commercialized. These efforts, especially from the Jülich group, catalyzed our understanding of surface chemistry.

The fundamental idea of HREELS is shown in figure 3.1a for our working example of the (2x2)-CCH_3 overlayer on Rh(111). Imagine that we have a monoenergetic electron beam with an initial energy of E_i (generally, the beam energy is 2-10 eV). After inelastic vibrational scattering from the ethylidyne overlayer,

High Resolution Electron Energy Loss Spectroscopy (HREELS)
Ethylidyne on Rh(111) Surface

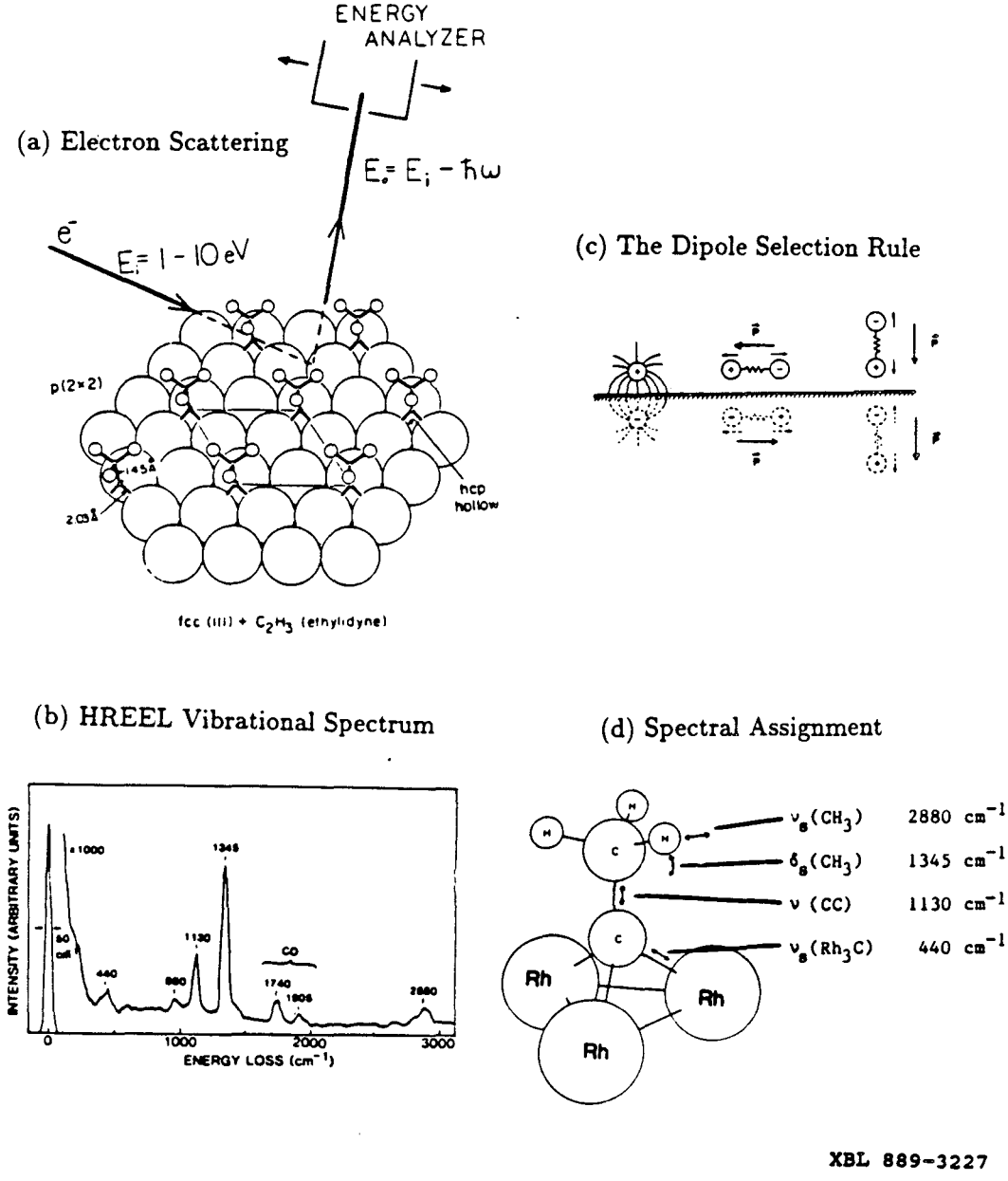

Figure 3.1: (a) Model of the scattering experiment; (b) example of a (2x2) ethylidyne spectrum on Rh(111); (c) the dipole scattering selection rule; (d) final spectral assignment for ethylidyne.

the electron will lose energy of $h\nu$ (20-400 meV) due to excitation of surface vibrational modes. Then we need to energy-analyze the electron beam with final energy $E_f = E_i - h\nu$.

In order to fulfill the task mentioned above, a number of different energy-dispersion devices using electrostatic deflection have been designed as HREELS spectrometers. These include the 127° cylindrical deflection sector, cylindrical mirror analyzer (CMA), and 180° spherical analyzer.

A schematic diagram of the 127° cylindrical deflection sector, which has been used in our laboratory, is shown in figure 3.2. The four major parts of this apparatus are a cathode to provide a source of electron beams, a monochromator, an analyzer as electron-energy filter to generate and detect highly monochromatized electron beams, and a detector to monitor and amplify the inelastic scattered electron as a function of energyloss. Several focusing lenses between these elements are also critical for retarding and focusing the electron beam at each stage.

The details of design considerations shown in figure 3.2 are listed below, A tungsten filament (power supply, Lambda LP-520-FM) running at 2.0 A provides a microampere electron beam by thermionic emission. These electrons are focused by an asymmetric, electrostatic Einsel lens onto the entrance slit of the monochromator. A 127° cylindrical deflector sector with both entrance and exit slits is used as monochromator. Lenses B1 and B2 are used as vertical and horizontal deflectors to focus the beam onto the sample, which is about 20-30 mm away from the last terminating shield. The sample is generally grounded, but sometimes a crystal-biased voltage can be applied to compensate for work function changes upon gas adsorption. After inelastically scattering away from the sample, the beam is refocused and energy-analyzed by a second electrostatic deflector. By sweeping the analyzer voltages of the inner and outer sectors, the inelastic electron intensity

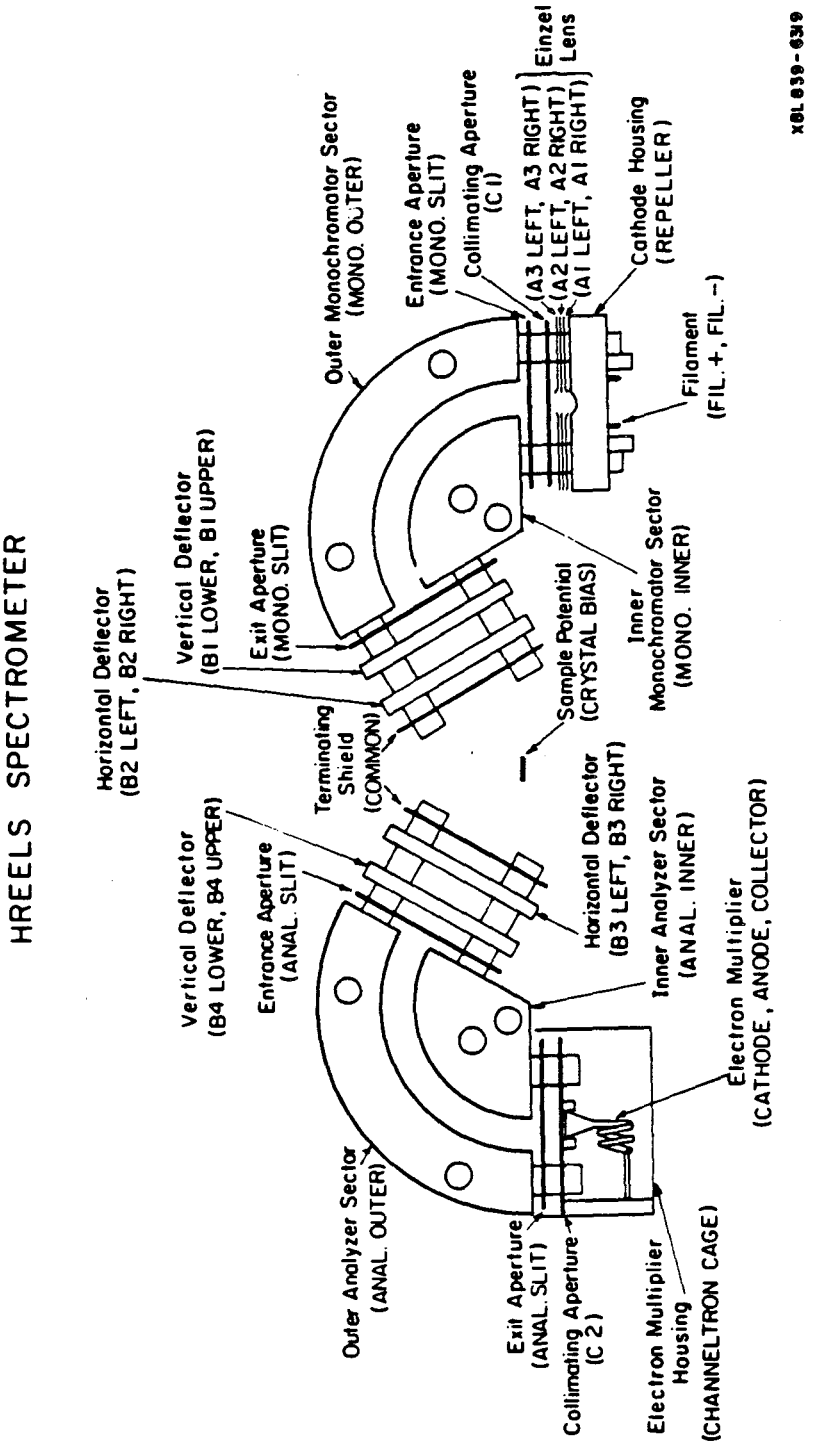

Figure 3.2: Design of the 127° cylidrical deflection sector. Details are labeled, and the elements of adjustable voltage at the front panel of the HREELS power supply are given in parenthesis.

can be selectively analyzed and passed through the analyzer slits and the last collimating aperture (C2) into the electron multiplier.

A HREELS power supply is used to provide voltages for each of the spectrometer lens and sector elements, and is also capable of rapid voltage scanning for the analyzer sector. A ramp generator (LBL 7S1113) is used to sweep the analyzer assembly voltages for scanning the whole spectrum. A Wavetek generator is also applied to repetitively scan the energy range at various frequencies. The generator is usually used to monitor elastic peak intensity during tunning. A separate high-voltage power supply (Fluke 2565018) is used to provide anode voltage for the electron multiplier (1800-3000 eV). For a new channeltron (Galileo 4028), a voltage increment, from 500 to 1800 V, is necessary to outgas the multiplier surface at the beginning. After two hours of outgassing, a steady signal at 1800 eV with ≤ 1 counts per second (cps) dark current is obtained. The electron pulse is then decoupled from the high voltage bias, amplified, shaped (Ortec 142PC preamplifier and Ortec 570 amplifier), discriminated (Ortec 550 SCA), and counted with a ratemeter (Ortec 449). The analog output of the ratemeter versus the energy-loss voltage is plotted on an x-y recorder. A typical loss spectrum for ethylidyne (CCH_3) adsorbed on Rh(111) is shown in figure 3.1b. Scattering intensities are typically 10^4-$2x10^5$ cps for elastic beams, and 1-10^4 cps for inelastic scattering.

As shown in figure 3.3, the scattering geometry of the spectrometer is fixed at a total angle of 120°. For specular reflection, the angles of incidence and reflection are both 60° relative to the normal direction of surface. For off-specular measurement, the sample (or the analyzer) can be rotated clockwise (positive) or counterclockwise (negative) to the desired angle.

From geometric trajectory calculation for an electron moving in a spectrometer [6], the pass energy E_0 is a linear function of the deflection potential ΔV as

High–Resolution Electron Energy Loss Spectrometer

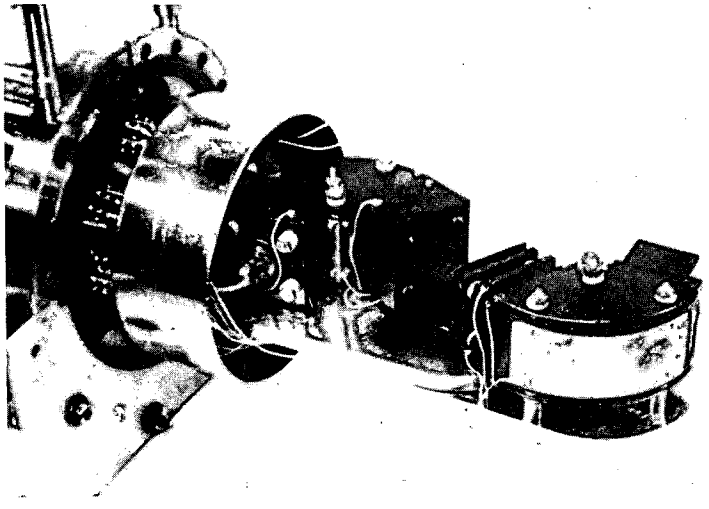

XBB 889-10129

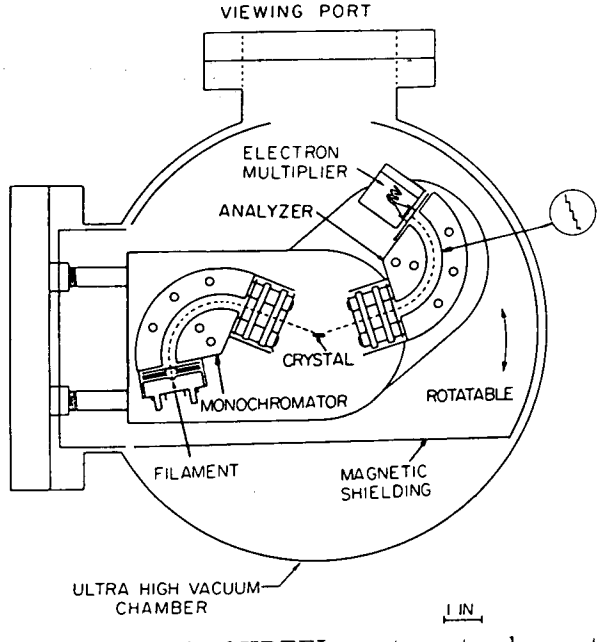

Figure 3.3: Upper: photograph of HREEL spectrometer; lower: top view of spectrometer in UHV chamber with $\theta_{in} = \theta_{out} = 60°$ relative to the surface normal. The whole spectrometer is surrounded by μ metal shielding to reduce stray magnetic fields.

follows:

$$E_0 = \frac{e\Delta V}{2}[ln(R_{outer}/R_{inner})], \tag{3.1}$$

where ΔV represents the voltage difference between the inner and outer sectors of both monochromator and analyzer. R_{outer} and R_{inner} are the radii of outer and inner sectors of the 127° cylindrical deflector. For the HREEL spectrometer described in figure 3.3, R_{outer}=41.40 mm and R_{inner}=31.39 mm. Inserting these values into the above formula,

$$E_0 = 1.81\Delta V. \tag{3.2}$$

both E_0 and ΔV are given in the same units such as electron volts.

The calculated energy resolution ($\Delta E_{1/2}$) is approximately given by the following equation [74]:

$$\Delta E_{1/2} = E_0(\frac{\Delta S}{R_{mean}} + \frac{1}{3}\alpha^2 + \beta^2), \tag{3.3}$$

where ΔS is the slit width, R_{mean} is the mean radius of the inner and outer sectors, and α and β are the angular apertures in and perpendicular to the plane of deflection, respectively.

In order to achieve high resolution, the broadband thermionic (or field) emission electron must be filtered and monochromatized to within a few meV. This is because the natural linewidth of vibrational modes is expected to be around ~4 cm^{-1} (0.5 meV). From the equations described above, low pass energy (~1 eV) or small deflection potential (~0.55 eV) is needed to meet the goal of such resolution [6]. However, the work function (or contact potential) of spectrometer elements may change as much as 1 eV for different crystallographic planes [6], and adsorbate contamination can also change the work function of spectrometer materials up to 1 eV [6]. The major consequence of these is that a limitation

of resolution will be reached for a monochromatized electron beam at low pass energy.

In practice, the energy width of an elastic beam will level off at 20 cm^{-1} for 0.2 eV pass energy [6,31]. The intensity (signal) of elastically scattered intensity I is calculated to be proportional to resolution ($\Delta E_{1/2}$), as follows [6,31]:

$$I \propto (\Delta E_{1/2} - 2)^{1.85}. \tag{3.4}$$

This describes a nearly square relationship between intensity and resolution and was generally determined experimentally [31].

The acceptance angle of the spectrometer can also change the intensity. Low angular resolution, though not easy to achieve experimentally, is recommended to reduce the space-charge effect for accepting more signal. The acceptance angle for our spectrometer is $\sim 4°$ [31].

In addition, the electron-beam energy can also change the intensity of the scattered beam. In order to have high reflectivity for various adsorption experiments, the power supply enables the beam energy to vary from 1 to 10 eV. For organic adsorbates studied in this thesis, a 2-3.5 eV beam energy was usually applied.

Good magnetic shielding is necessary to reduce the deviation of an electron beam when passing through a small deflecting field. For the cylindrical deflector, the deviation should be smaller than the height of slits, in order to avoid much distortion. The upper bound of the magnetic field in the spectrometer is then expected to be [6]

$$B \leq (h/r^2)1.37\sqrt{E_0}, \tag{3.5}$$

where h is the slit height and r is the mean radius of deflector (both in cm), E_0 is the beam energy (in eV), and B is the magnetic field (in Gauss).

With r=36.40 mm, h=3 mm, and E_0=3 eV, the static magnetic field should be

smaller than 48 mG. Strict restrictions are also needed for the AC magnetic field and homogeneity of the field, with 1 mG/cm as a typical value for the dimensions mentioned above. For the spectrometer shown in figure 3.3, the whole spectrometer was shielded by a metal cylinder around both sectors. Two holes at the center of about 5 cm diameter allowed translation of the sample in and out to the HREELS spectrometer.

Most of our spectrometer was made of copper. Molybdenum or copper-berillium was used as slit materials. Aerodag (colloidal graphite in isopropanol) was used as a protective coating on the surfaces to reduce charging effects and surface potential inhomogeneities. The 127° sector was also separately bakable by passing current through filaments wired around the outside.

Additional care was necessary to avoid some unwanted background scattering, which may either generate a long tail from the elastic peak or even create some additional loss structures called "ghost peaks." The former originates from electrons passing the analyzer at large angles. Both cathode emission or scattering from slits can generate such electrons. The latter so called "ghost peaks" are produced by scattering of electrons from the inner and outer deflection plates of the monochromator and analyzer, respectively. By using the basic resolution equation, the position of a ghost peak (ΔE_{gp}) can be related to $\Delta E_{1/2}$ as [6,7]

$$\Delta E_{gp} = 1.5\Delta E_{1/2}(R_{outer} - R_{mean})/S. \tag{3.6}$$

In order to place ΔE_{gp} in a very "high loss" position, a small slit size is preferable. An appropriate corrugation of the deflection plate is also helpful for further reduction of the ghost peak. The zigzag surfaces of analyzer and monochomator sectors are shown in a expanded insert of figure 3.3.

3.3 Inelastic Electron-Scattering Mechanism

Figure 3.4 shows the four electron-scattering mechanisms from a point scatterer "A" above a metal surface [6,56,75]. Both long- and short-range interactions are involved in these processes. In figure 3.4 (a) and (b), long-range dipole interactions are involved between the incident electric field and the vibrating adsorbate dipole potential. In (a), the electron is forward scattered by the adsorbate, then specularly reflected by the substrate. The reverse process can be seen in (b). Both kinds of dipole scattering are of small angle and near specular direction.

On the other hand, in figure 3.4 (c) and (d), the process involves short-range "impact scattering." More isotropic angular distributions are generally observed for this type of scattering. We will discuss dipole, impact, and resonance scattering separately in the following sections.

3.3.1 Dipole Scattering

Dipole scattering describes the interaction between the electrostatic potential of the electron beam and the time-dependent electric dipole moment of the vibrating adsorbate. Four major characteristics of such scattering mechanism are listed:

1. "Surface Dipole Selection Rule:" the selection rule of the dipole scattering process on a metal surface is shown in figure 3.1c. Only vibrational modes with a net change of dipole moment perpendicular to the surface are active. If ψ_i and ψ_f represent the initial and final vibrational states, respectively, the dipole scattering cross section is nonvanishing

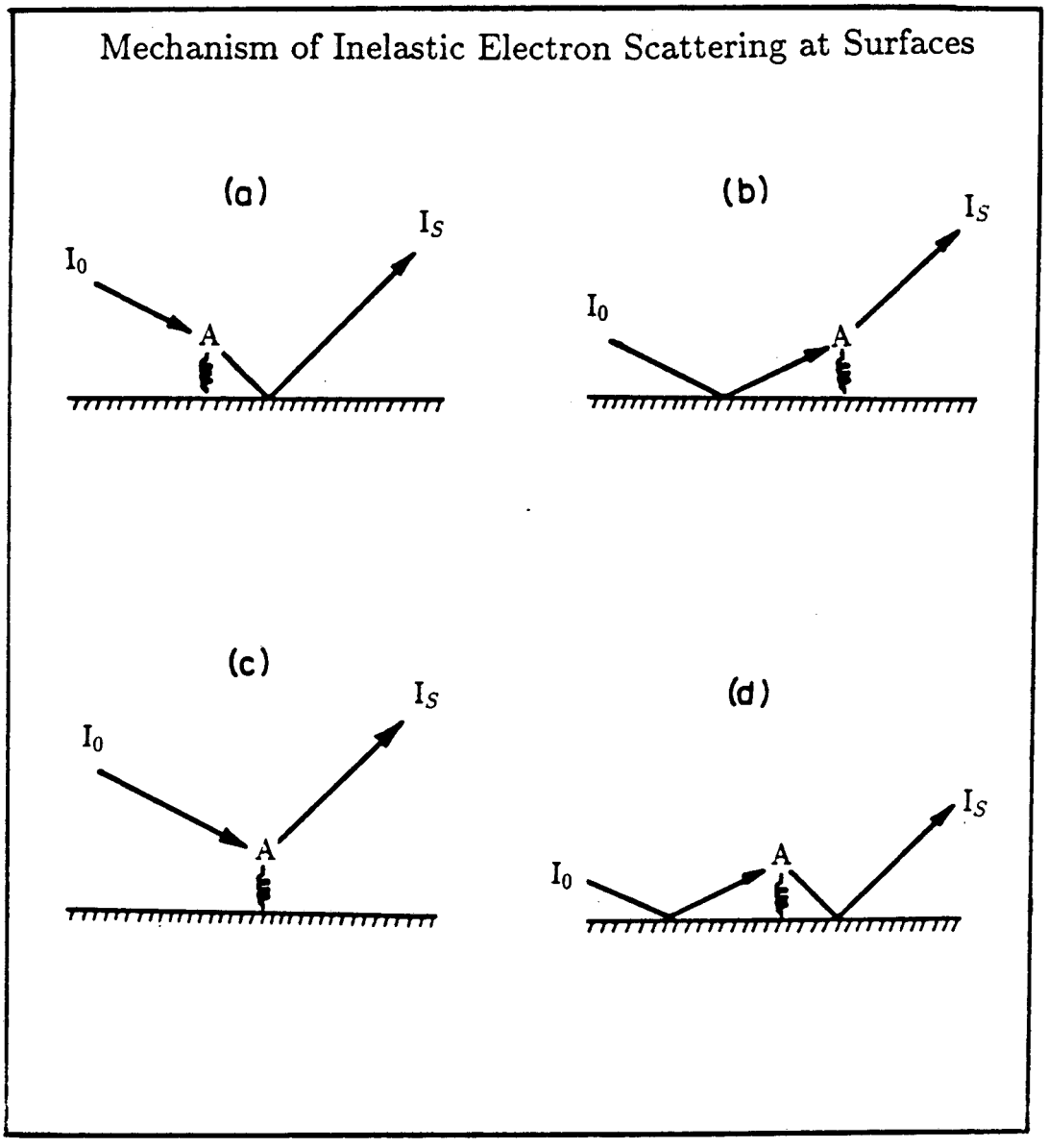

Figure 3.4: (a), (b) Details of dipole scattering; (c), (d) Processes of impact scattering. Both I_0 and I_s represent the initial and final intensities of the electron beam, and "A" represents adsorbed species on surfaces.

when matrix element $<\psi_i \mid \mu_z \mid \psi_f>$ is totally symmetric under all symmetry operations of a point group. Based on symmetry of the adsorbate, μ_z is the z component of the dipole moment operator and z is the direction normal to the surface. This also means that vibration belongs only to totally symmetric scattering, and that A_1, A', and A are observable as fundamentals under this scattering mechanism.

2. For high-reflectivity metal, processes (a) (b) in figure 3.4 will dominate the scattering, and inelastically scattered electrons will have a peak near specular.

3. The loss intensity increases with decreasing incident electron energy as $I_{loss} \propto E^{(-1/2)}$ if the incident energy is larger than the loss energy.

4. For strong dipole-dipole coupling between adsorbates, the scattering effect of the polarizability of an adsorbed monolayer could reduce the observed loss intensity.

Parallel vibrational modes can be excited by quadruple excitation, which leads to isotropic scattering, or they can couple into substrate vibrations with dynamic dipole fluctuations along the surface normal.

3.3.2 Impact Scattering

When incident electrons are within ~1 $\AA$ of the solid surface, short-range scattering by the localized atomic potential of the adsorbate and surface becomes possible. The momentum transfer is large, and broad angular distributions are observed. In principle, all vibrational modes are active via atomic potential scattering. The theory of this process is analogous to scattering in LEED. Although

the integrated cross section of impact scattering can be comparable to or larger than dipole scattering, for angular resolved HREELS studies, the impact scattering intensity is typically ~100 times lower.

This type of scattering is favorable for high-frequency modes (e.g., C-H stretch mode), and it is also most favorable for higher-energy electrons incident normal to the surface with the collector positioned at a near grazing direction [6,75]. The excitation probability of impact scattering may also vanish for certain geometries. This can be calculated based on time-reversal symmetry. For any scattered wave vector in the scattering plane, the scattering amplitude must vanish if the normal coordinate is antisymmetric under reflection at the scattering plane. This has been demonstrated by DiNardo et al. to determine the molecular symmetry of actylene on Ni(100) [76].

3.3.3 Resonance Scattering

The third scattering mechanism, resonance scattering, involves a temporary trapping of incident electrons to form a compound state. This short-range interaction is readily observed in the gas phase. The process can be separated into three events:

1. electron capture by the target to form an ion;
2. nuclear relaxation;
3. electron emission and excited neutral-state formation.

The incident electron must have the appropriate (resonance) energy to penetrate the barrier and become trapped by the target. Upon adsorption, the negative ion state may be strongly perturbed, and the surface may also change the lifetime

in step 3 for emission of an electron into vacuum, or even emission into empty band states of the substrate. The resonance could be broadened or even eliminated by this channel. Recently, various experiments have been performed to identify such scattering by monitoring the scattering cross section of vibrational modes as a function of beam energy. A lower resonance energy and energy-broadening effect were found for molecules adsorbed on Ag or Pd surfaces [75]. In general, resonance scattering has very high sensitivity and is capable of exciting dipole forbidden bands. Some surface-symmetry information and bonding geometry can also be obtained by this scattering mechanism.

3.4 Surface Structural Information by HREELS

In this section the data analysis and application of an HREEL spectrum will be discussed. These applications include spectral assignment, adsorption site, and surface symmetry analyses.

3.4.1 Assignment of HREEL Spectra

For a n-atom molecule in the gas phase, there are 3n degrees of freedom, including 3n−6 vibrational (or 3n−5 for a linear molecule), and three translational and three rotational (two for linear) motions [8,77,78]. When the molecule is adsorbed on a surface, all motions of the adsorbate towards the surface will be converted to a vibration against the surface [6,56]. For atomic adsorbates, such as H, O, N, C, and S, three translational motions will be converted to three vibrational motions. For physisorbed molecular adsorbates, the 3n−6 vibrational modes are likely to be similar to gas- or liquid-phase tabulated frequencies. For molecular

chemisorption, rearrangement and rehybridization can have a significant effect on the observed frequencies of internal vibrational modes of adsorbates. Thus the assignment and identification of surface species becomes nontrivial. Fortunately, there are a fair number of analogous coordination or organic compounds in organic and organometallic chemistry, where a complete vibrational mode and x-ray structure analysis have been done [15]. By comparing these data with the tabulated data mentioned above, the appropriate assignment of surface species and vibrational modes can be achieved. For simple hydrocarbons, isotopic substitution is quite useful for identifying C-H bending or stretching modes. However, substantial coupling between the C-H and C-C vibrational modes or insufficient spectral resolution may render this trick less useful for very large molecules. Dramatic frequency shifts are generally observed for chemisorbed unsaturated hydrocarbons, coadsorptions between alkali metal and CO or NO, surface hydrogen bonding of cyclohexane, and H_2O and NH_3 with group VIII transition metals.

A typical example of the spectral assignment of a (2x2)-CCH_3 (ethylidyne) overlayer on Rh(111) is shown in figure 3.1d. More case studies for the assignments of HREEL spectra will be discussed in the following chapters. In chapter 4, acetylene, ethylene, and benzene chemisorption on Rh(100) will be discussed. In chapter 5, the surface vibrational spectroscopy of NO and coadsorbed CCH_3 (ethylidyne)+NO on Rh(111) will be analyzed. In chapter 6, various coadsorbate-induced frequency shifts of CO and NO when coadsorbed with alkali metal and hydrocarbons on Rh(111) will be presented.

For the identification of surface species during thermal reaction on surfaces, other complementary techniques, like TDS, LEED, and XPS, are also quite helpful. For instance, the identification of surface fragments from ethylene decomposition on Pt(111) at 300 K was quite controversial for a while. Ethylidene ($CHCH_3$),

ethylidyne (CCH_3), and vinylidene (CCH_2) have all been proposed as possible surface species. This confusion arises from the different ways of assigning one HREEL spectrum for the surface fragment. It is not until the TDS work by Demuth et al. that a stoichiometry of C:H=2:3 was proposed based on the hydrogen desorption spectrum [79,80]. LEED studies suggest a perpendicular species with a single bond between two carbon atoms [81,82]. The spectrum was then reassigned as ethylidyne (CCH_3) [82] and the analogous tricolbalt-ethylidyne cluster was also synthesized and characterized by IR spectroscopy and x-ray diffraction [50,83]. Similar mode intensities and positions have been found between the HREELS results and IR frequencies of this tricobalt-ethylidyne cluster. All of the evidence supports the assignment of a surface ethylidyne species. A complete assignment of the ethylidyne spectrum on Rh(111) based on the analogous species within clusters and on other surfaces is shown in figure 3.1d.

In the case mentioned above, the analysis of the surface stoichiometry by TDS, the dynamical LEED structure analysis for the bonding geometry of atoms other than hydrogen, and vibrational mode comparison with possible organometallic compounds were all helpful for species identification and complete spectral analysis of the HREELS data. Several spectra assigning surface fragments from hydrocarbon dissociation will be presented in later chapters.

3.4.2 Surface Symmetry of Adsorbates by HREELS

Only ten point groups are observed to be compatible with the symmetry of surfaces, C_1, C_s, C_2, C_3, C_4, C_6, C_{2v}, C_{3v}, C_{4v}, and C_{6v}. The following discussion of surface symmetry will focus on the (100) and (111) surfaces of a face-centered cubic lattice. The possible surface symmetries on the Rh(111) hexagonal lattice

are C_{6v}, C_{3v}, C_{2v}, C_6, C_3, C_2, C_s, and C_1; while on Rh(100), C_{4v}, C_{2v}, C_4, C_2, C_s, and C_1 are appropriate symmetries of adsorbates adsorbed on this square lattice. Figure 3.5 shows the top view of both fcc(111) and fcc(100) surfaces, and various high-symmetry adsorption sites are also listed for comparison. For instance, the fourfold hollow site of the (100) surface and the threefold hollow site of the (111) surface have C_{4v} and C_{3v} symmetries, respectively.

Surface scientists often like to describe the chemical bonding of adsorbates as cluster-like. This description implies some analogies between top, bridge, and hollow sites of the fcc(111) surface to the bonding geometries in mono-, bi-, or trimetallic cluster compounds. The major problems are: (1) how many surface layers are necessary to describe the overall geometry? and (2) is this kind of local symmetry good enough or are more nearest neighbors needed?

To answer the first question, we need to know the layer structure of different surface geometries. For fcc(111) surfaces, the A-B-C type of layer structure causes the overall surface geometry to reduce from C_{6v} to C_{3v}, if we count the subsurface layers. There are then two types of threefold hollow sites, called fcc hollow sites when there are no second-layer atoms, or hcp hollow sites when there are second-layer atoms below the hollow sites. In chapter 5, we will discuss the coadsorption between CO or NO and ethylidyne on Rh(111), where the involvement of second-layer rhodium atoms to the chemical bonding can be resolved by LEED structural analysis.

For the fcc(100) surface, the overall surface symmetry maintains C_{4v} even if we take into account the A-B-A-B type of subsurface structure. This discussion holds true for unreconstructed surfaces. For reconstructed surface like Pt(100)-(5x20), the surface symmetry is reduced by the presence of some threefold coordination sites.

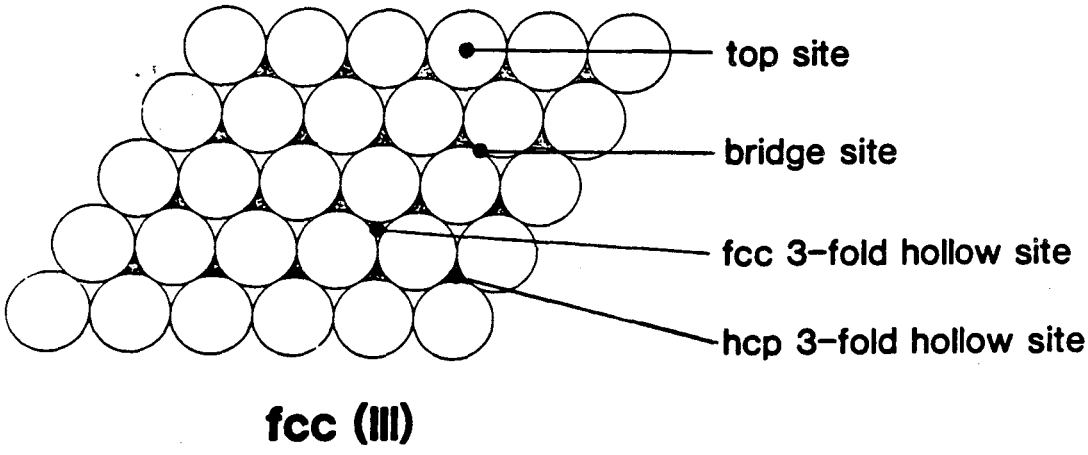

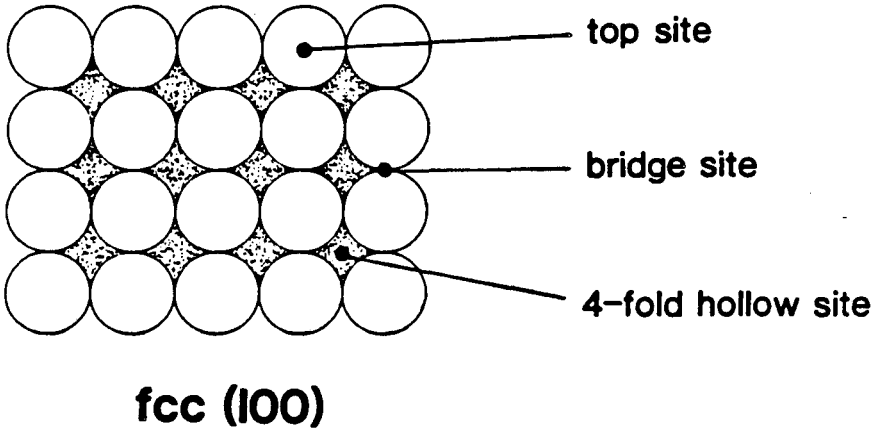

XBL 889-3222

Figure 3.5: Top view of unreconstructed fcc(111) and fcc(100) surfaces. Different adsorption sites on these two surfaces are labeled for comparison.

To answer the second question, it was suggested that the internal modes of an adsorbate could be less sensitive to the arrangement of surface atoms. A symmetry of C_{6v} may be possible for adsorption at the top site of an fcc(111) surface, while for other external vibrational modes like hindered parallel translation, the overall surface geometry is needed.

Several general symmetry properties of the adsorbing species and the surface complex, indicating appropriate combinations of substrate site and adsorbate necessary for overall surface symmetry, are summarized below.

- For atomic adsorbate or linear molecules (like CO or NO) bonded perpendicular to surface, the surface complex symmetry is the same as the bare site symmetry.

- For all other cases, the symmetry of the surface complex is determined by the compatibility between adsorbate and bare surface site symmetry. For instance, the surface complex methoxy (CH_3O) adsorbed on fcc(100) should have C_s symmetry. This is also the highest overlap symmetry between the subgroup of C_{4v} and C_{3v}.

- For an ordered array of adsorbates at high surface coverage, the symmetry property of the adsorption site depends on the local arrangement of other coadsorbed species within a unit cell.

In practice, by doing off-specular studies, the dipole-allowed vibrational modes can be identified. As mentioned earlier, the surface symmetry is lower, or at most equivalent, to the gas-phase symmetry. The correlation between gas-phase point groups and their subgroups with the appropriate surface bonding geometry is useful.

The surface symmetry of adsorbates could be deduced based on the number, frequency, and intensity of dipole-allowed modes. We will demonstrate this in chapter 4 by using typical examples of benzene chemisorption on the Rh(100) surface.

Chapter 4

Bonding and Reactivity of Unsaturated Hydrocarbons on Rh(100): Structure Sensitivity of Surface Chemical Reaction.

4.1 Introduction

The surface structure and thermal chemistry of organic monolayers on transition metal surfaces is very important for a basic understanding of heterogeneous catalysis. In general, these surface chemical processes can be divided into two major categories, structure-sensitive or structure-insensitive reactions [84]. For example, it has been found that the rates and selectivities of catalytic hydrocarbon reactions such as n-butane isomerization and alkane hydrogenolysis are strongly dependent on metal surface structure [84,85]. On the other hand, catalytic n-hexane isomerization and benzene hydrogenation is reported to be a relatively "structure-insensitive" reaction [84,86]. It is interesting that analogous processes may also exist for the stoichiometric chemistry of hydrocarbons on single-crystal transition metal surfaces. For example, the bonding and thermal decomposition

pathways for acetylene and ethylene on Pd(111) [87] and Pd(100) [88,89] surfaces in ultra-high vacuum (UHV) are substantially different, while chemisorption and fragmentation of benzene adsorbed on these two surfaces [90,91] seem relatively structure-insensitive.

In order to see if acetylene and ethylene shows generally structure sensitive chemistry on face-centered cubic (111) and (100) surfaces, while benzene does not, the surface structure and thermal chemistry of these prototypical unsaturated hydrocarbons on a Rh(100) surface in UHV have been studied and compared with previously published results on the Rh(111) surface [ethylene: [13,51,92,93,94], benzene: [95,96]].

In this chapter, the surface structure and thermal chemistry of prototypical unsaturated hydrocarbons acetylene, ethylene, and benzene adsorbed on Rh(100) surface have been studied by high-resolution electron energy loss spectroscopy (HREELS), thermal desorption spectroscopy (TDS) and low-energy electron diffraction (LEED) over the temperature range of 90-800 K. The combination of these spectroscopic techniques has been applied to provide information on the surface ordering, bonding geometry, binding energy, and thermal decomposition pathway of the organic overlayer.

It was found that both acetylene and ethylene show strongly chemisorbed species on Rh(100) below 250 K. Compared to the Rh(111) surface, the carbon-carbon bond of both molecular species was even closer to sp^3 hybridization on Rh(100). At $T \geq 250$ K, exactly the same surface fragments with similar HREELS and LEED patterns were observed for both acetylene and ethylene on Rh(100). Below 0.5 monolayer coverage, the dehydrogenation reaction was favored toward the formation of CCH (acetylide) species. Above this surface coverage, the fingerprint of ethylidyne begins to appear in the HREEL spectra. This represents a new reac-

tion channel involving both C-H bond forming and breaking processes. As to our knowledgement, this is also the first observation of ethylidyne formation on a surface without a threefold site. On the other hand, a relatively coverage-independent reaction was observed on the Rh(111) surface. Both vinylidene (CCH_2) and ethylidyne were predominant species from acetylene and ethylene fragmentation, respectively. These results indicate that acetylene and ethylene fragmentation on the Rh surface are structure sensitive.

Benzene adsorption on the Rh(100) surface has also been studied by HREELS, LEED, and TDS. Rather similar vibrational spectra were seen on both Rh(111) and Rh(100) surfaces. This leads toward the formation of similar surface fragments, CCH and CH species, on both metal surfaces at 400-510 K. The structure and chemistry of benzene adsorption on both surfaces indicates a rather structure-insensitive chemical interaction as compared to the case of acetylene and ethylene. Similar results have also been observed on Pd(111) and Pd(100), and this could be the general rule on other fcc metal surfaces. The data observed on the Rh(100) surface will be compared to previous work on other transition metal surfaces, and a correlation of HREELS results with the strength of the benzene chemical bonding will be proposed.

In the following sections, surface chemical bonding of acetylene on Rh(100) surface will be presented first. The fragmentation of both acetylene and ethylene will be analyzed in the second part. The structure and decomposition of benzene will be the focus of the third part.

4.2 The Surface Chemical Bond of Acetylene on Rh(100)

4.2.1 HREELS of Molecular Acetylene on Rh(100) at 90-250 K.

Figure 4.1 shows the HREEL spectra of 5.0 L acetylene adsorbed on Rh(100) at 175 K. The spectra were taken at 90 K, and both C_2H_2 and C_2D_2 spectra are shown for direct comparison. No significant change was observed over the temperature range of 90-250 K. It is unlikely that acetylene decomposes at 95 K, since the lowest fragmentation temperature reported for acetylene on group VIII transition metal surfaces is 180 K [97] and the decomposition temperature on Rh(111) is 270 K [21]. We attribute the features shown in figure 4.1 to molecular acetylene species.

The complete assignment of the spectra is quite straightforward by comparing the nondeuterated and deuterated acetylene spectra. The mode at 2865 cm^{-1} in the C_2H_2 spectrum, which shifts down to 2170 cm^{-1} upon deuteration, is due to the C-H stretching frequency. The three vibrational modes at 1120, 960, and 730 cm^{-1} in figure 4.1B, which shift to 955, 700, and 510 cm^{-1} in the C_2D_2 spectrum, can be assigned to three C-H bending modes. The peak at 510 cm^{-1} in the C_2H_2 spectrum is attributed to the metal-carbon stretching frequency of adsorbed acetylene, although the corresponding mode in the C_2D_2 spectrum is obscured by the intense C-D bending mode at 510 cm^{-1}.

The vibrational mode at 1155 cm^{-1} in the C_2D_2 spectrum was ascribed to the ν(C-C) mode of chemisorbed acetylene. The nondeuterated analog mode will be close to the peak at 1120 cm^{-1} shown in figure 4.1B. The extra peaks at about

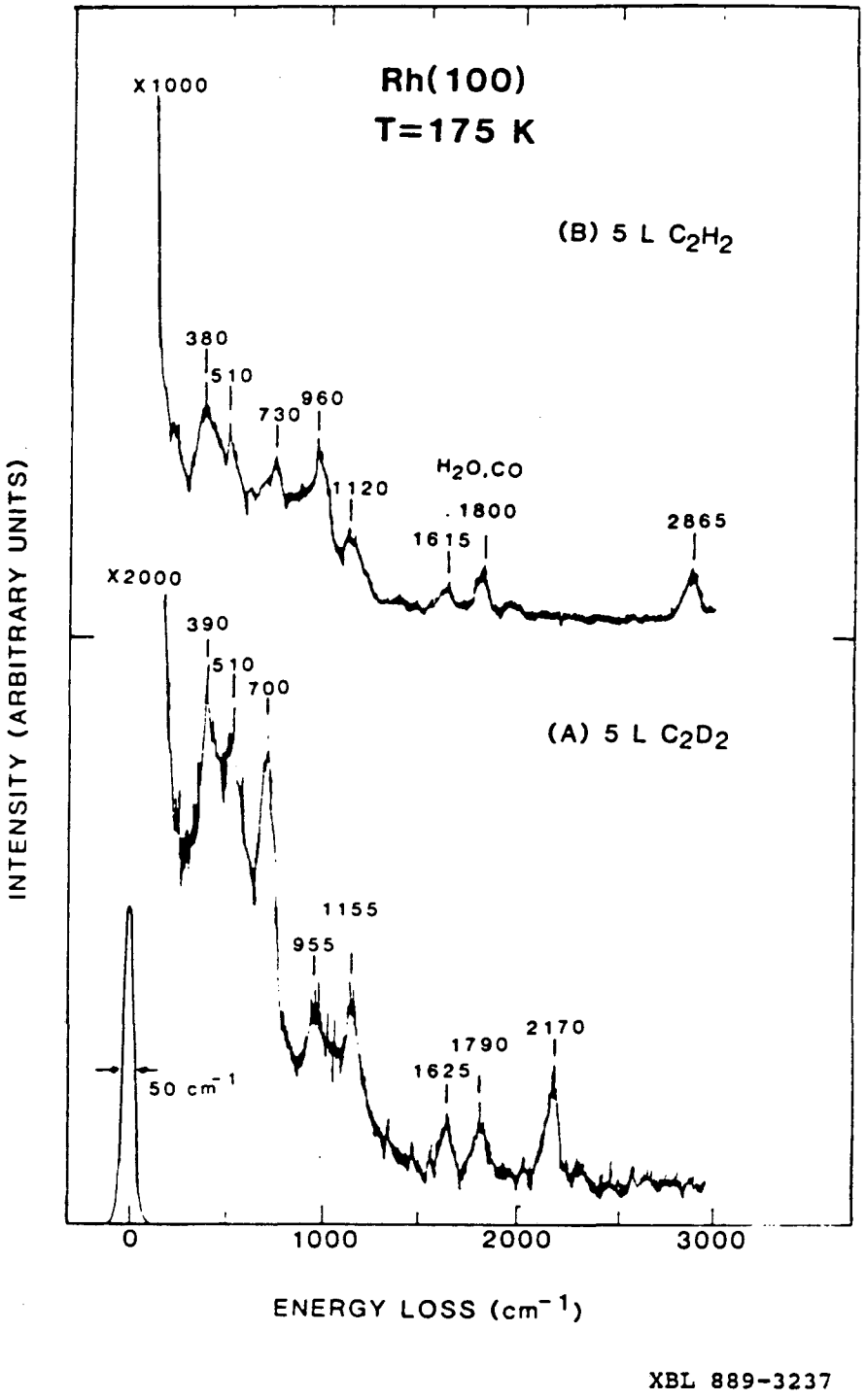

Figure 4.1: Surface vibrational spectra obtained by HREELS in the specular direction for (A) 5.0 L C_2D_2, and (B) 5.0 L C_2H_2 adsorbed on the Rh(100) surface at 175 K. The spectra were taken at 90 K.

1615 and 1800 cm^{-1} in both the C_2H_2 and C_2D_2 spectra are due to the H_2O and CO contamination from the background gas [98]. The summary of the assignments will be presented next by comparing them with other metal surfaces with similar acetylene bonding geometries.

4.2.2 The Structure of Molecular Acetylene on Rh(100)

Based on the HREELS results shown in figure 4.1, both C-C (1120 cm^{-1}) and C-H (2865 cm^{-1}) stretching frequencies for chemisorbed acetylene are dramatically shifted to lower frequencies in comparison to the gas-phase spectrum [ν(C-C)=1974 cm^{-1} and ν(C-H)=3300 cm^{-1}]. These frequency shifts indicate strong bonding of acetylene to Rh(100). Typical ν(C-C) frequencies for single, double, and triple bonded species are about 950, 1600, and 2100 cm^{-1}, respectively by averaging the spectra of various hydrocarbons [6]. The corresponding C-H stretching modes are 2800-3000, 3000-3100, and 3300 cm^{-1} for alkane, alkene or arene, and alkyne compounds [6].

The observed ν(C-C) values for acetylene on Rh(100) are consistent with a sp^3 hybridization of carbon atoms. The large degree of C-C bond rehybridization is characteristic of acetylene bonding to transition metal surfaces. In fact, on all metal surfaces studied to date by HREELS, including Ni(111) [99,100,101,102], Ni(110) [103,104], Ni(100) [76,105], Pd(111) [106,107,108], Pd(100) [109], Pd(110) [103], Pt(111) [110,111], Pt(100) [112], Cu(111) [103], Cu(110) [113], Ag(110) [114], Fe(111) [115], Fe(110) [116], Ru(0001) [117], Re(0001) [118], W(111) [119], W(100) [120], W(110) [121], Rh(111) [21,122], and semiconductor surfaces such as Si(111) [123], the acetylene C-C stretching frequency is shifted to below 1450 cm^{-1} (except for Ag(110) [114]), indicating rehybridizations between sp^2 and sp^3. Such

rehybridization of the carbon-carbon bond is generally explained by the Dewar-Chatt-Duncanson model for coordination of unsaturated C-C bonds to metal centers [124,125]. In this model, weakening and rehybridization of the C-C bond occurs because the highest occupied acetylene π orbital overlaps an empty metal d orbital, while the lowest unoccupied π^* orbital accepts charge backdonation from a filled metal d orbital. However, this explanation does not predict the binding site or adsorption symmetry for chemisorbed acetylene.

Information concerning the adsorption geometry of acetylene on Rh(100) can be obtained from relative peak intensities in the vibrational spectra. Sheppard [126] has noted that the HREEL spectra for chemisorbed acetylene appear to be of three basic types, which he labels A, A', and B. The classification is based mainly on the HREELS intensity profiles, since, in essence, the HREELS intensity profiles may be more indicative of the acetylene bonding configuration on the surface than are the vibrational frequencies. This proposal seems reasonable, since, as a consequence of the dipole selection rule discussed in chapter 3, the specular HREELS peak intensities are determined largely by the adsorbate symmetry and orientation.

By comparing the observed spectra in figure 4.1 to published spectra of three types of metallic surfaces, the profile of spectra for acetylene chemisorbed on Rh(100) is similar to both types A' and B. Although the intensity of ν(C-C) mode in figure 4.1 is within the two extremes of type A' (very intense) and B (very weak) spectra. We favor type A' because the relative intensity of the two C-H bending modes at 960 and 730 cm^{-1} and the peak position of each vibrational mode are more consistent with this type of spectrum [126]. The proposed structure of type A' spectra is for acetylene adsorbed at fourfold hollow sites on the fcc(100) surface.

Two kinds of high-symmetry bonding geometries, based on the crystal struc-

ture of analogous metal-alkyne cluster compounds, are possible for acetylene adsorbed at fourfold hollow sites on Rh(100) surface. The geometries for these two complexes in metallic clusters and for a fourfold hollow site acetylene on Rh(100) are shown in figure 4.2. Structure (a) can be explained based on a di-$\sigma+\pi$ type of bonding, i.e., σ-bonding to two metal atoms along the C-C axis direction, and π-bonding to the remaining two rhodium atoms. The analogous cluster compound is the tetracolbalt-acetylene complex with buckled planes of four cobalt atoms, as shown to the right in figure 4.2a [127]. This type of complex is also called a "butterfly compound."

Structure (B) represents four equivalent σ bonds between acetylene and the four rhodium atoms of the fourfold site. This is also similar to the bonding geometry of a tetra-iridium-alkyne complex and the C_2H_2 group within a cis-1,1,2,2-tetrabromoethane molecule ($C_2H_2Br_4$) [13,128].

Gas-phase acetylene is a linear tetra-atomic molecule with a symmetry of $D_{\infty h}$. Due to its interaction with the metal surface, the symmetry of chemisorbed acetylene is significantly reduced, and the highest surface symmetry of acetylene on Rh(100) is expected to be C_{2v}. By correlating the symmetry of each vibrational mode with the observed HREEL spectra, the surface point group of molecular acetylene can be determined. Such an analysis can only be done if a full off-specular HREEL spectra analysis is undertaken in the future. At this stage, further structural information can be obtained by comparing HREELS of acetylene on Rh(100) with the infrared spectra of analogous organometallic compounds. This is presented in table 4.1, where the vibrational frequencies of these compounds are listed. A progression of C-C stretch reductions from 1403 to 1199 cm^{-1} can be seen as the coordination number of C_2H_2 increases from 2 to 4. The tri-osmium cluster compound has been used as model complex for acetylene chemisorption

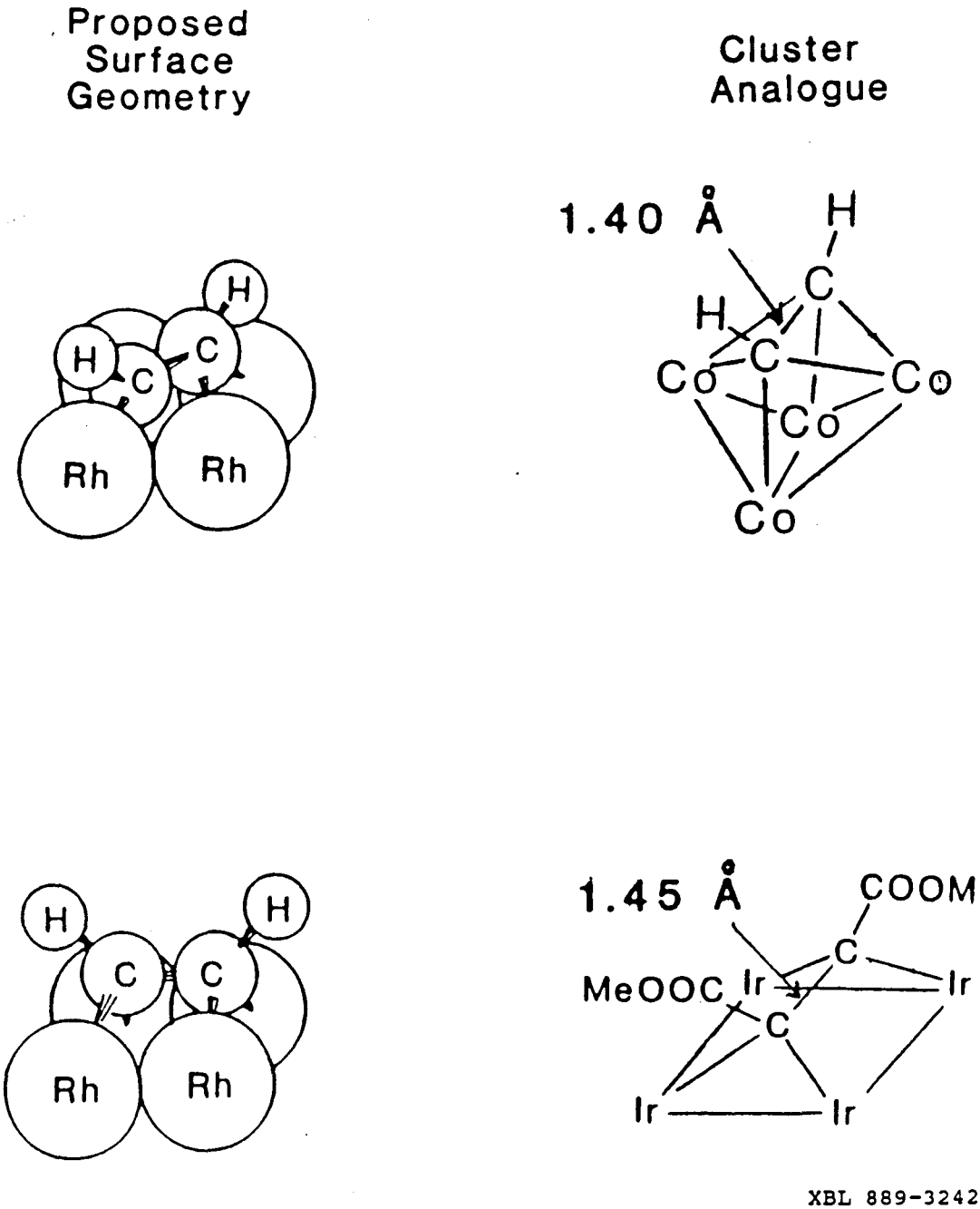

Figure 4.2: Cluster bonding geometries known for the fourfold coordinated C_2H_2 ligand in organometallic chemistry, along with the proposed acetylene bonding geometries on Rh(100).

Table 4.1: Vibrational frequencies (in cm^{-1}) for the C_2H_2 group on metal surfaces or in organic and organometallic compounds.

Formula	ν(MC)	γ_s(CH)	δ_s(CH)	δ_{as}(CH)	ν(CC)	ν(CH)	Reference
Gas Phase							
C_2H_2	—	612	612	729	1974	3374	[129]
$C_2H_2Cl_2$	—	697	1183	1303	1590	—	[129]
Cluster							
Co_2	—	—	768	894	1403	3116	[130,131]
Os_3	521	848	978	1035	1301	2996	[132]
Co_4	—	837	922	983	1199	3020	[127]
Surface							
Rh(111)	305	720	950	1120	1260	2960	[21]
Rh(100)	390	730	955	1120	~1155	2865	this work
Pd(100)	—	710	935	—	1210	2920	[109]
Ni(100)	~500	805	940	1125	1305	2915	[76,105]
Fe(111)	470	—	935	—	1145	2850	[115]

on Rh(111) [132], where similar dipole active modes and peak positions were detected. Following this trend of ν(C-C) reduction, the observed frequency on the Rh(100) surface at ~1155 cm^{-1}, 100 cm^{-1} lower than that on Rh(111), is also indicative of a fourfold coordinated acetylene on Rh(100). The spectroscopic resemblance between acetylene on Rh(100) and within the tetra-cobalt coordinated compound also favors structure (a) surface bonding geometry rather than structure (b). On the basis of these considerations, we assign our Rh(111)/molecular acetylene HREEL spectra in table 4.1 to type A' acetylene within Sheppard's classification scheme. Similar acetylene spectra have been reported on Ni(100) [76,105], Pd(100) [109], and Fe(111) [115] surfaces. The vibrational frequencies for acetylene on these type A' surfaces are listed in table 4.1 for comparison.

Compared to other fcc(100) metal surfaces, great similarity can be seen among Rh(100), Pd(100), and Ni(100). The strongly distorted acetylene was observed on Pd(100) [109] and Ni(100) [76,105] surfaces with a C-C stretching frequency of 1210 and 1305 cm^{-1}, respectively. The observed C-H stretch is ~2920 cm^{-1}

on both Pd(100) and Ni(100) surfaces, consistently implying a surface acetylene species with carbon hybridization of sp^2-sp^3. Based on the observed spectra shown in figure 4.1, both the C-C and C-H stretches are distorted toward even greater sp^3 hybridization on Rh(100), as compared to Pd(100) and Ni(100) surfaces. Furthermore, in comparison with Rh(111) [21,122], a 100 cm^{-1} downshift for both C-C and C-H stretches can be seen for acetylene on Rh(100). This indicates a stronger bonding of acetylene on the more open Rh(100) surface. The strength of acetylene-surface bond will follow the trend Ni(100) < Rh(111) < Pd(100) < Rh(100), according to the shifts of ν(C-C) relative to the gas-phase frequency.

4.3 Thermal Chemistry of Acetylene and Ethylene on the Rh(100) Surface

Here, because of the similarities of acetylene and ethylene fragmentation on Rh(100) at 200-800 K, only the results of ethylene will be discussed in detail. The LEED and HREELS results on the decomposition of ethylene on Rh(100) at surface temperatures between 200 and 380 K will be analyzed first. The coadsorption of CO and ethylene at room temperature, where surface ethylidyne was successfully isolated from other fragments, will be discussed to support the spectral assignment of ethylene fragmentation at room temperature. Subsequent decomposition of the room-temperature fragments as the temperature was increased up to 800 K is discussed, followed by a comparison with TDS studies. The thermal chemistry of both acetylene and ethylene on Rh(100) will be compared with the close-packed Rh(111) surface and other fcc(100) surfaces.

4.3.1 HREELS of Ethylene Decomposition at 200-380 K

Figure 4.3 shows HREEL spectra for the decomposition of saturation coverages of C_2H_4 and C_2D_4 on Rh(100) at approximately room temperature. All three monolayers showed c(2x2) LEED patterns. The monolayers in figure 4.3a and figure 4.3b are both the result of C_2H_4 adsorption, but in figure 4.3a, the ethylene was adsorbed at 210 K followed by warming to 273 K with the spectrum taken at 273 K; in figure 4.3b, the ethylene was adsorbed at a surface temperature of 310 K. The peak at 1825 cm^{-1} in figure 4.3a is from CO, presumably adsorbed during cooling to 210 K. The slightly different peak frequencies and intensities

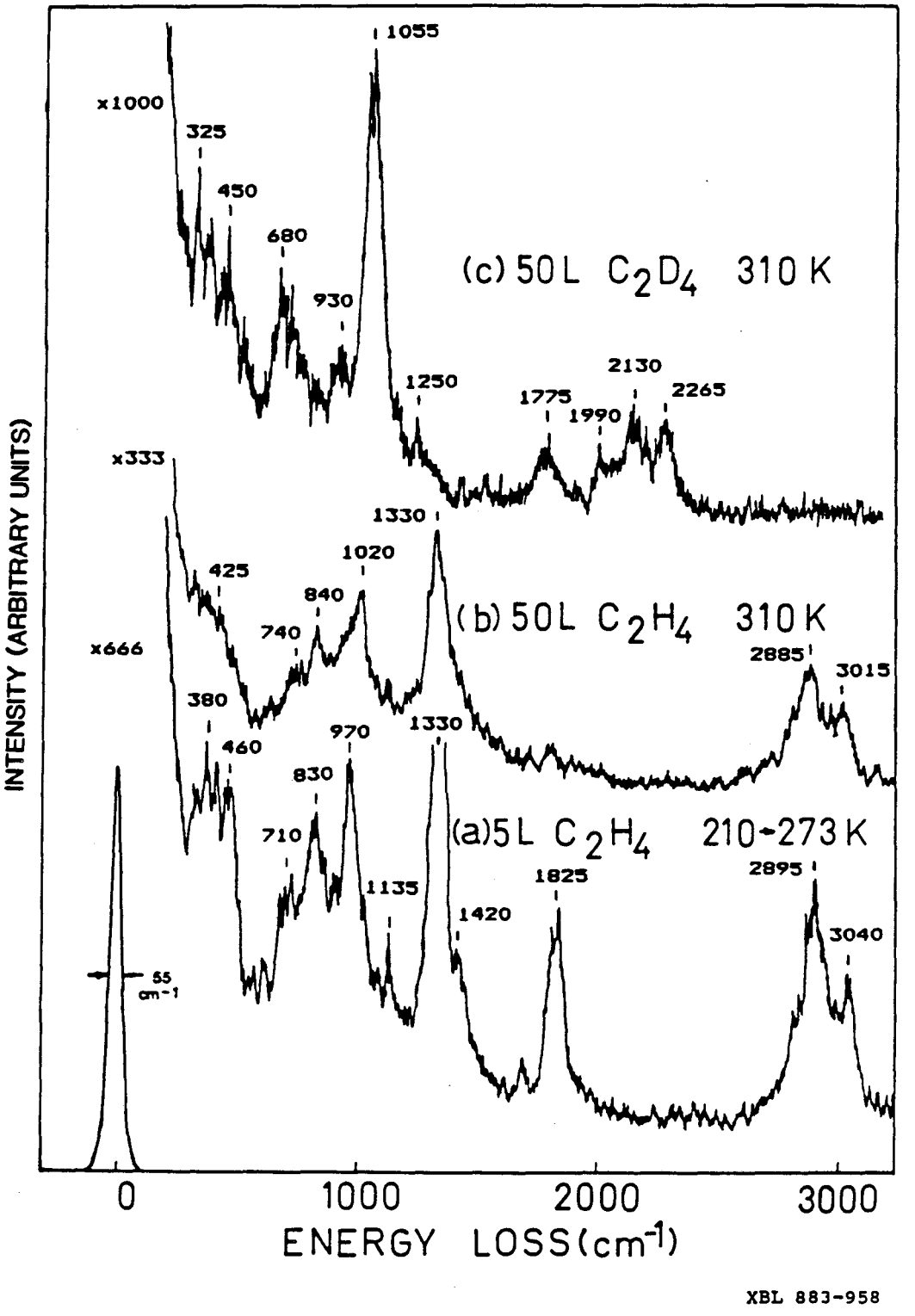

Figure 4.3: Specular HREELS of (a) 5 L C_2H_4, (b) 50 L C_2H_4 and, (c) 50 L C_2D_4 adsorbed on Rh(100) at 273-310 K.

of the remaining peaks in these two spectra are indicative of the variation we observed in the saturation-coverage HREEL spectra. This variability is not due to the different temperatures at which the spectra were taken (both monolayers in figures 4.3a and 4.3b are thermally stable up to 380 K), but is instead probably due to the complexity of ethylene decomposition on Rh(100). In particular, we have found that the ethylene decomposition pathway on Rh(100) is coverage dependent and highly sensitive to low levels of contamination.

Assignment of the complex HREEL spectra in figure 4.3 is facilitated by looking first at the low-coverage ethylene vibrational spectra. Further helpful information comes from the coadsorption studies of $CO+C_2H_4$ at room temperature [133]. Both results will be discussed in the following sections to support the assignment of figure 4.3 discussed later.

Low-Coverage Ethylene Fragmentation on Rh(100): The Formation of Surface Acetylide (CCH)

Figure 4.4 shows specular HREEL spectra for subsaturation coverages of C_2H_4 and C_2D_4 adsorbed on Rh(100) at 325 K. Figures 4.4B and 4.4C are for 1.0 L of ethylene and perdeuteroethylene, respectively; both of these adsorbed layers showed a c(2x2) LEED pattern. The lower-coverage 0.5 L spectrum for C_2H_4 in figure 4.3 shows a p(2x2) LEED pattern, but the vibrational features are quite similar to those for the higher-coverage c(2x2) structure in figure 4.4B. The major features in the hydrogenated spectra are two low-frequency modes at 350-450 cm^{-1}, a peak at 800-850 cm^{-1}, a weak mode at 1300-1350 cm^{-1}, and a peak at > 3000 cm^{-1}. The peaks at 1775-1950 cm^{-1} in figures 4.3 and 4.4 are due to the C-O stretch of carbon monoxide from background adsorption. The surface

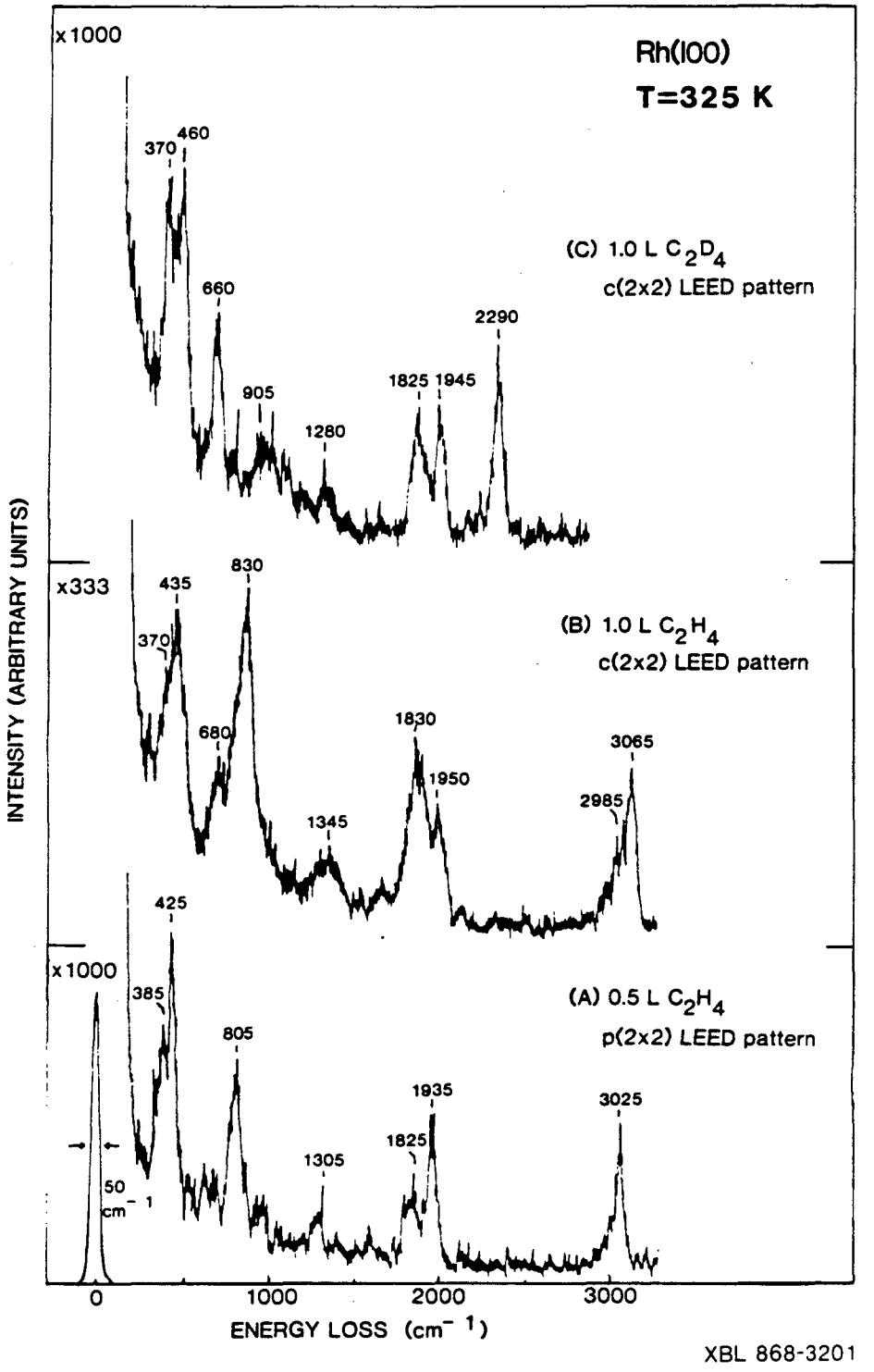

Figure 4.4: Specular HREEL spectra of (A) 0.5 L C_2H_4, (B) 1.0 L C_2H_4, and (C) 1.0 L C_2D_4 adsorbed on Rh(100) at 325 K. All spectra were taken at room temperature.

concentration of such contaminating species was estimated to be less than 0.07 monolayer coverage [40,134], and the shoulder at 680 cm^{-1} was suspected to be due to some contaminating hydroxyl species [135].

The low-frequency modes at 350-450 cm^{-1} are in the frequency range expected for metal-adsorbate vibrations. They may be partially attributable to CO contamination, but their relative intensity is much larger than that observed for a comparable coverage of CO on a clean Rh(100) surface [40,134]. We conclude that these modes are due primarily to metal-hydrocarbon fragment vibrations. Of the other hydrocarbon fragment peaks, the modes at ~800 and ~3050 cm^{-1} are readily attributable to CH bend and stretch motions, respectively, based on their downward frequency shifts by factors of 1.2-1.3 in the deuterated spectrum of figure 4.4C. The weak, broad feature at 1300-1350 cm^{-1} in the hydrogenated spectrum can be correlated with the 1280 cm^{-1} mode in the deuterated spectrum. We assign this peak to a C-C stretching vibration based on the small frequency shift with deuteration. The presence of this ν(C-C) mode indicates that the C-C bond remains intact when ethylene is adsorbed on Rh(100) at room temperature. We leave the broad hump at 905 cm^{-1} in the deuterated spectrum unassigned; it may be due to contamination.

The observed low-coverage modes for ethylene adsorbed at room temperature are consistent with C_2H (C_2D). This surface species accounts for the observed C-C stretch mode and the lone CH (CD) bend and stretch modes. Species with CH_2 and CH_3 groups can be discounted based on the absence of CH_x deformation modes in the 1300-1450 cm^{-1} region.

In table 4.2 we summarize our assignment of the spectra in figure 4.4 to this C_2H species. This assignment is compared with previous HREEL spectral assignments of C_2H species on Rh(111) [138], Pd(111) [88], Pd(100) [88], Ni(110) [136],

Table 4.2: Vibrational frequencies (in cm^{-1}) for CCH (acetylide) species on surfaces and within metallic clusters.

System	ν(MC)	ν(MC)+δ(CH)	δ(CH)	ν(CC)	ν(CH)	Reference
Ni(110)	380,465	1170	890	1290	2990	[136]
Ru(001)	435	—	750	1290	2960	[137]
Rh(100)	370,430	—	~805	1305	3025	this work
Pd(111)	—	—	750	1340	3000	[88]
Pd(100)	—	—	750	1340	3000	[88]
Rh(111)	490	1170	~815	1380	3020	[138]
Os_3	—	1259	854,861	1534	3157	[139]

and Ru(001) [137], as well as with infrared frequencies for a C_2H ligand coordinated to three osmium atoms in an organometallic cluster [139]. Consistent with the low ν(C-C) frequency of 1534 cm^{-1} in the cluster, the ν(C-C) mode of C_2H on these transition metal surfaces is shifted down by hundreds of cm^{-1} from the frequency for a gas-phase carbon-carbon triple bond of 1974 cm^{-1} [129]. This large frequency shift can be attributed to a bonding configuration of C_2H where the C-C bond interacts with several metal atoms, as is found for the triosmium complex [139].

The Surface Structure of Acetylide on Rh(100)

The surface acetylide species has been shown to be the only fragment at doses less than 1.0 L, where the formation of a sharp c(2x2) LEED pattern was observed on the Rh(100) surface. From the HREEL spectra shown in figure 4.4, only one C-H bending mode is observable in the specular scattering. According to the surface dipole selection rules, this result indicates a most probable surface symmetry of C_s for the acetylide fragment [6]. The C-C and C-H stretch are within the range of sp^2 to sp^3 hybridization, and the observed value for the carbon-carbon stretch is 40-60 cm^{-1} lower than the Rh(111) surface [96,138]. This also implies

a stronger interaction between the CCH entity and the Rh(100) surface. A possible bonding configuration on the fourfold hollow site has been proposed based on these observations.

While the triosmium complex is a poor structural model for a tilted C_2H species on a Rh(100) surface, there is a pentaruthenium complex in which a C_2(phenyl) ligand interacts directly with four metal atoms analogous to bonding in a fourfold hollow site on Rh(100) [140]. The observed C-C bond length of this cluster is 1.34 $\AA$, nearly sp^2 hybridized. The bonding geometry of this complex [140], along with its analogue for a Rh(100) surface, is shown in figure 4.5. A similar analogy between C_2H bonding in a triosmium cluster and to a Rh(111) surface is also shown at the top of this figure. The ν(C-C) vibrational frequency for the pentaruthenium complex has not been reported, but such a tilted geometry can account for both the low frequency and weak spectral intensity of the ν(C-C) mode on Rh(100).

It is interesting to note that a previous work on acetylene chemisorption on Ni(100) at 270 K [141] indicated a possible surface fragment adsorbed at the fourfold site with its C-C axis tilted 50° from the surface normal using LEED structural analysis of the observed c(2x2) pattern. It will be important to identify the surface species by HREELS to see if the ordered overlayer is CCH or not. Nevertheless, the observed c(2x2) LEED pattern on the Rh(100) surface is an excellent candidate for future structural analysis studies, since, to our knowledge, this is the only reported pattern for the surface acetylide species in the absence of coadsorbates.

Coadsorption of CO and Ethylene on Rh(100) Surface: The Formation of Ethylidyne.

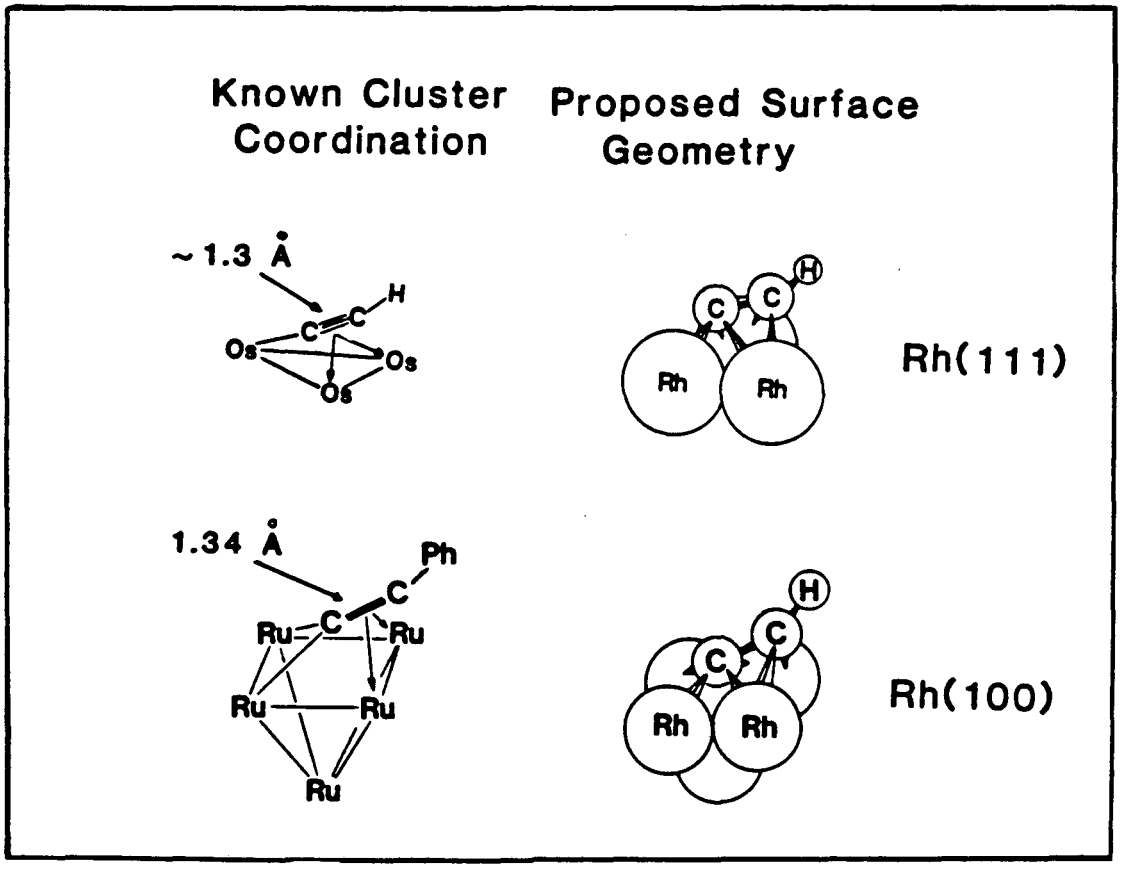

Figure 4.5: Proposed structure of surface acetylide (CCH) on Rh(111) and Rh(100) shown by comparison with known structures of analogous cluster compounds determined by x-ray diffraction.

The saturation-coverage HREEL spectra in figure 4.3 are quite different from the low-coverage acetylide spectra in figure 4.4. The most distinctive additional modes in the hydrogenated spectra of figure 4.3 are: (1) a lower-frequency ν(C-H) peak at ~2900 cm^{-1}, (2) an intense mode at 1330 cm^{-1}, (3) a peak at 970-1020 cm^{-1}, and (4) a shoulder at 700-750 cm^{-1}. The peak at 1330 cm^{-1}, which shifts down with deuteration, is characteristic of a methyl group, as is the 2900 cm^{-1} peak. As similar frequencies (with the exception of the 700-750 cm^{-1} peak) and relative intensities could also be generated by coadsorbed carbon monoxide and ethylene at room temperature [133], we attribute these extra peaks to be primarily due to the presence of ethylidyne above half-monolayer coverages. We will discuss the results of coadsorption experiments first and return to the complete assignment of figure 4.3 later.

In figure 4.6A the well-resolved HREELS obtained after passing 20 torr of ethylene and 100 torr of hydrogen contaminated with CO over a Rh(100) surface held at 380 K is presented [133]. This monolayer has a sharp c(4x2) LEED pattern. In figure 4.6B, the quite similar HREELS for c(4x2)-CO+CCH_3 on the Rh(111) surface is shown. The similar numbers of peaks, relative intensities, and peak frequencies for the Rh(111) and Rh(100) overlayers in figure 4.6 are strong evidence for the ethylidyne species on Rh(100).

Attempts were made to reproduce this high-pressure-derived Rh(100) monolayer under UHV conditions by coadsorbing CO and C_2H_4. Best results were obtained by preadsorbing 0.7 L of CO, corresponding to θ_{co}=0.5, followed by a saturation dosage of C_2H_4 at room temperature. The HREEL spectrum for such a monolayer is shown in figure 4.7A. With less preadsorbed CO, other hydrocarbon fragments (predominantly C_2H) were also formed, while more CO reduced the intensity of the "ethylidyne" peaks. Also shown in figure 4.7 are the 10° off-specular

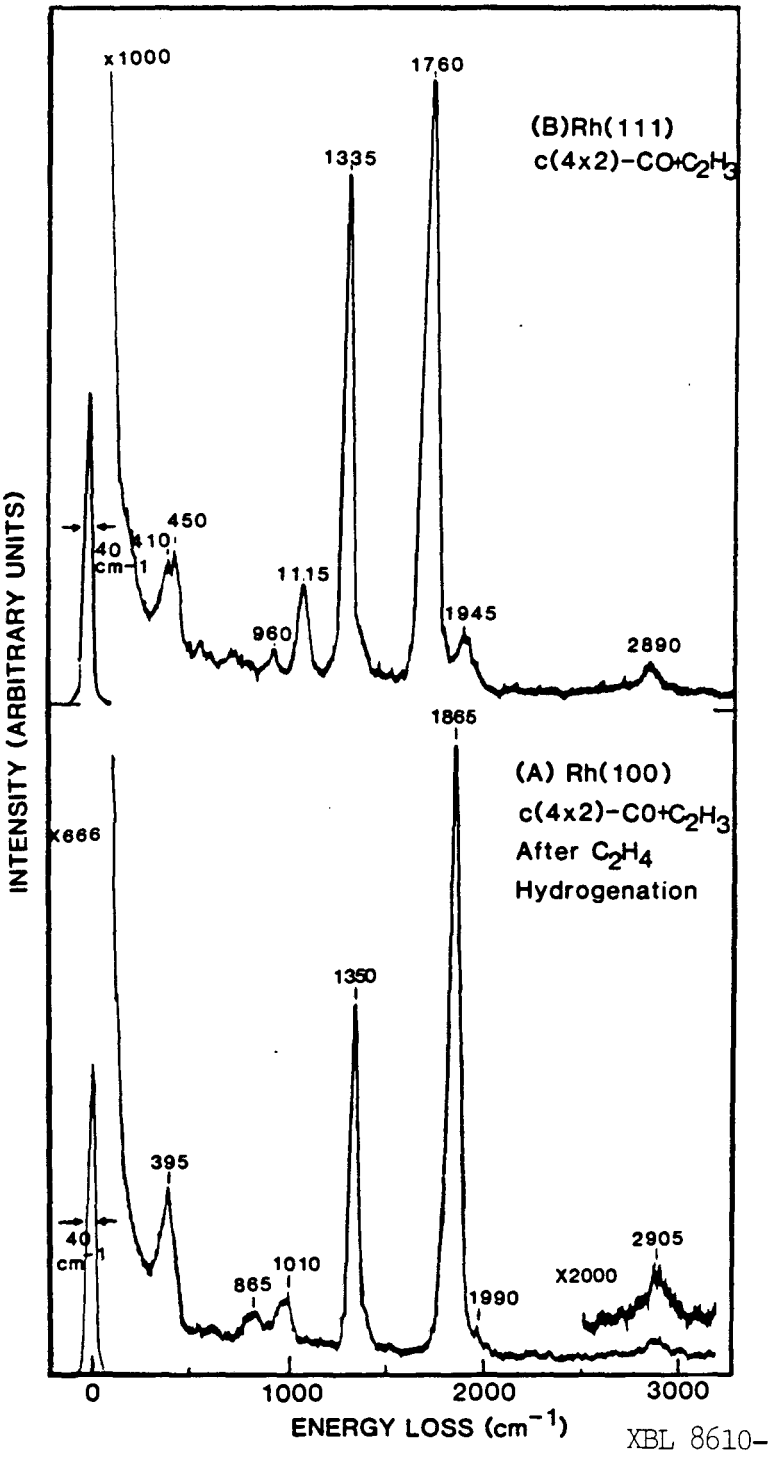

Figure 4.6: Specular HREELS of (A) Rh(100)/c(4x2)-2CO+CCH_3, which was produced accidentally after a catalytic ethylene hydrogenation reaction with contaminated CO; and (B) Rh(111)/c(4x2)-CO+CCH_3, which was formed by preadsorbing quarter-monolayer CO followed by saturation dosage (15 L) of ethylene. Both spectra were taken at room temperature.

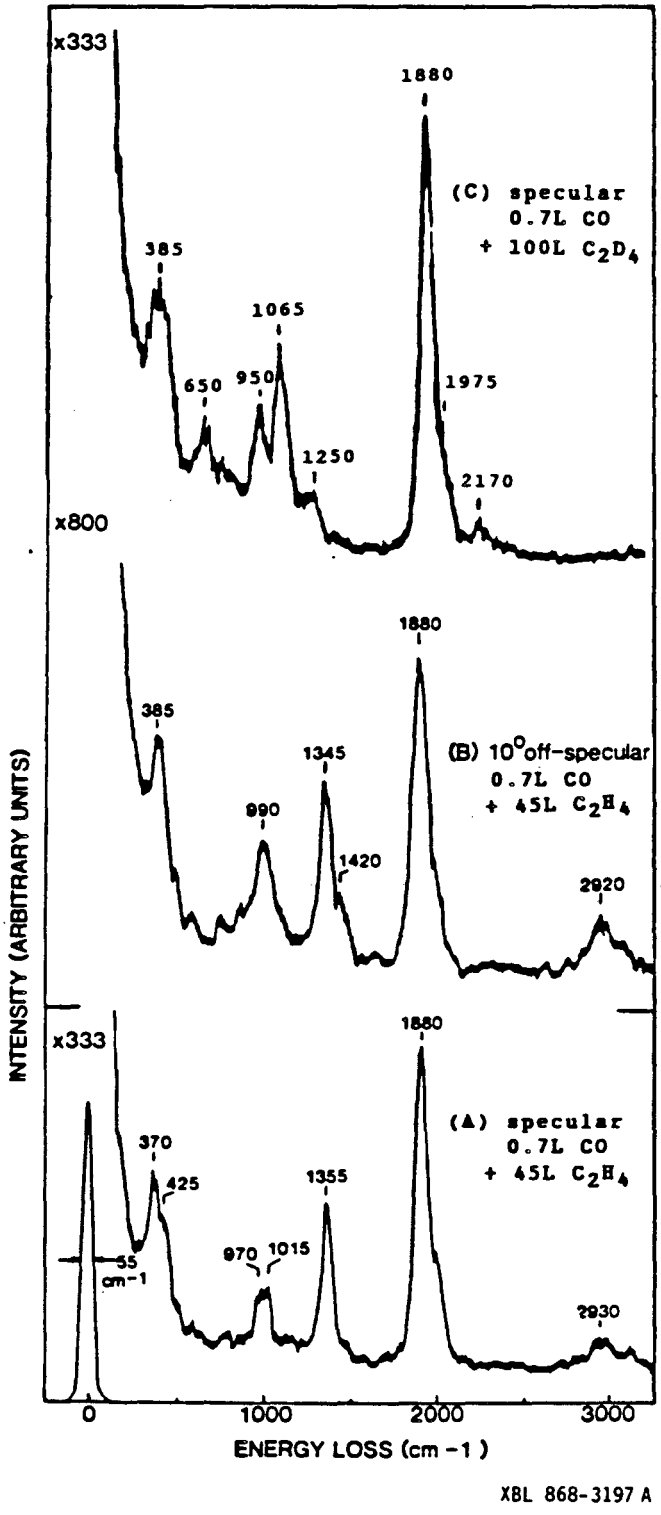

Figure 4.7: (A) Specular and (B) 10° off-specular HREELS of 0.7 L CO + 45 L C_2H_4 adsorbed on Rh(100) at 320 K. (C) Deuterated analogue of (A) (both 45 L and 100 L correspond to saturation dosage of ethylene). A split c(2x2) LEED pattern is observed for all three spectra.

Table 4.3: Vibrational frequencies (in cm^{-1}) for CCH_3 (ethylidyne) species on surfaces and within metallic clusters.

Substrate	ν(MC)	ν(CC)	$\delta(CH_3)$	$\nu_s(CH_3)$	Reference
Rh(100)	—	1015	1350	2915	this work, [133]
Pd(111)	409	1080	1335	2920	[142]
Rh(111)	435	1120	1335	2880	[143]
Pt(111)	435	1130	1350	2920	[144]
Pt(100)-5x20	440	1130	1350	2950	[111]
Ru(001)	480	1140	1370	2945	[145]
Co_3 cluster	401	1163	1355	2888	[146]
Os_6 cluster	—	1160	1381	2850	[147]

HREELS (figure 4.7B) and the specular spectrum for the CO+C_2D_4 analogue (figure 4.7C). These spectra will be used in the following to substantiate the formation of ethylidyne on Rh(100).

The HREEL spectra in figures 4.6A or 4.7A can be assigned to a mixture of CO and ethylidyne species as given in table 4.3. The 395 and 1865 cm^{-1} are typical values for the ν(M-C) and ν(C-O) frequencies of bridge-bonded CO on Rh(100) [40]. The remaining peaks near 2900, 1350, and 1010 cm^{-1} are attributable to ethylidyne. This assignment will be discussed in detail because this is the first observation of ethylidyne on a surface without threefold sites.

The intense 1350 cm^{-1} peak is typical for a methyl group symmetric CH_3 bending vibration. This so called "umbrella mode" occurs at 1335-1340 cm^{-1} for ethylidyne on Rh(111) [143,148] and at 1387 cm^{-1} for gas-phase CD_3CH_3 [129]. The fact that this peak shifts down with deuteration to 950 cm^{-1} (figure 4.7C) rules out a C-C stretching vibration, while the presence of the 1420 cm^{-1} peak in the off-specular spectrum (figure 4.7B) rules out a CH_2 group, which has only one peak (CH_2 scissor) in the range of 1300-1500 cm^{-1}. The 1420 cm^{-1} peak is assigned to the $\delta_{as}(CH_3)$ vibration which has the same frequency and similar

relative intensity for ethylidyne on Rh(111). The fact that the relative intensity of the $\delta_{as}(CH_3)$ mode increases substantially in the off-specular spectrum means that the methyl group is oriented with its threefold axis approximately along the surface normal. This conclusion is based on the surface dipole selection rule discussed in chapter 3 [6]. Further, it is unlikely that the C-C bond has broken to form surface methyl species at this temperature; methyl groups bound directly to Pt(111) have a strongly perturbed $\delta_s(CH_3)$ at 1220 cm^{-1} [149].

Other surface species such as vinyl ($CHCH_2$) and ethylidene ($CHCH_3$), which were previously proposed to explain the ethylidyne on the Pt(111) spectra, can be ruled out by the absence of the C-H bending mode at 1200-1300 cm^{-1} [129,150,151]. Thus, by observing intense $\delta_s(CH_3)$ at 1350 cm^{-1} and weak $\delta_{as}(CH_3)$ at 1420 cm^{-1} in the specular and off-specular spectra, and the absence of peaks in the 1100-1300 cm^{-1} range, the spectra in figure 4.7 can be assigned to ethylidyne formation on the Rh(100) surface. The peak at ~2900 cm^{-1}, which shifts to 2170 cm^{-1} upon deuteration, is due to $\nu_s(CH_3)$. The peak at 1010 cm^{-1}, which correlates with 1065 cm^{-1} mode in the deuterated spectrum, was ascribed to ν(C-C). This is also in the range of a single-bond ν(C-C) vibration. The Rh-C stretch, which was reported at 435 cm^{-1} on Rh(111) surface, could be obscured by the coadsorbed Rh-CO stretch at 370 cm^{-1}. The only extra peak at 1250 cm^{-1} in figure 4.7C, with no analogous mode in figure 4.7A, is probably due to a CH bending vibration of a partially H,D-exchanged methyl group [129]. It is possible that a small fraction of C_2D_3 undergoes H,D-exchange reactions with residual hydrogen atoms on the Rh(100) surface at room temperature.

It is worth looking at the differences between high-pressure-derived and UHV-derived monolayer of coadsorbed CO and ethylidyne. Not only are the observed HREELS peaks in figure 4.7A not as sharp as in figure 4.6A, but also the LEED

patterns for these two overlayers are different. The LEED picture of the high-pressure-derived c(4x2) pattern is shown in figure 4.8A, which should be compared with the more diffuse pattern shown in figure 4.8B for the UHV-derived structure. The pattern shown in figure 4.8B was denoted as split c(2x2), because of the way it is formed: the initially adsorbed 0.7 L CO creates a c(2x2) structure, and subsequent adsorption of ethylidyne causes a fourfold splitting of the c(2x2) spots.

The Structure Model of Rh(100)/c(4x2)-2CO+CCH_3

Ethylidyne (CCH_3) was the first organic surface fragment determined by HRE EL spectroscopy after adsorption of ethylene on Pt(111) at 300 K [152]. Since then, similar spectra have been observed on Rh(111) [153], Pd(111) [142], Ru(001) [145], and reconstructed Pt(100)-(5x20) [111], as listed in table 4.3. The bonding geometry on both Rh(111) [22,153] and Pt(111) [152] with or without coadsorbed CO or NO has also been analyzed by LEED crystallography. The favored adsorption site was threefold hollows on both surfaces. It is presumed that ethylidyne bonds in this manner on all of these surfaces, based on the similarity of HREEL spectra. Indeed, all of the surfaces mentioned above possess threefold hollow sites, which is consistent with this general argument. However, the observation of ethylidyne formation on the unreconstructed Rh(100) surface breaks this rule, and a new bonding geometry must be proposed for the c(4x2)-2CO+CCH_3 structure.

On Rh(100), the possible adsorption site of surface ethylidyne would be top, bridge, or fourfold hollows. Both top and bridge sites are less probable after comparing the observed vibrational frequencies to analogous organometallic compounds [13,133]. Further evidence favoring CCH_3 bonded at a fourfold hollow site comes from infrared spectroscopic studies of fourfold coordinated ethylidyne on

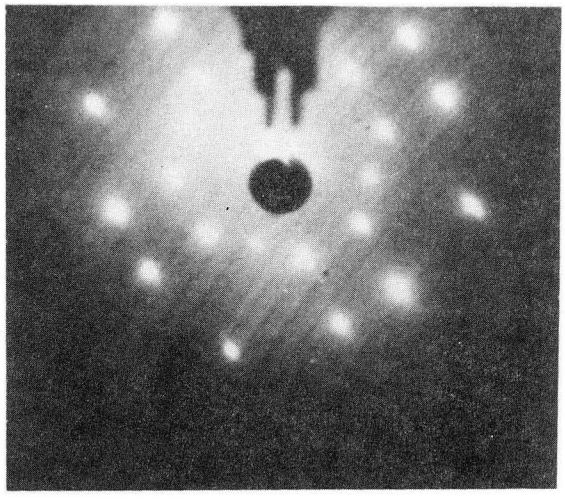

(A) c(4x2)

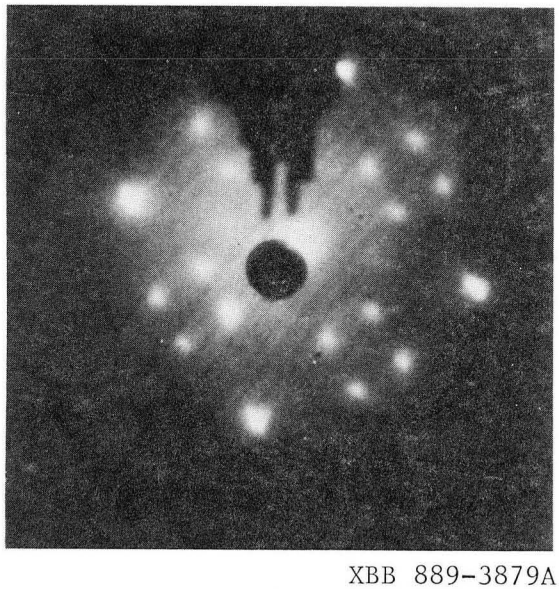

XBB 889-3879A

(B) split c(2x2)

Figure 4.8: (A) c(4x2) LEED pattern was observed for the high-pressure-derived monolayer of figure 4.6A. (B) Split c(2x2), which was attributed to small domains of c(4x2) with antiphase boundaries, found for the UHV-derived monolayer in figure 4.7.

$Os_6(CO)_{16}(CCH_3)_2$ [147], also listed in table 4.3. As can be seen from table 4.3, a great similarity exists between ethylidyne on Rh(100) and in the hexaosmium cluster. The only difference is the ν(C-C) position at 1010 cm^{-1} on Rh(100), which is about 100 cm^{-1} lower than the frequency observed in the cluster. However, this could be due to the presence of coadsorbed CO, or the difference in chemical bonding environment on the Rh(100) surface and hexaosmium cluster compounds. A plausible structural model of the high-pressure-derived c(4x2)-2CO+CCH_3 is shown in figure 4.9. The unit cell consists two CO molecules adsorbed at the bridge site, as determined by ν(C-O) at 1865 cm^{-1}, and one ethylidyne species adsorbed on top of a fourfold hollow site.

In comparing ethylidyne spectra on Rh(111) and other transition metal surfaces listed in table 4.3, a low ν(C-C) value was observed on Rh(100). This indicates that a stronger chemical bonding between ethylidyne and the surface causes a weakening of the C-C bond on this more open surface. This is also consistent with thermal fragmentation of the surface ethylidyne on Rh(100), as will be discussed in the following sections.

The Formation of Acetylide and Ethylidyne by Saturated Ethylene Adsorption on Rh(100)

Let us now return to assign the spectra in figure 4.3. These spectra could be grossly attributed to a mixture of acetylide and ethylidyne. The acetylide-related modes are assigned as follows (deuterated frequencies in parenthesis): 3040 (2265) = ν(C-H), 830 (680) = γ(C-H); the 1250 cm^{-1} mode in the deuterated spectrum is assigned as ν(C-C), and the corresponding mode in the nondeuterated spectrum is obscured by the intense 1330 cm^{-1} peak. The ethylidyne peaks are assigned based

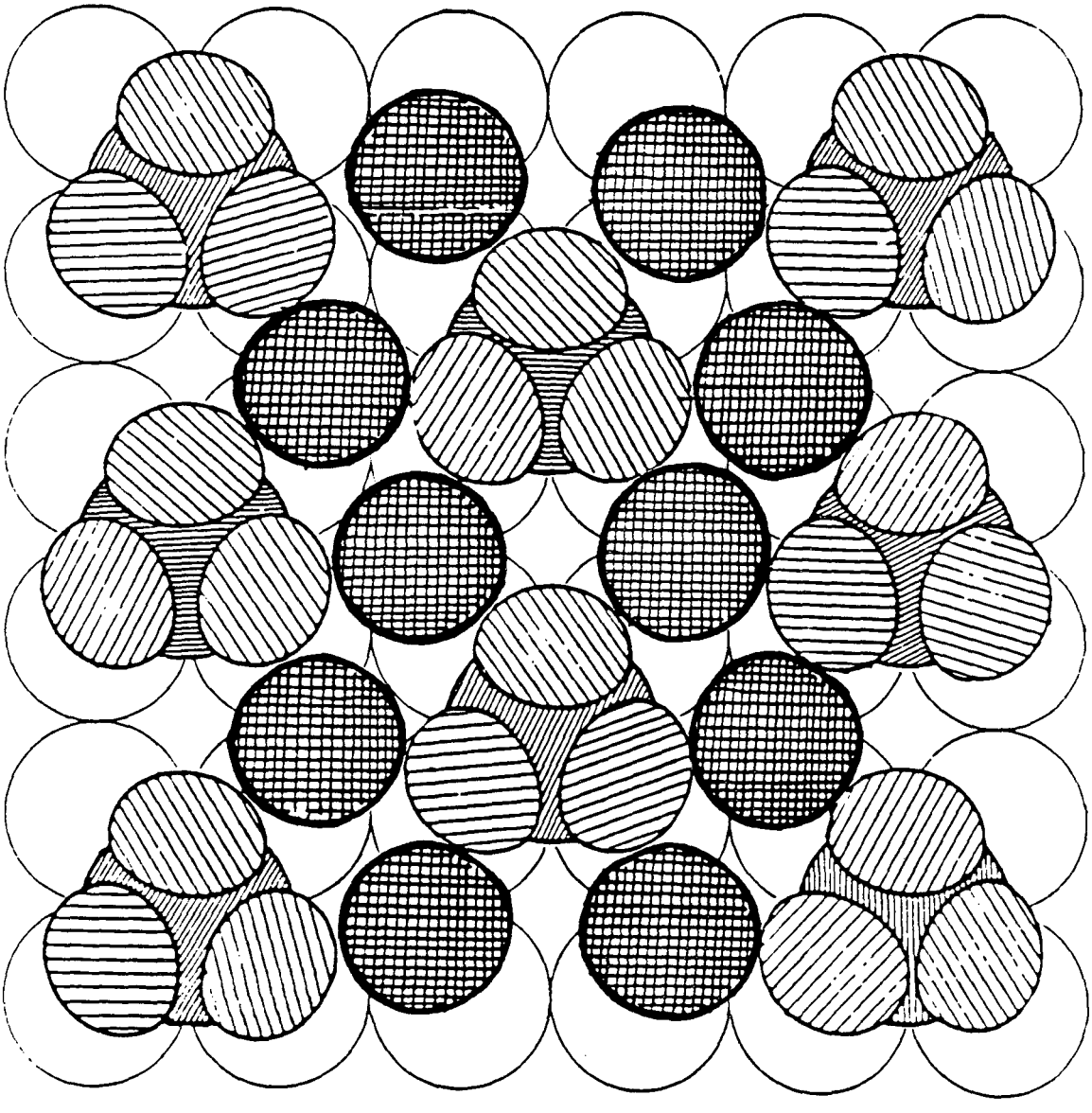

XBL 868-3192

Figure 4.9: Proposed arrangement of ethylidyne species coadsorbed with CO in a c(4x2) structure on a Rh(100) surface.

on the previous discussion as follows (deuterated frequencies in parenthesis): 2890 (2130) = $\nu(CH_3)$, 1330 (930) = $\delta_s(CH_3)$, and ~1000 (1055) = ν(C-C). We note that other fragments such as CCH_2 may also be present as minority species. The presence of such a fragment could account for unassigned modes at 700-740 cm^{-1} and at 1135 cm^{-1} in the hydrogenated spectra.

It is worth mentioning that the spectra in figure 4.3 correlate with ethylidyne formation after the Rh(100) surface was covered by half a monolayer of acetylide (CCH), while the spectra in figure 4.7 are composed of ethylidyne coadsorbed with half a monolayer of CO. It seems that half a monolayer of either CO or acetylide could promote further ethylidyne formation from ethylene decomposition on the Rh(100) surface. No ethylidyne was detected at less than half a monolayer coverage of either CCH and CO, while less ethylidyne was formed by preadsorbing more than half a monolayer CO. These observations imply that a site-blocking mechanism is involved during the formation of ethylidyne from ethylene fragmentation on Rh(100) at room temperature. Site blocking can be accomplished by preadsorbing the surface with either CO [133] or CCH, or even other atomic adsorbates such as sulfur or carbon [154].

4.3.2 HREELS of Ethylene Decomposition Above 380 K

The HREEL spectra for thermal decomposition of a CCH_3 + CCH monolayer above 380 K on Rh(100) are shown in figure 4.10. Most of the features in these spectra are attributable to the decomposition of CCH_3 on Rh(100). The CCH species, in addition to having relatively few vibrational modes, is already highly dehydrogenated, and further dehydrogenation leads to surface carbon, which has no sharp vibrational modes on Rh(100).

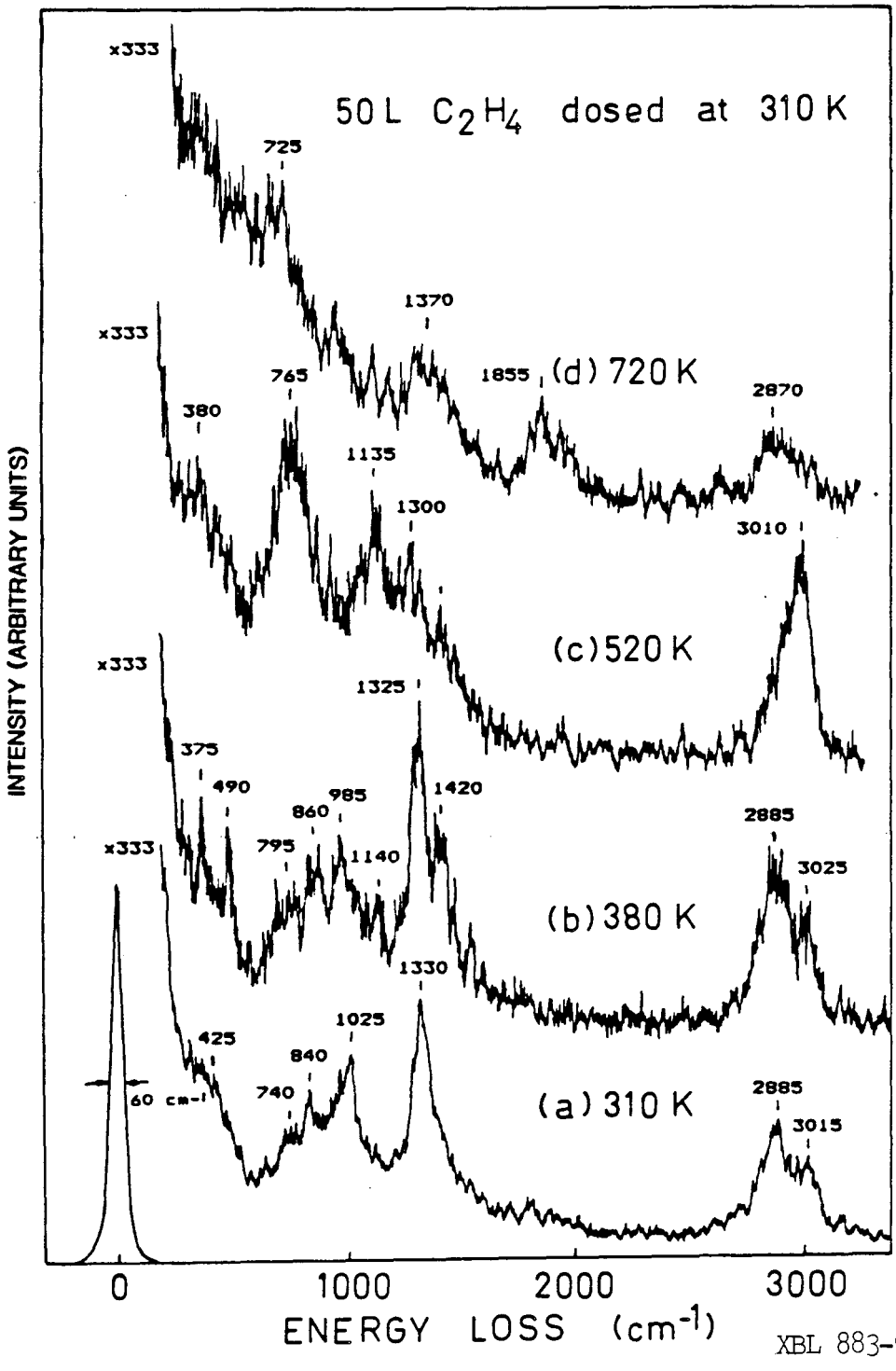

Figure 4.10: Specular HREELS of 50 L C_2H_4 (corresponds to saturation dosage) adsorbed on Rh(111) at 310 K, and sequentially annealed to the indicated temperature. All spectra were taken at 300 K.

The HREEL spectra for decomposition of CCH_3 in the absence of CCH but coadsorbed with CO are shown in figure 4.11; they are indeed quite similar to those spectra with CCH present in figure 4.10. The starting monolayer of CCH_3 in figure 4.11A was prepared by coadsorption of ethylene and carbon monoxide [133]: first 0.7 L of CO was adsorbed to give a c(2x2) LEED pattern, followed by adsorption of 160 L of ethylene at 300 K. We suspect that the differences in the peak frequencies and intensities in the 380 and 520 K spectra of figure 4.11 in comparison with the analogous monolayers in figure 4.10 are due to varying degrees of dehydrogenation (there is continuous hydrogen evolution from the surface from 380-700 K) rather than to the effects of CO vs. CCH on CCH_3 decomposition.

The complex HREEL spectra in figure 4.11 for ethylidyne decomposition above 380 K on Rh(100) can not be definitively assigned. Probably a mixture of surface species is present on the surface at these elevated temperatures. We can say that ethylidyne begins to decompose at about 380 K on Rh(100), since in the 380 K spectrum (CCH_3 + CO; fig. 4.11B) all the ethylidyne modes have essentially disappeared. The 380 K spectrum for CCH_3 + CCH decomposition in figure 4.10b still shows some ethylidyne based on the presence of the 1325 cm^{-1} peak, but the changes in the lower-frequency modes and the appearance of the 1420 cm^{-1} peak indicate significant decomposition.

A chemically reasonable explanation for the complex spectra in figures 4.10b and 4.11B is that the major decomposition product from CCH_3 is CCH_2. Other more highly dehydrogenated species (even mixtures of species) would be too vibrationally simple to account for the many modes observed. The peaks in the range of 1300-1450 cm^{-1} are almost certainly due to CH deformation modes in CH_2 and/or CH_3 groups, because ν(C-C) modes are generally weak and modes for CH groups occur at lower frequencies. Based on the published spectra of surface [155]

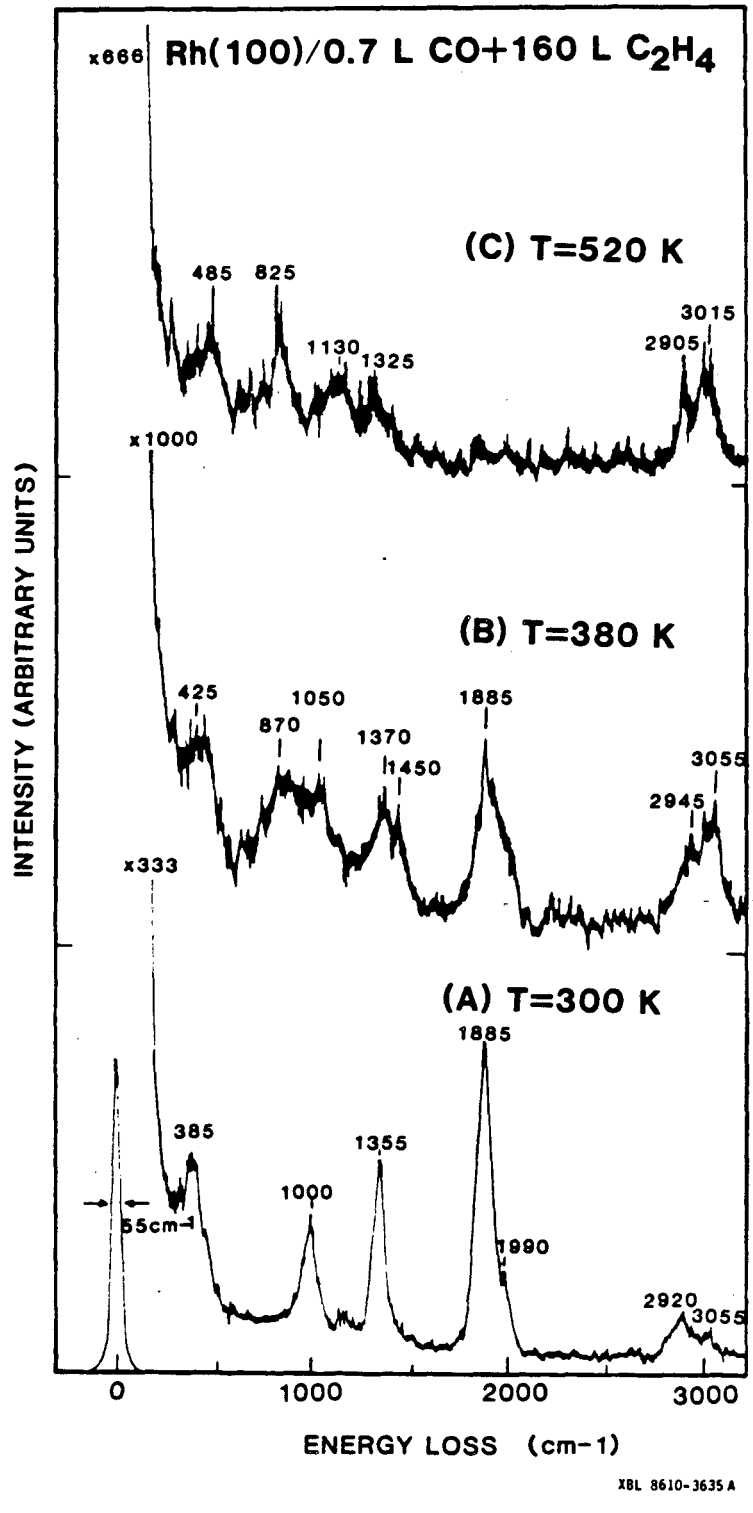

Figure 4.11: Specular HREEL spectra of a Rh(100) surface after dosing 0.7 L CO + 160 L C_2H_4 at 300 K and annealing to the indicated temperature. The surface species in (A) are CO + ethylidyne. Further decomposition of ethylidyne to CCH_2 in (B) and CCH species in (C) was discussed in the text.

and cluster [156] bound CCH_2 species, this ligand is expected to have multiple vibrational peaks in the 800-1450 cm^{-1} region. Also, since C_2H is expected from organometallic chemistry to bond with a tilted geometry on a clean transition metal surface [155,156], the highest possible adsorption symmetry on Rh(100) is C_s. This low-adsorption symmetry means that most of the vibrational modes will be dipole active [6], which can account for some of the complexity in figures 4.10b and 4.11B.

The ethylene decomposition spectra above 380 K on Rh(100) show qualitatively the same features found for high-temperature decomposition of unsaturated hydrocarbons on a number of transition metal surfaces, including Rh(111) [96,138], Pt(111) [157], Ni(111) [158], and Ru(001) [137]. These spectra have been attributed to polymeric C_xH species [96,138] or CH species [137,157,158]. In each of these cases, the mode at 700-850 cm^{-1} is assigned to a CH bend and/or metal-carbon stretch, while the peak at ~3000 cm^{-1} is assigned to a CH stretch. The blob at ~1300 cm^{-1} has been attributed to C-C stretching modes in polymeric species. We know of no satisfactory explanation of the mode frequently observed at ~1150 cm^{-1} or the ν(C-H) frequency shift down below 3000 cm^{-1} just prior to complete dehydrogenation [96], as seen in figure 4.10d.

4.3.3 HREELS of Acetylene Fragmentation

The molecular acetylene spectra were unchanged over the temperature range of 90-250 K. Above 250 K, new features were observed at different surface coverages. Figure 4.12A shows the HREEL spectrum at 0.5 L C_2D_2 dosage, and figure 4.12B and 4.12C compare the saturation dosage of deuterated and nondeuterated acetylene spectra at 320 K. Comparing the spectra of ethylene decomposition at low

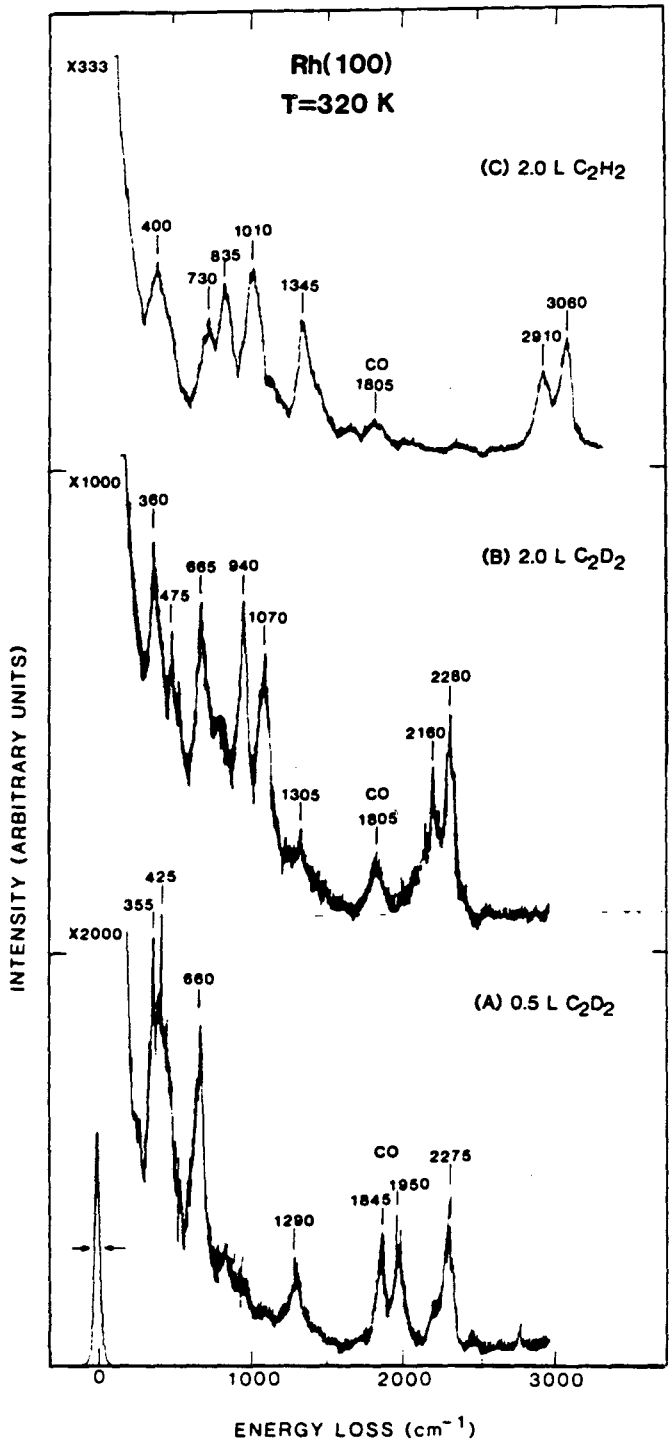

Figure 4.12: Surface vibrational spectra of acetylene adsorbed on Rh(100) at the sample annealing temperature of 320 K: (A) 0.5 L C_2D_2, (B) 2.0 L C_2D_2, (C) 2.0 L C_2H_2. The observed peaks at 1805, 1845, and 1950 cm^{-1} are due to a small amount of coadsorbed CO contamination from ambient gas. All three spectra were taken at room temperature.

and saturation coverages, great similarities can be seen between figure 4.4C and figure 4.12A, as well as figures 4.3b and 4.12C. This implies that both acetylene and ethylene generate the same surface fragments, CCH and CCH_3, at low and near-saturation coverages. The complete assignment of both CCH and CCH_3 spectra has already been described in great detail in previous sections for ethylene fragmentation on Rh(100). Only a brief assignment of the spectra in figure 4.12 will be given below.

In figure 4.12A, the peak at 1290 cm^{-1} was assigned as a carbon-carbon stretch of the deuterated species, and two peaks at 2275 and 660 cm^{-1} in figure 4.12A were attributed to both C-D stretch and bending modes, respectively. These observed features are consistent with a surface deuterated acetylide (CCD) species, which can formed by breaking one C-D bond from acetylene. The extra peaks at 1800-2000 cm^{-1} were due to ν(C-O) from background CO adsorption. At surface doses higher than 1.0 L, which correspond to a sharp c(2x2) LEED pattern, new modes at 940, 1070, and 2160 cm^{-1} begin to grow, as shown in figure 4.12B. The corresponding peaks in the nondeuterated spectrum are displayed in figure 4.12C at 1010, 1345, and 2910 cm^{-1}. The peaks were attributed to surface ethylidyne species and assigned as follows (deuterated peak position in parenthesis): at 1010 (1070) = ν(C-C), 1345 (940) = $\delta_s(CH_3)$, and 2910 (2160) = $\nu_s(CH_3)$.

Further dehydrogenation of the surface species was observed at T>400 K. Figure 4.13 shows the spectra of 2.0 L acetylene at 520 and 620 K. By comparing with the spectra at 320 K shown in figure 4.12, the modes at 2910, 1345, and 1010 cm^{-1}, which were attributed to the surface ethylidyne, disappeared. This is also consistent with the observation, shown in figure 4.5, for a similar overlayer generated from ethylene decomposition. In fact, similar peak positions and relative intensities can again be seen by comparing figures 4.13A and 4.10c, as well as

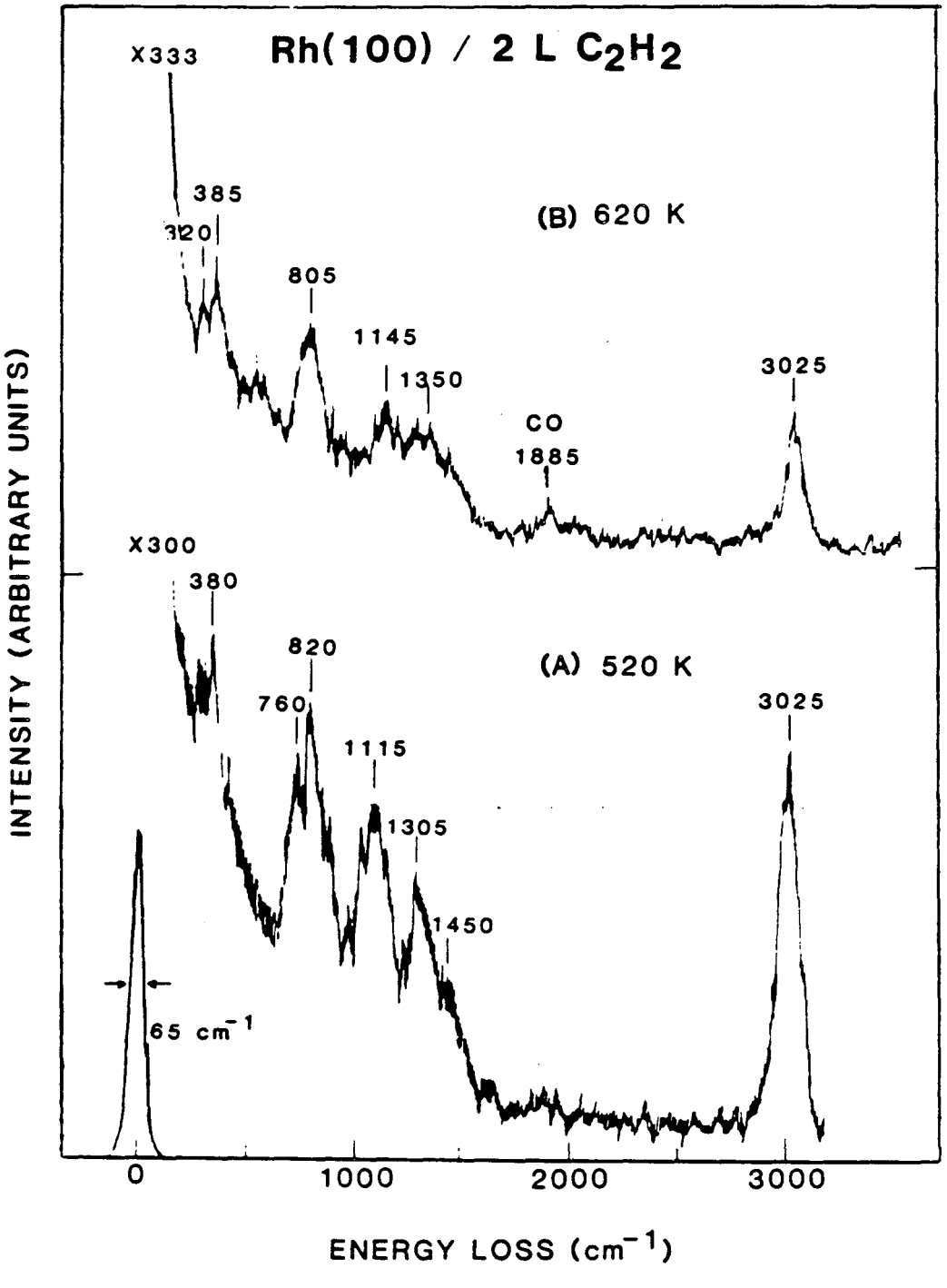

Figure 4.13: Vibrational spectra of 2.0 L C_2H_2 adsorbed on Rh(100) at sample annealing temperatures of (A) 520 K, (B) 620 K, respectively. Both spectra were taken at room temperature in the specular direction. The observed peaks at 1830 and 1885 cm^{-1} are due to CO contamination from background gas.

figures 4.13B and 4.10d. In figure 4.13A, the two most intense modes are the peaks at around 820 and 3025 cm^{-1}, which persist from the 320 K spectra and were assigned as the C-H bending and stretching modes of the CCH species, and the modes at 1305 and 380 cm^{-1} can be assigned as the C-C and Rh-C stretches of such species. The new mode observed at 1115 cm^{-1}, which shifts down to 805 cm^{-1} upon deuteration, is probably due to the C-H bending of some CH_x species ($1 < x < 3$); and the rest of the modes can be obscured by the predominant CCH species. Figure 4.13B shows the spectrum at 620 K. Clearly, the mode at 1350 cm^{-1} is much broader than the peak at 1305 cm^{-1} of the 520 K spectrum. We ascribed this to a carbonaceous overlayer with a generalized formula of C_xH ($x \geq 2$). Such species can have the similar observable modes as surface acetylide with wider C-C stretch mode distributions.

4.3.4 Thermal Desorption Spectroscopy of Acetylene and Ethylene

TDS of Ethylene and Coadsorbed CO+CCH_3 on Rh(100)

Hydrogen thermal desorption spectra for ethylene adsorption on Rh(100) are difficult to interpret both because of the coverage dependence of the surface decomposition pathway and because several dehydrogenation reactions occur at or below the temperature where surface hydrogen atoms recombine and desorb. The thermal desorption spectra can, however, provide some support for our interpretations of the HREEL spectra.

Hydrogen TD spectra for ethylene adsorbed at < 150 K on Rh(100) are shown in figure 4.14A. The absence of hydrogen desorption below 200 K is consistent with the observation that C_2H_4 adsorbs without dissociation in this temperature

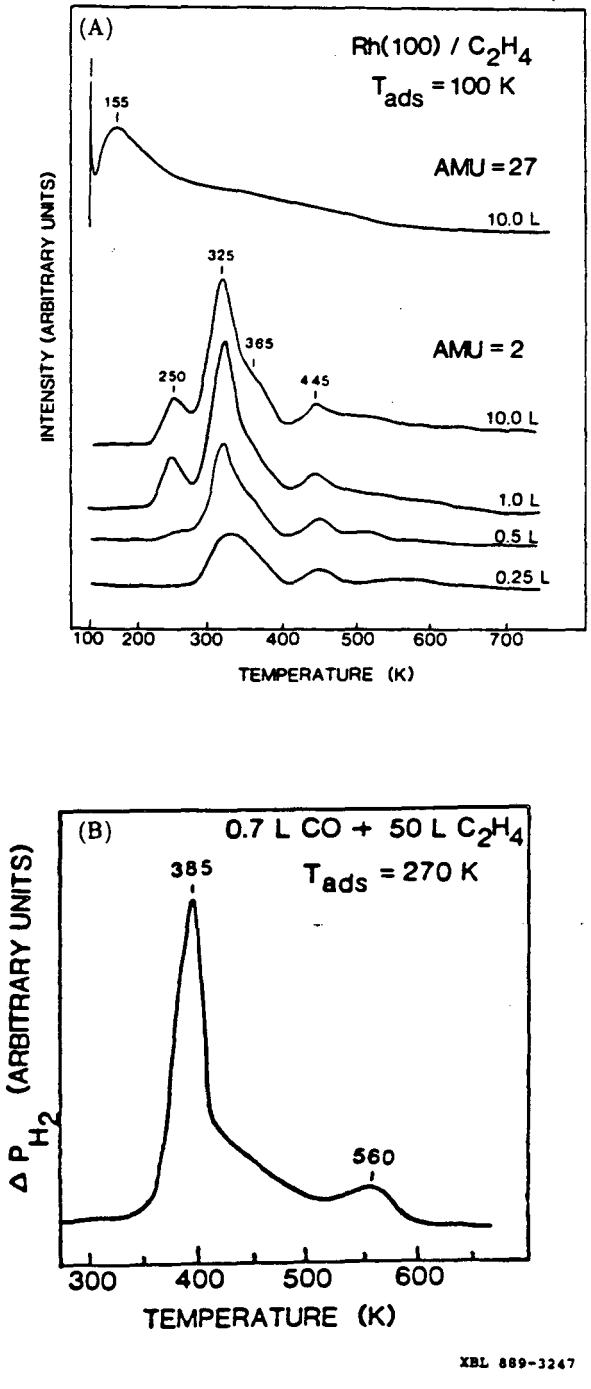

Figure 4.14: (A) Mass 2 and 27 TDS for ethylene on Rh(100) at 100 K as a function of dosage. (B) Hydrogen TDS for ethylene adsorbed on a Rh(100) surface predosed with 0.7 L of CO at 270 K. The surface species at the adsorption temperature are ethylidyne and CO. The heating rates were 17 and 10 K/sec for (A) and (B), respectively.

regime [51]. Also shown is the mass 27 desorption for a saturation exposure of ethylene. As the desorption temperature of molecular ethylene from other group VIIIB transition metal surfaces occurs above 200 K, both the low peak temperature (155 K) and the broadness of this peak imply this m/e = 27 spectrum is probably due to desorption from the Ta support wires. The 0.25 and 0.5 L H_2 TD spectra in figure 4.14A are consistent with CCH formation and decomposition. The first peak at 300-400 K is due to desorption of surface hydrogen produced in the formation of CCH below room temperature. The 450 K peak is then a result of CCH dehydrogenation. The integrated ratio of these 350 and 480 K peaks (2.8:1) is consistent with the stoichiometry of CCH species to within the ~10% uncertainty of TDS.

The higher-exposure TDS in figure 4.14A are more complex because both CCH_3 and CCH species form. It is interesting but not understood why a lower-temperature H_2 desorption peak appears at 250 K for higher ethylene exposures. Presumably, both this 250 K peak and the 325 K peak are due to desorption of hydrogen bound to the Rh(100) surface. These peaks are absent for ethylene adsorption at 300 K.

The origin of the 250 K peak is unclear. It may be due to a second surface state for hydrogen, although no such peak has been seen from the adsorption of hydrogen alone [40,159]. Alternatively, it might result from direct emission of hydrogen from dehydrogenation once the available surface has become saturated with hydrogen. This would, of course, require the saturated surface to act as the catalyst for dehydrogenation.

Attempts to investigate the source of the 250 K TDS peak more closely, by taking HREEL spectra near 273 K following dosing at 210 K, were largely unsuccessful. The result for a 5 L dose was given in figure 4.3a and has been discussed

previously. Results for doses of 1 L or less were irreproducible because of surface contamination occurring while the spectra were being taken. The TDS spectra at these low coverages were, however, very reproducible and are believed to reflect accurately the hydrocarbon decomposition.

The H_2 TDS for coadsorbed CO+CCH_3 in the absence of CCH and adsorbed hydrogen atoms is shown in figure 4.14B [133]. In this spectrum, a peak is clearly observed at 385 K. According to our HREELS analysis (figure 4.11B), this peak can be attributed to conversion of CCH_3 to CCH_2 with subsequent conversion to CCH. The desorption tail at still higher temperature then represents dehydrogenation and polymerization of C_xH species.

TDS of Acetylene on Rh(100)

The thermal desorption studies after deuterated acetylene adsorption on Rh(100) at 200 K are shown in figure 4.15. Only mass 4 (deuterium) desorption was detected, indicating irreversible chemisorption of C_2D_2. No significant change can be observed for doses higher than 2.0 L, and two major deuterium desorption peaks at 450 and 620 K have been observed at doses above 1.0 L. At lower surface coverage, both peaks shift down by about 20-40 K, with a nearly one-to-one peak-area ratio, as shown in the 0.3 L spectrum. Such a result is consistent with the HREELS assignment of a CCH species for doses less than 0.5 L, and the first peak at 400 K is due to hydrogen desorption from the decomposed acetylene.

The fragmentation process starts at 250 K, is based on the HREELS results discussed in the previous section. This temperature lower than the desorption tail of the first D_2 peak at 320 K, which means that the first desorption peak is limited by the deuterium desorption temperature. The ethylidyne starts to form

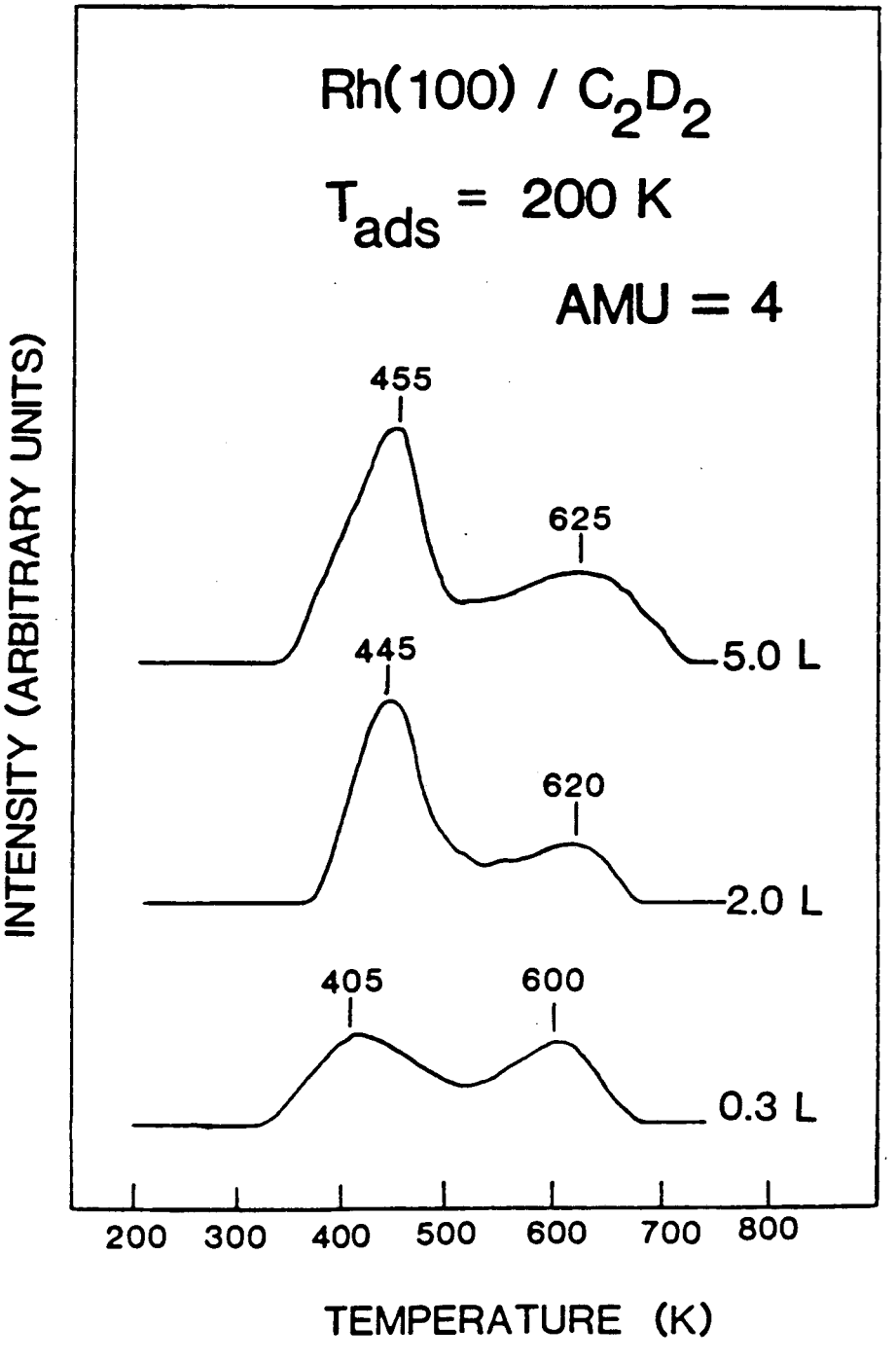

XBL 889-3232

Figure 4.15: Thermal desorption spectra for C_2D_2 adsorbed on Rh(100) at 200 K. Only deuterium (Amu=4) desorption was detected over the whole coverage range and is shown as a function of deuterated acetylene exposure. The heating rate was 17 K/sec in all cases.

at acetylene dosage above 1.0 L, where the first desorption peak becomes more intense and shifts to 450 K. This could be correlated with the hydrogen desorption from ethylidyne decomposition, and the low-coverage peak at 400 K was obscured by the 450 K peak. Further dehydrogenation with the formation of a polymerized overlayer corresponds to the second broad peak.

4.3.5 Thermal Chemistry of Ethylene on Rh(100) and Comparison to Rh(111)

Our HREEL spectroscopic studies clearly show that the kinetically stable intermediates formed during ethylene decomposition on Rh(100) change with coverage. For coverages (θ) less than 0.5, the stable decomposition intermediate at room-temperature is C_2H. At higher ethylene exposures, the stable room temperature decomposition fragment is CCH_3 (ethylidyne) rather than C_2H. These ethylidyne species begin to decompose at 380 K on Rh(100), while the CCH species are stable above 400 K. Our HREELS studies suggest that ethylidyne decomposes on Rh(100) to give predominantly CCH_2 species, but other more highly dehydrogenated fragments are probably also present. All of these partially hydrogenated fragments on Rh(100) decompose above 500 K to give a monolayer attributed to a mixture of CH and/or polymeric C_xH species.

The thermal chemistry of ethylene and ethylene coadsorbed with carbon monoxide on Rh(100) is summarized and compared to that for ethylene on Rh(111) in figure 4.16. Probably the most significant difference in the thermal fragmentation of ethylene on these surfaces is the coverage dependence of the chemistry on Rh(100) versus the coverage independence found on Rh(111). At room temperature and coverages less than $\theta \leq 0.5$, dehydrogenation is more extensive on

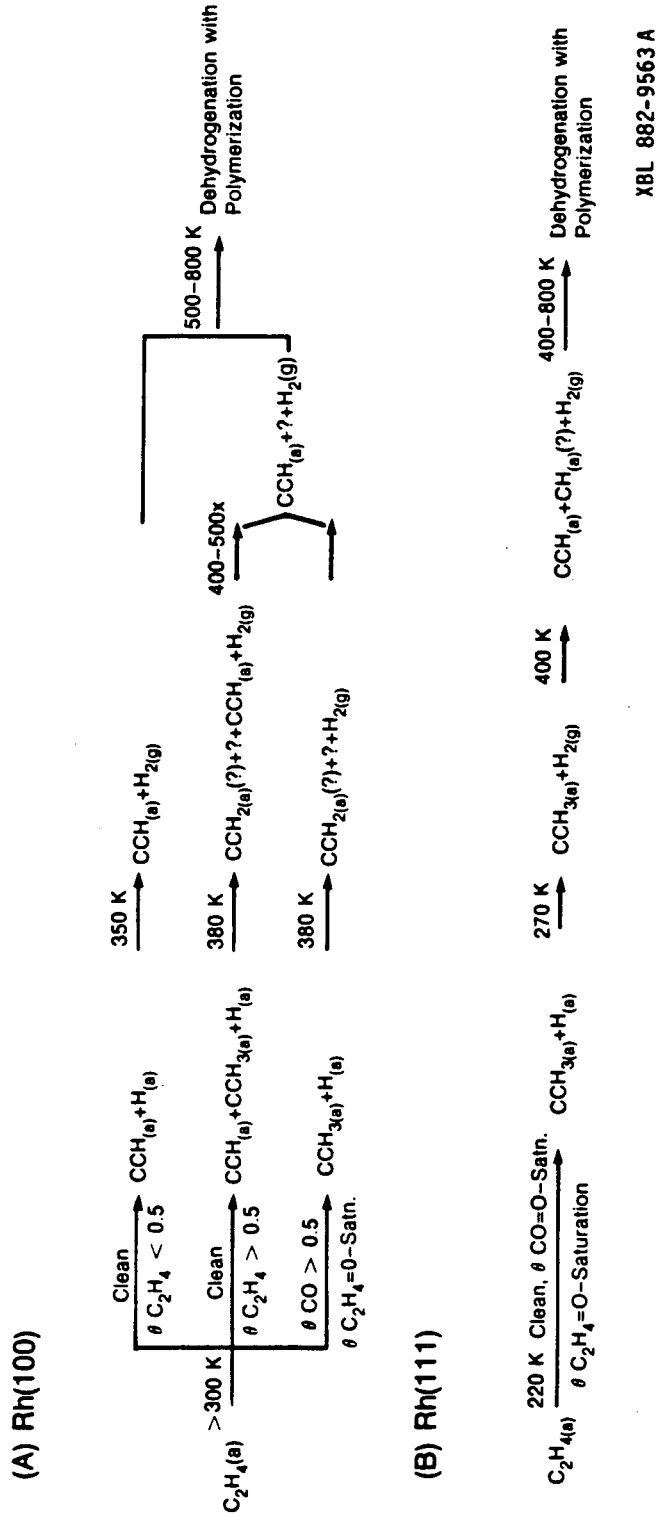

Figure 4.16: Thermal fragmentation pathways of ethylene on (A) Rh(100) and (B) Rh(111) surfaces with or without coadsorbed CO as a function of coverage and temperature are shown for comparison.

Rh(100) than on Rh(111). At higher coverages, this enhanced dehydrogenation on Rh(100) is suppressed, and the decomposition fragments on the two surfaces are quite similar.

It is interesting that half a monolayer of either CO or CCH species prevents the room-temperature decomposition of ethylene to CCH on Rh(100). Further, preliminary studies indicate that half a monolayer of carbon or sulfur atoms also has a similar effect on ethylene decomposition on Rh(100). Since CO bonds in top and bridge sites on clean Rh(100) [40,134], while sulfur [160] (and possibly carbon and CCH) bond in fourfold hollow sites, decomposition of ethylene to CCH probably involves a small ensemble of sites rather than a specific site. Based on the fact that the coverage of these adsorbates must be θ_{ads}= 0.5 before CCH formation is completely blocked, the ensemble size is between 2 and 4 metal atoms. Also, since similar decomposition to CCH does not occur on Rh(111) at room temperature, the ensemble probably requires at least one fourfold hollow site. It is not yet clear whether ethylidyne is an intermediate in CCH formation and is only kinetically stable on Rh(100) at high adsorbate coverages or whether two different decomposition pathways occur – one that produces CCH at low coverage and another which produces CCH_3 at high coverage.

4.3.6 Thermal Chemistry of Acetylene on Rh(100)

Concerning the thermal evolution of acetylene on Rh(100), we will compare the results with other transition metal surfaces including Pd(100) and Rh(111), where complete HREELS studies have been made. A correlation between observed molecular spectra based on Sheppard's classification and thermal evolution pathways of surface acetylene will also be addressed.

On Rh(100), a coverage dependent fragmentation of acetylene was observed, and the major species at doses less than 1.0 L is CCH. The acetylide fragment has also been formed on Pd(100) from acetylene decomposition at 400 K, but no ethylidyne was observed on this metal surface. The similarity between Rh(100) and Pd(100) again shows in the formation of acetylide at T > 400 K on both metal surfaces, although the unique feature of Rh(100) is the capability to form ethylidyne at T > 250 K at acetylene doses above 1.0 L. The fragmentation process of acetylene on Rh(100) is exactly the same as for ethylene on this surface. A reasonable dehydrogenation mechanism would have ethylene dehydrogenate to acetylide through an acetylene intermediate, although we were not able to isolate acetylene during ethylene fragmentation, which could be due to the fact that both ethylene and acetylene decompose over a comparable temperature range near 250 K.

Quite different chemistry was observed on Rh(111), where a coverage-independent thermal chemical process was observed and the rearrangement of acetylene to vinylidene (CCH_2) was the predominant channel at 270 K [21]. From such comparisons between the Rh(100) and Rh(111) surfaces, it is clear that Rh(100), which is more open than Rh(111) by 20%, is more capable of dehydrogenating both acetylene and ethylene to form acetylide at less than half-monolayer coverage.

An attempt was also made to hydrogenate the surface acetylide to ethylidyne by either coadsorbing acetylene with hydrogen at temperatures less than 200 K or by exposing the acetylide layer to $1x10^{-5}$ torr hydrogen near room temperature. In both cases, incomplete conversion was observed, although an enhancement of the surface ethylidyne concentration was detected. This also suggests a higher barrier for conversion of acetylide to ethylidyne in comparison to the hydrogenation of vinylidene to ethylidyne on Rh(111) surface, which has been observed at 240 K by

Dubois et al. [92]. Another separate study of ethylene hydrogenation at ethylene and hydrogen pressures of 100 and 20 torr, respectively, at 380 K does indicate a complete conversion of acetylide to the surface ethylidyne with the observation of a sharp c(2x2) LEED pattern after the reaction. It is possible that the pressure of hydrogen plays an important role in the conversion of acetylide to an ethylidyne overlayer.

Further dehydrogenation of the acetylide plus ethylidyne overlayer occurs at T > 450 K, where a polymerized species of $C_xH(x > 2)$ was observed from HREEL spectra shown in figure 4.13, corresponding to a broad hydrogen desorption peak centered around 620 K shown in figure 4.15. Such a polymerization and dehydrogenation process in the temperature range of 450-800 K has been observed in ethylene [51] and benzene [96] fragmentation on Rh(111) surface. The stability of such a carbonaceous overlayer on different low-Miller-index surfaces suggests an importance of this overlayer to some heterogeneous catalytic reactions.

The acetylene thermal chemistry on transition metal surfaces determined by HREELS is summarized in figure 4.17. The various classes (A, A', B) of molecular acetylene adsorption are noted; however, there are not enough data to determine whether types of molecular adsorption can be correlated with thermal fragmentation pathways. There do appear to be significant differences between the 3d and 4d/5d metals, with the former, such as Ni and Fe, showing increased dehydrogenation and C-C bond breaking at any given temperature. The differences in the amount of dehydrogenation on the 3d and 4d/5d metals may be amplified by the hydrogenation that can occur on the 4d/5d metals. For example, acetylene is hydrogenated and converted to ethylidyne on Rh(111) [92], Pt(111) [144], and Pd(111) [142] when hydrogen is added.

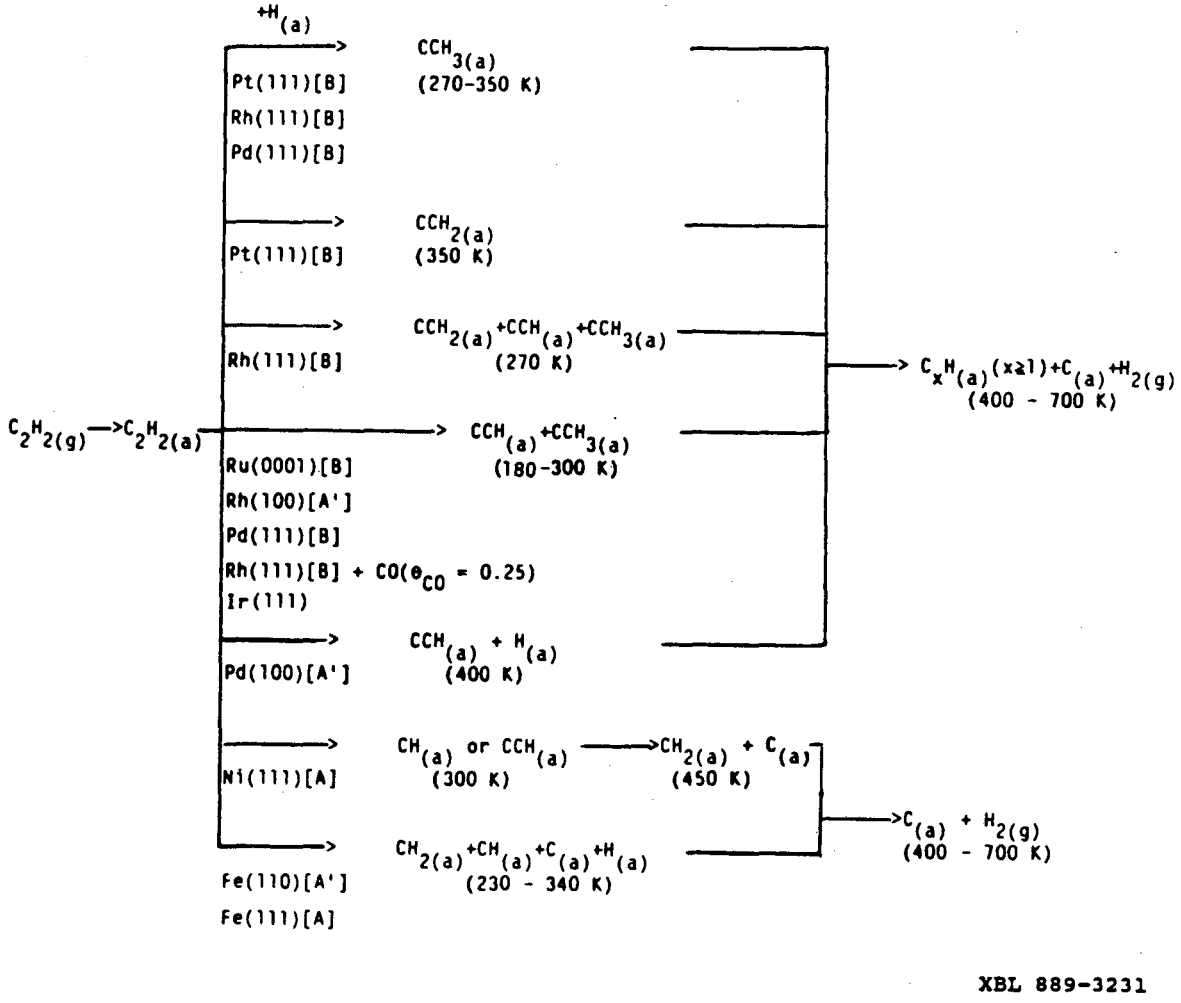

Figure 4.17: Thermal fragmentation pathways of acetylene on various transition metal surfaces are shown for comparison. The metal substrates are classified into three categories, A, A', and B, based on vibrational profiles of surface acetylene species as proposed by Sheppard [126].

4.3.7 Summary of Acetylene and Ethylene Thermal Chemistry on the Rh(100) Surface

- We have shown, based on our HREELS results, that the thermal fragmentation pathway of the acetylene is the same as the result for the ethylene on the same substrate.

- The decomposition of both acetylene and ethylene on Rh(100) is coverage dependent. At 380 K and for coverages of less than one-half monolayer, ethylene dehydrogenates to CCH (acetylide) species; ethylene adsorbed in excess of $\theta = 0.5$ is converted to CCH_3 (ethylidyne) species.

- Preadsorbed half-monolayer CO can block the decomposition channel of CCH formation from ethylene and favors the ethylidyne formation. A structure model is proposed to account for the arrangement of CO and ethylidyne within the coadsorbed c(4x2) unit cell.

- The HREEL spectra for subsequent decomposition of surface species above 380 K are complex, suggesting that a mixture of surface species are present at all temperatures between 400 and 800 K. The spectra do provide some evidence that CCH_3 decomposes above 380 K predominantly to CCH_2, which subsequently dehydrogenates and polymerizes to C_xH species.

- The high-coverage fragments for ethylene on Rh(100) are quite similar to the previously reported coverage-independent chemistry of ethylene on Rh(111); however, at low coverages, dehydrogenation is much more extensive for both acetylene and ethylene on Rh(100) than on Rh(111). Therefore, the thermal chemistry of both acetylene and ethylene are sensitive to the crystallographic orientation of the rhodium surface.

4.4 The Structure and Thermal Chemistry of Benzene on Rh(100)

4.4.1 Background

Benzene, C_6H_6, is one of the simplest and most important aromatic compounds. It consists of a six-carbon member ring with two resonance structures. Based on valence bond theory, each carbon atom bonds with one hydrogen and two nearest carbon atoms by sp^2 hybridization. There are three extra π bonds formed by overlapping p_z orbitals contributed from each carbon atom. Due to the existence of the two resonance structures, the strength of each carbon-carbon bond is equivalent. The C-C bond order is 1.5 with a distance of 1.4 $\AA$.

The chemisorption of benzene on transition metal surfaces, in particular group VIII metals, have been studied by a combination of surface science techniques. Many spectroscopic studies have helped to conclude that benzene chemisorbs molecularly on these metal surfaces with its ring plane parallel to the surface plane. The surface chemical bond of benzene can be described by charge transfer from the HOMO (highest occupied molecular orbital) E_{1g} orbital of benzene to vacant surface d orbitals of appropriate symmetry. Such a π-d interaction is also indicated by chemical shifts of bonding π orbital relative to σ orbital by ARUPS (angle resolved ultraviolet photoelectron spectroscopy).

Both HREELS and dynamical LEED analysis have been applied to monitor the strength of this chemical interaction. A 50-170 cm^{-1} shift of the intense out-of-plane bending mode (γCH) was generally detected by HREELS on low-Miller-index surfaces (except Ag(111) [161]). However, due to the similarity of the remaining vibrational modes to the gas-phase frequencies, most studies still

claim that benzene will retain its delocalized symmetric structure when bound to a metal surface. A NEXAFS study on Pt(111) concluded that the adsorbed benzene molecules lie flat on the surface with C-C distance of 1.4 $\AA$, a very small distortion relative to gas phase benzene [162].

The results mentioned above were challenged by recent LEED structural analysis work on Rh(111) [163,164], Pt(111) [165], and normal coordinate analysis on the Ni(111) surface [166], where a Keküle distortion with averaged C-C bond order of one was found. Further support for this type of distortion comes from recent molecular orbital calculations, where a strong Keküle distortion is expected on Rh(111), Pt(111), and Ru(001) surfaces, and less distortion is expected on the Pd(111) surface [167,168]. A STM study of the Rh(111) surface also suggests a threefold symmetric benzene adsorbed on Rh(111), consistent with the results obtained by LEED analysis [169]. At this stage, the controversy as to the degree of benzene ring distortion still exists, and more study, both theoretical and experimental, is needed to unravel this mystery.

The chemisorption of benzene on Rh(111) has been studied by LEED [163,164], HREELS [95,96], TDS [96], ARUPS [170,171], and work function measurements [32]. One ordered structure has been observed by saturating the surface with benzene at room temperature. Two other new LEED patterns, induced by CO coadsorption, have been studied by dynamical LEED analyses [163,164]. The proposed structure involves benzene adsorption at hcp hollow sites with significant Keküle distortion. Decomposition of the benzene overlayer was found at 400 K, with the formation of surface acetylide (CCH) and methylidyne (CH) species. An acetylene intermediate during benzene decomposition was proposed based on C-C bond alternation. A similar process, decyclotrimerization from benzene to three acetylene, was found on a supported rhodium surface by Raman spectroscopy [172].

In this section, the surface structure and thermal chemistry of benzene adsorbed on Rh(100) in the temperature range of 300-800 K will be presented. HREELS and LEED will be applied to monitor the surface bonding geometry, surface ordering, and coverage of adsorbed benzene. For pure benzene adsorption, a c(4x4) ordered structure was found at saturation dosage at near room temperature. The surface coverage is estimated to be 0.125, based on a packing model of benzene on the surface lattice. Compared to Rh(111), the HREELS on Rh(100) indicates a less distorted benzene, according to the shift of the out-of-plane (γCH) bending vibration relative to the gas phase. This is opposite to the trend of acetylene and ethylene chemisorption, where more strongly rehybridized species were formed on the Rh(100) surface.

A CO coadsorption experiment was performed to test coadsorbate-induced ordering on the Rh(100) surface. We found that a new surface structure can be formed by mixing CO and benzene at a relative surface coverage of two to one. Only minor perturbations to the benzene structure were observed, as indicated by the resemblance of the HREEL spectra with or without coadsorbed CO; however, significant reduction in the ν(CO) frequency, in accordance with a top to bridge site shift, was observed by benzene coadsorption. Similar phenomena have also been observed on Rh, Pt, Pd, and Ru surfaces. It is presumed that charge transfer from the benzene π orbital to the $2\pi^*$ orbital of CO through the metallic substrate is responsible for this frequency and site shift effect. The details of coadsorbate interaction will be discussed. Two structural models of the observed LEED patterns with or without coadsorbate will be proposed based on vibrational spectroscopic analysis.

The thermal chemistry of benzene will be discussed based on temperature-dependent HREELS studies and complementary TDS at saturation coverage. Pre-

dominantly irreversible chemisorption was observed for benzene on Rh(100). Both CCH and CH species were the predominant surface fragments formed above 450 K. Essentially the same carbonaceous overlayer was observed on Rh(111) at 400 K [96]. The higher decomposition temperature on the Rh(100) surface supports a weaker interaction between benzene and this surface. The results indicate structure-insensitive reactions on both rhodium surfaces, in contrast to relatively structure-sensitive fragmentation reactions for acetylene and ethylene.

The subsections are divided as follows: The adsorption of benzene and coadsorption of benzene with CO will be described first, followed by thermal decomposition measurements. The bonding and reactivity of benzene on Rh(100) will be compared with other transition metal surfaces in the last section.

4.4.2 Surface Ordering of C_6H_6 and Coadsorbed CO+C_6H_6 Monolayer on Rh(100) at 300-800 K

Only one LEED pattern, c(4x4), was observed for the pure benzene overlayer on Rh(100) at room temperature. This was generated by dosing with more than 5 L benzene, which corresponds to saturation coverage at 300 K. This ordered structure was stable in the temperature range of 300-450 K. Above 520 K, a c(2x2) pattern could be formed, in accordance with benzene decomposition, as will be discussed later. Further annealing to 750 K caused the disappearance of this c(2x2) structure, and only a (1x1) pattern with a diffuse background, indicative of a disordered overlayer, remained. Based on the packing model of the benzene molecule within the ordered c(4x4) unit cell, the saturation coverage of benzene is expected to be 0.125 of a monolayer. This is equivalent to a surface carbon to rhodium ratio of 0.75. A similar benzene pattern has been reported on the Ni(100)

surface with basically the same surface concentration [173]. It is interesting to note that the relative ratio of acetylene and ethylene is about 1.0-1.5, indicating a more efficient packing of surface carbons with these molecules. On Rh(111), a $(2\sqrt{3}x3)$rect structure was reported by saturating the surface with 0.17 monolayer benzene coverage [95,19].

By coadsorbing CO with benzene at 300 K, a new phase, $c(4\sqrt{2}x2\sqrt{2})R45°$, can be generated. The best way to obtain this coadsorbed overlayer is by predosing the surface with 0.5 L CO (θ_{CO}= 0.25, as calibrated by TDS), followed by saturation dosage of benzene ($\geq$ 5 L) at 300 K. The CO coverage was determined to be 0.25 ML, as calibrated by TDS and ordered CO LEED patterns described in chapter 2. Again, the surface coverage of benzene is 0.125 ML, as judged by the packing of parallel oriented benzene within the lattice. The relative ratio of CO and benzene is two to one. As the benzene coverage is the same for both c(4x4) and $c(4\sqrt{2}x2\sqrt{2})R45°$, such a phase transition upon CO coadsorption is expected in order to better spatially accommodate two CO molecules within a unit cell. We will come back to this point when we propose the structural models for both ordered overlayers.

The observation of a new structure by coadsorbing benzene with CO on the Rh(100) surface is important. This is because all previous reports of coadsorption-induced ordering were done on hexagonal close-packed surfaces. The observation of this $c(4\sqrt{2}x2\sqrt{2})R45°$-$2CO+C_6H_6$ coadsorbed, ordered structure and the c(4x2)-$2CO+CCH_3$ overlayer on Rh(100) discussed earlier extend the generality of this phenomenon to fcc(100) surfaces. We will discuss the mechanism of such interactions in chapter 6 in detail. The complete HREELS analysis of these two ordered benzene structures will be given next.

4.4.3 HREELS Studies of Benzene Adsorption on Rh(100) at 300-350 K

In order to have a better idea of the surface structure and coverage of the adsorbed benzene overlayer, only the HREEL spectra corresponding to the two ordered LEED patterns will be analyzed in this section. Representative specular scattering from a c(4x4) benzene monolayer on Rh(100) at 340 K is shown in figure 4.18A. The HREEL spectra of coadsorbed c($4\sqrt{2}$x$2\sqrt{2}$)R45°-2CO+C_6H_6 and its deuterated analogue are shown in figures 4.18B and 4.18C, respectively. Comparing figures 4.18A and 4.18C, the major differences are the observation of two extra peaks, 425 and 1800 cm^{-1}, by coadsorbing with CO. These two features, which do not shift upon deuteration, are assigned as ν(Rh-C) and ν(C-O) of coadsorbed CO vibrations. Minor CO contamination (~0.01 ML) of the c(4x4)-C_6H_6 monolayer also produced two loss peaks at 420 and 1735 cm^{-1}, as shown in figure 4.18A. Besides these vibrational modes, the remaining features of figures 4.18A and 4.18B are quite similar, indicating similar benzene bonding geometries with or without coadsorbed CO. In figures 4.18A and 4.18B, the losses at 760, 1105, and 2995 cm^{-1}, which shift to 570, 825, 2290 cm^{-1} in figure 4.18C due to isotope substitution, establish these as C-H vibrations; while the other modes at 305, 840, 1315, and 1420 cm^{-1}, correlating to modes at 305, 825, 1160, and 1355 cm^{-1} in the C_6D_6 spectrum, are attributed to Rh-C and C-C vibrations.

Representative specular and off-specular HREEL spectra for coadsorbed CO with benzene that yields the c($4\sqrt{2}$x$2\sqrt{2}$)R45° surface structure are shown in figure 4.19. The off-specular spectrum shown in figure 4.19B was taken after a 10° rotation of the Rh(100) surface normal toward the analyzer, which corresponds to 20° off-specular scattering. The major purpose is to differentiate between two

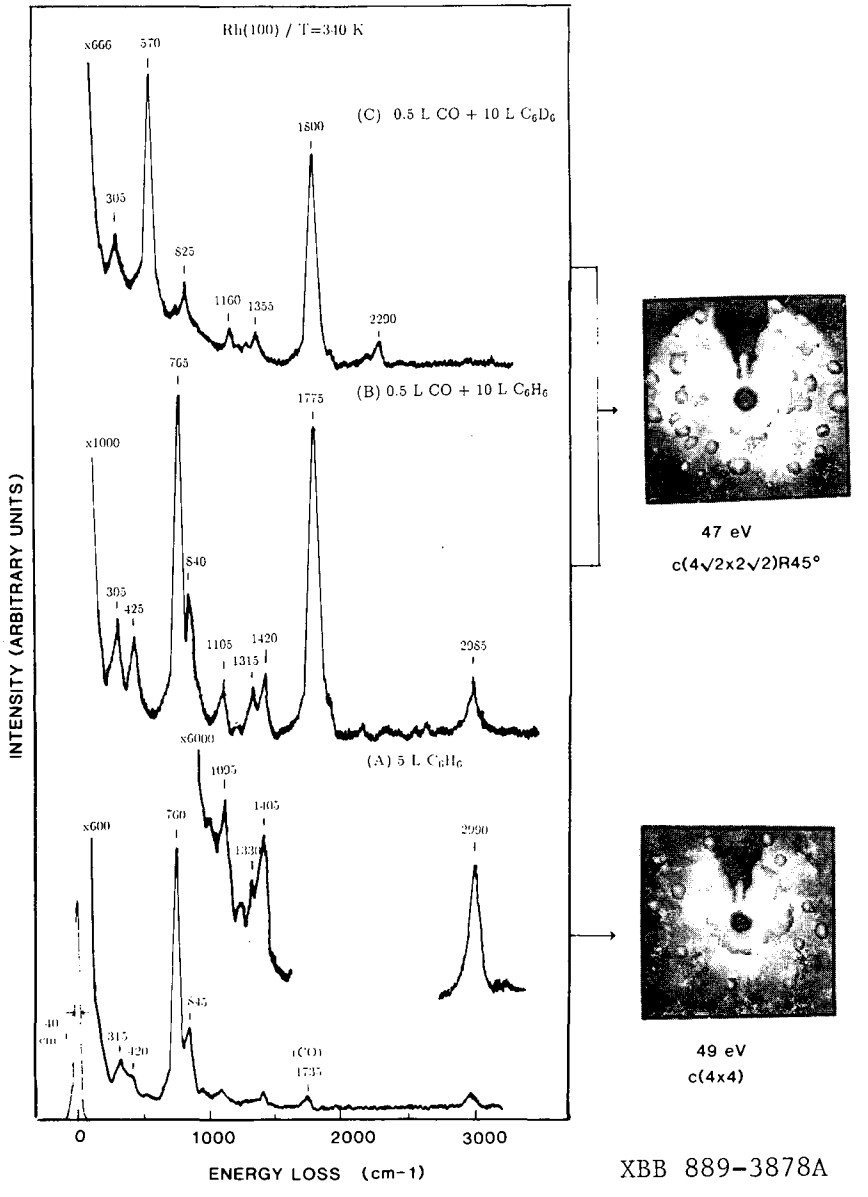

Figure 4.18: Specular HREEL spectra, recorded at 300 K of (A) 5 L C_6H_6, (B) 0.5 L CO + 10 L C_6H_6, and (C) the deuterated analogue of (B). The observed LEED pictures are shown at the right.

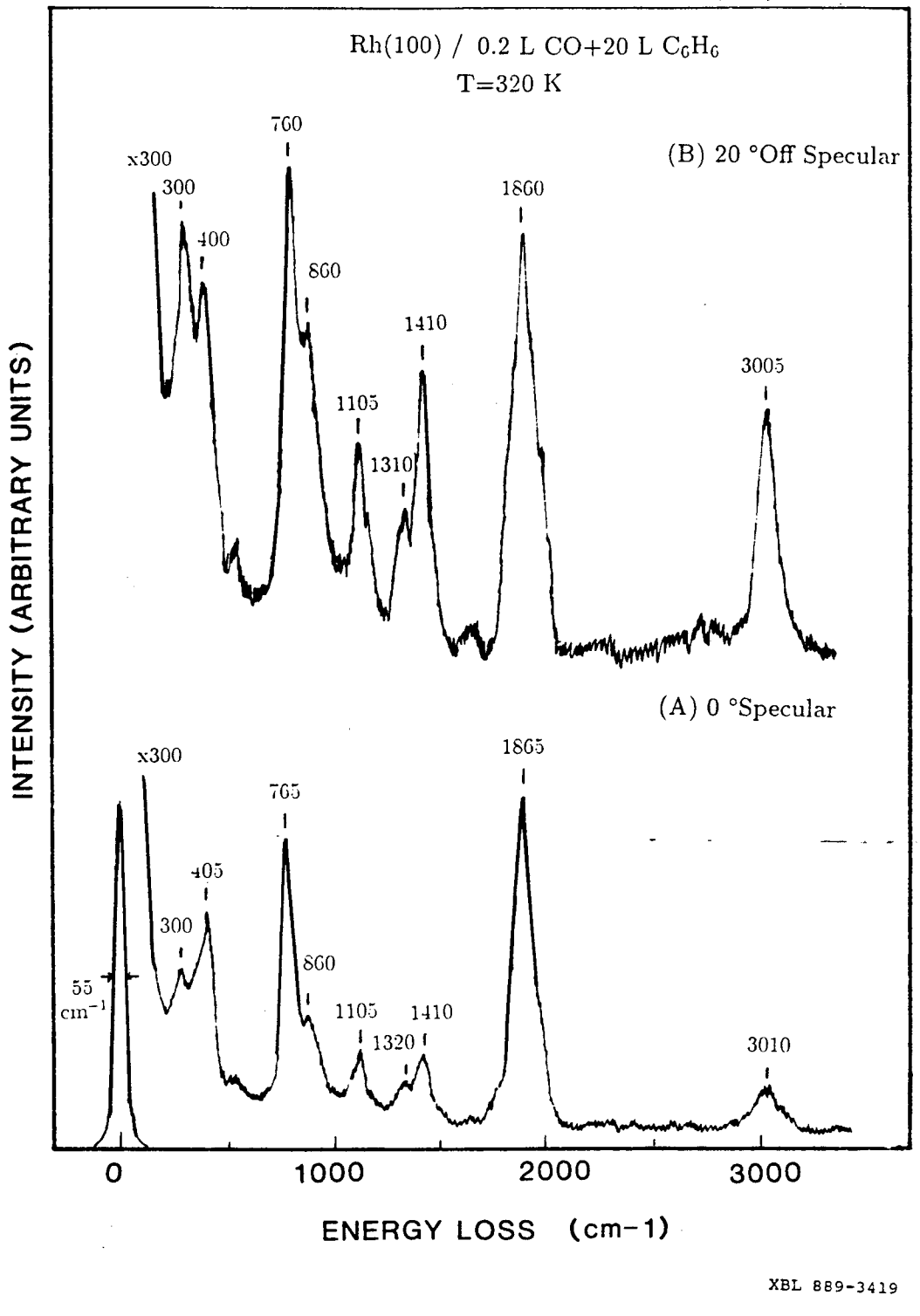

Figure 4.19: HREELS of 0.2 L CO coadsorbed with 20 L C_6H_6 on Rh(100) at 320 K at (A) specular and (B) 20° off-specular positions.

inelastic scattering mechanisms, dipole and impact scattering, of each vibrational mode. The predominate scattering process is determined from the behavior of vibrational loss intensity as a function of off-specular angle. Vibrational modes that obey a surface dipole selection rule (with dynamic dipole component perpendicular to the surface) exhibit a strong specular electron-scattering lobe of narrow angular width; while modes that exhibit a broad angular distribution are ascribed to a short-ranged impact scattering mechanism. On Rh(100), moving from specular to 20° off-specular scattering decreases the intensities of the losses at 840, 1105, 1315, 1420, and 2985 cm^{-1} by factors of ~1.2-2.0, implying predominantly impact scattering; while it decreases the intensities of the losses at 760 and 305 cm^{-1} by factors of ~4-5, indicating predominantly dipole scattering. Concurently, the elastic peak intensity decreases by a factor of 16. However, from the intensity variation of these modes with angle, it is clear that all seven losses have dipole scattering contributions. The CO related peaks at 420 and 1895 cm^{-1} reduce in intensity by factors of 7.5 and 9.5, respectively. This strong dipole activity of both ν(Rh-C) and ν(C-O) is expected for CO adsorption perpendicular to metal surface.

By correlating dipole active peaks to specific vibrational modes belonging to a symmetry group, further structural information, such as the surface symmetry of the benzene monolayer on Rh(100), can be deduced. This was done by comparing figure 4.18 with the spectra of benzene in the gas phase, as listed in table 4.4 [129]. The numbering of each vibrational mode is based on Herzberg's notation, which is more commonly used in vibrational spectroscopy than Wilson's notation. In total, 30 vibrational modes are expected for the 12-atom benzene molecule in the gas phase. These include 20 fundamental vibrational frequencies, 10 of which are doubly degenerate. Of these, however, only 4 are IR active: 3 involving dipole

moment changes parallel to the C_6 ring (ν_{12}, ν_{13}, and ν_{14} with E_{1u} symmetry), and one involving changes perpendicular to the plane (ν_4 with A_{2u} symmetry). Upon chemisorption, the fixing of the molecule gives rise to six new vibrational modes, called "frustrated translations and rotations." Among six of them, only the vibration of the benzene molecule against the surface (T_z with A_{2u} symmetry) involves dipole moment changes perpendicular to the ring plane.

In figure 4.18, the most intense feature, as already shown to be due to dipole active C-H vibration, is assigned to the out-of-plane CH bending mode (γCH). This feature, coupled with the absence of any intense E_{1u} modes and several other vibrations (such as A_{1g}, B_{1u}, and E_{2g}) expected for upright and tilted benzene, allows us to conclude that the benzene molecule is adsorbed with C_6 ring parallel to the Rh(100) surface at 300 K. The low-frequency mode at 305 cm^{-1}, which shows strong dipole activity, is assigned to ν(Rh-C) of the frustrated translational motion along the surface normal. The remaining five modes with dipolar contributions are due to the motions in the C_6 ring plane of the molecule, and therefore have relatively less intensities. Although we have separated these five modes into C-H and C-C vibrations, the detailed assignment to specified normal vibrational motions of benzene is still nontrivial. For instance, the δ(C-H) mode at 1105 cm^{-1} can be assigned to either ν_{10} or ν_{17} with very close gas-phase frequencies. A similar controversial assignment also happens for the ν(C-C) mode at 1420 cm^{-1}, which can be attributed to either ν_{13} or ν_{16}. However, by looking at the expected vibrational modes for different symmetry groups, we can propose a reasonable assignment for the observed peaks in figure 4.18.

This is done in table 4.4, which lists the dipole activity of various normal modes as a function of symmetry group. On Rh(100), the highest surface symmetry of chemisorbed benzene is presumed to be C_{2v}; therefore only C_{2v}, C_s are listed in

Table 4.4: Dipole activity (denoted as "a") of the fundamental modes of benzene as a function of symmetry group.

Mode	D_{6h}	C_{2v}	C_2	$C_s(\sigma_v)$	$C_s(\sigma_d)$
$\nu_1(\nu CH)$	A_{1g}	a	a	a	a
$\nu_2(\nu CC)$	A_{1g}	a	a	a	a
$\nu_3(\delta CH)$	A_{2g}		a		
$\nu_4(\gamma CH)$	A_{2u}	a	a	a	a
$\nu_5(\nu CH)$	B_{1u}			a	
$\nu_6(\delta CC)$	B_{1u}			a	
$\nu_7(\gamma CH)$	B_{2g}			a	
$\nu_8(\gamma CC)$	B_{2g}			a	
$\nu_9(\nu CC)$	B_{2u}				a
$\nu_{10}(\delta CH)$	B_{2u}				a
$\nu_{11}(\gamma CH)$	E_{1g}			a	a
$\nu_{12}(\nu CH)$	E_{1u}			a	a
$\nu_{13}(\nu CC)$	E_{1u}			a	a
$\nu_{14}(\delta CH)$	E_{1u}			a	a
$\nu_{15}(\nu CH)$	E_{2g}	a	a	a	a
$\nu_{16}(\nu CC)$	E_{2g}	a	a	a	a
$\nu_{17}(\delta CH)$	E_{2g}	a	a	a	a
$\nu_{18}(\delta CC)$	E_{2g}	a	a	a	a
$\nu_{19}(\gamma CH)$	E_{2u}	a	a	a	a
$\nu_{20}(\gamma CC)$	E_{2u}	a	a	a	a
$T_z(\nu MC)$	A_{2u}	a	a	a	a

this table. As can be seen from the table, even for the C_{2v} group, ten vibrational modes are expected to be dipole active, in contrast to seven observable modes shown in figure 4.18. This could be due either to limited HREELS resolution or to a weak dipole scattering cross section of some in-plane vibrational modes, as discussed earlier. Similar problems have also been found on Pd(100) [174] and Ni(100) surfaces [173]. On the other hand, the observed vibrational features do show most of the expected modes of C_{2v} symmetry. Moreover, the detection of one C-H out-of-plane bending mode (γCH) instead of two, which is expected for the C_s symmetry group as observed on Pd(111) and (100) surfaces [174], also suggests a higher surface symmetry on Rh(100). On behalf of these considerations, the most probable surface symmetry of benzene within the unit cell of the two observed LEED patterns on Rh(100) is C_{2v}.

Strict adherence to the dipole selection rule leads to the following assignments within the C_{2v} symmetry group: 840 cm^{-1}, ring stretch (νCC, ν_2); 1105 cm^{-1}, C-H bend (δCH, ν_{10}); 1315 cm^{-1}, ring stretch (νCC, ν_9); 1420 cm^{-1}, ring stretch and deformation (νCC, ν_{16} and/or ν_{13}); and 2985 cm^{-1}, C-H stretch (νCH, ν_1).

The complete assignment of C_6H_6 and C_6D_6 spectra, along with gas-phase frequencies, is listed in table 4.5. The ratio of $\nu(C_6H_6)$ to $\nu(C_6D_6)$ of nondeuterated and deuterated spectra is also listed to support our assignment. The vibrational peak at 1420 cm^{-1}, due to its proximity to a gas-phase frequency at 1486 cm^{-1}, is believed to be mainly contributed from ν_{13} mode. This is usually a preferred assignment for benzene either adsorbed on other metal surfaces or coordinated to metallic clusters. However, we cannot rule out a contribution to the 1420 cm^{-1} intensity from ν_{16}. This is because (1) the isotope shift of the 1420 cm^{-1} peak shows better agreement with the ν_{16} mode and (2) a recent normal-mode analysis for benzene on Ni(111) indicates a possible shift of ν_{16} from the gas-phase frequency

Table 4.5: Assignment of the observed vibrational frequencies (in cm^{-1}) for gas-phase benzene and benzene chemisorbed on Rh(100) using the Herzberg representation of vibrational modes.

Mode Number	Symmetry D_{6h}	Gas Phase $C_6H_6(C_6D_6,C_6H_6/C_6D_6)$	Rh(100) $C_6H_6(C_6D_6,C_6H_6/C_6D_6)$
$\nu_1(\nu CH)$	A_{1g}	3062(2293,1.34)	2985(2290,1.30)
$\nu_2(\nu CC)$	A_{1g}	992(943,1.05)	840(825,1.02)
$\nu_3(\delta CH)$	A_{2g}	1326(1037,1.28)	—
$\nu_4(\gamma CH)$	A_{2u}	673(497,1.35)	765(570,1.34)
$\nu_5(\nu CH)$	B_{1u}	3068(2292,1.34)	—
$\nu_6(\delta CC)$	B_{1u}	1010(969,1.04)	—
$\nu_7(\gamma CH)$	B_{2g}	995(827,1.20)	—
$\nu_8(\gamma CC)$	B_{2g}	703(601,1.17)	—
$\nu_9(\nu CC)$	B_{2u}	1310(1286,1.02)	1315(1160,1.13)
$\nu_{10}(\delta CH)$	B_{2u}	1150(824,1.40)	1105(825,1.34)
$\nu_{11}(\gamma CH)$	E_{1g}	849(662,1.28)	—
$\nu_{12}(\nu CH)$	E_{1u}	3063(2287,1.34)	—
$\nu_{13}(\nu CC)$	E_{1u}	1486(1335,1.11)	1420(1355,1.05)
$\nu_{14}(\delta CH)$	E_{1u}	1038(814,1.28)	—
$\nu_{15}(\nu CH)$	E_{2g}	3047(2265,1.35)	—
$\nu_{16}(\nu CC)$	E_{2g}	1596(1552,1.03)	1420(1355,1.05)
$\nu_{17}(\delta CH)$	E_{2g}	1178(867,1.36)	1105(825,1.34)
$\nu_{18}(\delta CC)$	E_{2g}	606(577,1.05)	—
$\nu_{19}(\gamma CH)$	E_{2u}	975(795,1.23)	—
$\nu_{20}(\gamma CC)$	E_{2u}	410(352,1.16)	—
$T_z(\nu MC)$	A_{2u}	—	305(305,1.00)

at 1596 cm^{-1} to 1444 cm^{-1} upon chemisorption. It is worth mentioning that the 825 cm^{-1} peak in the deuterated spectrum, too intense to be exclusively due to the δ(CD) mode (ν_{10}), is also correlated to a molecular ring stretch (νCC, $_{nu2}$) at 840 cm^{-1} in the C_6H_6 spectrum.

While the C_{2v} adsorption-site symmetry does predict most of the observable modes to be dipole active, it has the drawback of predicting several "unobserved" dipole active modes. This point deserves further elaboration. All of the predicted but unseen dipole active modes belong to the representations E_{2g} and E_{2u} of the gas-phase point group D_{6h}. Of these modes, only those belonging to the E_{2u} representation are out-of-plane vibrational modes. Thus, it is not too surprising that some of the modes belonging to the E_{2g} representation are not seen. The absence can be further attributed to (1) low dipole activity due to the planar nature of their motions, and/or (2) proximity to a stronger mode that obscured these modes. Two modes, ν_{19} and ν_{20}, belong to the E_{2u} representation. The ν_{19} mode has a gas-phase frequency of 975 cm^{-1}, and so it may be obscured by the strong loss of approximately 840 cm^{-1}. Finally, the ν_{20} mode has a gas-phase frequency of 410 cm^{-1} and could be partially responsible for the loss of ~420 cm^{-1}, which we alternatively assign to ν(Rh-C) of coadsorbed or contaminated CO in figure 4.18.

Based on these assignment of the observed HREELS shown in figure 4.18 and table 4.5, the preferred surface symmetry of benzene on Rh(100) is C_{2v} with its ring plane parallel to surface. Further comparison to other surfaces will be presented in the discussion sections.

4.4.4 Thermal Decomposition of Benzene on Rh(100) at 450-800 K

Figure 4.20 shows the TDS spectrum for hydrogen following 5.0 L C_6H_6 exposure to Rh(100) at 300 K. The first small peak at 395 K is due to a small amount of background adsorbed hydrogen, and a similar contaminant peak position has also been reported for benzene TDS on Rh(111) [96,31]. The dominant desorption peak at ~545 K corresponds to the initial dissociation of hydrogen from molecular benzene. The disordering of the LEED pattern of benzene at 450 K coincides with the onset of this major H_2 desorption state, giving the temperature when significant benzene decomposition begins. The tail of continuous hydrogen evolution following this peak is due to further dehydrogenation of the remaining carbonaceous layer. The desorption is continuous to nearly 800 K, with a small peak centered at 720 K. The carbon-to-hydrogen ratio of the surface layer also continuously increases with temperature, until 800 K, where all hydrogen has been removed, leaving only a carbon-covered surface.

The HREELS measurements have been performed as a function of surface temperature to identify stable surface fragments during benzene decomposition on Rh(100). In agreement with LEED and TPD data, no change in molecular benzene spectra was detected until 450 K. Figure 4.21 shows the hydrogenated and dehydrogenated spectra for the surface species at 510 K. The surface layer left at this temperature can be assigned to a combination of CCH+CH (CCD+CD) fragments on the Rh(100); very similar spectra have been obtained in a previous discussion of ethylene and acetylene decomposition on the same surface, as shown in figures 4.5 and 4.13. Based on the former assignment, the spectral features attributable to the CCH (CCD) fragment are a weak ν(CC) mode at 1335

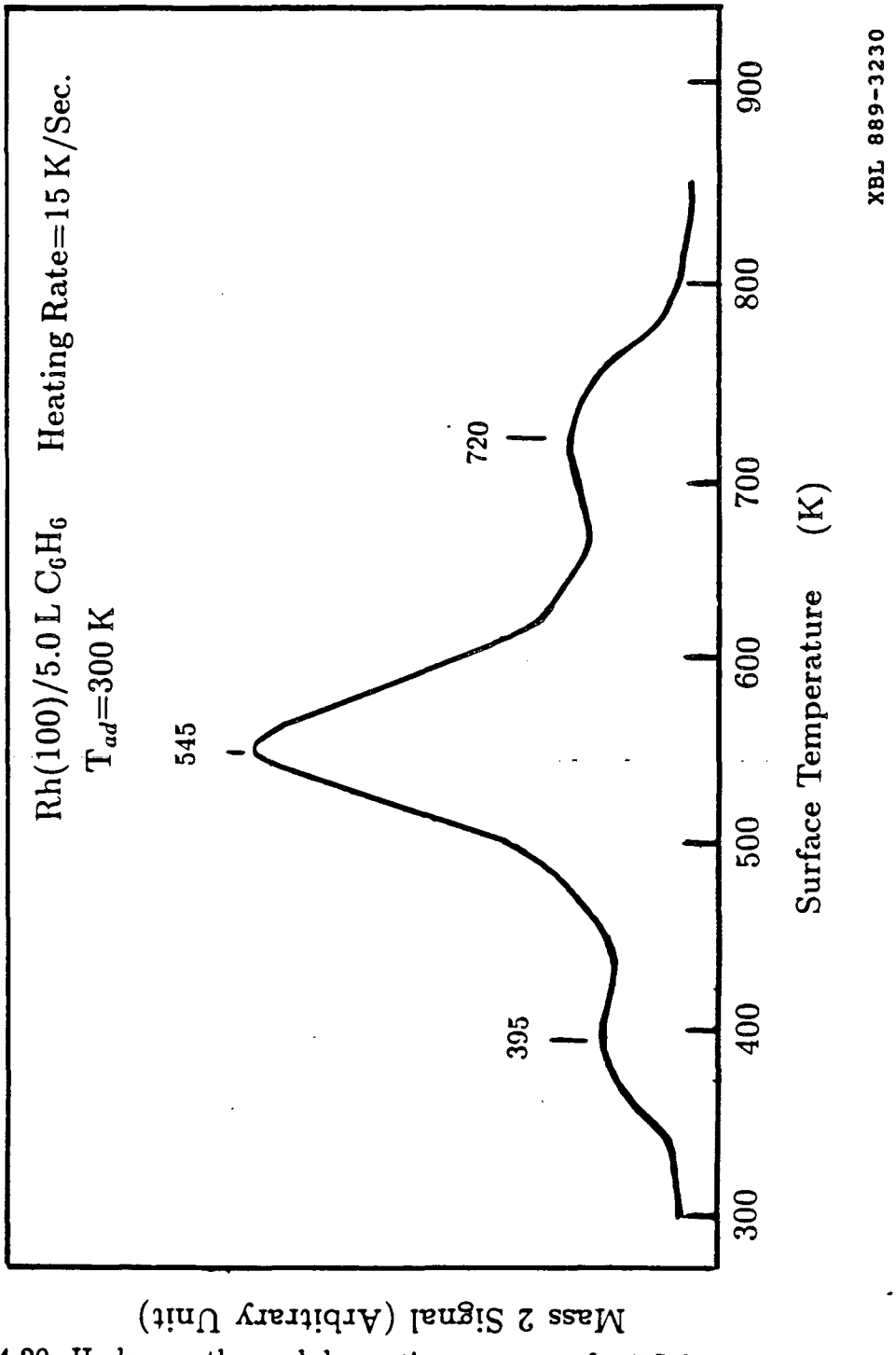

Figure 4.20: Hydrogen thermal desorption spectrum for 5 L benzene adsorbed on a Rh(100) surface at 300 K. The heating rate was 15 K/s.

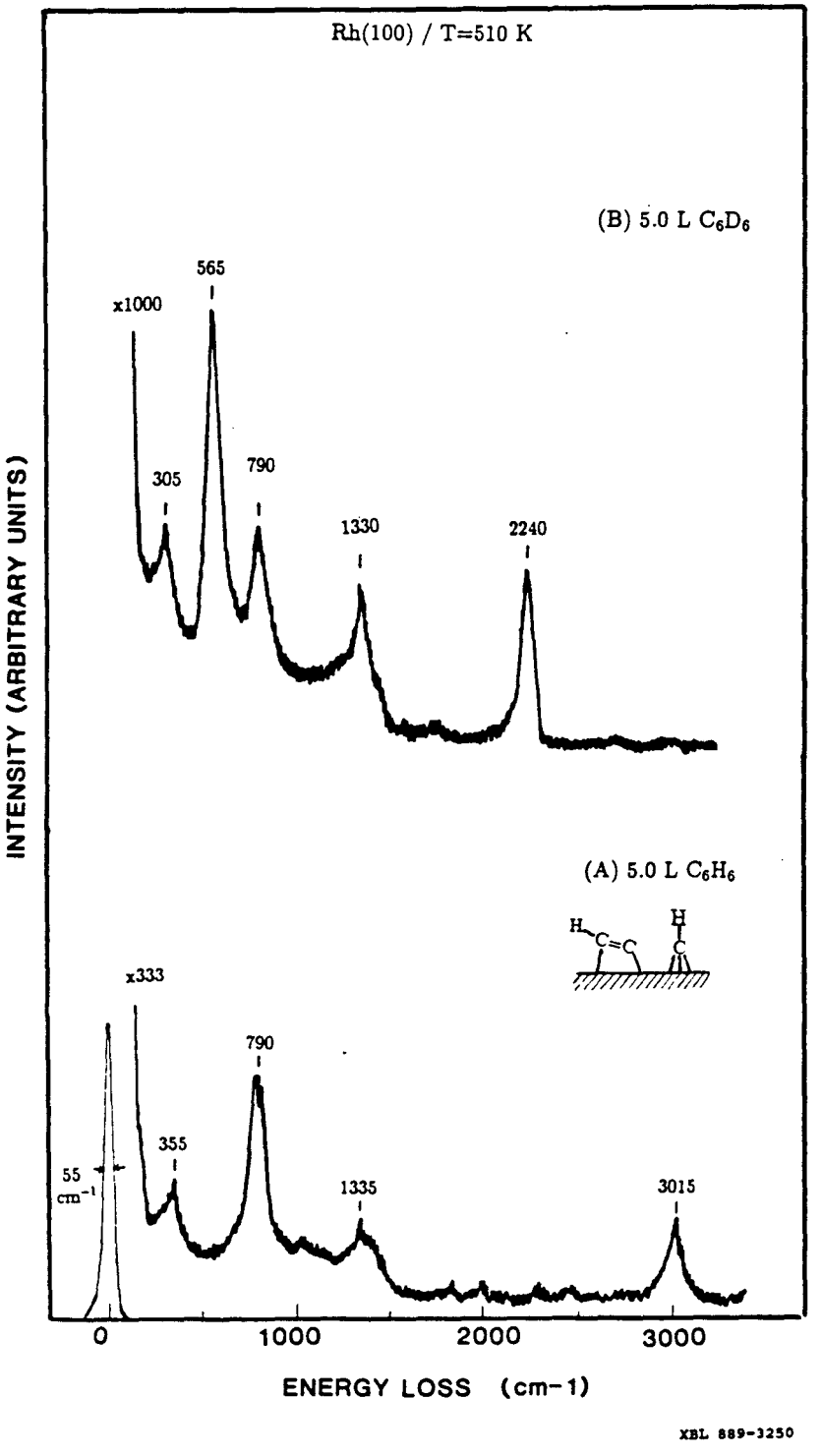

Figure 4.21: Specular HREELS of surface fragments formed from (A) 5 L C_6H_6 and (B) C_6D_6 decomposition on Rh(100) at 510 K.

(1330) cm^{-1}, a δ(C-H) bending mode at 790 (565) cm^{-1}, a ν(C-H) mode at 3015 (2240) cm^{-1}, and a ν(Rh-C) at 355 (305) cm^{-1}.

It is worth mentioning that the observation of an ordered c(2x2) LEED pattern in the temperature range of 510-700 K could be correlated with the formation of surface CCH species, as a similar pattern and fragment was observed from ethylene fragmentation at room temperature, as discussed earlier. The vibrational features observed for the CH fragment are mostly obscured by the modes from the CCH fragment. The strongest evidence for the CH fragment is a mode at 790 cm^{-1} in the deuterated spectrum, which can be assigned as ν(Rh-C) mode (the corresponding mode in the nondeuterated spectrum overlaps with the 790 cm^{-1} peak). However, we cannot rule out the possibility of some polymerized C_xH (x>2) species on the surface. In fact, the broad C-C stretching peak may indicate that some polymerization occurs during the dehydrogenation of benzene at T$\geq$450 K. Further dehydrogenation above 545 K is almost certainly accompanied by polymerization until all the hydrogen desorbs, leaving a graphitic overlayer at 800 K. These decomposition reactions are similar to those observed during benzene decomposition on Rh(111) [96], indicating structure-insensitive reaction for benzene on Rh(111) and Rh(100) surfaces.

4.4.5 The Structure of Benzene on Rh(100) and Various Transition Metal Surfaces

The adsorption of benzene on a number of low-Miller-index transition metal surfaces has been studied with surface vibrational spectroscopy by HREELS. Data are available on Ag(111) [161], Ni(111) [98,175], Ni(100) [173], Ni(110) [176], Pd(111) [174,177,178], Pd(100) [174], Pt(111) [98], Pt(110) [179], Rh(111) [19,95],

Re(001) [180], and Ru(001) [181] surfaces. These data have been reviewed in a recent publication by Sheppard [182]. One striking observation is on the similarity of the profile of the vibrational modes, which is independent of the crystallographic orientation of the various materials. The strong dipole enhancement of the out-of-plane bending mode (γCH), relative to other much weaker in-plane vibrational modes, suggests that benzene is associatively adsorbed with its ring parallel to the surface. This proposed orientation of benzene chemisorption is also supported by other spectroscopic techniques, including angle-resolved UPS (ARUPS) and dynamical LEED analysis.

On the other hand, further clues to the strength of the surface chemical bonding between benzene and various transition metals can be obtained by looking at the changes of vibrational frequencies upon chemisorption. In general, the observed C-H bending vibration of gas-phase molecules is a strong function of hybridization of the carbon atom, increasing in frequency with increasing hybridization ($sp<sp^2<sp^3$). A similar trend occurs on metal surfaces, where the γ(C-H) (ν_4) out-of-plane bending frequency increases as the metal-benzene interaction becomes stronger.

This is evident in table 4.6, where the vibrational data for benzene adsorption on various metal surfaces, along with IR spectra of gas-phase benzene and mono-, bi-, and trimetallic benzene cluster compounds, is summarized. The table illustrates that the perturbation from gas-phase benzene increases as one moves down the table, toward higher-frequency γ(C-H) vibrations. Similar trends are seen in benzene coordinated to metallic clusters, as shown at the bottom of the table. The magnitude of the frequency shifts in this mode for these complexes is similar to that observed for benzene chemisorption on transition metal surfaces. Sometimes there is another γ(C-H) mode at a higher frequency, as listed in the table,

Table 4.6: Vibrational frequencies (in cm^{-1}) for C_6H_6 vibrational modes on metal surfaces, in metallic clusters, and in gas-phase compounds.

Formula	ν(MC)	γ(CH) (ν_4)	γ(CH)	ν(CC) (ν_2)	δ(CH) (ν_{10})	ν(CC)	ν(CC)	ν(CH) (ν_1)
Gas	—	673	849	995	1150	1310	1486	3062
Surface								
Ag(111)	410	675	820	1000	1155	—	1480	3030
Ni(110)	—	700	—	845	1110	—	1420	3020
Pd(111)	265,470	720	810	—	1100	—	1410	2990
Pd(100)	280,435	720	870	900	1115	1320	1425	3010
Re(001)	—	740	845	835	—	—	—	3050
Ni(111)	300,400	745	820	875	1120	1320	1420	3020
Ni(100)	360	750	845	845	1120	1330	1430	3025
Ru(001)	290	750	860	860	1110	1260	1410	3020
Rh(100)	305	765	—	840	1105	1315	1420	2985
Rh(111)	345,550	776	819	880	1130	1320	1420	3000
Pt(110)	340,565	830	910	—	1140	—	1440	3025
Pt(111)	345,550	840	920	—	1145	—	1405	3005
Cluster								
μ_1-Cr_3	—	803	—	971	1159	1315	1445	3116
μ_2-V_2	—	739	—	—	1127	—	1462	3075
μ_3-Ru_6	—	854	—	887	1163	1320	1399	3100

which was assigned as due either to benzene adsorption at different sites [95,98] or to a new ν_{11} mode of low-symmetry molecular benzene [174]. This controversial argument again demonstrates the difficulty of HREELS assignment without ambiguity.

In addition to the out-of-plane bending mode, the M-C stretching vibrations should also increase as the interaction with the surface increases. A similar trend was also reported for benzene π-complexed to nickel, cobalt, iron, and chromium [183]. The remaining five modes, three ν(C-C), one δ(C-H) and one ν(C-H), all generally decrease from their gas-phase value. In particular, the ν_2 ring breathing mode shifts down by as much as 100-150 cm^{-1} (except Ag(111) [161]) from the gas-phase value of 995 cm^{-1}. This again implies a weakened C-C force constant and lengthened C-C bonds of benzene on surfaces. Furthermore, the CH stretch decreases by 30-60 cm^{-1} typically for adsorbed benzene from the gas-phase value (3062 cm^{-1}), indicating that benzene is rehybridized toward sp^3 upon chemisorption.

On the other hand, the relatively small shift of ν(C-H) indicates that direct hydrogen-metal interaction does not occur, since a large decrease in the CH stretching vibration is typically associated with such an interaction (for instance, the C-H-M bonding between cyclohexane and a metal surface shows a ν(C-H) softening mode at 2600-2700 cm^{-1} [6]). Such an observation also favors the model that the C-H bond of benzene probably bends outward instead of inward to the surface.

The frequency of the ν(M-C) (metal-ring) vibration is another good indicator of the strength of the metal-benzene interaction. In fact, it has been found that when benzene is π complexed to transition metal, the smaller shift upwards in the ν_4(CH) bending frequency is combined with lower frequency of ring-metal vi-

bration ν(MC). The proportionally related ν(MC) and ν_4 (out-of-plane bending) modes indeed correlate rather well with this trend. According to this rule, the strength of benzene-surface bonding follows this sequence: Ag(111) < Ni(110) < Pd(111), Pd(100) < Re(001) < Ni(111), Ni(100) < Ru(001) < Rh(100) < Rh(111) < Pt(110) < Pt(111). It can be seen that no general rule can be deduced as to the relationship of the frequency shift to either the position of the element within the periodic table or to the different crystallographic orientation of the same materials. For instance, the presumably more electropositive Ru(001) surface shows a weaker interaction with benzene than do the Rh(111) and Pt(111) surfaces, contrary to a trend expected from recent molecular orbital calculations [167]. It is also rather surprising that a weaker interaction is observed for benzene on corrugated Ni(110) [176], compared to more close-packed (111) [175] or (100) [173] surfaces. The resemblance of benzene adsorption on Ni(111) and (100) (also Pd(111) and (100) surfaces [174]) indicates that similar surface symmetry and/or adsorption sites are involved on both surfaces. This is in sharp contrast to studies of acetylene and ethylene, where a strongly structure-sensitive bonding is generally observed. One possible explanation is that the benzene surface interaction involves a more delocalized and averaged chemical bonding between the aromatic ring and the surface.

Compared with Rh(111) [95], a lower Rh-C stretch and a smaller shift of ν_4 mode on Rh(100) imply a weaker interaction between benzene on this more open surface. This is consistent with the higher decomposition temperature, 450 K on Rh(100), instead of 400 K reported on the Rh(111) surface. This conclusion contrasts with that for acetylene and ethylene, where a stronger adsorbate-surface bond is observed on the Rh(100) instead of the Rh(111) surface.

In order to determine the real space structure of benzene on metal surfaces, a

number of dynamical LEED studies for benzene adsorbed on Rh(111) [163,164], Pt(111) [165], and Pd(111) [184] with or without coadsorbed CO were carried out by our group. The presence of adsorbed CO can induce the formation of new LEED diffraction patterns.

For three Rh(111)/benzene regular arrays, as shown in figure 4.22, the site symmetry appears to be $C_{3v}(\sigma_d)$ for the two arrays coadsorbed with CO, and C_{2v} (if we ignore the second layer) for chemisorbed benzene alone. For the coadsorbed structure on Rh(111) shown at the bottom of figure 4.22, the LEED results show the presence of an alternating CC bond length of 1.46/1.58 $\AA$ and 1.33/1.81 $\AA$, respectively, around the benzene ring at the hcp hollow site. The short bonds are over Rh atoms, and the longer ones are between pairs of Rh atoms.

In the case of Pt(111), an opposing pair of bonds over bridge site Pt atoms had CC bond lengths of 1.65 $\AA$, and the other four bond lengths were 1.76 $\AA$. The mean CC bond length in these three cases is therefore 1.52, 1.57, and 1.72 $\AA$, reflecting the presence of single CC bonds. This is in agreement with the conclusions of a recent normal coordinate analysis for benzene on Ni(111), based on the assignment of the ν_2 mode at 875 cm^{-1}. In spite of the Keküle distortion observed for benzene adsorbed at bridge and hollow sites, a C_6 ring expansion from 1.41 $\AA$ on Pd(111) to 1.72 $\AA$ on Pt(111) was also detected. Furthermore, a systematic increase of M-C distance, and therefore a decrease of benzene-surface bond strength, follows the sequence Pt(111) < Rh(111) < Pd(111). This is consistent with the decrease of the ν(MC) mode and γ(CH) out-of-plane bending mode observed by HREELS.

On the other hand, several other ARUPS studies show that the energy shift of the benzene π orbital is associated with π-d chemical bonding of the adsorbed benzene with metal surfaces. The strength of adsorbate-substrate interactions decreases for the various metals studied in the order Os > Ir > Pt > Rh, based on

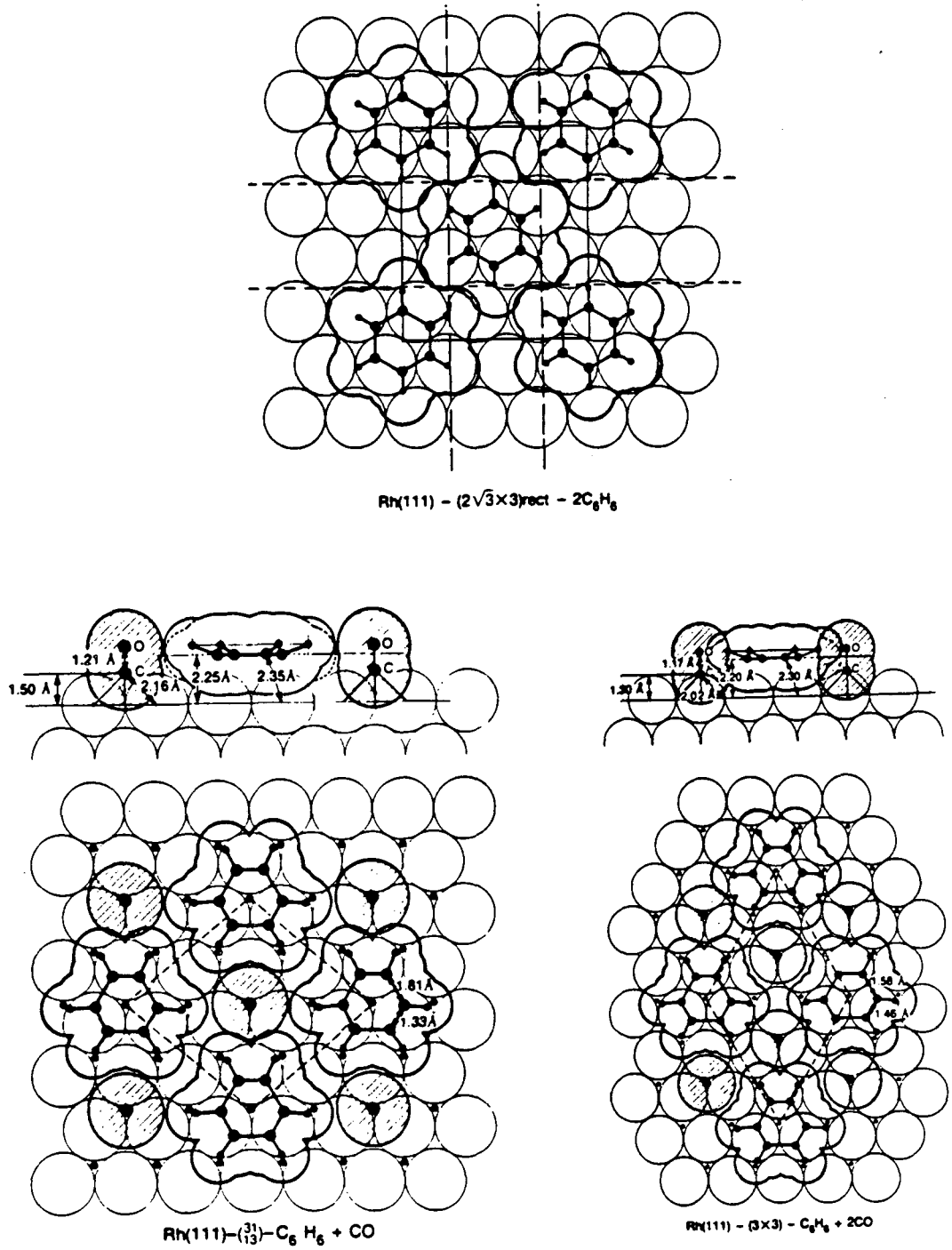

Figure 4.22: Upper: proposed arrangement of benzene in the $(2\sqrt{3}x3)$rect unit cell on Rh(111); lower: two CO+benzene structures analyzed by dynamical LEED calculations shown in side and top view. All plots include van der Waals contours of molecules.

the π shift. The surface symmetry of benzene was also deduced to be sixfold on Rh(111) [171,170] and threefold on Pt(111) [185], Ir(111) [186], and Os(001) [187] surfaces, in contrast to the LEED calculation. It may be that ARUPS is not sensitive enough to determine the distortion observed on the Rh(111) surface.

Finally, we would like to consider possible structural models for the observed LEED patterns of benzene on Rh(100). From the HREELS measurement, the surface symmetry of benzene is expected to be C_{2v} with its C_6 ring parallel to the surface. The similarity of Rh(100)/c(4x4)-C_6H_6 and c($4\sqrt{2}x2\sqrt{2}$)R45°-2CO+C_6H_6 vibrational spectra also suggests that similar adsorption sites exist for benzene within these two lattices. Possible high-symmetry adsorption sites for benzene include top, bridge, or fourfold hollows. We prefer bridge sites for the following reasons: (1) the weaker surface-benzene interaction on Rh(100), in comparison to Rh(111), indicates the most probable coordination number for benzene on Rh(100) is $\leq$3; (2) by looking at table 4.6, much similarity can be seen between benzene adsorbed on Rh(100) and within the divanadium cluster with bridge-site bonding geometry. In particular, the out-of-plane bending mode at 750 cm^{-1} on Rh(100), which determines the degree of interaction, is much closer to the value of 740 cm^{-1} of bridge-bonded benzene within the divanadium compound.

Based on these considerations, we propose in figure 4.23 a bridge-bonded benzene within the unit cell of c(4x4)-C_6H_6 on the Rh(100) surface at 0.125-ML coverage. The van der Waals radii of the benzene molecule are also demonstrated to show the proximity of nearest neighbors at saturation coverage.

The model of another CO coadsorbed structure, c($4\sqrt{2}$x$2\sqrt{2}$)R45°-2CO +C_6H_6, is shown in figure 4.24. This is based on the fact that CO prefers bridge sites, as indicated by the ν(CO) frequency at 1800 cm^{-1}, and the maintenance of bridge site benzene. The ratio of surface CO concentration to benzene is 2:1, as calibrated

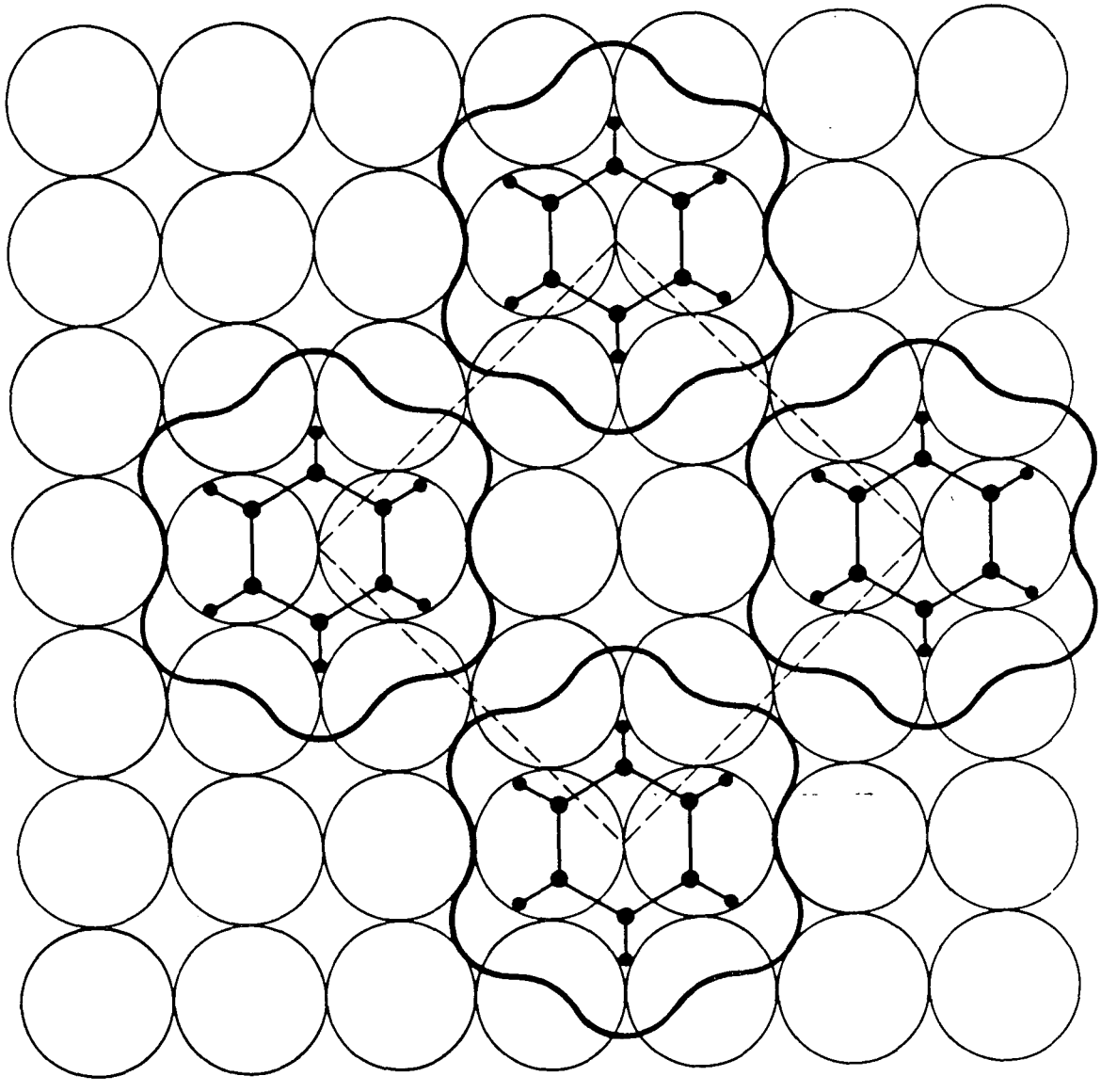

Figure 4.23: Proposed real-space structure based on HREELS measurements of benzene adsorbed on Rh(100) within a c(4x4) unit cell (indicated by dashed line). The top view of benzene molecules centered over the bridge site, and the van der Waals radii of 1.67 and 1.2 Å for C and H, respectively, are included to demonstrate the packing density.

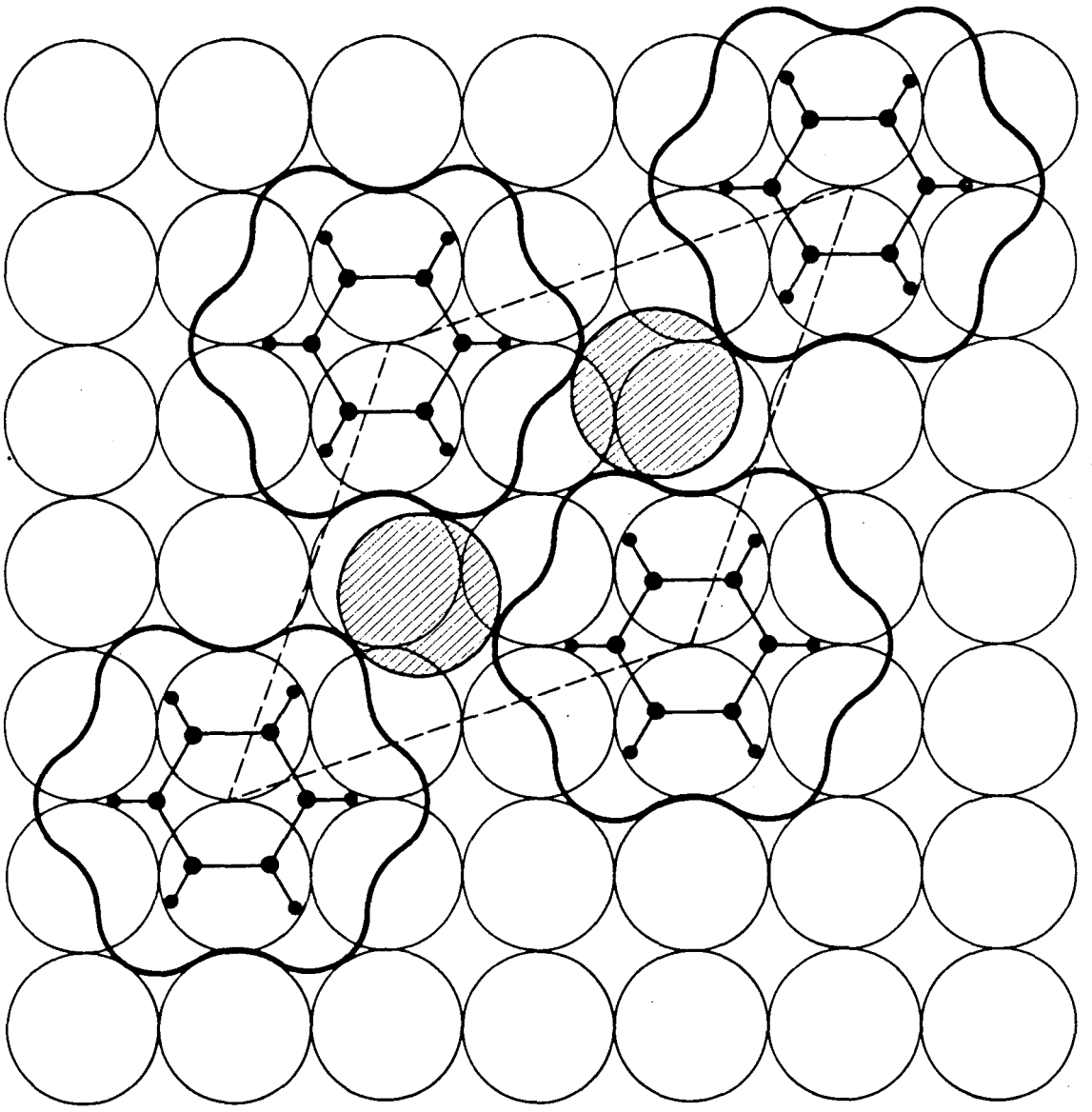

$$Rh(100)/c(4\sqrt{2} \times 2\sqrt{2})\ R45° - 2CO + C_6H_6$$

XBL 888-8959 A

Figure 4.24: Top view of proposed coadsorbed structure of benzene and CO on Rh(100), based on HREELS observations. The van der Waals radii for each atom are O = 1.50 Å, C = 1.67 Å, H = 1.2 Å.

by CO TDS discussed earlier. Comparing to c(4x4), the c($4\sqrt{2}$ x 2 $\sqrt{2}$)R45°-2CO+C_6H_6 unit cell does have more room to accommodate two CO molecules within the unit cell. However, there also seems to be enough room to occupy one extra CO per c(4x4) unit cell, although the experimental evidence shows no evidence of CO coadsorption. Further LEED structural analyses are necessary to substantiate these proposed structural models.

4.4.6 Summary of Benzene Chemisorption on Rh(100)

In order to understand the bonding and reactivity of molecular benzene on Rh(100) surface, a series of HREELS, LEED, and TDS studies has been performed in the temperature range of 300-800 K. The important features of these observations can be summarized as follows:

- Two ordered overlayers, c($4\sqrt{2} \times 2\sqrt{2}$)R45°-2CO+$C_6H_6$ and c(4x4)-C_6H_6, can be formed by adsorbing benzene with or without coadsorbed CO at 300 K. Both correspond to benzene adsorbed with its ring parallel to the (100) surface, as indicated by a strong out-of-plane bending mode at 750 cm^{-1}. The models of both proposed structures are shown in figures 4.23 and 4.24, based on HREELS analyses.

- The strength of the benzene-surface bond is weaker on Rh(100) than Rh(111), as determined by a smaller γ(CH) frequency shift relative to the gas phase.

- The weaker interaction of benzene on Rh(100) also accounts for a higher decomposition temperature, 450 K, instead of 400 K on Rh(111); however, similar surface fragments (CCH and CH) are detected on both surfaces, implying a structure-insensitive reaction for benzene on Rh surfaces. This is

in sharp contrast to the structure-sensitive thermal chemistry observed for both acetylene and ethylene on the same metal surfaces.

Chapter 5

The Surface Structure and Chemistry of NO and Coadsorbed CCH_3+NO on Rh(111) by HREELS and Dynamical LEED Analysis

5.1 Bonding and Reactivity of NO on the Rh(111) Surface

The bonding and reactivity of nitric oxide on group VIII transition metal surfaces have been studied extensively in the past few years. In practice, group VIII metals such as rhodium, platinum, and palladium are active catalysts for the reduction of NO to N_2, which is an important process in automobile exhaust control [188]. Several recent works focus on the kinetic studies of the NO reduction reaction on platinum or rhodium foils and single crystals [189,190]. Although there are several different suggested mechanisms for the NO reduction reaction on these surfaces, the dissociation of NO to form atomic oxygen and nitrogen is thought to be an important step of such reactions [191]. The fundamental chemisorption

studies of nitric oxide on various single-crystal surfaces can give us insight into such a process.

Nitric oxide has a half-filled $2\pi^*$ antibonding orbital, which can either accept or donate electrons when it interacts with a metal surface [192,193]. This is in contrast to CO chemisorption, where the empty $2\pi^*$ orbital is a pure electron-accepting orbital. In metal-nitrosyl compounds, due to the presence of the extra anti-bonding electron, a new group having a bent NO bonding geometry with no CO analogues was found [192,194,195]. This makes the chemisorption bond of NO become more complex and not as well understood as in the case of CO. Also, as the bond dissociation energy of NO is 151 kcal/mole, in comparison with 257 kcal/mole for CO, the N-O bond is easier to dissociate than the C-O bond [196]. The dissociation process of NO to atomic oxygen and atomic nitrogen was observed to be very sensitive to surface-defect concentration [197], coordination number [198], and surface coverage of NO [199].

Most of the surface structural information for NO chemisorption is from high-resolution electron energy loss spectroscopy (HREELS) studies. A correlation between the observed N-O stretching frequencies and the possible bonding geometries has recently been summarized [6,200]. Such a relationship is based on the comparison with the observed infrared (IR) frequencies in metal-nitrosyl compounds, which have analogous local bonding geometries. A direct comparison of the NO surface structural determination with the bulk crystal structure of the metal-nitrosyl compound is necessary to justify such a surface-cluster bonding analogy.

The chemisorption of NO on Rh(111) has been studied by several research groups by LEED [201], TDS [201,202], XPS [197], and HREELS [203]. The general observation is dissociative adsorption at low coverage and predominantly molecu-

lar adsorption at saturation dosage. At least two molecular states, β_1 and β_2, were observed for room-temperature adsorption by XPS. These two states were correlated to linear and bent nitric oxide, with a formal charge for nitrogen of +1 and -1, respectively [197]. Two ordered LEED patterns, c(4x2) and (2x2), were observed by Castner and Somorjai [201]. They suggested a structural model involving two different NO adsorption sites in a single (2x2) unit cell at 0.75-monolayer coverage.

On the other hand, in the HREELS studies by Root et al. at 95-1500 K, only bridge-site NO was observed throughout the whole coverage and temperature range [203]. They also believed that the (2x2) LEED pattern observed by Castner et al. is actually due to three domains of (2x1)-O from NO dissociation.

In order to resolve the disagreement between the studies at both 95 and 300 K, we have performed our HREELS measurements at surface temperatures in the range of 120-480 K. At 120 K, a c(4x2) LEED pattern is observed around 0.8 L NO dosage, which corresponds to a bridge-site NO at half-monolayer coverage. We also found that the (2x2) pattern can be observed at saturation dosage above 5.0 L with ambient NO pressure of $1x10^{-7}$ torr at 250 K. The HREELS results indicate two new N-O stretch frequencies at 1515 and 1830 cm^{-1} for the (2x2) LEED pattern. This is in agreement with the LEED structural analysis for this (2x2)-3NO overlayer. In the first part of this chapter, we will discuss our HREELS data first, and then the LEED analysis work. The structure of (2x2)-3CO on the same metal surface and the vibrational spectra of NO on other transition metal surfaces will also be compared.

The coadsorption of NO with ethylidyne on Rh(111) surface, where a perturbation of surface structure could be induced by the presence of coadsorbates, will be presented in the second part of this chapter. A similar structure was also observed for CO coadsorbed with ethylidyne; however, both CO and NO select different

threefold hollow sites upon coadsorption. It is hoped that these systems could lead to a possible way to study site-selective structure and chemistry.

5.2 Results and Interpretation

In this section we will first present surface ordering of NO adsorption on Rh(111) at 120-350 K. The HREELS data for molecular NO adsorption on Rh(111) at 120-350 K will be analyzed in the second part; this will be followed by thermal desorption and dissociation of the overlayer in the temperature range of 360-480 K. The LEED structural analysis of (2x2)-3NO on Rh(111) will be presented in the last part.

5.2.1 Surface Ordering of NO in the Temperature Range of 120-350 K

Two ordered LEED patterns, c(4x2) and (2x2) at 0.5 and 0.75 monolayer coverages, respectively, have been observed in the temperature range of 120-350 K. The c(4x2) pattern was observed by dosing 0.5-1.0 L NO at a surface temperature of 120 K. Subsequent annealing to temperatures above 320 K caused a disordering of the LEED pattern. We also found that this c(4x2) overlayer is extremely electron beam sensitive. An exposure of 5 μA current for 20 seconds causes the complete disappearance of such a pattern.

The best way to generate the (2x2) saturation NO overlayer is by dosing $\geq$ 5.0 L NO at a surface temperature of 250-320 K. The (2x2) pattern disorders above 350 K regardless of exposure to more NO. In comparison to a similar structure of (2x2)-3CO on the same metal surface [18,204], less NO ambient pressure ($1x10^{-7}$

torr) is needed to form the (2x2)-3NO overlayer at 0.75-monolayer coverage; while for the case of the CO structure, an ambient pressure of $1x10^{-6}$ to $1x10^{-5}$ torr of CO is necessary to produce a (2x2) pattern near room temperature at saturation dosage.

In the next section, the HREEL spectra of the observed NO LEED patterns will be presented to provide an initial surface structural model.

5.2.2 HREELS Studies of Molecular NO Chemisorption at 120-350 K

The HREEL spectra corresponding to both the c(4x2) and (2x2) LEED patterns are shown in figures 5.1A and C, respectively. In figure 5.1A, 0.8 L of NO was adsorbed at 120 K with the formation of a c(4x2) LEED pattern. Only two distinct modes, at 435 and 1590 cm^{-1}, were observed. Upon increasing the dosage to 10.0 L at 120 K , the 1590 cm^{-1} mode shifts up to 1635 cm^{-1}, as shown in figure 5.1B. The low-frequency mode at around 435 cm^{-1} also shows a slight red shift to 405 cm^{-1}.

The possibility of other surface species, such as $(NO)_2$ dimer [205], NO_2 [206], or N_2O [207], can be ruled out due to the simplicity and position of the observable modes. The presence of multilayer NO is unlikely at this temperature. This is due to the following facts: (1) The desorption temperature of multilayer NO adsorbed on metal surfaces is around 100 K [208]. (2) We do not see any vibrational mode around 1876 cm^{-1}, which is the characteristic N-O stretch mode of physisorbed nitric oxide from infrared spectroscopy [209]. We therefore assign the peaks at 435 and 1590 cm^{-1} in figure 5.1A as Rh-NO and N-O stretching frequencies, respectively. A slight change in the positions of these two modes to 405 and

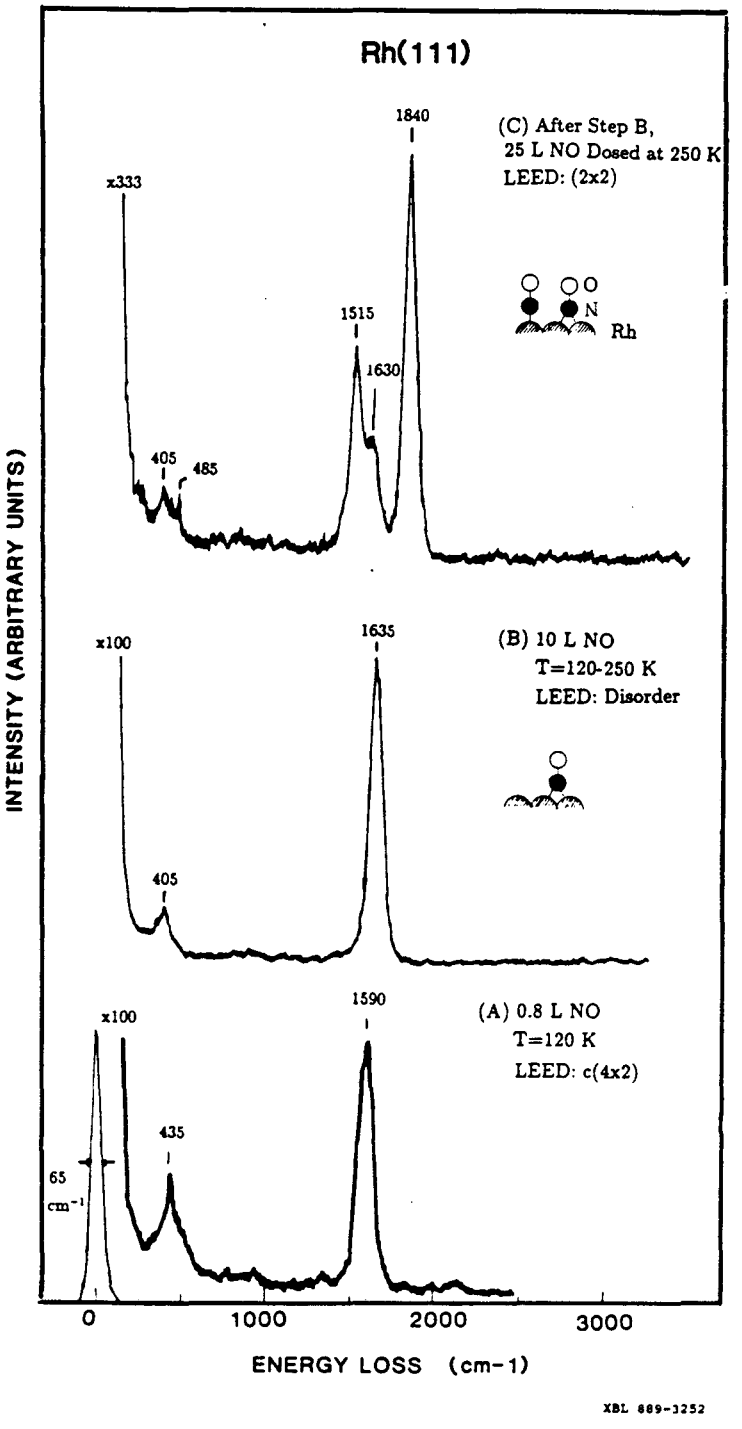

Figure 5.1: Specular HREEL spectra shown as a function of adsorption temperature and dosage. (A) 0.8 L NO dosed at 120 K. LEED showed c(4x2) pattern. (B) 10 L NO dosed at 120 K. LEED showed disordered pattern. (C) 25 L NO dosed after step (B) at 250 K; a new (2x2) sharp LEED pattern was observed. All spectra recorded at 95 K.

1635 cm^{-1} due to the increase of surface coverage can be seen in figure 5.1B. The observed red shifts of N-O stretching modes in both figures 5.1A and 5.1B, relative to gas-phase NO, are in the range of 240-280 cm^{-1}. This is indicative of new chemisorbed molecular NO states on Rh(111) at 120 K.

The number of dipole active modes in HREEL spectra at the specular position is determined by the symmetry of various NO bonding geometries. On a fcc(111) surface there are four most probable bonding geometries. For NO adsorption at top, bridge, or hollow sites with the N-O axis perpendicular to the surface plane, the dipole active modes are both M-NO and N-O stretching frequencies [6]. For the bent bonding geometry with the M-N-O bond angle in the range of 120-140° [6,200], the surface symmetry is C_s, and the expected dipole active vibrational modes are ν(N-O), ν(M-NO), and two δ(M-NO) bending modes. Although one of the δ(M-NO) modes, a frustrated translational mode, is usually below the scanning range of the HREEL spectrum ($\leq$200 cm^{-1}) [6,200], we still expect at least three dipole active modes for such a NO bonding geometry. There are only two features for NO in figures 5.1A and 5.1B; therefore, we believe the surface symmetry of NO is higher than C_s. The most likely structure for NO on Rh(111) will have the N-O axis normal to the surface.

We now compare the observed N-O stretching mode on a Rh(111) surface to that of an analogous metal-nitrosyl compound. Based on the infrared and x-ray crystallographic work of metal-nitrosyl complexes, it is usually suggested that N-O vibrational frequencies in the range of 1650-2000, 1480-1550, and 1320-1410 cm^{-1} correspond, respectively, to top [192], bridge [210], and threefold hollow [211,212] adsorption sites with the NO axis perpendicular to the surface. The bent NO configuration would have two modes, one ν(N-O) in the range of 1530-1700 cm^{-1} and the other N-O bending mode around 700 cm^{-1} [194,195,200]. Although the

observed N-O stretch, 1590-1635 cm^{-1}, is within the range of terminal bent metal-nitrosyl compounds, the number of observable modes at the specular position is more consistent with a high symmetric bonding site. This implies either the top or the bridge site will be a more probable adsorption site for NO on Rh(111).

Root et al. previously studied NO adsorption at 95 K on Rh(111) by HREELS [203]. A gradual shift in N-O stretch from 1480 to 1630 cm^{-1} from 0.025- to 0.68-monolayer coverage was reported in their work. They attribute the blue shift of the N-O stretching mode to a coverage-dependent dipole-dipole interaction of bridge-site NO. Considering the range of N-O stretching frequencies and the number of observable modes, our data at 120 K are within the range of the medium (0.5) to high coverage (0.68) NO data of their results. We tentatively assigned the modes in figure 5.1A and 5.1B to bridge-site NO adsorption. The N-O stretch frequency of the c(4x2)-NO structure shown in figure 5.1A is 1590 cm^{-1}, in accordance with previous results at 0.50-monolayer coverage. The N-O stretch for the 10 L NO dosage at 1635 cm^{-1} is close to the 0.68 monolayer of NO reported at 95 K. The ν(Rh-NO) modes at 405 and 435 cm^{-1} in figure 5.1A and 5.1B are better resolved in this work, while a broad loss peak at around 360 cm^{-1} with high background intensity was observed previously [203].

Figure 5.1A and 5.1B represents a single bridge-site NO to be favored at an adsorption temperature of 120 K. By changing the adsorption temperature from 120 K to above 250 K, a new (2x2) LEED pattern is observed at near 0.75 monolayer coverage, and its HREELS spectrum is shown in figure 5.1C. In this case we dose an additional 25 L of NO at a surface temperature of 250 K after the 10 L dosage at 120 K. Immediately after the adsorption, a (2x2) LEED pattern is observed, and three new vibrational peaks, at 485, 1515, and 1830 cm^{-1}, were observed in the HREEL spectrum of figure 5.1C. This spectrum is quite repro-

ducible by direct saturation dosage of NO at surface temperatures in the range of 250-320 K. The only difference is that the 1630 cm^{-1} mode intensity decreases as NO adsorbs at higher temperatures; i.e., if we adsorb NO at a surface temperature of 300 K or above, this peak almost disappears or remains only as a small shoulder of the 1515 cm^{-1} mode. We also notice the disappearance of the (2x2) LEED pattern at 350 K in conjunction with the disappearance of these two vibrational modes.

Based on the data mentioned above, we believe there are two major NO species coexisting in the (2x2) ordered overlayer. This indicates that the local surface coverage of NO is 0.75. Both the 1830 cm^{-1} and 1515 cm^{-1} peaks are in the range of N-O stretching frequencies for terminal and bridge-bonded metal-nitrosyl compounds. We attribute these to be due to top and twofold bridge-site adsorbed NO, respectively. The two peaks at 400 and 485 cm^{-1} can be attributed to Rh-NO stretching frequencies for these two species. In the following section, the LEED structural analysis will be applied to substantiate the HREELS assignment in figure 5.1C.

It is worth mentioning that by looking at the profile of the (2x2)-3NO HREEL spectrum shown in figure 5.1C, the relative intensity ratio of N-O stretching frequencies for top (1840 cm^{-1}) and bridge-site (1515 cm^{-1}) NO is about 2:1. This is very similar to the HREEL spectrum of the (2x2)-3CO structure, where two top sites and one bridge site were found to occupy a single unit cell [18,204]. Indeed, this type of structural model is exactly what we found by LEED structural analysis of (2x2)-3NO, which will be discussed in section 5.2.5.

5.2.3 HREEL Spectra in the Temperature Range of 350-480 K

Figure 5.2 shows the specular HREEL spectra of (2x2)-3NO as a function of surface annealing temperature. As we mentioned in the previous section, the saturation dosage of NO at 250 K can generate a (2x2) overlayer. Figure 5.2A shows one of the (2x2) pattern HREEL spectra at 25.0 L NO dosage and 250 K. The spectrum is similar to that shown in figure 5.1C, and the predominant surface species are top and bridge-site NO.

By slowly increasing the surface temperature, the (2x2) LEED pattern disappears at 350 K. The HREEL spectrum shows a significant change at 360 K in figure 5.2B. The top-site NO with characteristic ν(N-O) and ν(Rh-NO) vibrational modes at 1830 and 480 cm^{-1} disappears at 360 K, which is the starting temperature of NO desorption from TDS studies [201,202]. The features in figure 5.2 are similar to those in figure 5.1B, and only bridge-bonded molecular NO species exist on the surface. The frequencies at 1630 and 405 cm^{-1} are due to ν(N-O) and ν(M-NO), respectively. No mode at 520-580 cm^{-1}, which could be due to the Rh-O stretch of atomic oxygen from NO dissociation, is observed. This implies that the predominant surface species at this temperature is still molecular NO adsorbed at the bridge site.

At surface temperatures above 360 K, the 1630 and 405 cm^{-1} modes gradually disappear. Until 480 K is reached, the complete disappearance of these two molecular NO modes is in accordance with the appearance of a new vibrational peak at 530 cm^{-1}, as shown in figure 5.2C.

From previous TDS studies by several groups [201,202], the desorption of NO at 350-450 K is accompanied by dissociation to atomic nitrogen and oxygen. The

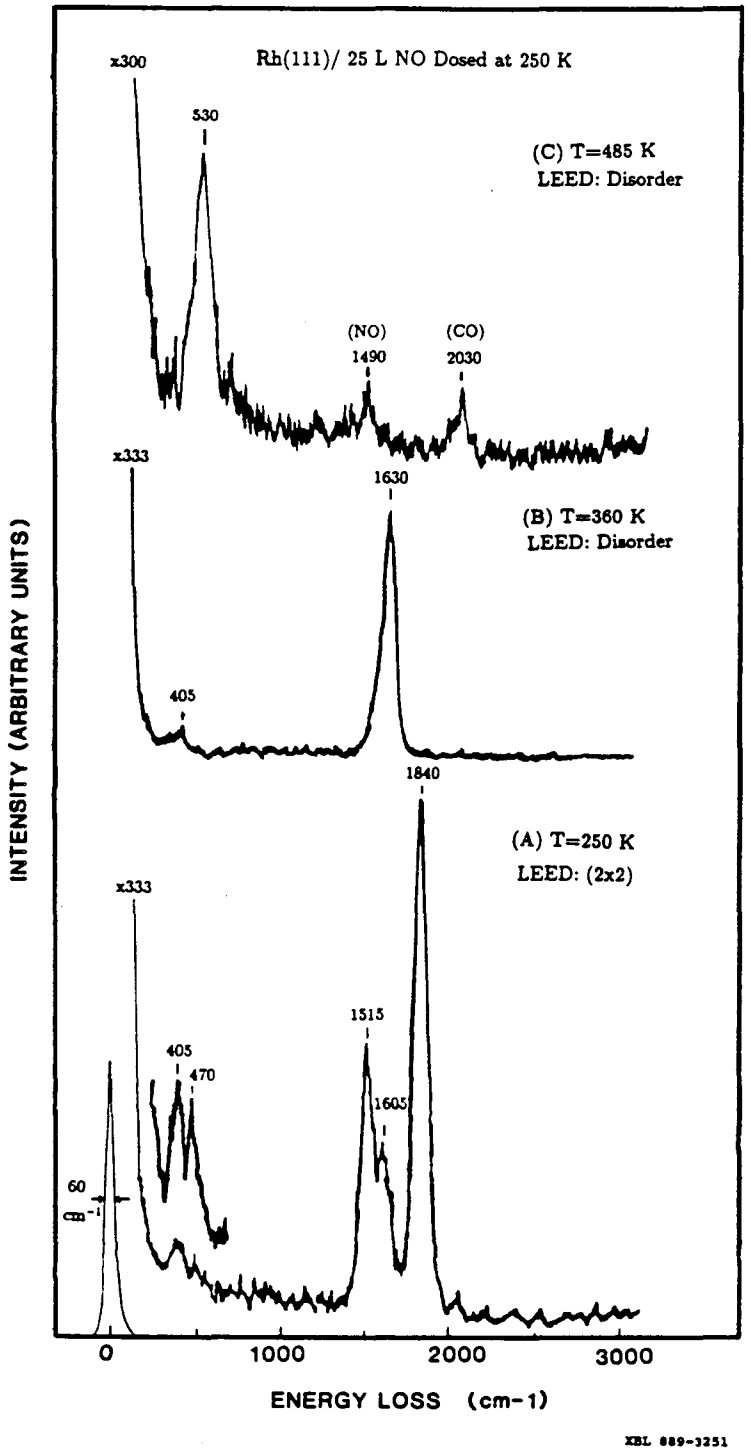

Figure 5.2: (A) 25 L NO dosed at T = 250 K; this spectrum is similar to that in figure 5.1C. Subsequent annealing to (B) T = 360 K, LEED showed a disordered pattern; (C) T = 480 K, where complete dissociation of NO was observed. LEED showed disordered pattern. All three specular spectra were taken at 95 K.

residual nitrogen desorbs in the temperature range of 400-700 K, followed by oxygen desorption at 1000-1400 K. At 480 K all molecular NO species are either dissociated or desorbed, and most of the atomic nitrogen is expected to recombine to desorb as molecular nitrogen already. The major surface species left will be atomic oxygen. We therefore assign the 530 cm^{-1} peak to the Rh-O stretching frequency of atomic oxygen from NO dissociation. Two other small peaks, at 1490 and 2030 cm^{-1}, are due to ν(N-O) and ν(C-O) from background adsorption during our data collection.

5.2.4 Theory of LEED Calculation

We have applied LEED calculational methods that are very similar to those used in the structural analysis of Rh(111)-(2x2)-3CO [18,204]. Those methods explored the validity of a number of approximations so that we can apply them now with confidence. For the NO adsorption structure, we have chosen to ignore the multiple scattering occurring directly between molecules. This leads to what we now call "kinematic sublayer addition" (KSLA) within the "beam set neglect" (BSN) method [164,213]. All multiple scattering is allowed within individual molecules, by means of "matrix inversion" in the spherical-wave representation [16,214]. With this approximation and for the relatively close-packed molecular layers in question, the structural uncertainties are maintained within 0.1 $\AA$ [18,204]. Between the substrate layers and between the overlayer and the substrate, we use renormalized forward scattering in the plane-wave representation.

The physical parameters used in the calculations are the same as those in the earlier CO adsorption calculations [18,204]. The only exceptions are different phase

shifts for NO, obtained from a cluster calculation of NO on 8 Rh atoms. Theory and experiment were, as usual in our molecular overlayer studies, compared with a set of five R-factors and their weighted average value [18,204]. These include both the Zanazzi-Jona and Pendry R-factors.

5.2.5 Dynamical LEED Analysis of Rh(111)/(2x2)-3NO

Based on our earlier analysis of the analogous (2x2)-3CO overlayer [18,204] and based on the evidence from HREELS, we have made the following structural assumptions for Rh(111)-(2x2)-3NO. The substrate is taken to be bulk-like. The NO molecules are taken to be intact and perpendicular to the surface, no matter how low the symmetry of their bonding site. Three NO molecules fit in each (2x2) unit cell (but we have also investigated one molecule per cell). The molecules tend toward high-symmetry sites like top, bridge, and hollow sites, to the extent compatible with close packing. In each structure tested the N-O bond length was kept the same for all molecules, but that common length was allowed to vary.

Figure 5.3 shows a model satisfying these criteria. It is also our best-fit model. In this model, one of the three NO molecules in the unit cell occupies a bridge site, while the two other NO molecules occupy equivalent "near-top" sites: we label this model "1-bridge/2-top." Here the symmetrical bridge site anchors the structure, while the near-top sites adjust themselves accordingly.

We also tried a "1-top/2-bridge" model, in which the role of the bridge and top sites is reversed. It is obtained from the "1-bridge/2-top" model of figure 5.3 by a shift of the overlayer such that the bridge-site NO molecules end up exactly and symmetrically at the top sites. The two other NO molecules then adjust themselves at near-bridge sites. This model reverses the relative occupation of

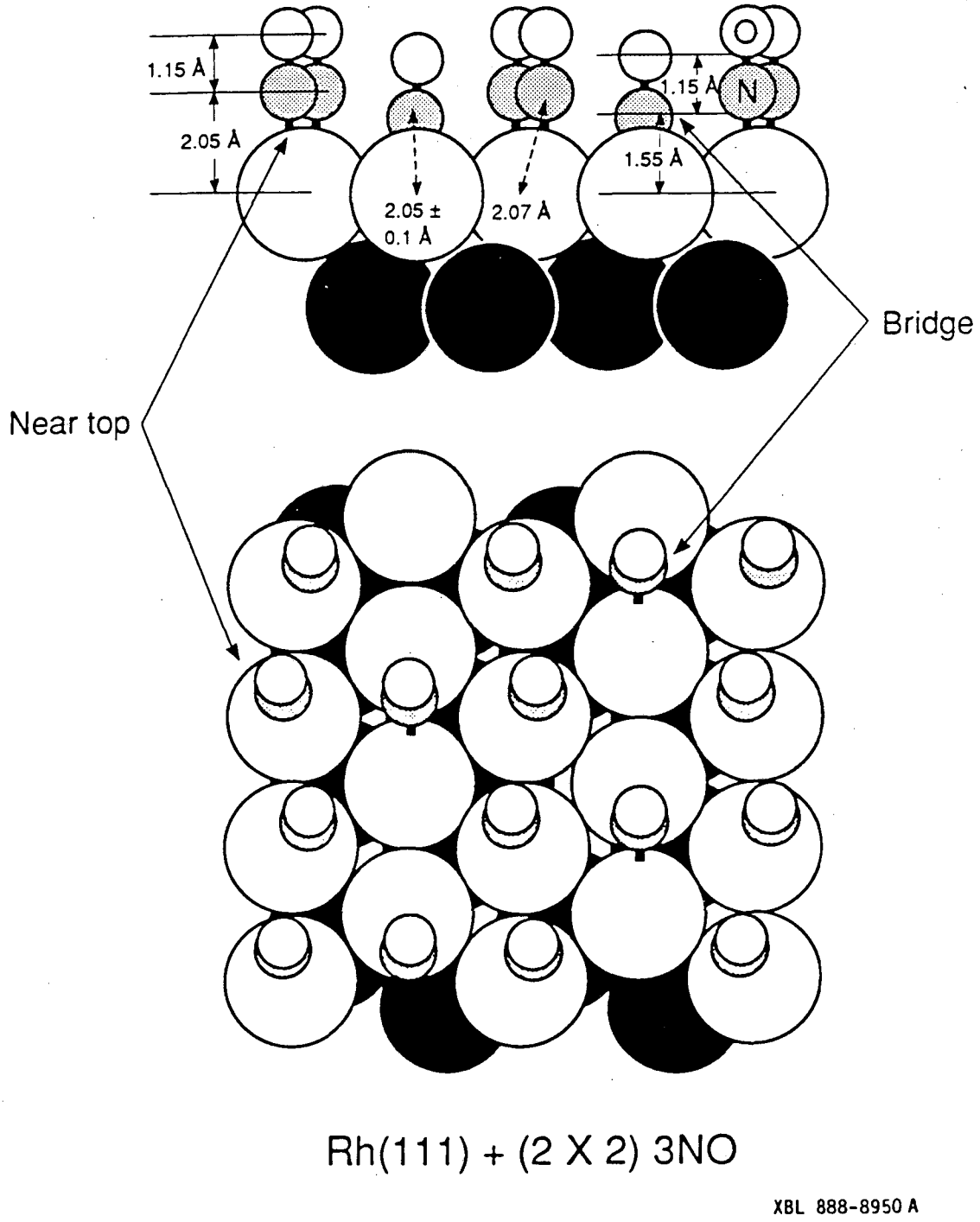

Figure 5.3: Side and top view of a best-fit model of the (2x2)-3NO structure, shown at the upper and lower part of the figure. Covalent radii of nitrogen (small closed circle, 0.75 Å) , oxygen (small open circle, 0.73 Å), and rhodium (large circle, 1.35 Å) are used [215].

Table 5.1: Summary of structural parameters (in $\AA$) that have been used in different models of Rh(111)/(2x2)-3NO by dynamical LEED analysis.

Model	$d_\perp$(Rh-NO)	$d_\perp$(N-N)	$d_\parallel$(N-N)	$d_\perp$(N-O)
1-bridge/2-top	1.25(0.1)1.65	0.1(0.1)0.8	2.2(0.1)3.0	1.05(0.1)1.35
1-top/2-bridge	1.5(0.1)1.9	0.2(0.1)0.6	2.6(0.1)3.4	1.05(0.1)1.35
1-top	1.5(0.1)1.9	—	—	0.95(0.1)1.35
1-bridge	1.25(0.1)1.65	—	—	0.95(0.1)1.35
1-hollow(both)	1.25(0.1)1.65	—	—	0.95(0.1)1.35

bridge vs. top sites.

For comparison, we have also tested several structures with just one NO molecule per unit cell. This molecule was explored at the four high-symmetry sites: top, bridge, hcp-hollow and fcc-hollow.

In all cases, we have varied the Rh-N interlayer spacings [$d_\perp$(Rh-NO)], as well as the N-O bond-length [$d_\perp$(N-O)], as table 5.1 summarizes. For the structure models of "1-top/2-bridge" and "1-bridge/2-top", the parallel [$d_\parallel$(N-N)] and perpendicular [$d_\perp$(N-N)] (with relative to surface plane) distances for two types of NO within the (2x2) lattice were also adjusted, as listed in table 5.1. For example, the N-O bond lengths were varied from 0.95 to 1.35 $\AA$ in 0.1 $\AA$ increments, shown in table 5.1 as 0.95(0.1)1.35.

Table 5.2 shows, for each basic model, the best-fit structural parameters and the R-factor value achieved. The models with only one NO per (2x2) cell are clearly incorrect. The 1-bridge/2-top model is favored, but the 1-top/2-bridge model gives a theory-experiment fit of comparable quality (but with somewhat different bond lengths than for the 1-bridge/2-top model).

Our best 5-R-factor value of 0.279 can be compared with the value of 0.19 for the analogous CO structure (which used a better theoretical approximation, thereby in part improving the R-factor) [18,204]. The simpler Rh(111)-($\sqrt{3}$ x$\sqrt{3}$)R3

Table 5.2: Summary of best observed LEED R-factors between theory and experiment for different models of Rh(111)/(2x2)-3NO.

Model	$d_\perp$(Rh-NO)	$d_\perp$(N-N)	$d_\parallel$(N-N)	$d_\perp$(N-O)	R-factor
1-bridge/2-top	1.55	0.5	2.6	1.15	0.279
1-top/2-bridge	1.70	0.2	2.8	1.15	0.298
1-top	1.70	—	—	1.15	0.358
1-bridge	1.55	—	—	1.05	0.359
1-hollow(both)	1.25	—	—	1.15	0.362

0°-CO structure yielded an R-factor value of 0.23 [216]. The coadsorption structures of NO or CO, on the one hand, and ethylidyne (CCH_3), on the other hand, gave best-fit R-factor values of 0.294 and 0.242, respectively, for NO and CO [22].

5.3 Discussion

In this section, we will first discuss the surface ordering and LEED crystallographic studies of the (2x2)-3NO structure on a Rh(111) surface, and compare it to a similar structure for CO on the same metal surface. This will be followed by a general discussion of the bonding and reactivity of NO adsorbed on various metal surfaces.

5.3.1 Surface Ordering of NO on Rh(111)

A (2x2) LEED pattern was observed by saturation nitric oxide adsorption on Rh(111) at surface temperatures of 250-350 K. This is in agreement with previous work by Castner and Somorjai [201]; however, Root et al. reported a streaky (2x2) pattern at 250 K by adsorbing NO at 95 K, which they attributed to three domains of atomic oxygen (2x1) patterns from NO decomposition at surface tem-

peratures above 250 K [203]. In order to resolve these controversial results, we have compared (2x2)-3NO LEED intensity vs. voltage curves for the (1.0, -0.5) beam with two other published structures, (2x1)-O [16] and (2x2)-3CO [18,204], which are shown in figure 5.4. Quite different diffraction features can be seen between (2x1)-O and our experimental data; while many similar peak positions can be seen between (2x2)-3NO and (2x2)-3CO.

It is unlikely to have domains of 0.5-monolayer oxygen from NO dissociation at 250 K, as only approximately 3% of saturation NO coverage was reported to dissociate at room temperature by previous XPS measurements [197]. The difference between our (2x2) and the (2x1) patterns observed previously [203] could be due to differences in adsorption temperature and dosing pressure [204], defect concentration [197], or small amounts of surface contaminant present on the Rh(111) crystal surface [217]. All of these factors could change the surface oxygen and nitrogen atom concentrations from NO decomposition at $T \geq 250$ K, and this could lead to the change of surface coverage, adsorption site, and the fragmentation probability for the NO molecule.

At 120-320 K, another c(4x2) LEED pattern was observed for half a monolayer NO adsorption on Rh(111). The observed N-O stretch at 1590 cm^{-1} shown in figure 5.1A is consistent with a previous published frequency [203]. A similar pattern and coverage of NO adsorption on a Pd(111) surface was also reported by Conrad et al. [218]. Based on our HREELS data, only one N-O stretch at 1590 cm^{-1}, in the range of bridge site NO, is observed on Rh(111). This result is indicative of single bridge-site NO adsorption in the c(4x2) unit cell at half a monolayer coverage, similar to the model proposed by Conrad et al. for the Pd(111) surface [218]. To substantiate the proposed structural model, the dynamical LEED analyses of c(4x2)-NO on both Rh(111) and Pd(111) are in progress in our laboratory to

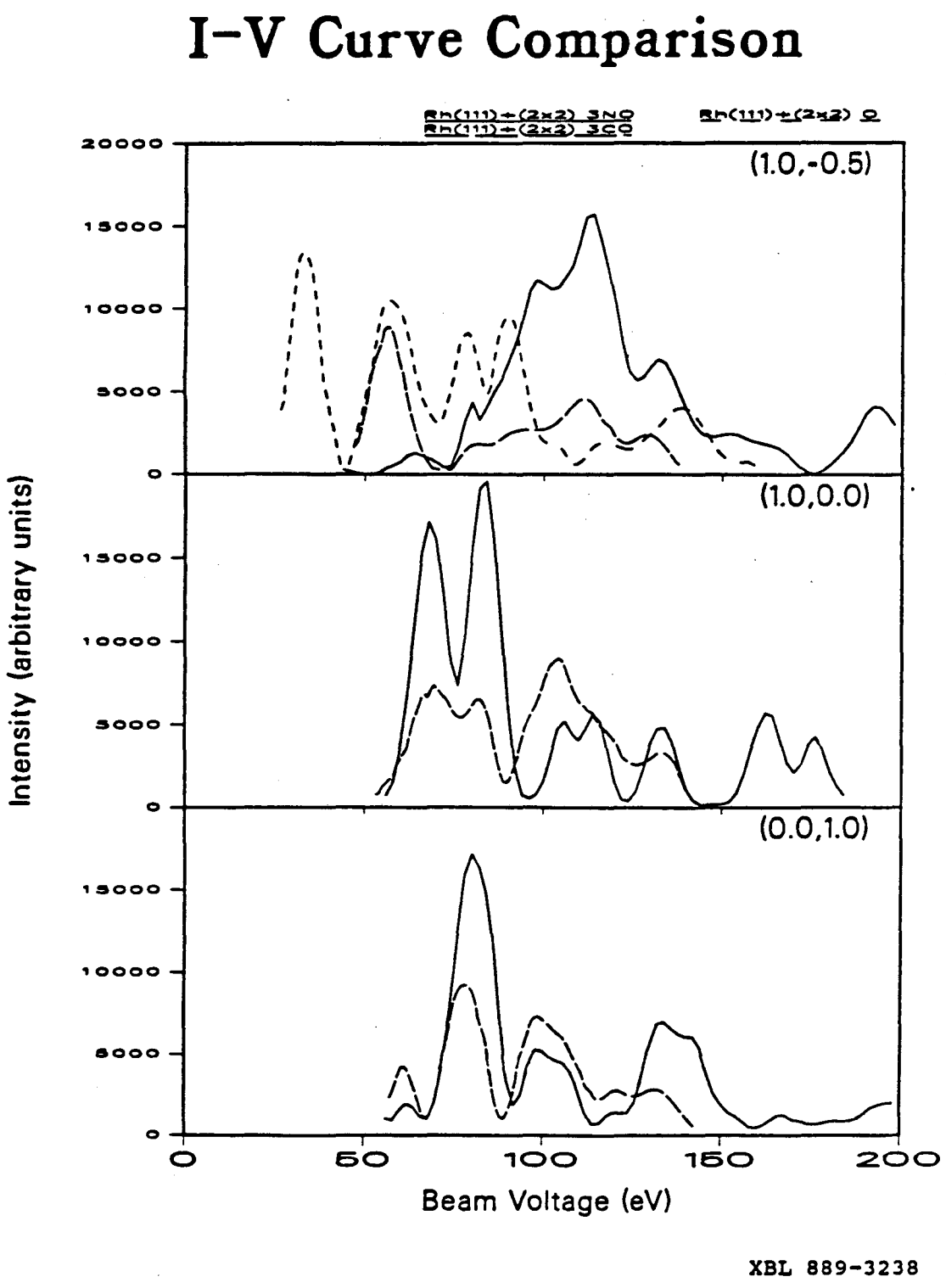

Figure 5.4: Experimental LEED intensity vs. voltage (I-V) curves comparing three different ordered structures, (2x2)-3NO, (2x2)-3CO [18,204], and (2x1)-O [16], on the Rh(111) surface.

resolve the real-space structures.

5.3.2 Surface Structure of Rh(111)/(2x2)-3NO

Figure 5.3 shows top and side views of the best-fit structure for (2x2)-3NO by dynamical LEED analysis. Due to lateral interactions between chemisorbed NO at 0.75-monolayer coverage, two near-top-site NO molecules were observed with parallel axes shifted 0.38 $\AA$ from the center of the metallic rhodium atom. This is 0.15 $\AA$ smaller than (2x2)-3CO [18,204], which could be due to the size difference between CO and NO molecules. Figure 5.5A shows our optimal structure for the NO overlayer in Rh(111)-(2x2)-3NO, using van der Waals spheres for N and O to exhibit the molecular packing. Figure 5.5A can be compared with the corresponding CO structure shown in figure 5.5B [18,204]. The smaller van der Waals size of the nitrogen atom compared to the carbon atom accounts very well for the obvious difference in packing; the near-top site CO molecules are kept farther away from the ideal top sites than the corresponding NO molecules. (Figure 5.3, which uses covalent radii, clearly shows the relationship to the adsorption site in the NO case.) The tighter packing of CO compared to NO is likely to be responsible for the more difficult preparation of the CO overlayer: the CO overlayer forms only with a background pressure above 10^{-6} torr, while for NO an exposure of 25 L at 10^{-7} torr is sufficient to generate a (2x2) LEED pattern.

The calculated N-O bond length is 1.15±0.1 $\AA$ for both near-top and bridge-site NO in the (2x2) unit cell, which can be seen from the side-view picture of the real-space structure in figure 5.3. The perpendicular distances between the topmost rhodium layer and the nitrogen atoms of near-top and bridge-site NO are 2.05±0.1 $\AA$ and 1.55±0.1 $\AA$, respectively. These values correspond to Rh-NO

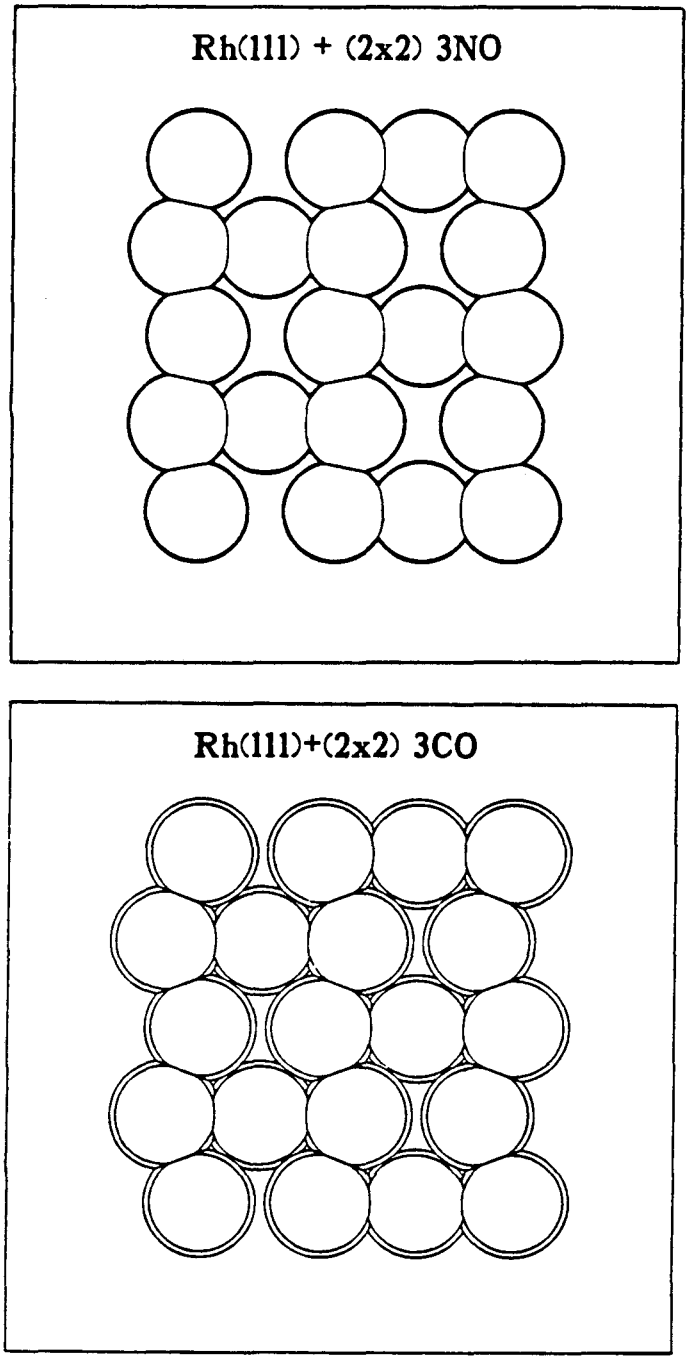

Figure 5.5: Van der Waals radii of NO and CO molecules used to indicate the close proximity between adsorbates within a (2x2) unit cell at 0.75-monolayer coverage. The radii for each atom are: N=1.55 $\AA$, C=1.67 $\AA$, O=1.50 $\AA$.

bond distances of 2.08±0.1 *Å* and 2.05±0.1 *Å* for near-top and bridge-site NO, respectively. These numbers agree reasonably well (within the error bar indicated) with the bond lengths of analogous metal-nitrosyl compounds, as determined by x-ray crystallography [15,219].

To our knowledge, the (2x2)-3NO structure is the first complete structural analysis for a molecular NO overlayer on transition metal surfaces and is also the first direct calibration of a NO HREELS assignment by LEED crystallography.

5.3.3 Surface Chemical Bond of NO adsorbed on Transition Metal Surfaces

The chemisorption of NO on transition metal surfaces has been of recent interest to different research groups. Besides our LEED analysis for the structures mentioned above, the major structural information still relies on the application of vibrational spectroscopy; both HREELS and reflection-absorption infrared spectroscopy have been used. The observed vibrational frequencies for NO adsorbed on metal surfaces are summarized in table 5.3. Sequential adsorption at different adsorption sites is generally observed. For instance, on Ru(001) at a surface temperature of 120 K, NO adsorbed at the threefold hollow site at low coverage and at the twofold bridge and top sites at higher surface coverages [227,228,229]. For our study on Rh(111), and for the work on Pd(111) [220], Pt(111) [222,223,224], and Pd(100) [221], bridge-site NO is followed by top-site NO at low and near-saturation coverage.

Another type of bonding geometry, bent NO with M-N-O bond angle less than 180°, has also been proposed on several metal surfaces. This includes Pt(100)-(1x1) [200], Pt(100)-(5x20) [200,230], Ni(111) [199], and Rh(100) [225]. The

Table 5.3: Assignments of HREEL spectra of NO on various metal surfaces.

Substrate	Adsorption Site	ν(N-O) (cm^{-1})	ν(M-NO) (cm^{-1})	δ(M-NO) (cm^{-1})	References
Ni(111)	bent	1490	400	740	[199]
	bridge	1600	375	—	
Pd(111)	bridge	1510-1660	460-490	—	[220]
	top	1720-1850	510-550	—	
Pd(100)	bridge	1505-1510	—	—	[221]
	top	1660-1720	—	—	
Pt(111)	bridge	1476-1516	306	—	[222,223,224]
	top	1700-1725	450	—	
Pt(100)-(1x1)	bent	1645	230	380	[200]
Pt(100)-(5x20)	bent	1690-1790	310	465	[200]
Rh(111)	bridge	1480-1635	405	—	[203],this work
	top	1815-1840	485	—	
Rh(111)/CCH_3	hollow	1405-1435	—	—	[22]
Rh(100)	bent	910	—	—	[225]
	bridge	1600	—	—	
Rh(331)	bent	1704	—	403	[226]
	top	1815	—	—	
Ru(001)	hollow	1400	680	—	[227,228,229]
	bridge	1500	410	—	
	top	1783-1823	510-570	—	

reported δ(M-NO) and ν(N-O) frequencies extend from 380-840 cm^{-1} and 910-1790 cm^{-1}, as shown in table 5.3. The observation of a strongly perturbed bent NO [ν(N-O)=910 cm^{-1})] species on the Rh(100) surface is in contrast to bridge-site NO on Rh(111) at low coverage [203]. Surface crystallographic studies are necessary to substantiate this type of bent NO bonding geometry.

The adsorption sites of NO also strongly depend on surface temperature. On Ru(001), a metastable top-site NO was observed at 78 K. Subsequent annealing to 120 K caused an irreversible top-to-bridge-site transformation [208]. The barrier of such surface hopping was determined to be 5.9 kcal/mole. On Rh(111), as shown in figure 5.1A and 5.1B, bridge-site NO is the predominant species by adsorbing NO at 95-120 K [203], while saturation adsorption at 250 K can induce the formation of a compact (2x2)-3NO overlayer. This is accompanied by a significant bridge (from ~0.7 to 0.25 monolayer coverage) to top-site (from 0 to 0.5 monolayer) shift, which can be seen in figure 5.1C and in the real-space structure shown in figure 5.3. Previous studies have indicated significant surface diffusion of NO on Rh(111) at 250 K [189]. The barrier of surface diffusion has been recently measured to be 7.0 kcal/mole by the laser-induced surface diffusion technique [231]. We believe this could be one of the reasons why the compression of (2x2)-3NO was observed only by adsorbing NO above 250 K on Rh(111).

By comparison with other fcc(111) surfaces, a great similarity between NO chemisorption on both Rh(111) and Pd(111) is observed. Recent HREELS studies in our group also indicate that the adsorption site of NO on Pd(111) depends on surface temperature and coverage [220]. The observed N-O and Pd-NO stretching frequencies are included in table 5.3. Bridge-site NO, with an N-O stretch in the range of 1510-1660 cm^{-1}, populates first at both 130 K and room temperature; while top-site NO, with ν(N-O) of 1720-1830 cm^{-1}, exists only below 250 K at high

surface coverage on Pd(111). At room temperature all the top-site NO desorbs first, followed by bridge-site desorption at 400 K. Two ordered structures, c(4x2) and (2x2), at 0.5 and 0.75 monolayer coverages, respectively, were also found for NO adsorption on Pd(111) at 130 K [218,220]. These results that imply a similar structural model for c(4x2) and (2x2) NO overlayers on Pd(111) can be proposed based on our LEED and HREELS data on Rh(111).

The similarity of NO chemisorption on Rh(111) and Pd(111) at low temperature is in contrast to the case of CO adsorption, where top-site CO populates first on Rh(111) [216], while the threefold hollow-site CO is the favored species on Pd(111) at low coverages [232,233].

5.3.4 Reactivity of Nitric Oxide on Metal Surfaces

Based on the observed spectra shown in figure 5.2, we believe the top-site NO either desorbs or shifts to bridge-site NO instead of dissociating; however, the bridge-site NO is the major contributor to the dissociation of NO to atomic oxygen and nitrogen in the temperature range of 350-480 K. Similar findings have also been reported on other metal surfaces, such as Ru(0001) [229]. The desorption and dissociation barriers of bridge-site NO were previously measured to be 30 and 19.2 kcal/mole, respectively [202,203].

To compare with the Rh(100) surface, where a bent NO bonding geometry was proposed based on HREELS measurements [225], the observed dissociation barrier is 10.5 kcal/mole and starts at 170 K. Rh(100) is more reactive toward NO dissociation than the hexagonal close-packed Rh(111) surface. Recent XPS and field electron microscopy studies have reported an even higher reactivity on Rh(331) and Rh(321) surfaces, where fewer coordination number sites at step

and kink positions have high surface concentrations [234]. This trend of surface reactivity has been modeled using conservation of orbital symmetry rules with reasonable success by Banholzer et al. [235]. The active site for NO dissociation is proposed to consist of a specific arrangement of atoms instead of just a single step on the surface [236]. Further systematic studies on different materials are necessary to test such a model.

Not only does the reactivity toward NO dissociation depend strongly on crystallographic orientation, but it also depends on the substrate material or the presence of coadsorbates. Dissociative chemisorption is generally observed for NO adsorption on the left-side transition metals at room temperature. This includes W(100) [237], Fe(110) [238], and Re(0001) [239] surfaces; however, on the right-side series, such as Pd(111) [218,220] and Pt(111) [222,223,224], associative adsorption is the predominant process at room temperature. In the catalytic industry, a three-way catalyst including Rh, Pt, and Pd has been used to catalyze the NO reduction reaction [188].

5.4 The Bonding Geometry of c(4x2)-CCH_3 + NO and c(4x2)-CCH_3 + CO on Rh(111) Surface: The Site-Shift Effect Induced by Coadsorption

In the first part of this chapter, the chemisorption of submonolayer NO on Rh(111) was discussed and compared with a similar CO structure on the same metal surface. Although the preferred adsorption site at low coverages is bridge for NO and top for CO, both NO and CO could form a (2x2) structure at saturation (θ=0.75) coverage with two near-top sites and one bridge site within a unit cell. These results demonstrate that adsorbate-substrate interaction is more important in determining different adsorption sites for NO and CO at low coverages; while adsorbate-adsorbate interaction, which causes the formation of an out-of-registry top site due to van der Waals interactions between nearest neighbors, plays a significant role at near-saturation coverage.

No matter what interaction is involved, it is almost certain that the chemistry of either NO or CO will be limited to top or bridge sites on a clean Rh(111) surface. This means that the details of threefold site chemistry will be inaccessible by adsorbing NO or CO alone; however, it is always a scientist's dream that we can control chemical processes in a certain fashion. In other words, it is hoped that by playing certain "tricks" on metallic surfaces, the adsorption site of adsorbates can be controlled, and that it would then be possible to study site-selective chemistry. Indeed, throughout the efforts spent in our laboratory, it was found by appropriate combination of various coadsorbates that the adsorption site of both adsorbates could be varied. The surface chemistry could also be changed in the presence of

coadsorbates. One typical example has already been shown in chapter 4, where preadsorbed CO can enhance the selectivity of ethylidyne formation from ethylene dissociation on the Rh(100) surface [133].

In the next part of this chapter, the surface structure and chemical stability of two similar coadsorption systems, c(4x2)-CCH_3+NO and c(4x2)-CCH_3+CO on the Rh(111) surface, will be presented. By combining the results of HREELS and dynamical LEED analysis, the real-space structures of these two structures can be resolved. Both CO and NO move to hcp and fcc hollow sites, respectively, and leave the other hollow site to the coadsorbed ethylidyne. A 0.03 $\AA$ bond elongation for both CO and NO is also observed by LEED analysis and implies a weakening of the N-O or C-O bond upon coadsorption. HREELS frequencies of ν(N-O) and ν(C-O) show a downward shift of 150-200 cm^{-1} in the presence of ethylidyne. These data also support the site shift and the bond weakening of NO and CO induced by coadsorbed ethylidyne.

The ordered c(4x2)-CCH_3+NO overlayer was observed to have higher thermal and pressure stability. A separate HREELS study has shown the stability of this ordered monolayer film after exposure to the air. This is also the first observation of a coadsorbed monolayer with stability toward a reactive environment.

5.5 Results and Interpretation

In the following sections, the results of surface ordering, LEED structural analysis, and HREELS of coadsorbed CCH_3+NO and CCH_3+CO on Rh(111) surface will be discussed first. The stability of these monolayer films in air studied by HREELS will be presented second. The significance of coadsorbate-induced ordering and structural change will be discussed third. It is hoped that these data

could lead to a new era of site-selective chemistry by coadsorption.

5.5.1 Surface Ordering of Chemisorbed C_2H_3, NO, and CO Overlayers on Rh(111)

In this section, we will discuss the surface ordering of ethylidyne and NO adsorption and coadsorption on Rh(111). As mentioned earlier, for molecular NO adsorption, two ordered LEED patterns [c(4x2) and (2x2)] were obtained at 0.5 and 0.75 monolayer coverage at 120-350 K [240]. No other LEED patterns were seen below the coverage of 0.5 monolayer. HREELS data indicate predominant bridge-site adsorption below 0.5 monolayer coverage, while a bridge-to-top-site conversion was seen by saturation dosage at 250 K.

On the other hand, for molecular ethylene adsorption on Rh(111), two distinct ordered structures [(2x2) and ($\sqrt{3}$ x $\sqrt{3}$)R30°] were seen at 0.25 and 0.33 monolayer coverage at 70 K. This is also the lowest ordering temperature for molecular ethylene on transition metal surfaces [241]. At 220 K, approximately 25% of surface ethylene desorbs into the gas phase; the rest decomposes thermally to ethylidyne (CCH_3) plus hydrogen [51]. The disappearance of the ($\sqrt{3}$ x $\sqrt{3}$)R30° pattern at this temperature is accompanied by the appearance of a (2x2)-CCH_3+H overlayer on the Rh(111) surface [51,93].

The structure of surface ethylidyne within the (2x2) unit cell has been studied by dynamical LEED analysis [93]. The best resolved structure of ethylidyne with the C-C axis normal to surface plane at hcp hollow site was found. At 270 K, the extra 0.25 monolayer of hydrogen atoms desorbs as molecular hydrogen. A partial disordered structure with diffuse intensity near the (1/2, 1/3) position, called a split ($\sqrt{3}$ x $\sqrt{3}$)R30°pattern, replaces the previous (2x2) ordered array [51]. Upon

annealing at 400 K, ethylidyne dissociates to a combination layer of CCH and CH, and a disordered pattern with high diffuse background intensity is shown on the LEED screen [13,51].

For the mixed overlayer of NO or CO coadsorbed with ethylidyne, only one LEED pattern, c(4x2), is observed throughout the whole range of combined coverages. The best way to generate this coadsorbed CCH_3+NO overlayer is to saturate the surface with ethylidyne by 10.0 L dosage of ethylene at 300 K. A subsequent saturation dosage (10.0 L) of NO can cause reordering of the disordered ethylidyne overlayer into a c(4x2) lattice.

For CO+CCH_3, both post-dosing saturation of ethylidyne to the preadsorbed 0.25-monolayer CO or the other way around can produce a c(4x2) ordered pattern, although the former is more successful in generating a sharper LEED pattern. We have noted a previous report of c(4x2)-ethylidyne structure formation by slow annealing from 200 to 250 K on Rh(111) [143]; recently an ion-scattering experiment by Levis et al. also suggested that this c(4x2) ordered structure is due to adsorption of half a monolayer of ethylidyne by a compact zig-zag packing within the unit cell [242]. Though we were unable to reproduce the results mentioned above, it is possible that an undetected surface contaminant was responsible for their work.

5.5.2 HREELS Study of Coadsorbed Rh(111)/c(4x2)-CCH_3 + NO and c(4x2)-CCH_3 + CO

In order to understand the surface structure changes upon coadsorption, we have taken a series of HREELS spectra of NO and CCH_3 adsorbed on Rh(111) with or without coadsorbates. Figure 5.6 shows the HREELS spectra of NO, CCH_3, coadsorbed c(4x2)-CCH_3+NO, and the deuterated analog of CCD_3+NO

on Rh(111) near 300 K.

The reported NO spectrum in figure 5.6A was done by dosing 10 L NO at 120 K. A 0.7-monolayer coverage with two vibrational modes at 405 and 1630 cm^{-1} is observed; these can be assigned as the Rh-NO and N-O stretches of chemisorbed species. This assignment is consistent with the high coverage spectra observed by Root et al. [203]. In their work, the ν(N-O) mode was observed to be coverage dependent, and a change from 1545 to 1630 cm^{-1} was detected in going from 0.25 to 0.7 monolayer coverage [203].

The HREEL spectrum in figure 5.6B is characteristic of normal ethylidyne adsorption in the temperature range of 200-400 K. This is generated by dosing the Rh(111) surface with 10.0 L C_2H_4 at 300 K with the formation of partially disordered split ($\sqrt{3}$ x $\sqrt{3}$)R30°. The modes at 1130, 1345, and 2880 cm^{-1} can be assigned as ν(C-C), $\delta(CH_3)$, and $\nu(CH_3)$. Both the ν(C-C) stretch (1130 cm^{-1}) and the ν(C-H) stretch (2880 cm^{-1}) suggest single bonded (sp^3 hybridization) carbon atoms within the moiety of the CCH_3 structure. The observation of only one intense symmetric $\delta(CH_3)$ deformation mode in the specular position is indicative of a CCH_3 species with the C-C axis perpendicular to the surface. All of these observations are consistent with previous HREELS and dynamical LEED structural analyses of (2x2)-CCH_3+H.

After the formation of the CCH_3 overlayer at room temperature shown in figure 5.6B, another 10.0 L NO was post-dosed to generate a new c(4x2) ordered structure. The spectrum of such a coadsorbed monolayer is shown in figure 5.6C. Comparing figure 5.6B with figure 5.6C, the major difference is the formation of a new peak at about 1435 cm^{-1}; the positions of the rest of the ethylidyne-related modes do not change significantly upon coadsorption. We also noticed there is no other mode between 1545 and 1630 cm^{-1}, which is observed for the N-O stretch

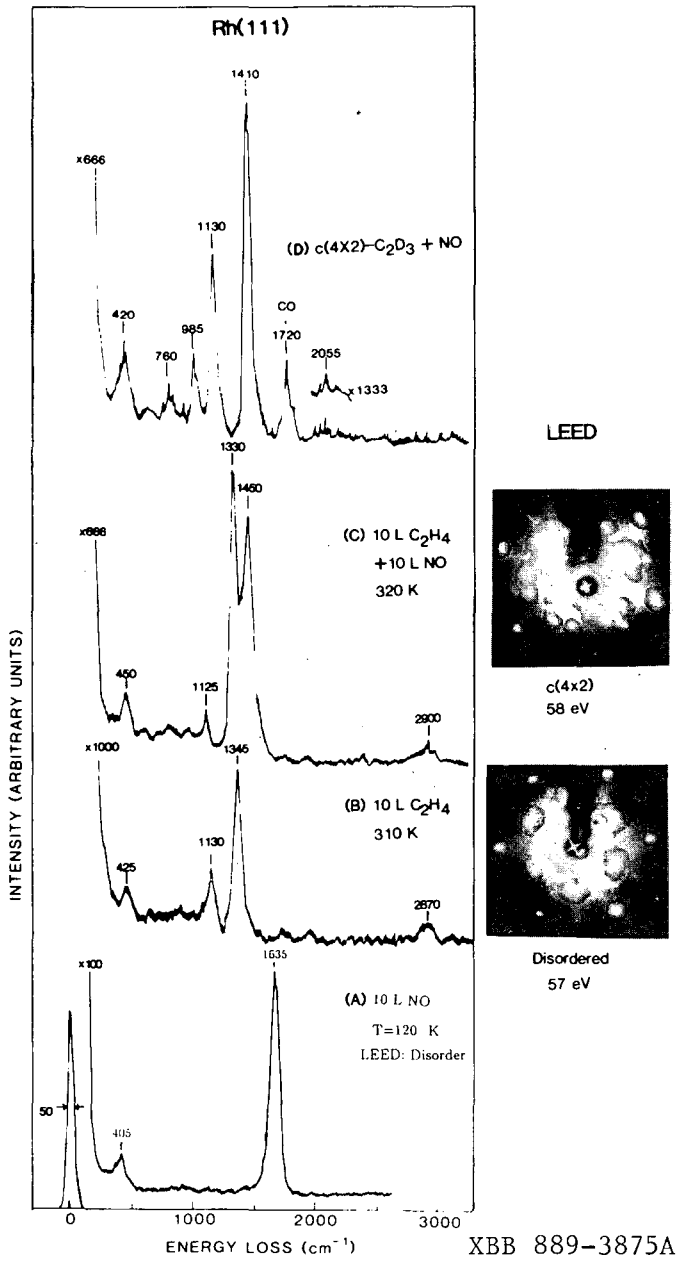

Figure 5.6: (A) 10 L NO adsorbed on Rh(111) at 120 K. This corresponds to ~0.7 monolayer NO coverage. (B) 10 L C_2H_4 dosed at 310 K. A saturated ethylidyne was formed with 0.3-monolayer coverage, as shown by the formation of a partially disordered LEED pattern. (C) 10 L ethylene and 10 L NO dosed sequentially at 320 K, resulting in the formation of a c(4x2)-CCH_3+NO coadsorbed structure. (D) Deuterated analogue of (C).

of mono-adsorbed NO above a 0.25-monolayer coverage. There are two major possibilities for the assignment of the 1435 cm^{-1} peak in figure 5.6C: (a) ν(N-O) of coadsorbed NO species, or (b) $\delta_{as}(CH_3)$ of a tilted ethylidyne species. (A mode around 1420 cm^{-1} is generally observed in the off-specular spectrum of ethylidyne and is attributed to the asymmetric methyl (CH_3) group deformation mode).

In order to resolve the problem, the coadsorption of deuterated ethylidyne and NO was performed. The spectrum of CCD_3+NO is shown in figure 5.6D. As expected, the previously assigned modes of $\nu(CH_3)$ and $\delta(CH_3)$ at 2870 and 1345 cm^{-1} shift down to 2055 and 985 cm^{-1} upon deuteration, while the ν(C-C), ν(Rh-C) modes at 1130 and 430 cm^{-1} do not show any significant change upon deuteration. The important fact is that the mode at about 1420 cm^{-1} in figure 5.6C can be correlated with a sharp mode at 1410 cm^{-1} in the deuterated spectrum. This is suggestive of a non-(C-H) vibrational mode, and the second possibility for the assignment as $\delta_{as}(CH_3)$ can be ruled out.

Based on the experimental evidence mentioned above, we can assign this 1430 cm^{-1} mode to a ν(N-O) stretching frequency, and the corresponding ν(Rh-NO) could be obscured by the ν(Rh-C) stretch of an ethylidyne species. This frequency of ν(N-O) is at least 120 cm^{-1} lower than the isolated ν(N-O) frequency ($\sim$1545 cm^{-1} for 0.25-monolayer coverage) and is in the range of three fold coordinated NO in the metal-nitrosyl compound [6,211,212].

Another separate study of HREELS spectra of coadsorbed c(4x2)-CCH_3+CO by our group shows a 260 cm^{-1} shift in ν(C-O) from 2050 cm^{-1} when adsorbed alone to 1790 cm^{-1} in the coadsorbed c(4x2)-CCH_3+CO overlayer [13,22]. This ν(C-O) frequency of coadsorbed CO is also in the range of threefold coordinated CO with metal cluster compounds.

Based on these HREELS results, we can now propose a structural model for the

c(4x2) ordered coadsorbed monolayer. Both N-O and C-O stretching frequencies shift to a lower frequency upon coadsorption with ethylidyne (~120 cm^{-1} for NO, ~260 cm^{-1} for CO). The peak positions are indicative of threefold hollow-site bonding geometry based on the comparison with vibrational frequencies of metal-carbonyl and metal-nitrosyl compounds [6]. These empirical relationships between frequencies and bonding geometries have been substantiated by bulk x-ray crystallography studies. No big effect except the relative intensity of each vibrational mode is observed for ethylidyne adsorbed on Rh(111) with or without NO (or CO). This implies that the bonding geometry of CCH_3 does not change too much upon coadsorption. A previous LEED crystallography study of (2x2)-CCH_3+H showed that ethylidyne sits at the hcp hollow site [153,243]. It is then reasonable to propose that within c(4x2)-CCH_3+NO (or CO), one carbon atom of ethylidyne bonds to three rhodium atoms on a threefold site.

Although the HREELS measurement can provide some information about the possible adsorption site, orientation of the molecule, and surface geometry of the coadsorbed monolayer, surface crystallography is still necessary to determine the bonding geometries and parameters like bond lengths and angles. These will be quite helpful in a further understanding the interaction between coadsorbates.

5.5.3 LEED Structural Analysis of Rh(111)/c(4x2)- CCH_3 + NO and c(4x2)-CCH_3 + CO

Based on the HREELS data presented in the last section, the following assumptions were made about our LEED structural models of c(4x2)-CCH_3+NO. Both adsorbates are intact nitric oxide and ethylidyne. The molecular adsorbates stand essentially normal to the Rh(111) surface, although minor tilting away from

Table 5.4: Summary of structural parameters (in $\AA$) that have been used in different models of Rh(111)/c(4x2)-CCH_3+3NO by dynamical LEED analysis.

NO/CCH_3 site	$d_\perp$(Rh-NO)	$d_\perp$(N-O)	$d_\parallel$(N-O)
hcp/fcc	1.1(0.1)1.4	1.15	0
fcc/hcp	1.1(0.1)1.4	1.15	0
fcc/hcp	1.1(0.1)1.4	1.15(0.025)1.2	0
fcc/hcp	1.1(0.1)1.4	1.10,1.175,1.20,1.25	0
fcc/hcp	1.1(0.1)1.4	1.175	0.15,0.30

NO/CCH_3	$d_\perp$[N(NO)-C(CCH_3)]	$d_\perp$(C-CH_3)	$d_\parallel$(C-CH_3)	R-factor
hcp/fcc	0.25(-0.1)0.05	1.25(0.1)1.55	0	0.3265
fcc/hcp	0.25(-0.1)0.05	1.25(0.1)1.55	0	0.3011
fcc/hcp	0.1(-0.1)0.1, -0.05(-0.1)-0.25	1.25(0.1)1.55	0	0.2961
fcc/hcp	0.2(-0.1)0.0	1.25(0.1)1.55	0	0.2943
fcc/hcp	0.2(-0.1)0.0	1.25(0.1)1.55	0	0.3003

surface normal was tried. No relaxation or reconstruction of the Rh(111) substrate from the bulk structure has been allowed, since none was found in the previous LEED studies of molecules on Rh(111).

Six structural patterns were varied independently during our model calculations of theoretical I-V curves. Table 5.4 shows the range of variation. The interlayer spacings between N and O of NO, and between the two carbon atoms of C_2H_3 were varied. For example, the C-C bond lengths were varied from 1.25 to 1.55 $\AA$ in 0.1 $\AA$ increments, shown in table 5.4 as 1.25(0.1)1.55. A total of 576 distinct model geometries was generated from the variations of the parameters. The R factors, which compare the similarity of experimental and theoretical I-V curves based on different structural models, are listed in the last column for reference.

The preferred structure for Rh(111)/c(4x2)-CCH_3+NO, based on the best R-factor comparison, is shown in figure 5.7. The side view of the structure, with structural parameterss, is shown at the top of figure 5.7. At the bottom of this figure is the corresponding top view of the c(4x2) lattice. As we can see from the re-

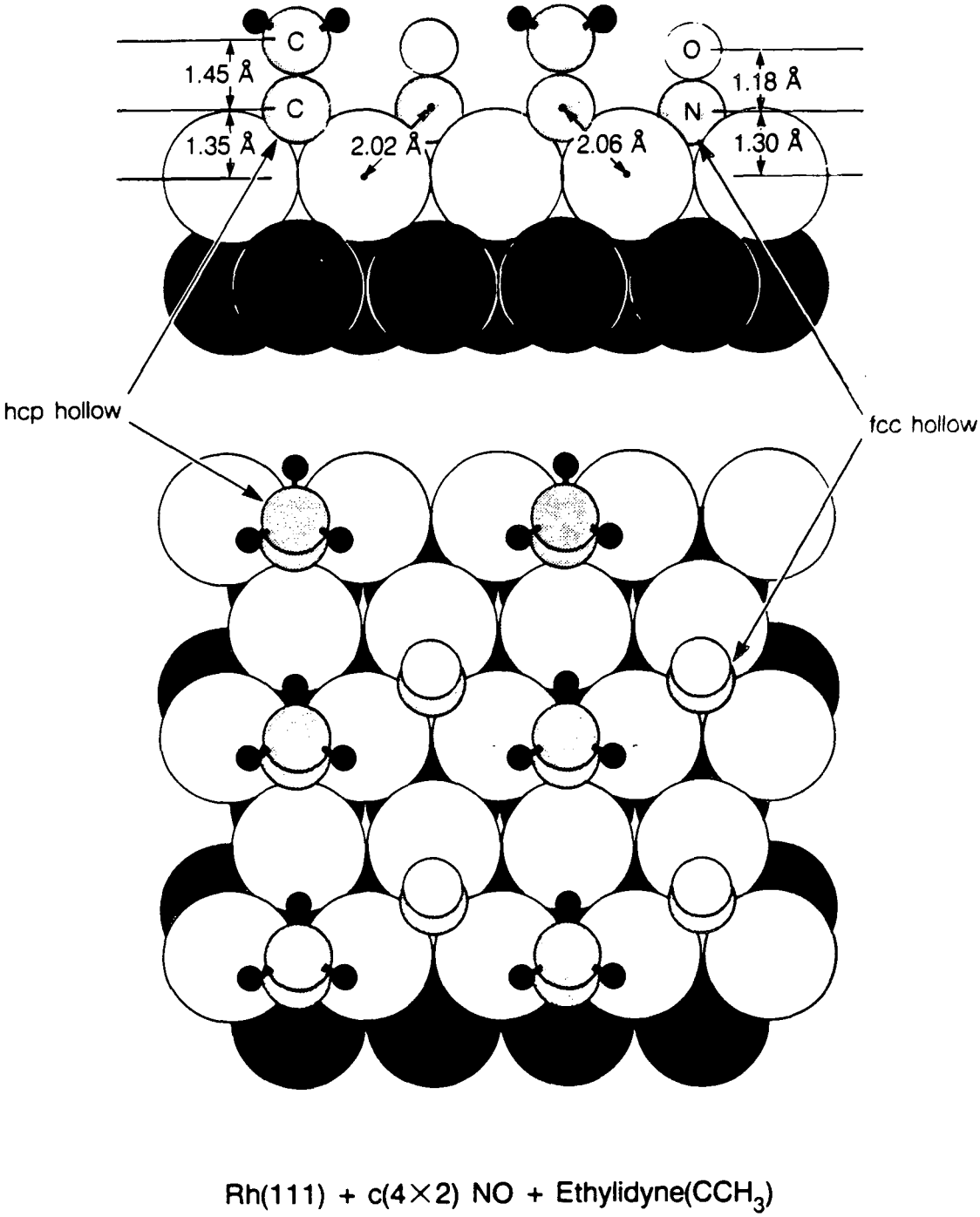

Figure 5.7: Real-space structure of preferred structure of c(4x2)-CCH_3+NO in side view (top panel) and near-perpendicular view (bottom panel) relative to surface plane, showing both bond lengths and adsorption sites.

solved real-space structure, a fcc hollow-site NO with Rh-N and N-O bond lengths of 2.02±0.03 *Å* and 1.175±0.05 *Å*, respectively, are observed. For coadsorbed ethylidyne, no significant change in structure parameter was detected, which is consistent with previous HREELS studies. The C-C and Rh-C bond lengths are 1.45±0.05 *Å* and 2.06±0.03 *Å*, respectively.

5.5.4 High-Pressure Stability of c(4x2)-CCH_3+NO Films on Rh(111) in Air

As we can see from the real-space structures of both c(4x2)-CCH_3 + NO and CCH_3 + CO, the total surface coverage of the coadsorbate is 0.5 (0.25 monolayer of ethylidyne and 0.25 monolayer of NO or CO). If we take into account of the van der Waals radii of either coadsorbate, this c(4x2) structure represents a rather close-packed coadsorbed structure. In order to understand the stability of such a monolayer, both thermal and pressure stability were studied.

We found this c(4x2) coadsorbed structure to have a high thermal stability in maintaining surface order. As we have mentioned before, no ordered structure is expected for the 0.25 monolayer of CO, NO, or ethylidyne when adsorbed alone at 220-400 K. However, by mixing CO, NO, and ethylidyne, a new c(4x2) ordered structure can be detected up to 400 K. This c(4x2) ordered structure represents higher stability than would be found with each coadsorbate. This stability, we believe, is due to attractive interaction between NO or CO with ethylidyne, and we discuss this in chapter 6.

An interesting result was obtained when we exposed the c(4x2)-CCH_3+NO overlayer to a high-pressure gas environment. In this situation, the c(4x2) ordered structure was prepared, and both HREELS and LEED patterns were taken, as

shown in figure 5.8A. The crystal was then enclosed in the high-pressure reaction cell, and room air was leaked in through the gas inlet manifold. After 10 minutes of exposure, the air in the high-pressure cell was pumped out to lower than 10^{-4} torr, and the crystal surface was reexposed to the UHV environment by opening the cell. Both HREELS and LEED were retaken after the air exposure and are shown in figure 5.8B. The surface still maintains a c(4x2) ordering, with both the CCH_3 and NO fingerprint spectra showing from HREELS measurements; a small amount of hydrocarbon cracking was observed with a broad peak at ~750-800 cm^{-1}. This is accompanied by a small reduction in the sharpness of c(4x2) pattern shown in the LEED picture taken after air exposure. There is no doubt that both CCH_3 and NO retain their surface integrity even after exposure to 760 torr of air for 10 minutes. As far as we know, this is the first report of an air-insensitive coadsorbed monolayer on a transition metal surface.

5.6 Discussion

5.6.1 The Variation of NO, CO, and Ethylidyne Surface Structures upon Coadsorption

Figure 5.9 shows the summary of the ordering phenomena, as well as the structural model based on our HREELS and LEED measurements, for both c(4x2)-CCH_3+NO and c(4x2)-CCH_3+CO on Rh(111). As we can see, this type of ordering phenomenon can be observed only upon coadsorption. The interaction between NO or CO with ethylidyne favors the formation of a new c(4x2) ordered structure of the mixed overlayer. In the following chapter, we will discuss the mechanism of such an interaction in the formation of a variety of new ordered structures upon coadsorption.

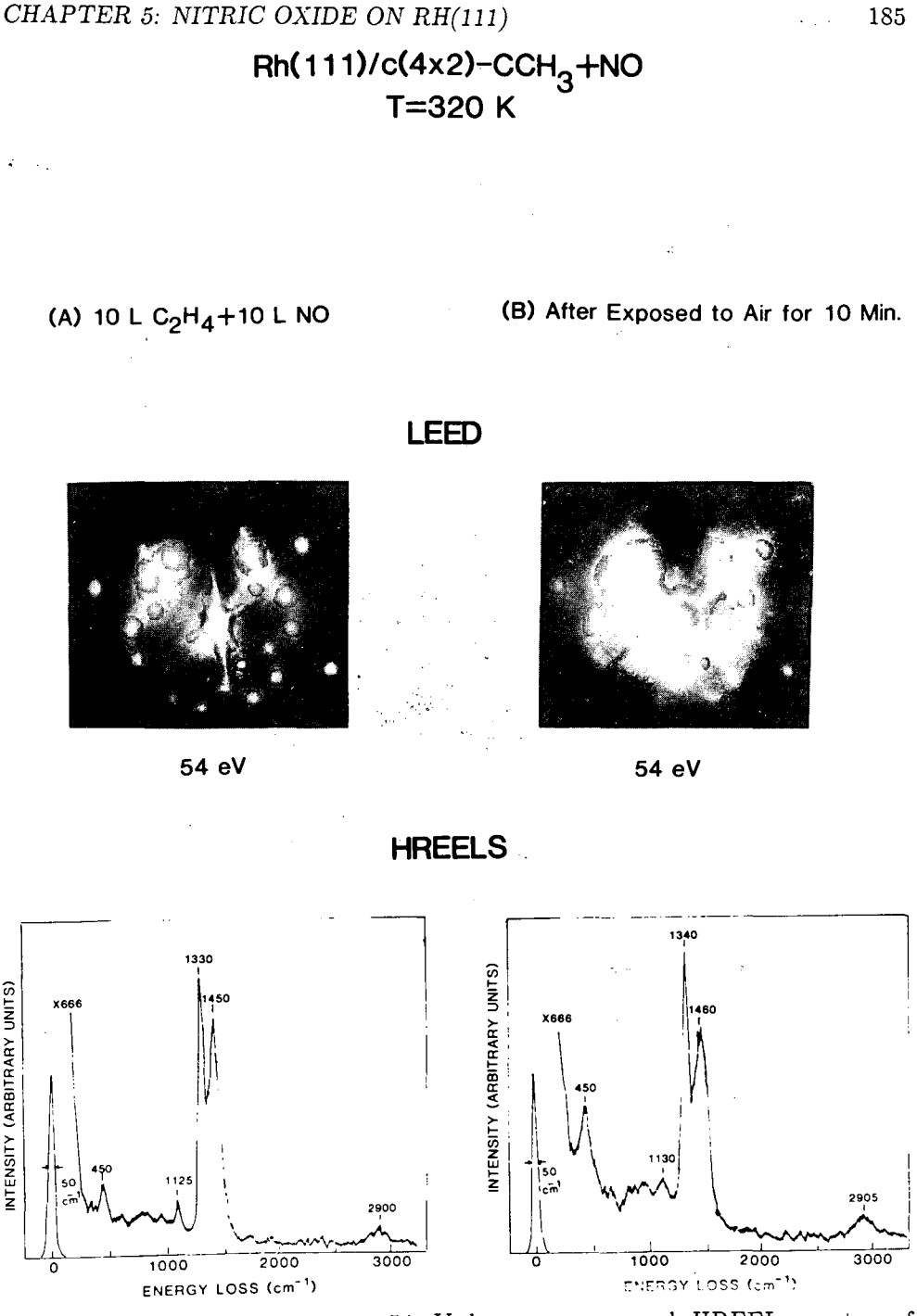

Figure 5.8: LEED pattern at 54-eV beam energy and HREEL spectra of CCH_3+NO overlayer taken (A) right after sample preparation and (b) after exposure to air for 10 min and pumpdown to UHV. (XBB 879-9080A)

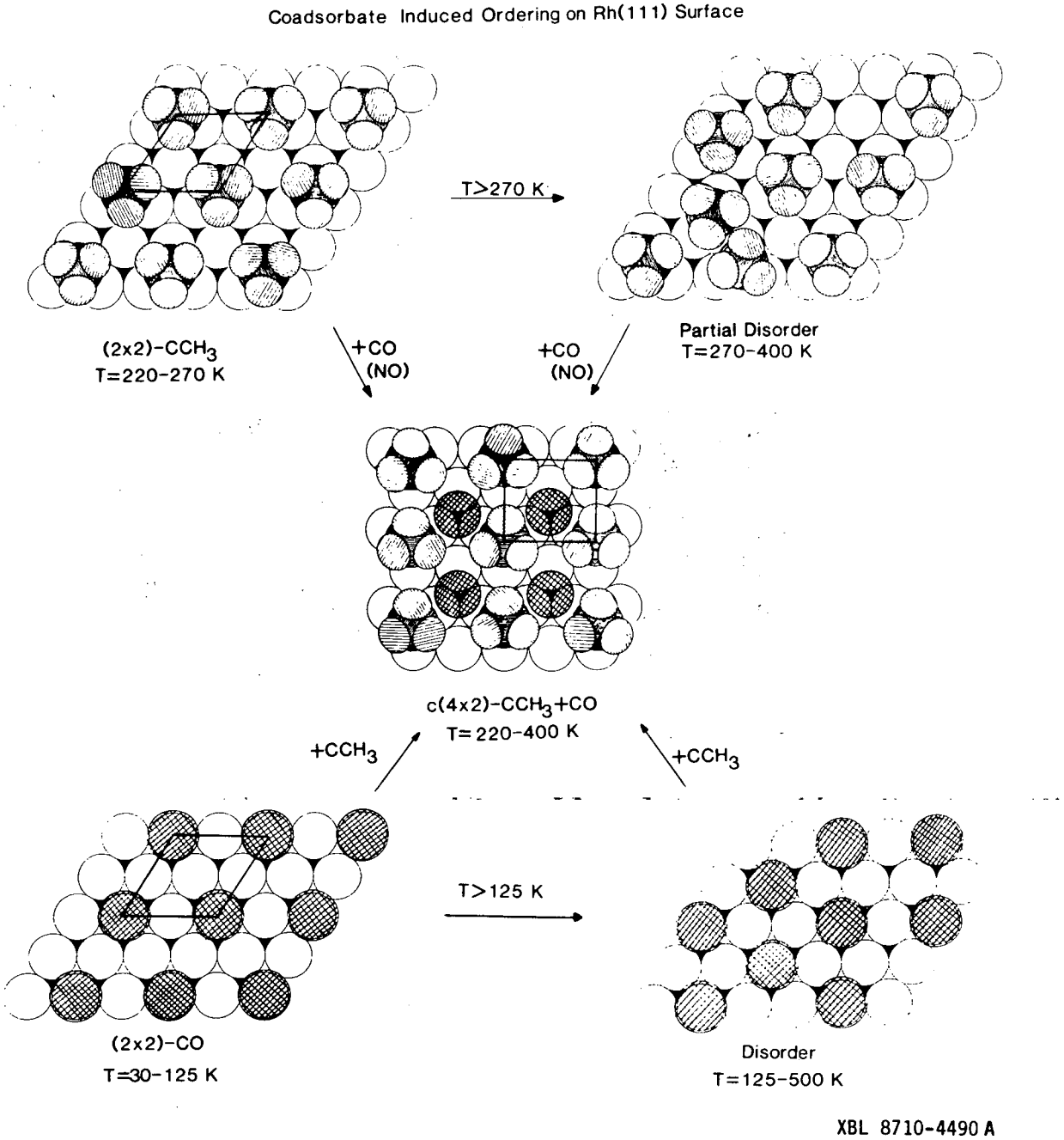

Figure 5.9: Surface ordering and structural model, obtained by LEED and HREELS analysis, for CO (bottom) and ethylidyne (top) on Rh(111) as a function of surface temperature. The formation of a new coadsorbed structure, c(4x2)-CO+CCH_3, is shown in the middle.

Table 5.5: Summary of observed bond lengths (in $\AA$) and adsorption sites of NO or CO on Rh(111) by LEED analysis.

Adsorbate(s)	d(Rh-NO) or d(Rh-CO)	$d_\perp$(Rh-NO) or $d_\perp$(Rh-CO)	d(N-O) or d(C-O)	NO or CO adsorption site
$(\sqrt{3}x\sqrt{3})R30°$-CO	1.95±0.1	1.95±0.1	1.07±0.1	top
(2x2)-3CO	1.94±0.1	1.87±0.1	1.15±0.1	near top
	2.03±0.1	1.52±0.1	1.15±0.1	bridge
c(4x2)-CCH_3+CO	2.02±0.03	1.30±0.05	1.18±0.05	hcp hollow
(2x2)-3NO	2.07±0.1	2.05±0.1	1.15±0.1	near top
	2.05±0.1	1.55±0.1	1.15±0.1	bridge
c(4x2)-CCH_3+NO	2.02±0.03	1.30±0.05	1.18±0.05	fcc hollow

Both HREELS and dynamical LEED analysis of the surface structure of coadsorbed c(4x2)-CCH_3+NO and c(4x2)-CCH_3+CO on Rh(111) provide us with some insight into surface interaction. Without coadsorbed ethylidyne, NO and CO prefer bridge and top adsorption sites, respectively, at 0.25-monolayer coverage. Upon coadsorption, both species shift to a threefold coordination site. Surprisingly, NO and CO do not pick up the same threefold site when coadsorbed with ethylidyne in a c(4x2) unit cell. The adsorption sites of NO and ethylidyne in a c(4x2) unit cell are fcc and hcp hollow sites, respectively [22], while a reverse in adsorption site was found for c(4x2)-CCH_3+CO [22]. We found not only that ethylidyne can shift the adsorption site of NO from a bridge site to a threefold hollow site, but also that noticeable changes in the N-O (1.18±0.05 $\AA$) and the Rh-NO (2.02±0.05 $\AA$) bond lengths were also resolved. In table 5.5, we summarize the structural parameters of both c(4x2)-CCH_3+NO and c(4x2)-CCH_3+CO, as well as the previously analyzed LEED structures of $(\sqrt{3}$ x $\sqrt{3})R30°$-CO, (2x2)-3CO, and (2x2)-3NO. In this table, adsorption site, bond length, and interlayer spacing are all listed for direct comparison. The shift in the adsorption site of CO or NO upon coadsorption can easily be seen. The observed ν(N-O) (or C-O) and ν(Rh-NO) (or Rh-CO) values,

based on HREELS measurements, are also listed.

The ethylidyne adsorption site also changes in the presence of different coadsorbates. Hcp hollows were observed when ethylidyne was coadsorbed with NO, while fcc hollows were preferred when ethylidyne was coadsorbed with CO. It seems that CO and NO adsorb in the site most favorable for them, while ethylidyne is left to choose among the remaining sites. This also implies that surface interdiffusion is necessary to rearrange the coadsorbate to the preferred adsorption sites. A previous LEED study of (2x2)-CCH_3+H on Rh(111) has shown that ethylidyne prefers hcp hollows in the (2x2) unit cell at 0.25-monolayer coverage [153]. The coadsorbed hydrogen site cannot be resolved by LEED due to the weak scattering intensity of the hydrogen atom. The most probable adsorption site is hcp hollows at the center of a (2x2) lattice. After hydrogen desorbs around 270 K, a partial disordered LEED pattern of ethylidyne is formed [13,51].

This (2x2)-CCH_3+H pattern represents another example of coadsorbate-induced ordering. CO, NO, and H can induce surface ethylidyne to c(4x2), c(4x2), and (2x2) unit lattices, respectively. We believe that the difference in the formation of two types of coadsorbed lattices is due to the size of van der Waals radii between CO, NO, and the hydrogen atom. The radii for CO and NO are 1.67 and 1.55 $\AA$, respectively, in contrast to a much smaller radius of 1.1 $\AA$ for hydrogen. As we can see from the real-space structure of (2x2)-CCH_3+H [153,243] and c(4x2)-CCH_3+NO (or CO) [22], after ethylidyne is placed onto a threefold hollow site, the c(4x2) lattice can provide enough space for both CO or NO to occupy the other type of threefold site. On the other hand, the (2x2) unit cell does not have enough space to allocate an extra CO and NO molecule in one unit cell. The c(4x2) lattice is a more efficient way to pack two coadsorbates in one unit cell, and such a pattern has also been observed when CO is coadsorbed with C_2H_2 or

Na on the Rh(111) surface [20,21,32].

The NO molecule, when coadsorbed with ethylidyne, bonds in a fcc hollow site with a N-O stretching frequency of 1435 cm^{-1}. Previous HREELS results by Root et al. for NO adsorbed alone on Rh(111) showed that ν(N-O) shifts from 1545 to 1630 cm^{-1} with increasing NO coverage from 0.25 to 0.68 monolayer [203]. As the local coverage of NO is still 0.25 monolayer, the calculated ν(N-O) shifts would be about 110 cm^{-1}. Such a downward shift would be attributed either to dipole-dipole interaction of coadsorbed NO and ethylidyne, or to the shift in the adsorption site. The change of adsorption site from top to bridge or to threefold hollows could also induce a 100-400 cm^{-1} red shift in the ν(N-O) frequency. This follows the trend that more back donation from the occupied surface d orbital to the NO antibonding orbital, which weakens the N-O bond and lowers ν(N-O), is possible during top to bridge to hollow site transitions. The observed ν(N-O) is also analogous to the IR studies of metal-nitrosyl cluster compounds with similar local bonding geometries. For instance, the inorganic compound $(C_5H_5)_3Co_3(NO)_2$ has a strong ν(N-O) mode at 1405 cm^{-10} [244,245], and the Rh analog of the above cobalt cluster has been reported to have a N-O stretch at 1392 cm^{-1} [246]. Both studies assign these modes to NO bonded to three metal atoms in a hollow site.

On the Ru(001) surface, a ν(N-O) mode at 1379 to 1525 cm^{-1} was observed and was attributed to threefold-site NO [227,228,229]. The LEED observation of NO adsorbed onto fcc hollow sites in the c(4x2)-CCH_3+NO unit cell is a direct calibration of N-O stretch at 1435 cm^{-1}, based on HREELS measurements. This is also the first complete surface structural analysis of NO containing a coadsorbed structure. The power of dynamical LEED analysis in resolving the differences between hcp and fcc hollow sites is also demonstrated in this work.

In the presence of other coadsorbates like oxygen or sulfur, the reactivity of

the metal substrate toward NO dissociation is suppressed significantly [221,247]. Both electronic and site-blocking models have been used to explain the observed data from HREELS and TDS [247]. On the other hand, by coadsorbing NO with potassium or boron on a Rh(111) surface, the reactivity toward NO dissociation is increased [248]. These results indicate that different coadsorbates can either enhance or poison the surface reactivity of transition metals. Further studies are necessary to understand the detail of such interactions.

5.7 Summary

In summary, a significant amount of structural and chemical reactivity information of NO chemisorption on Rh(111) has been accumulated based on the present study. These include the following:

- Two ordered molecular NO structures, c(4x2) and (2x2), at 0.5 and 0.75 monolayer NO coverages, respectively, are observed at 120-350 K. The c(4x2) unit cell consists of a single bridge-site NO with ν(N-O) and ν(Rh-NO) at 1630 and 405 cm^{-1}, respectively.

- The first complete LEED analysis has been performed for the (2x2)-3NO structure. The best structural model, with an 0.279 R-factor, consists of two near-top and one bridge-site NO molecules in one unit cell. This is similar to the model determined for (2x2)-3CO on the same metal surface. A 0.38-$\AA$ lateral shift from the perfect top site was observed for (2x2)-3NO and is attributed to van der Waals interaction between adsorbates.

- The surface ordering and structure of NO on Rh(111) is similar to NO on Pd(111). Rh(111) is observed to be more reactive to NO dissociation at

360-480 K than is Pd(111), but it is less reactive than the Rh(100) surface. The dissociation of nitric oxide on these transition metals is, therefore, a structure-sensitive reaction.

- In the presence of coadsorbed ethylidyne at 0.25-monolayer coverage, a new coadsorbed structure of c(4x2)-CCH_3+NO can be generated. The adsorption sites of NO and ethylidyne were determined to be the fcc and hcp hollow sites, respectively. The ordered c(4x2) array has higher thermal and pressure stability due to the attractive interaction between coadsorbates.

Chapter 6

The Interaction Between Coadsorbates on Rh(111) and Rh(100) Surfaces: Importance of Surface Dipole Moment

6.1 Introduction

In the previous chapters, the surface structure and reactivity of single chemical species, including organic or inorganic adsorbates on Rh(111) and Rh(100), have been presented. In many situations, two or more surface species can be coadsorbed and can interact with each other during the surface chemical reaction. For instance, the Fisher-Tropsch synthesis of organic compounds from CO and hydrogen could involve coadsorption of CO with atomic hydrogen and some hydrocarbon intermediates. The study of the detailed interaction between these coadsorbates on transition metal surfaces could be helpful to a fundamental understanding of heterogeneous catalytic reactions.

In this chapter the coadsorption of carbon monoxide or nitric oxide with various organic coadsorbates [acetylene, ethylidyne(C_2H_3), benzene, etc.] and sodium on

Rh(111) and Rh(100) over the temperature range of 30-800 K will be presented.

Both the structural and chemical effects of these pair-wise combinations of coadsorbates were studied by HREELS, dynamical LEED structural analysis, and work function measurement. We found that the presence of a coadsorbate not only changes the long-range ordering, but also affects local bonding geometry and the thermal chemistry of coadsorbed overlayer as well.

In chapter 5, we illustrated the structural effect by a complete LEED analysis of c(4x2)-C_2H_3+NO on Rh(111), where the adsorption site and bonding geometry of NO change upon coadsorption with C_2H_3. This ordered overlayer was observed to have higher thermal and pressure stability. A separate HREELS study has shown the stability of this ordered monolayer film after exposure to ambient air.

A chemical effect is indicated by the change in the decomposition pathways of the organic overlayer due to the coadsorbates. In chapter 4, coadsorption between CO and ethylene on Rh(100) was presented. It was found that CO can block the dissociation from ethylene to acetylide (CCH) and favor the formation of ethylidyne (CCH_3) near room temperature. This is also the first observation of ethylidyne formation on a surface without threefold hollow sites.

For the coadsorbate-induced ordering phenomena, a model is proposed based on dipole-dipole interaction of coadsorbates to explain the ordering mechanism. The dipole moment of coadsorbates was extracted from work function measurements, while the interaction energy was calculated based on a classical electrostatic interaction between dipole arrays on surfaces. An attractive energy from -0.1 to -0.7 eV is generally observed for ordered coadsorbed overlayers on Rh(111). Other types of interactions, such as direct chemical interaction or through substrate interaction, could also contribute to the stabilization energy of the coadsorbed monolayer. The coadsorbate-induced ordering is expected to be a general phenomenon

induced by a combination of antiparallel dipole coadsorbates (or donor-acceptor coadsorbates) on metal surfaces.

Besides the two coadsorption systems described in chapter 4 and chapter 5, several other combinations of coadsorbates have also been tested to monitor the surface ordering and interaction between adsorbates upon coadsorption. We found that CO (and sometimes NO) can induce the formation of new ordered structures upon coadsorption with benzene, ethylidyne, acetylene, propylidyne, flourobenzene, and sodium on the Rh(111) surface. These ordered LEED patterns cannot be formed by adsorbing either adsorbate on Rh(111) alone. We call this phenomenon "coadsorbate-induced ordering." The formation of these ordered, coadsorbed structures provides an excellent system to study the interaction between coadsorbates under conditions in which relative geometry, stoichiometry, and surface structure can be established by LEED, TDS, and HREELS studies.

In the following sections, coadsorbate induced ordering by coadsorbing CO with coadsorbates, such as Na, C_6H_6, C_6H_5F, and CCH_3 on Rh(111), and the reduction in ν(C-O), can both be correlated to the surface dipole of adsorbates. We determine these dipole moments by measuring work function changes as a function of coverage. We found that coadsorbate-induced ordering occurs when adsorbates with antiparallel dipoles are coadsorbed on Rh(111), while disordering or segregation occurs when parallel oriented dipoles are coadsorbed on the surface. The magnitude of the ν(C-O) reduction can be related to the surface dipole moment of the coadsorbates. Similar results have also been observed on Rh(100) surface. These results will be compared with the data obtained on other metal surfaces by different research groups, and the mechanisms of adsorbate-adsorbate interaction within the coadsorbed monolayer will be discussed.

6.2 HREELS Analysis of a Coadsorbed Monolayer on Rh(111) and Rh(100) Surfaces

In chapter 5 the coadsorption of $CO+CCH_3$ and $NO+CCH_3$ on the Rh(111) surface at 300 K was presented. A noticeable reduction of ν(C-O) and ν(N-O) frequencies upon coadsorption with ethylidyne was resolved by HREELS [22]. This also induces an adsorption site shift of CO from top to hcp hollows, and a similar effect was also observed for NO. The proposed surface structures and bonding geometries were substantiated by a complete LEED analysis discussed in the previous chapter. A similar effect was also observed for other combinations of coadsorbed, ordered overlayers on Rh(111) and Rh(100) surfaces, as shown in figure 6.1 and figure 6.2, respectively. For all of the coadsorbed, ordered monolayers shown in both figures, a universal reduction of ν(C-O) was observed. On the Rh(111) surface, a pure CO overlayer shows a ν(C-O) of 2010 cm^{-1} at 0.33-monolayer coverage, where an ordered $(\sqrt{3} \times \sqrt{3})R30°$ pattern was detected. This corresponds to a top-site CO adsorption based on LEED structure analysis [216]. From figure 6.1, the C-O stretching frequency is greatly reduced from that of CO adsorbed alone and ranges from 1790 cm^{-1} for CO in the c(4x2)-$CO+CCH_3$ structure to 1410 cm^{-1} in the c(4x2)-CO+Na structure. If we assume that CO bonds at hollow sites in all of the coadsorbed structures, as borne out for those structures that have been determined by dynamical LEED analysis, then this 380 cm^{-1} spread of ν(C-O) would indicate that interactions of varying strength occur between the CO molecule and various coadsorbates. Based on the red shift of ν(C-O), the order of such interactions follows the sequence of $CCH_3 < C_6H_5F < C_6H_6 <$ Na for the coadsorbed structure shown in figure 6.1, where there is one CO

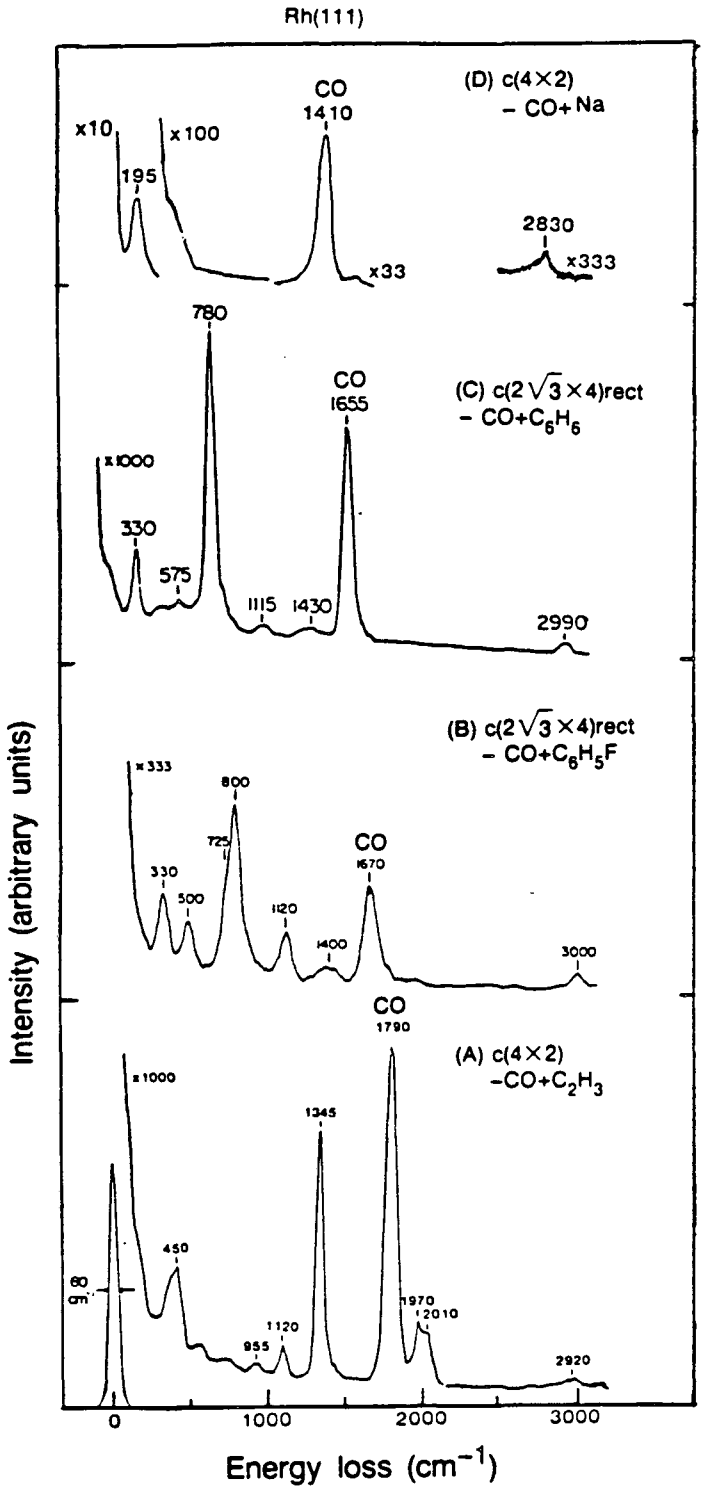

XBL 882-9564

Figure 6.1: Vibrational spectra obtained by HREELS for ordered, coadsorbed structures on Rh(111) at 300 K, where there is one CO per coadsorbate within the unit cell.

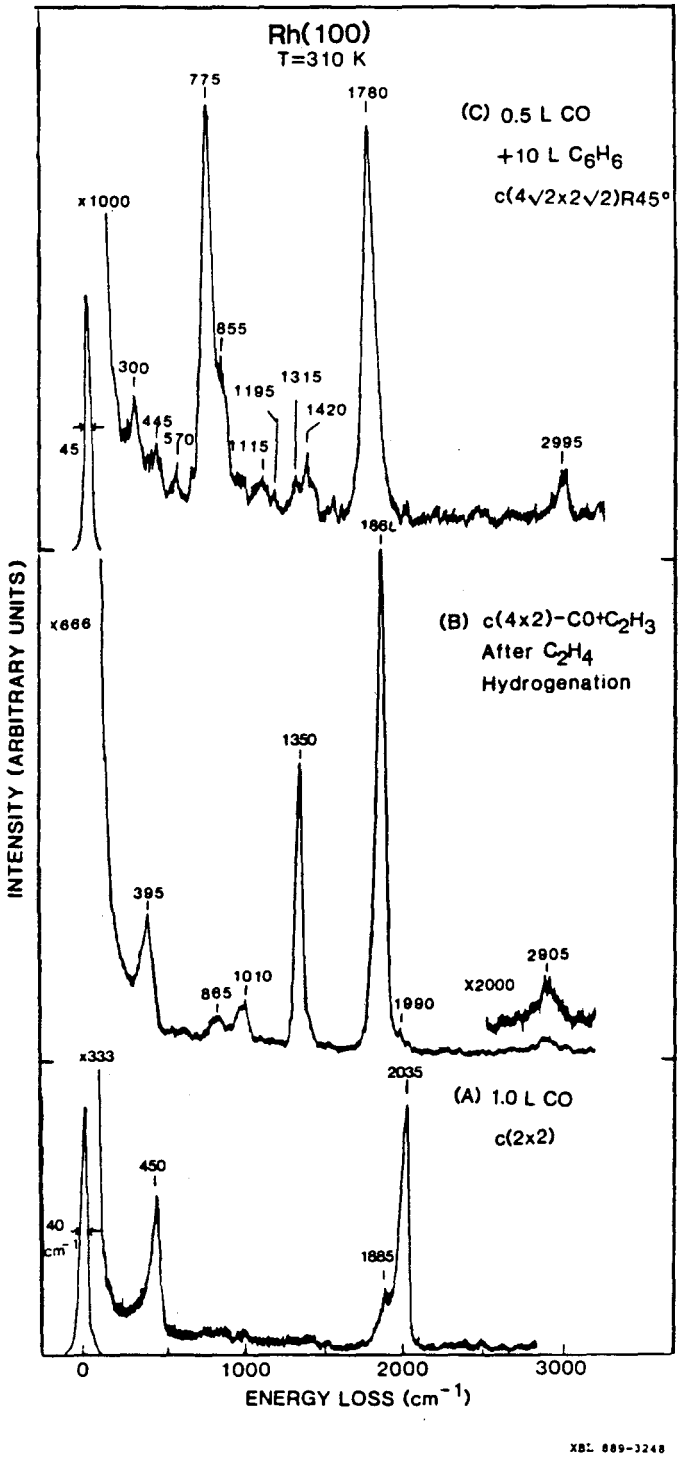

Figure 6.2: Vibrational spectra obtained by HREELS for ordered structures of CO with or without coadsorbates on Rh(100) at 300 K.

molecule per coadsorbate. This trend also follows the strength of surface dipoles of these coadsorbates, as determined from work function measurements presented in the following sections. The significance of these results to the mechanisms of coadsorbate interaction will be discussed later.

A similar phenomenon was also observed on Rh(100), where the reduction of ν(C-O) can be easily seen in figure 6.2. Figure 6.2A represents pure CO adsorption on Rh(100) at 0.5-monolayer coverage with the formation of a c(2x2) ordered pattern. Only one major ν(C-O) peak, at 2015 cm^{-1}, was observed. This is similar to the results obtained on the Rh(111) surface and could be attributed to top-site adsorption. Above 0.5-monolayer coverage another peak at ~1885 cm^{-1} starts to grow and shifts to 1920 cm^{-1} at saturation coverage, where a new $(4\sqrt{2}\times\sqrt{2})$R45° structure can be seen [40]. This was attributed to bridge-site CO populating after the top sites are filled above 0.5-monolayer coverage. However, as the coadsorption experiments were done at CO coverages at less than 0.5 monolayer, we should only focus on the effect of coadsorbates on top-site CO adsorption shown in figure 6.2A.

By coadsorbing CO with ethylidyne or benzene, the ν(C-O) frequency shows downward shifts to 1865 and 1780 cm^{-1}, as shown in figures 6.2B and C respectively. Two coadsorbed, ordered structures, c(4x2)-2CO+CCH_3 and c($4\sqrt{2}$x$2\sqrt{2}$)R 45°-2CO+C_6H_6, were observed. Both have two CO molecules per coadsorbate in one unit cell, and the CO coverages are 0.5 and 0.25, respectively. Following the same argument used in the previous paragraph, the strength of the coadsorbate interaction shows the trend of CCH_3 < C_6H_6. This is also consistent with the trend on the Rh(111) surface.

If we use c(2x2)-CO as a standard point for ν(C-O), the shift of C-O stretching frequency will be 150 and 235 cm^{-1} for the coadsorbed structures shown in figures 6.2B and C. The observed frequencies are in the range of bridge-site CO on

transition metal surfaces [6]. These data can be correlated with a site-shift effect of CO from top to bridge upon coadsorption, which is in contrast to a top-to-hollow site shift observed on the Rh(111) surface.

Table 6.1 summarizes the coadsorbate-induced ordering on various metal surfaces studied in our laboratory, including Rh(111), Rh(100), Pt(111), and Pd(111). The observed LEED patterns, ν(C-O) or ν(N-O) frequencies, and C-O or N-O bond lengths by HREELS and dynamical LEED analysis are listed for reference. The adsorption sites of CO or NO were deduced from HREELS frequencies, and some of them have been proven by direct surface structural analysis. In general, a 100-600 cm^{-1} shift of ν(C-O) or ν(N-O) to lower frequencies is observed for these ordered, coadsorbed monolayers. A concurrent site-shift effect induced by the coadsorbate can also be seen from this table, except on the Pd(111) surface. On Rh(100) and Pt(111) surfaces, a top-to-bridge-site shift of CO was obtained in the presence of ethylidyne or benzene as a coadsorbate. On Rh(111) surface, a top-to-hollow-site shift can be seen for CO in the presence of the coadsorbates listed in table 6.1, while a bridge-to-hollow-site shift was detected for NO coadsorbed with ethylidyne. This type of CO or NO site-shift effect induced by coadsorbed hydrocarbons or alkali metals could be important for future developments in site-selective chemistry.

By increasing the interaction strength between CO or NO with these coadsorbates, the adsorption site of either CO or NO follows the sequence top $\longrightarrow$ bridge $\longrightarrow$ hollow site. This is also accompanied by an elongation of the C-O or N-O bond length in the presence of a coadsorbate, as determined by LEED crystallography. In particular, the C-O bond length increases from 0.15±0.1 $\AA$ to 0.17±0.05 $\AA$ when coadsorbed with ethylidyne on a Rh(111) surface. Further increase to 1.21±0.05 $\AA$ was observed for the c($2\sqrt{3}$x4)rect-CO + C_6H_6 structure.

Table 6.1: Coadsorbate-induced ordering on various transition metal surfaces.

Surface	LEED Pattern	νCO or νNO(cm^{-1})	d(C-O) or d(N-O)(Å)	CO (NO) Site
Rh(111)	$(\sqrt{3} \times \sqrt{3})$R30°-CO	2010	1.07 ± 0.1	top
	(2×2)-3CO	2060	1.15 ± 0.1	near top
		1855	1.15 ± 0.1	bridge
	c(4×2)-CO+CCH_3	1790	1.18 ± 0.05	hcp hollow
	$(2\sqrt{3} \times 2\sqrt{3})$R30°-CO+$3CCH_2CH_3$	1750	—	hollow*
	c(4×2)-CO+C_2H_2	1725	—	hollow*
	(3×3)-2CO+C_6H_5F	1720	—	hollow*
	c$(2\sqrt{3} \times 4)$rect-CO+C_6H_5F	1670	—	hollow*
	(3×3)-2CO+C_6H_6	1700	1.17 ± 0.1	hcp hollow
	c$(2\sqrt{3} \times 4)$rect-CO+C_6H_6	1655	1.21 ± 0.05	hcp hollow
	$(\sqrt{3} \times 7)$rect-7CO+4Na	1695	—	hollow*
	c(4×2)-CO+Na	1410	—	hollow*
	(2x2)-3NO	1840	1.15 ± 0.05	near top
		1515	1.15 ± 0.05	bridge
	c(4×2)-NO+$\equiv CCH_3$	1405	1.18 ± 0.05	fcc hollow
Pt(111)	c(4×2)-4CO	2100	1.15 ± 0.05	top
		1850	1.15 ± 0.05	bridge
	$(2\sqrt{3} \times 4)$rect-4CO+$2C_6H_6$	1800	1.15 ± 0.1	bridge
	$(2\sqrt{3} \times 5)$rect-6CO+$2C_6H_6$	1815	—	bridge*
Pd(111)	$(\sqrt{3} \times \sqrt{3})$R30°-CO	1840	1.15 ± 0.1	fcc hollow
	(3×3)-2CO+C_6H_6	1735	1.17 ± 0.05	fcc hollow
Rh(100)	c(2×2)-CO	2015	—	top*
	c(4×2)-CO+CCH_3	1865	—	bridge*
	c$(4\sqrt{2} \times 2\sqrt{2})$R45°-CO+$C_6H_6$	1780	—	bridge*

* Indicates the adsorption site of CO or NO determined by HREELS frequencies.

This sequence of C-O or N-O bond-length elongation is in good agreement with the reduction of ν(C-O) or ν(N-O), also listed in table 6.1.

On a Pd(111) surface, CO prefers the fcc hollow site without a coadsorbate, and no further site shift could be obtained by coadsorbing with benzene. However, due to the interaction between CO and benzene, a 0.02 $\AA$ longer C-O bond was resolved within the (3x3) structure. This is also consistent with a lower ν(C-O) value of 1735 cm^{-1} for the CO+C_6H_6 overlayer in comparison to 1840 cm^{-1} without a coadsorbate.

Another interesting observation is the resolution of LEED structural analysis to various adsorption sites of CO or NO with or without coadsorbates. For instance, the hcp hollow site is the preferred adsorption site when CO is coadsorbed with ethylidyne or benzene on the Rh(111) surface, while the fcc hollow site is the choice of CO with coadsorbed benzene on the Pd(111) surface. As we have discussed in previous chapters, the subtle difference between these two types of threefold hollow sites is the existence of a second-layer metal atom below the hcp hollow, while there is a vacancy below the fcc hollow. These results again imply the involvement of the second-layer orbital in the chemical interaction of coadsorbates with metal surfaces. Further theoretical work is necessary to understand the importance of such interactions.

6.3 Work Function Measurement

In this section, we will present our work function measurements by adsorbing a single species on Rh(111) first. We then discuss two other coadsorption systems: coadsorption of adsorbates with (1) parallel dipoles and, with (2) antiparallel dipoles.

6.3.1 Adsorption of Negative Dipole Adsorbate: CO on Rh(111)

Figure 6.3 shows the work function changes as a function of CO coverage on Rh(111). The relative surface coverages of CO were determined by TDS yield of mass 28 at different CO dosages, then calibrated against the dosage of a $(\sqrt{3}x\sqrt{3})R30°$ pattern, which corresponds to 0.33 monolayer [216]. Below this coverage ($\theta_{co} < 0.33$), only top-site CO was observed by HREELS and LEED [216,249]. We can fit the work function change by a classical model for mobile adsorption at less than 0.33-monolayer coverage.

The work function change ($\Delta\phi$) can be related to the surface density N, initial dipole moment μ_0, and polarizability α of an isolated adsorbed species by the following expression (in SI units) [250,251]:

$$\Delta\phi = \frac{-eN\mu_0}{\epsilon_0[1 + (9/4\pi)\alpha N^{3/2}]}, \qquad (6.1)$$

where ϵ_0 is the vacuum permittivity. A good fit for $\theta_{co} \leq 0.33$ (shown by the dashed curve in figure 6.3) can be obtained with $\mu_{co} = -0.67x10^{-30}$C·m (about -0.2 Debye) and $\alpha_{co} = 0.34x10^{-28}$ m^3.

At $0.33 < \theta_{co} < 0.75$, $\Delta\phi$ increases rapidly until reaching 1.05 eV at saturation coverage (θ_{co}=0.75), where a (2x2)-3CO LEED pattern was observed. In order to obtain this pattern, it is necessary to cool the sample to 170 K at a dosing pressure of $\geq 1x10^{-6}$ of CO, while the other coverages can be done at 300 K. At these high coverage conditions CO starts to populate some bridge sites as well as the top sites [249,252]. As determined by HREELS and LEED, we attribute this increase in $\Delta\phi$ for $\theta_{co} > 0.33$ to bridge-bonded CO, which has a larger surface dipole than top-site CO. Since we are unable to determine the relative coverage of these two

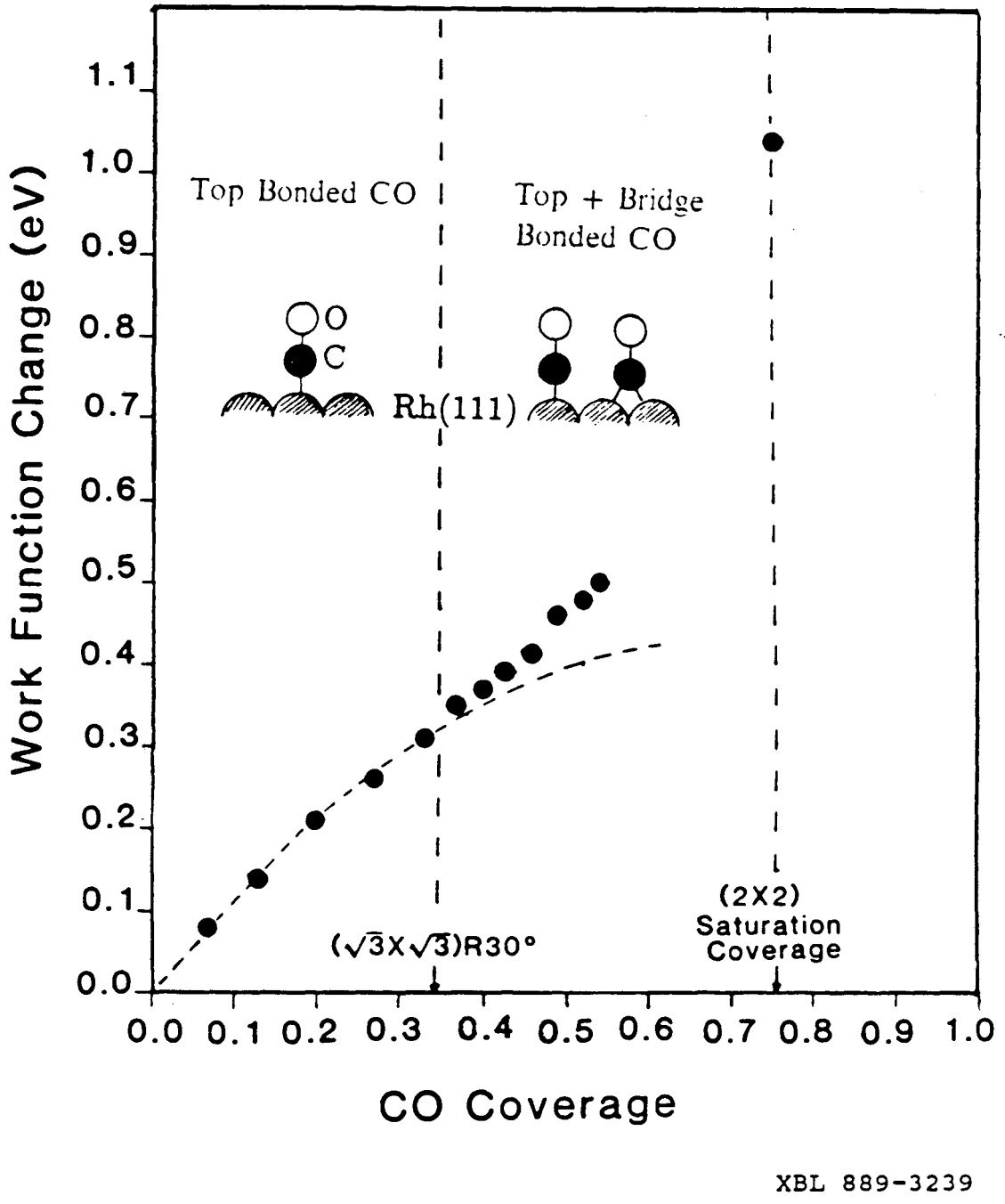

Figure 6.3: Measured work function change of the Rh(111) surface as a function of CO coverage. The dashed curve represents the best fit by using model calculations discussed in the text.

types of CO, we are not able to model this system at coverages between 0.33 and 0.75 monolayer.

6.3.2 Adsorption of Positive Dipole Adsorbates: Na and Hydrocarbons on Rh(111)

Figure 6.4 shows the work function of the Rh(111) surface as a function of sodium coverage. The value of 5.4 eV for the work function of the clean Rh(111) surface is from Berko et al. [253]. Sodium coverages were determined from the sodium thermal desorption yield and calibrated against the $(\sqrt{3} \times \sqrt{3})$R30° and close-packed LEED structure [254]. Using the same model as for adsorbed CO, we deduce a surface dipole moment of $+17\text{x}10^{-30}$ C·m (+5.1 D), and a polarizability of $2.9\text{x}10^{-28}$ m^3 for low sodium coverage. Similar values have been observed for alkali adatoms on Rh(111) and other metal surfaces. The dashed line in figure 6.4 shows that we can achieve a good fit for these values for $\theta < 0.4$. Above θ=0.5, the work function of the surface increases until it reaches the value for sodium metal at just over the coverage needed to form one hexagonally close-packed monolayer.

Figure 6.5a shows the work function of the Rh(111) surface as a function of benzene and fluorobenzene exposure. The work function decrease of 1.36 eV for a saturation coverage of benzene on Rh(111) is in excellent agreement with the value of $\Delta\phi = -1.35$ eV measured by Bertel et al. using ultraviolet photoemission spectroscopy (UPS) [171]. For benzene adsorbed on Rh(111), we determined from the H_2 desorption yield that the benzene coverage is a linear function of exposure up to saturation coverage. (Only a small fraction, 10%, of benzene desorbs molecularly [255].) If we assume that the fluorobenzene is also linear as a function of exposure, and if we use 0.17 and 0.16 for the saturation coverages of benzene [19]

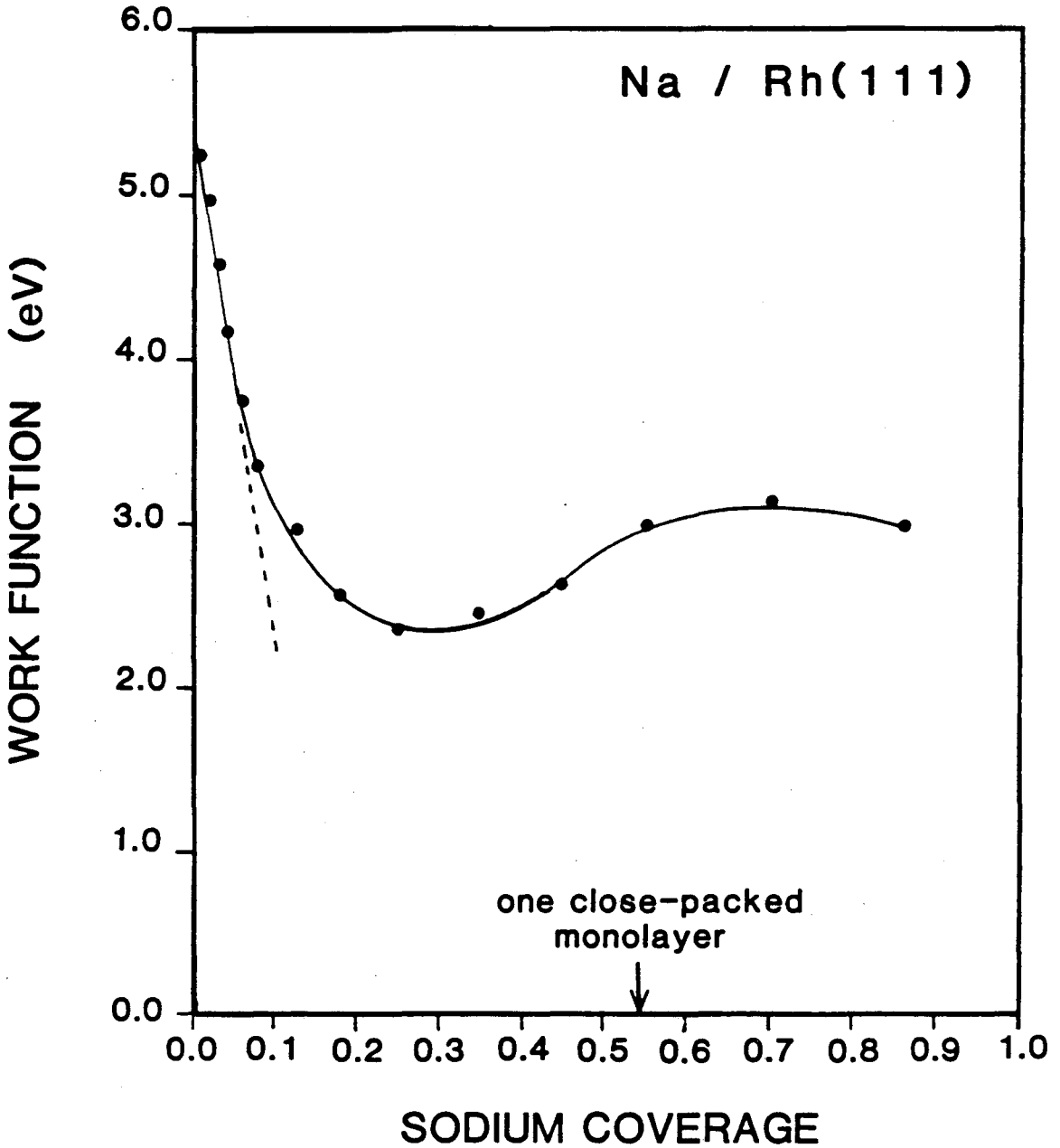

Figure 6.4: Work function of Rh(111) surface as a function of sodium coverage at 300 K. The clean Rh(111) work function is from [171]. The dashed curve represents the fit by the model discussed in the text.

Rh(111)/T=300 K

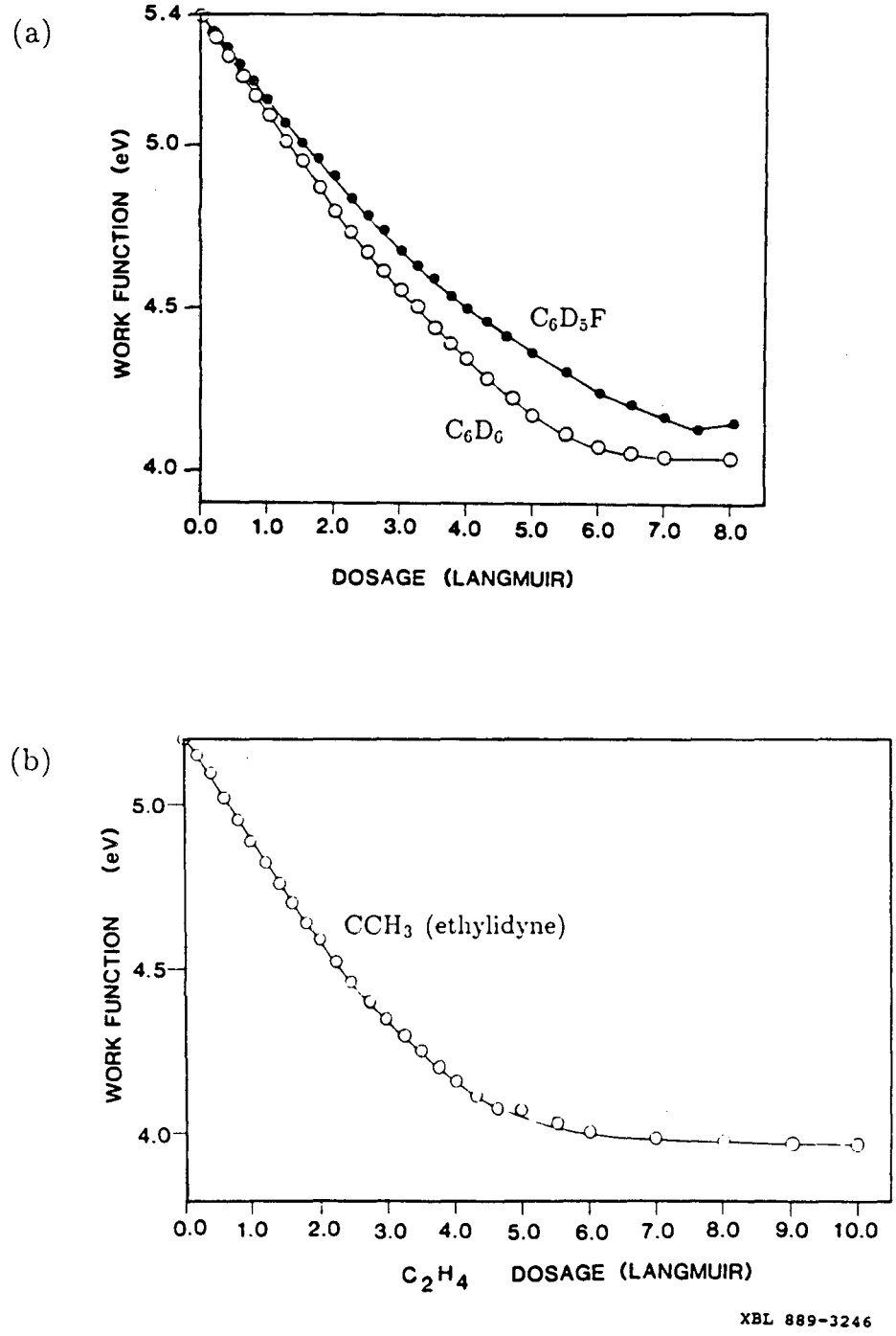

Figure 6.5: Work function of Rh(111) surface as a function of (a) benzene (open circles) and fluorobenzene (closed circles) exposure, and (b) ethylene exposures at 300 K. The clean Rh(111) work function is from [171].

and fluorobenzene [32], respectively, we can deduce, for benzene and fluorobenzene, surface dipole moments μ_{bz} = 6.7x10^{-30} C·m (+2.0 D) and μ_{fbz}= 6.5x10^{-30} C·m (+1.9 D), and polarizabilities α_{bz}= 1.3x10^{28} m^3 and α_{fbz}= 1.5x10^{28} m^3, respectively. It should be noted that the benzene/fluorobenzene values are within experimental error of each other. The difference in work function for the saturated layers of benzene and fluorobenzene is then attributed to the slight difference in saturation coverage.

Figure 6.5b shows the work function of the Rh(111) surface at 310 K as a function of ethylene exposure. At this temperature ethylene decomposes to form ethylidyne (CCH_3), which saturates at a coverage of 0.30 monolayer [13,51]. If we assume that the ethylidyne coverage is linear with ethylene exposure up to saturation coverage, then we find μ_{eth}= +3.1x10^{-30} C·m(+0.9 D) and α_{eth}= 0.62x10^{-28} m^3. If the ethylene sticking probability actually decreases with increasing coverage, as often occurs for adsorption processes, then μ_{eth} would be smaller than determined here.

6.3.3 Coadsorption of Similarly Oriented Dipoles

Table 6.2 lists the surface dipole moments and the polarizabilities of the adsorbates when adsorbed alone on the Rh(111) surface. Adsorbed CO has a negative surface dipole moment, while the other adsorbates, which all form oriented structures with coadsorbed CO, have positive surface dipole moments. Therefore, it appears that CO-induced ordering occurs when CO is coadsorbed with an adsorbate with an oppositely oriented surface dipole moment.

To further test the hypothesis that ordering of coadsorbed molecules is driven by having opposite dipole moments within the ordered unit cells, we have coad-

Table 6.2: Effective dipole moments μ and polarizability α for adsorbates alone on Rh(111).

Adsorbate	μ		α
	(x10^{-30} C m)	Debye(D)	(x10^{-28} m^3)
CO(top site)	-0.67	-0.2	0.34
Na	+17	+5.1	2.9
C_6D_6	+6.7	+2.0	1.3
C_6D_5F	+6.5	+1.9	1.5
$\equiv CCH_3$	+3.1	+0.9	0.62

Table 6.3: Combinations of adsorbates with parallel dipoles coadsorbed on the Rh(111) surface.

Coadsorbate	LEED patterns observed
CO+NO	Disordered or compressed (2x2)-3CO
Na+C_2H_2	Disordered
Na+$\equiv CCH_3$	Disordered
Na+C_6H_6	$(\sqrt{3} \times \sqrt{3})$R30°-Na + $(2\sqrt{3} \times 3)$rect-C_6H_6

sorbed molecules whose surface dipole moments are nominally oriented in the same direction and have found these combinations are disordered or segregated. Table 6.3 lists these results. In these experiments we tried to coadsorb the molecules at coverages and conditions similar to those where CO-induced ordering of coadsorbed structures was observed. As discussed below, it appears that the dipole-dipole interaction energy promotes the formation of the ordered, coadsorbed structures for oppositely oriented dipoles, but not for the systems with similarly oriented dipoles.

6.3.4 Coadsorption with CO

We have also measured the work function for several of the ordered structures formed with coadsorbed CO on Rh(111). Table 6.4 lists the work functions ob-

Table 6.4: Work function of the Rh(111) surface at 310 K for various ordered structures, with or without coadsorbed CO (or NO).

Coadsorbate	No. of COs(or NO) per coadsorbate	LEED pattern	Work function (eV)*
Na	0	(2x2)	2.50
	1	c(4x2)	2.80
C_6D_6	0	$(2\sqrt{3}x3)$rect	4.04
	1	$c(2\sqrt{3}x4)$rect	4.76
	2	(3x3)	5.14
C_6D_5F	0	$(\sqrt{19}x\sqrt{19})R23.4°$	4.16
	1	$c(2\sqrt{3}x4)$rect	4.79
	2	(3x3)	5.16
$\equiv CCH_3$	0	split $(\sqrt{3}x\sqrt{3})R30°$	4.17
	1(CO)	c(4x2)	5.08
	1(NO)	c(4x2)	4.62

* For reference, the work function of clean Rh(111) surface is 5.4 eV.

served for the structures formed by the organic adsorbates, both with and without coadsorbed CO. As can be seen from this table, the work function increases as the ratio of CO to coadsorbate is increased, indicating that CO still has a negative surface dipole moment within the coadsorbed structures. Accurate determination of the dipole moments within the coadsorbed structure is difficult and would require detailed measurements of work function changes as a function of coverage of both surface species; however, if we assume that benzene, fluorobenzene, and ethylidyne have the same surface dipole moment when coadsorbed with CO as when adsorbed alone on Rh(111), then we are able to estimate that CO has an effective surface dipole moment of $\sim$ -2.4x10^{-30} C·m (-0.8 D) in the structure listed in table 6.4. The assumption that benzene, fluorobenzene, and ethylidyne have the same dipole moments when coadsorbed with CO as when adsorbed alone is reasonable, since previous HREELS studies indicate no significant changes in the adsorbate's internal structure when coadsorbed with CO [19,20,22,32].

We have also measured the work function changes when NO, a ligand chemically similar to CO, is coadsorbed with a saturation coverage of ethylidyne. NO, like CO, forms a c(4x2) LEED structure on Rh(111) when coadsorbed with ethylidyne. Both NO and ethylidyne occupy fcc and hcp hollow sites, respectively, within the c(4x2) lattice. When NO is coadsorbed to form the c(4x2) structure, the work function increases by 0.45 eV, indicating that NO, like CO, has a negative dipole moment when coadsorbed with ethylidyne.

Figure 6.6 shows the work function of a Rh(111) surface as a function of exposure to CO when the surface has been precovered with 0.15 and 0.25 monolayer of sodium. For both sodium coverages, the work function increases toward the clean metal value with increasing CO exposure, indicating that the CO still has a negative surface dipole moment when coadsorbed with sodium. For θ_{Na}=0.25, The initial dip in work function can be explained using a model developed by Albano [256]. This model shows that an initial dip in work function can occur, due to a cross depolarization effect, when a surface precovered with an adsorbate with a positive surface dipole moment is exposed to an adsorbate with a negative surface dipole moment. A dip occurs if the adsorbate with a positive surface dipole moment (i.e., Na) has a much larger polarizability than the adsorbate with a negative dipole moment (i.e., CO). In this case, the dipole moment of adsorbed CO induces, initially, an increase in the dipole moment of adsorbed Na larger than the dipole moment of the adsorbed CO, leading to an initial decrease in work function with the addition of CO.

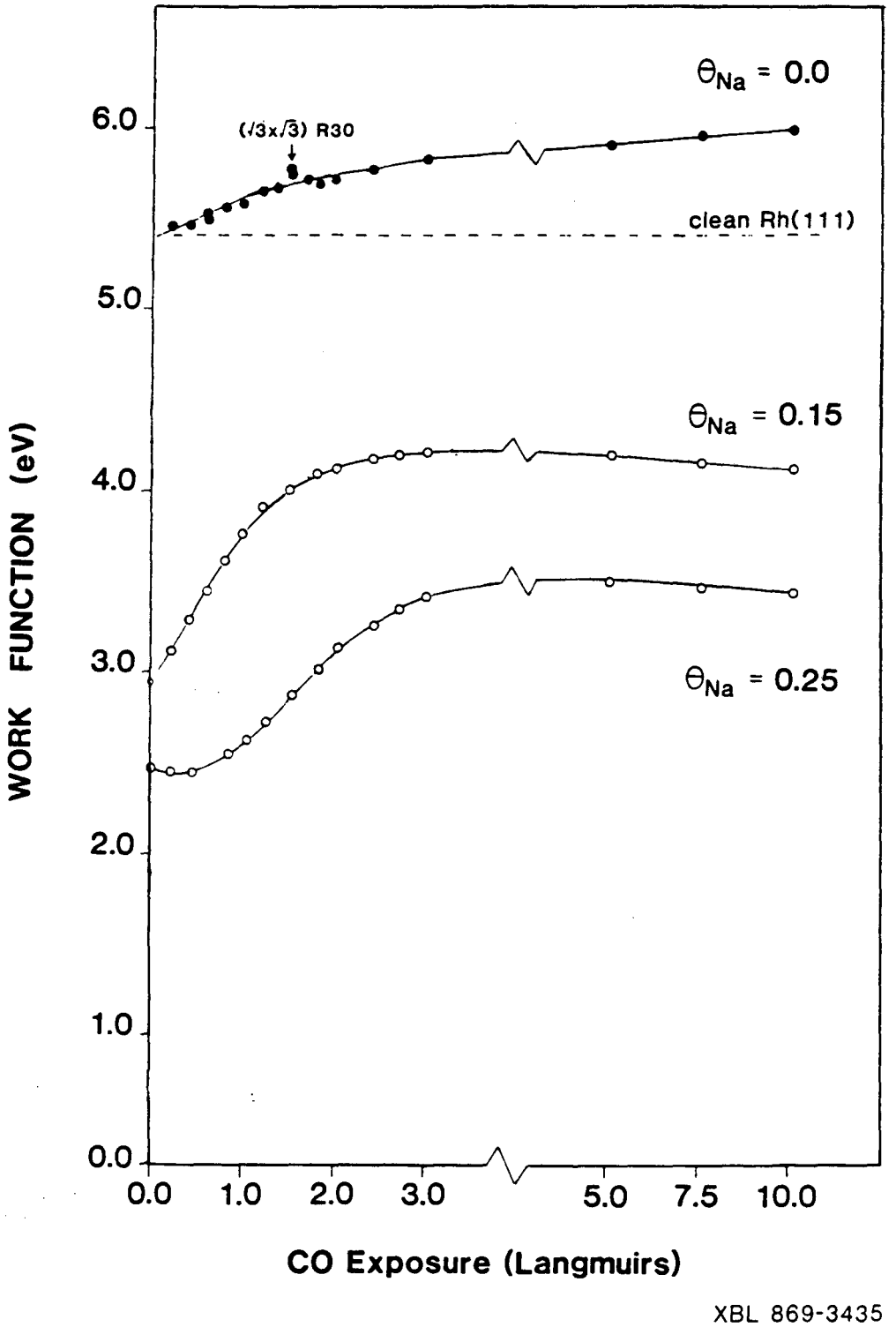

Figure 6.6: Work function of the Rh(111) surface at 310 K as a function of CO exposure when the surface was first precovered with θ_{Na}=0.0, 0.15, and 0.25.

6.4 Discussion

6.4.1 Mechanisms of Adsorbate-Adsorbate Interaction of Coadsorbed Monolayer

Three distinct mechanisms have been proposed as responsible for the interaction between coadsorbates on surfaces. A pictorial view of these interactions is shown in figure 6.7 and is discussed in the following sections.

Dipole-Dipole Interaction

Figure 6.7a shows a simplified picture of surface dipoles arising by coadsorbing two covalent chemisorbed molecules. The distance between the charge centers of gravity is represented by d_c, with the subscript "c" denoting chemisorption. According to the charge separation of coadsorbed surface dipoles, the dipole-dipole interaction can be subdivided into either "attractive" or "repulsive." For instance, coadsorption of parallel dipole molecules corresponds to repulsive interaction, while two antiparallel dipole coadsorbates attract to each other. Typical examples of attractive interactions include the coadsorption between CO or NO with hydrocarbons or alkali metals. On the other hand, coadsorption pairs like CO plus oxygen, CO plus hydrogen, and alkali metals plus hydrocarbons (particularly unsaturated hydrocarbons like benzene or acetylene) are predominately repulsive to each other.

The importance of the surface dipole-dipole interaction between coadsorbates can be detected from vibrational spectroscopy. This is because the strength and direction of the electric field generated from surrounding dipoles can have a strong

Mechanisms of Coadsorbate Interaction on Metal Surfaces

(a) Dipole-Dipole Interaction:

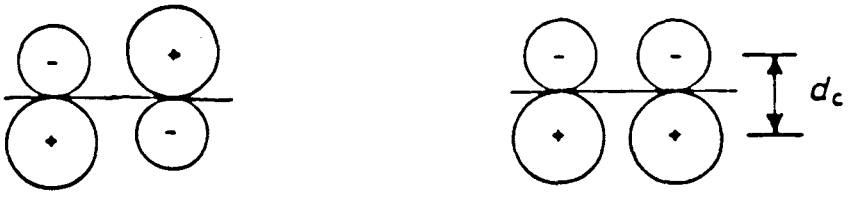

Attractive Repulsive

(b) Charge Transfer Through Substrate:

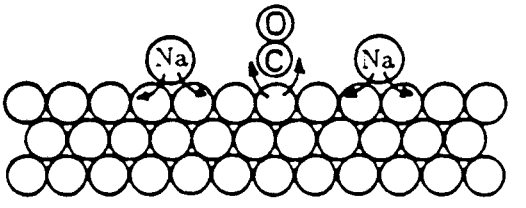

(c) Chemical Complex Formation: CO + K

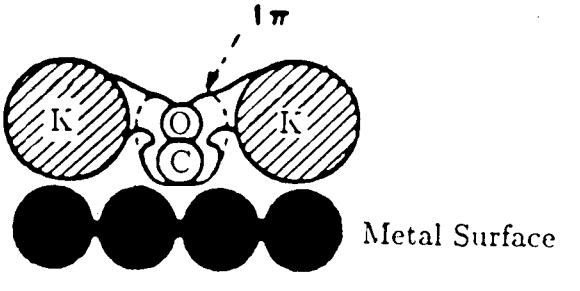

XBL 889-3226 A

Figure 6.7: (a) Dipole-dipole interaction of coadsorbed CO + CCH_3 overlayer; (b) charge transfer through substrate of coadsorbed CO + Na overlayer; (c) direct chemical interaction by the formation of a new surface complex, $CO^{-2}+2K^{+1}$.

perturbation on the vibrational frequencies and relative intensities of coadsorbates. For example, a vibrational Stark effect, where the reduction in ν(C-O) frequency is proportional to the electric field at the CO molecule, has been observed on various transition metal surfaces [257,258,259,260,261,262]. Furthermore, for a coadsorbed monolayer of CO and ethylidyne on Rh(111), the relative intensities of ethylidyne vibrational modes can also be changed by the surrounding dipoles [13,22].

Besides the permanent surface dipole interactions discussed above, it is also possible for both coadsorbates to have induced dipole interaction within close proximity. This type of van der Waals interaction is important for a close-packed overlayer at high surface coverages. Such an adsorbate-adsorbate interaction can be strong enough to cause lateral movement away from high-symmetry sites. Usually an out-of-register adsorption site of an adsorbed monolayer, such as in (2x2)-3NO and (2x2)-3CO discussed in chapter 5, can be detected.

Charge Transfer Through Substrate: Donor-Acceptor Interaction

In figure 6.7b, a charge-transfer interaction is depicted using sodium and CO coadsorption on a metal surface as an example. The interaction involves charge donation from the 2s orbital of Na to the surface, and charge acceptance from the surface by the $2\pi^*$ anti-bonding orbital of the adsorbed CO [263,264,265,266,267]. In this case sodium is behaving like an electron donor, and CO is behaving like an electron acceptor. The metallic substrate, which provides surface orbitals to that accept electrons from sodium and then back-donates them to the $2\pi^*$ orbital of CO, is a charge-transfer medium. Similar donor-acceptor interaction mechanisms can also applied to other combinations of coadsorbates, such as alkali metal plus

NO, hydrocarbons plus CO, etc. In general, for a molecular adsorbate, most unsaturated hydrocarbons and their fragments are classified as donor adsorbates, while CO and NO are classified as acceptor adsorbates on group VIII metal surfaces. For an atomic adsorbate, the donor-acceptor property depends on the relative electronegativity of the adsorbate and substrate materials. Overall, oxygen and halides are good acceptors; alkali metals are good donors on group VIII metal surfaces.

Direct Chemical Interaction: Chemical Complex Formation

The possible formation of a surface chemical complex between neighboring CO and potassium (K) is demonstrated in figure 6.7c. This type of direct chemical interaction has been proposed to contribute to the interactions between CO (or NO) and alkali metals on transition metal surfaces [268,269,270,271,272]. Shushunov has also suggested a $K_2(C_2O_2)$ complex formed by adsorbing CO with a thin film of potassium condensed on a Cu surface at 100 K [273]. However, this interaction is expected to be significant only where stable compounds can be formed between coadsorbates, while for the coadsorbed monolayer generated from CO plus hydrocarbons, no direct chemical interaction was observed based on HREELS analyses.

6.4.2 Stretching Frequency of Coadsorbed CO

The C-O stretching frequency can be a sensitive indicator of the chemical environment of adsorbed CO; however, a shift in the C-O stretching frequency away from the gas-phase value of 2145 cm^{-1} can originate from several different chemical and physical effects. In this section, we show that the stretching frequency

of coadsorbed CO on Rh(111) is correlated with the surface dipole moment of the coadsorbates. We discuss this correlation in terms of various combinations of coadsorbate interactions discussed above.

The correlation between the C-O stretching frequency and the surface dipole moment of the coadsorbates can be seen most effectively by plotting the C-O stretching frequency vs. the dipole moment, as shown in figure 6.8, for the coadsorbed, ordered structures where there is only one CO per adsorbate. Even though only a few data points are available, it appears that the larger the surface dipole moment of the coadsorbate, the lower the C-O stretching frequency of coadsorbed CO.

In order to see how the interactions that reduce the C-O stretching frequency can be related to the surface dipole moment, one can to compare the CO molecules in the c(4x2)-CO+CCH_3 and c(2$\sqrt{3}$x4)rect-CO+C_6D_6 structures. In both cases, the coadsorbed CO molecules have been determined by dynamical LEED analysis to be bound at hcp hollow sites [22,164,274]. In order to better understand how the interactions affect coadsorbed CO in these two structures, it is important to know the C-O stretching frequency of CO bonded to a hollow site without any adsorbate. As CO does not bond to this site when adsorbed alone on Rh(111), the stretching frequency cannot be determined, so we will estimate its value to be 1825 cm^{-1}, the same as CO bound to a hollow site on the chemically similar Pd(111) surface [232,233]. A check on this estimate can be made by extrapolating the results in figure 6.8 to a coadsorbate with zero dipole moment; this extrapolation predicts a ν(C-O) of 1825 cm^{-1}.

For CO in the c(4x2)-CO+CCH_3 structure, a vibrational Stark effect is probably responsible for most of the decrease in the CO stretching frequency to 1790 cm^{-1}. For a vibrational Stark effect, the decrease in C-O stretching frequency is propor-

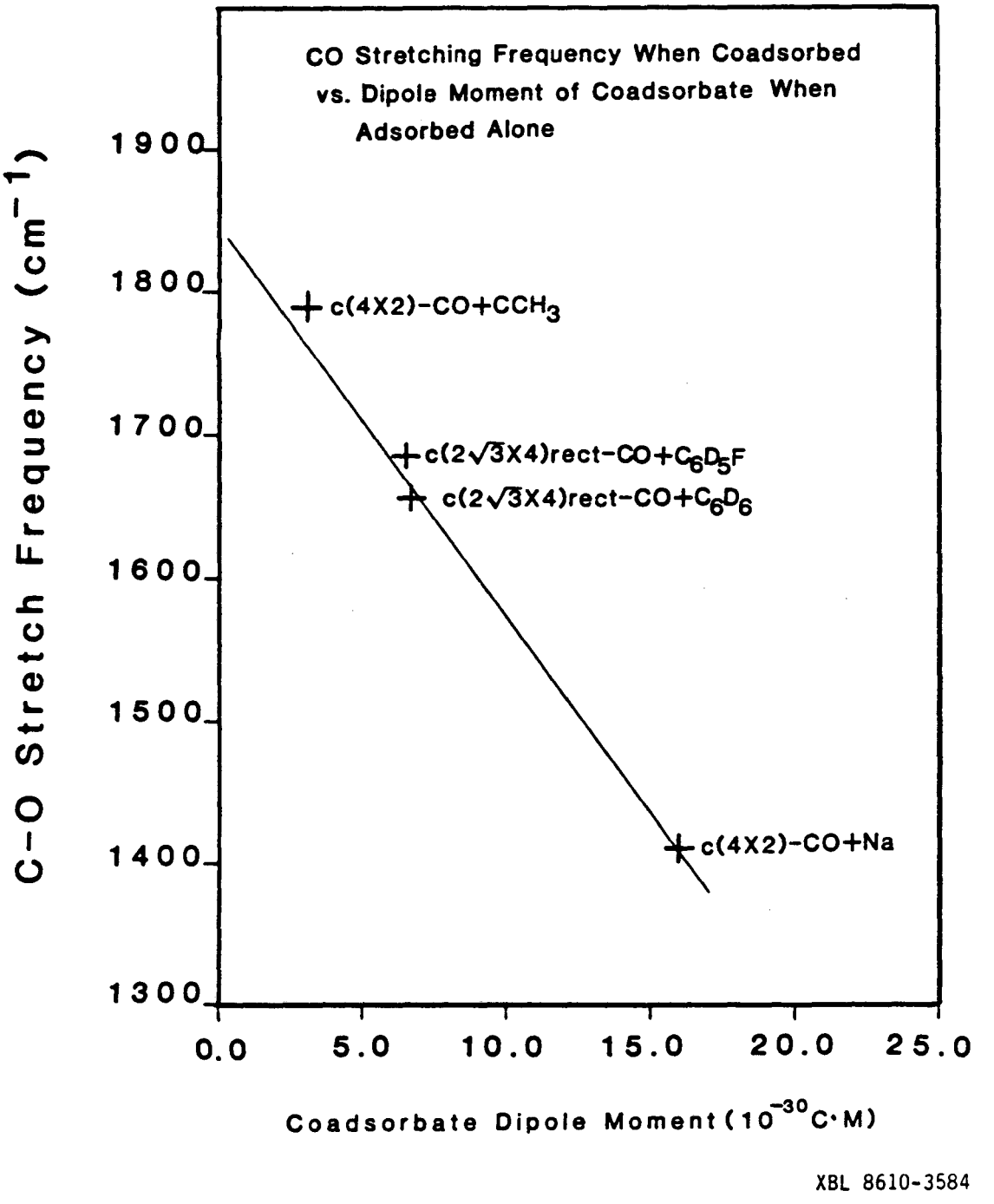

Figure 6.8: C-O stretching frequency in structures that have one CO per coadsorbate, plotted against the effective surface dipole moment of the coadsorbate when adsorbed alone on the Rh(111) surface.

tional to the electric field experienced by the CO oriented along its axis. The Stark tuning rate has been determined by Lambert for CO adsorbed on Ni(110) as 110±40 $cm^{-1}/V\AA^{-1}$ [261] and on Ni(100) as 130 $cm^{-1}/V\AA^{-1}$ [262]. Using the value for Ni(100) and our calculated value for the electric field of 0.23 $V/\AA$, we calculate a Stark shift of 30 cm^{-1} for CO in the CO+CCH_3 structure. Adding the Stark shift to the observed frequency of 1790 cm^{-1} yields a value of 1820 cm^{-1}, close to the frequency of 1825 cm^{-1} estimated for CO adsorbed at a hollow site alone on Rh(111).

For CO in the c(2$\sqrt{3}$x4)rect-CO+C_6D_6 structure, the C-O stretching frequency of 1665 cm^{-1} is shifted down $\sim$ 190 cm^{-1} from the estimated frequency of CO bound at a hollow site on Rh(111). As the calculated electric field at CO when coadsorbed with benzene is similar to that when coadsorbed with ethylidyne, a Stark effect would only account for approximately 15% of the 190 cm^{-1} reduction in stretching frequency. Within the c(2$\sqrt{3}$x4)rect structure, CO and benzene are separated by van der Waals dimensions [274], so direct chemical interaction between coadsorbed CO and benzene is unlikely to be responsible for the observed reduction in the C-O stretching frequency. Therefore, the most likely interaction reducing the C-O frequency is one mediated by the rhodium surface, such as charge donation to the surface by the benzene, which is then back donated into the $2\pi^*$ orbital of coadsorbed CO. The surface dipole moment, therefore, may be an indication of how much charge the benzene donates to the surface, which is then available to be accepted by the coadsorbed CO.

Now we discuss the two other points in figure 6.8, the c(2$\sqrt{3}$x4)rect- CO+C_6D_5F and c(4x2)-CO+Na structures. As C_6D_5F is chemically similar to C_6D_6, the reduction in the C-O stretching frequency for CO coadsorbed with fluorobenzene probably has the same origin as when coadsorbed with benzene, namely a small

Stark effect plus an interaction mediated by the rhodium surface. For CO coadsorbed with Na in the c(4x2) structure, the C-O stretching frequency of 1410 cm^{-1} indicates a highly perturbed CO molecule within the unit cell. At the CO molecule the electric field of 1.5 $V/\AA$ normal to the surface is fairly strong. Assuming a Stark tuning rate of 130 $cm^{-1}/V\AA^{-1}$, we calculate a Stark shift of 200 cm^{-1}, or about half of the observed reduction from 1825 cm^{-1} to 1410 cm^{-1}. The other half of the reduction in C-O stretching frequency presumably comes from charge transfer through the substrate or even possibly the formation of a CO-Na chemical complex. Several research groups have proposed that CO and alkali adatoms form chemical complexes when coadsorbed on metal surfaces [268,269,270,271,272]. Evidence for the formation of chemical complexes comes from the similarity of the low C-O stretching frequencies (1200-1600 cm^{-1}) observed for the coadsorbed CO to those of polymeric CO anions in solid salts of alkali metals with CO [268], and from ARUPS [269,270,272] and XPS [271] results for CO coadsorbed with potassium on Cu(100), Ru(001), and Fe(100) that indicate that $2\pi^*$ and 1π orbitals of CO are involved in a short range interaction with the coadsorbed potassium.

So the correlation shown in figure 6.8, that the larger the surface dipole moment of the coadsorbate, the lower the C-O stretching frequency of coadsorbed CO, appears to have a fairly complex origin. For CO coadsorbed with an adsorbate with a small surface dipole moment like ethylidyne, a Stark effect appears to be responsible for the slight reduction in the stretching frequency. For CO coadsorbed with an adsorbate with a medium surface dipole moment, like benzene or fluorobenzene, other effects, such as charge transfer through the surface, become important for reducing the C-O frequency. For CO coadsorbed with an adsorbate with a large surface dipole moment and, therefore, a large degree of interaction with the surface, all effects – Stark effect, charge transfer, and even direct chemical

bonding between coadsorbates – become important in causing the large reduction observed in the C-O stretching frequency.

6.4.3 Interaction Energies

A necessary condition for the formation of intermixed, ordered structures when CO is coadsorbed with other adsorbates is that the Helmholtz free energy is lower for the ordered structure compared to that of a disordered overlayer:

$$F_{ord} - F_{disord} = (U_{ord} - U_{disord}) - T(S_{ord} - S_{disord}) < 0 \qquad (6.2)$$

The difference in free energy, $\Delta F = F_{ord} - F_{disord}$, between an ordered and disordered overlayer is composed of two terms: an entropy term, $T\Delta S = T(S_{ord} - S_{disord})$, that drives the system toward disorder, and an interaction energy term, $\Delta U = U_{ord} - U_{disord}$, that drives the system toward order.

Our results indicate that the interaction energy, ΔU, favors ordered coadsorbed systems when the coadsorbed molecules have oppositely oriented surface dipoles. In this section, we examine various possible contributions to the interaction energy between the coadsorbed molecules. First, we discuss the dipole-dipole interaction energy.

Obviously, oppositely oriented dipoles are attached to each other, while similarly oriented dipoles repel each other; therefore, structures with oppositely oriented dipoles adjacent to each other are more energetically favorable than those with similarly oriented dipoles. To have a better feel for the magnitude of the dipole-dipole interaction energies of coadsorbed molecules, we have carried out model calculations for ordered arrays of dipoles to compute the dipole-dipole interaction energies for several of the ordered, coadsorbed structures on Rh(111), as well as the dipole electric field normal to the surface within the unit cells.

In our model calculations we first calculate, for an ordered array of dipoles, the electric fields normal to the surface at the two coadsorbates within the unit cell, and then use the electric fields to determine the dipole-dipole interaction energies. We make the simplifying approximation that the dipole moments of the coadsorbed species can be treated as point dipoles lying in the same plane. We also assume that CO has a dipole moment of -2.4x10^{-30} C·m, the estimated value for coadsorbed CO, while the other coadsorbates are assumed to maintain the dipole moments when adsorbed alone on Rh(111). The screening effects due to the metallic substrate are also neglected in our calculation.

Consider two type of dipoles, A and B, coadsorbed in an ordered array and oriented perpendicular to the surface. Then the electric field normal to the surface at A from all other dipoles is given by (in SI units)

$$\xi(A) = -\frac{1}{4\pi\epsilon_0}[\mu_A' \sum(\frac{1}{r_{AA}})_{ij}^3 + \mu_B' \sum(\frac{1}{r_{AB}})_{ik}^3], \tag{6.3}$$

where μ_a' and μ_B' are the apparent dipoles of A and B, r_{AA} and r_{AB} the distances between A and either the other A-type dipoles or the B-type dipoles, and the sums run over either all the A dipoles or over all the B dipoles. The apparent dipoles μ_A' and μ_B' are related to the effective dipoles by

$$\mu_A' = \mu_A + \alpha_A \xi(A) \tag{6.4}$$

and

$$\mu_B' = \mu_B + \alpha_B \xi(B). \tag{6.5}$$

If A and B occupy sites on identical lattices but are displaced from each other, then we can define

$$\Sigma \equiv \sum \frac{1}{4\pi\epsilon_0 (r_{AA})_{ij}^3} = \sum \frac{1}{4\pi\epsilon_0 (r_{BB})_{ij}^3}, \tag{6.6}$$

and

$$\Sigma' \equiv \sum \frac{1}{4\pi\epsilon_0 (r_{AB})_{lk}^3} = \sum \frac{1}{4\pi\epsilon_0 (r_{BA})_{lk}^3}. \tag{6.7}$$

By solving for the electric field at the A dipole, one obtains

$$\xi(A) = \frac{\mu_A \Sigma + \mu_B \Sigma' + \mu_A \alpha_B [\Sigma^2 - (\Sigma')^2]}{\alpha_A \alpha_B [(\Sigma')^2 - \Sigma^2] - (\alpha_A + \alpha_B)\Sigma - 1}. \tag{6.8}$$

A similar expression can be derived for the electric field at the B dipole.

The dipole-dipole interaction energy for an A dipole and all the other dipoles is then given by

$$U_{dip} = -\mu_A' \xi(A), \tag{6.9}$$

which we found during our calculations could be accurately approximated by

$$U_{dip} = -\mu_A \xi(A). \tag{6.10}$$

In order to determine the net reduction or increase in energy due to the interaction of the two types of dipoles, we have defined the interaction energies to be the difference, per CO-coadsorbate pair, between the case where the dipole-dipole interaction energy of the dipoles is in the coadsorbed lattice and the case where the dipoles are in two separate lattices. For example, when CO and ethylidyne are coadsorbed in a c(4x2) lattice, U_{dip}(CO) = −0.034 eV and U_{dip}(ethylidyne) = −0.019 eV when coadsorbed, while U_{dip}(CO) = 0.026 eV and U_{dip}(CCH_3) = 0.039 eV when adsorbed alone on a c(4x2) lattice. Consequently, the interaction energy between the different types of dipoles, as we have defined it, would be (−0.034−0.019)−(0.026+0.039) = −0.12 eV.

The results of these calculations based on the scheme above are listed in table 6.5. A negative sign for the interaction energy indicates that the coadsorbed structures are more energetically favorable, as one would expect for oppositely oriented dipoles. The dipole-dipole interaction energies range from -0.09 eV for

Table 6.5: Calculated electric fields and interaction energies for ordered arrays of coadsorbed dipoles.

Structure	Electric field at CO (V/Å)	Electric field at the coadsorbate (V/Å)	Interaction energy (eV)
c(4x2)-CO+≡CCH_3	-0.23	0.098	-0.12
($2\sqrt{3}$x3)rect-CO+ C_6D_6	-0.23	-0.46	-0.09
c(4x2)-CO+Na	-1.5	-0.56	-0.7

the c($2\sqrt{3}$x4)rect-CO+benzene structure to -0.7 eV for the c(4x2)-CO+Na structure. The CO+Na dipole-dipole interaction energy of 0.7 eV is comparable to the CO-Rh surface bond energy of 1.4 eV obtained from a thermal desorption measurement [31].

Norskov et al. have theoretically investigated in more detail the dipole-dipole interaction of two coadsorbed species using an effective-medium theory that considers the effect of the electrostatic potential induced by one adsorbate on a neighboring adsorbate [275,276]. These calculations take into account the rearrangement of charge between the adsorbate and the surface as well as the effect of screening of the electrostatic potential by the metal. They find, for example, that the interaction energy for CO and potassium coadsorbed on Fe(110) ranges between 0.1 and 0.3 eV, smaller than the value of 0.7 eV that we estimate for Na and CO on Rh(111), probably because our calculation does not include screening effects.

It is reasonable to ask if any direct interaction (not through the substrate) occurs between the coadsorbates other than dipole-dipole interactions. Other types of direct interaction for most of the coadsorbed structures are unlikely except maybe for van der Waals interactions, as the coadsorbed molecules are found to be separated by at least their van der Waals dimensions in those cases where the

structure has been determined by dynamical LEED analysis [22,164,274]. The van der Walls interactions between closely packed adsorbed molecules, however, can be quite significant, as shown by Gavezzotti et al. [277]. For example, these authors have calculated a van der Waals packing energy of -0.12 eV per molecule(-2.7 Kcal/mole) for benzene in a c($2\sqrt{3}$x4)rect unit cell without coadsorbed CO, the same order as for the dipole-dipole interaction energy. A case where a strong, direct interaction may occur is for CO coadsorbed with Na in the c(4x2) structure. The very low C-O stretching frequency of 1410 cm^{-1} is less than the value of 1445 cm^{-1} observed in the CO-alkali complex of potassium deltate, $K_2(CO)_3$ [278], suggesting that CO and Na may form a chemical complex on the surface. This possibility is discussed further in the next section on the vibrational frequencies of coadsorbed CO.

Another possible interaction, mediated by the metal surface, is charge transfer from one adsorbate to another through the substrate. Such an interaction has been widely discussed in the literature as occurring between CO and alkali adatoms coadsorbed on metal surfaces [263,264,265,266]. Here, the electropositive alkali adatom is thought to donate charge to the surface, which is then backdonated into the $2\pi^*$ orbital of adsorbed CO. It is tempting to suggest that the surface dipole moments measured in our experiments are related to the amount of charge transfer between the adsorbate and the surface. While this may be the case for an alkali atom, like sodium, adsorbed on metal surface, the situation for a molecular adsorbate is more complex, since it can also have a dipole moment associated with its molecular structure, as well as one associated with charge transfer to the surface. As is discussed in the following section, however, the vibrational frequencies of coadsorbed CO indicate that some degree of charge transfer into the $2\pi^*$ orbital of CO occurs for several of the coadsorbed structures.

Finally, we should mention that the addition of CO to an adsorbed overlayer can also reduce the entropy of the system. The reduction in entropy comes about from CO blocking not only its own adsorption site, but also, due to a steric effect, preventing coadsorbates from occupying neighboring sites. For example, CO when coadsorbed with benzene blocks a total of seven hcp hollow sites from benzene adsorption on Rh(111). Since the sites blocked by the adsorbed CO are correlated with each other, the number of possible configurations for the coadsorbed system is reduced along with the entropy of a disordered overlayer, thereby making an ordered overlayer relatively more energetically favorable. Also, as the entropy for an intermixed overlayer is higher than for a segregated overlayer, the entropy helps promote intermixed structures over segregated structures. Even though entropy considerations help to explain why ordered coadsorbed structures occur, they do not account for only coadsorbed structures with oppositely oriented dipoles being observed, indicating that interaction energies play a dominant role.

6.4.4 Comparison to Cluster Compounds

Often a surface chemical bond of molecular adsorbates can be thought of as "cluster like;" i.e., that the molecular bonding geometry and chemical interaction of the molecular metal clusters can provide a good model for the analogous surface chemical bond [14,15,279]. For example, good agreement is observed between the reported ν(C-O) frequencies of CO bound to one, two, or three metal atoms in metal-carbonyl complexes and for CO chemisorbed with a similar bonding geometry on transition metal surfaces [6,233]. Consequently, it is interesting to see if CO coadsorption with other molecular adsorbates on Rh(111) can be compared with the analogous organometallic compounds; i.e., the substituted metal-carbonyl

with CO and other ligands bound to the metallic center [280,281,282,283]. As described in the previous sections, on a surface the dipole-dipole interaction and interactions mediated by the substrate are the most common interactions between molecules coadsorbed on surfaces. However, in the substituted metal-carbonyl compounds, generally no significant direct interaction occurs between CO and the other molecular ligands, although a second-order interaction between the ligands is usually observed to occur through the metallic center, which may be similar to the substrate-mediated interactions that occur on surfaces.

In substituted metal-carbonyl complexes, a charge-transfer interaction between CO and other ligands is quite commonly observed, similar to the mechanism that appears to occur on metal surfaces. For the case of CO coadsorption with benzene or Na on Rh(111), we attribute part of the reduction in the C-O vibrational frequency to the charge transfer from benzene or sodium to the metal substrate, which then enhances the back donation to the $2\pi^*$ antibonding orbital of CO.

In cluster complexes, both infrared spectroscopy and x-ray photoelectron spectroscopy (XPS) have been used to study how substituted ligands affect the degree of back donation to the $2\pi^*$ CO orbital [282,283]. A shift in ν(C-O) to a lower frequency and a corresponding lower force constant for the C-O bond is generally observed in the presence of π-electron donating ligands, and it is attributed to charge transfer through the metallic center from the π-donating ligand to the $2\pi^*$ CO orbital [280,282]. This lowering of the C-O force constant is seen for ligands like C_6H_6 and C_5H_5 in chromium and manganese carbonyl compounds [282]. Also, for a series of $RMn(CO)_5$ (R=ligand), the C-O force constant follows the sequence with ligands R: $C_3H_5 < CH_3 < I < Br < Cl < CF_3 < SiF_3$. The difference here can be explained by the electron donating or withdrawing ability of each ligand: the better the electron donating group, the more the back bonding between the

metallic center and CO.

For similar ligands like CH_3 and CF_3, the "inductive effect" plays the most important role in making up the difference. When a better electron-withdrawing atom (fluorine) substitutes for hydrogen in the methyl group, there is more electron withdrawing and less donating capability for CF_3 in compared to CH_3. This is also a commonly observed phenomenon in organic chemistry. In our work, the slightly higher (1670 cm^{-1}) C-O frequency of CO when coadsorbed with C_6H_5F in comparison with 1655 cm^{-1} of CO coadsorbed with C_6H_6 in a c($2\sqrt{3}$x4)rect structure, could be due to the "inductive effect" of the fluorine atom, similar to the effect observed between CF_3 and CH_3 in metal-carbonyl compounds. Consequently, it would be interesting to extend the present work to more highly fluorine-substituted benzene to see if the trend to higher C-O frequencies continues.

6.4.5 Coadsorbate-Induced Ordering on Transition Metal Surfaces

As mentioned at the beginning of this paper, CO-induced ordering of adsorbates has been observed on several other metal surfaces besides Rh(111). To date, CO induced ordering has been observed for benzene on Pt(111) [19], Pd(111) [284], and Rh(100) [286], for ethylidyne on Rh(100) [133], for potassium on Ru(001) [263] and Ni(110) [287], and for hydrogen on Ni(100) [288]. Only for a few of these cases are work function measurements available. For benzene adsorbed on Pt(111), work function measurements by Gland and Sormorjai [289] show that, for low benzene exposure, the work function decreases, indicating that benzene on Pt(111) has a positive surface dipole moment. With increasing exposure of the Pt(111) surface to benzene, which in our experience is an effective way to introduce coadsorbed CO

to form ordered, coadsorbed structures, Gland and Somorjai observed an increase in the work function, indicating that CO coadsorbed with benzene on Pt(111) has a negative surface dipole moment.

Other work function measurements made for adsorbates adsorbed alone on surfaces have shown the work function decreases for benzene adsorbed on Pd(111) [290] and Ni(111) [291] and for potassium on many metal surfaces, while when CO (or NO) is adsorbed the work function generally increases [292]. Therefore, the results for CO (or NO) induced ordering on other metal surfaces support, in general, the hypothesis that ordering occurs when species with oppositely oriented dipoles are coadsorbed.

6.5 Summary

To better understand the interactions responsible for coadsorbate-induced ordering, we have measured the changes in work function of the Rh(111) surface when benzene, fluorobenzene, ethylidyne, sodium, and CO are adsorbed, both alone and coadsorbed with CO. We find that coadsorbate-induced ordering occurs when CO is coadsorbed with adsorbates that have an oppositely oriented surface dipole moment. Model calculations indicate that the attractive dipole-dipole interaction energy is largely responsible for the formation of ordered structures containing oppositely oriented dipoles.

We also find that the reduction in the C-O stretching frequency of coadsorbed CO correlates with the magnitude of the surface dipole moment of other coadsorbed species. The reduction in the C-O stretching frequency is thought to originate from several effects: a Stark effect for CO coadsorbed with ethylidyne, charge transfer through the surface into the CO $2\pi^*$ orbital as well as a small Stark effect

for CO coadsorbed with benzene and fluorobenzene, and a combination of a Stark effect, charge transfer, and even possibly the formation of a chemical complex for CO coadsorbed with sodium.

References

[1] G.A. Somorjai. *Chemistry in Two Dimensions: Surfaces.* Cornell University Press, Ithaca, 1981.

[2] J.F. Nicholas. *An Atlas of Models of Crystal Surfaces.* Gordon and Breach, New York, 1965.

[3] C.-M. Chan, P.A. Thiel, J.T. Yates, Jr., and W.H. Weinberg. *Surf. Sci.* **76** (1978) 296.

[4] P.R. Watson, F.R. Shepherd, D.C. Frost, and K.A.R. Mitchell. *Surf. Sci.* **72** (1978) 562.

[5] G.A. Somorjai. *Principles of Surface Chemistry.* Prentice-Hall, Englewood Cliffs, 1972.

[6] H. Ibach and D.L. Mills. *Electron Energy Loss Spectroscopy and Surface Vibrations.* Academic, New York, 1982.

[7] H. Froitzheim, H. Ibach, and S. Lehwald. *Rev. Sci. Instrum.* **46** (1975) 1325.

[8] G. Herzberg. *Molecular Spectra and Molecular Structure II: Infrared and Raman Spectra of Polyatomic Molecules.* Van Nostrand Reinhold, New York, 1945.

[9] G.A. Somorjai and B.E. Bent. *Progr. in Coll. and Polymer Sci.* **70** (1985) 38.

[10] G.A. Somorjai, M.A. Van Hove, and B.E. Bent. *J. Phys. Chem.* **92** (1988) 973.

[11] E.L. Muetterties. *Chem. Soc. Rev.* **11** (283) 1982.

[12] N.D.S. Canning and R.J. Madix. *J. Phys. Chem.* **88** (1984) 2437.

[13] B.E. Bent. PhD thesis, University of California, Berkeley, 1986.

[14] E.L. Muetterties, T.N. Rhodin, E. Band, C.F. Brucker, and W.R. Pretzer. *Chemical Reviews* **79** (1979) 91.

[15] M.R. Albert and J.T. Yates, Jr. *The Surface Scientists Guide to Organometallic Chemistry.* ACS, Washington, D.C., Washington, D.C., 1987.

[16] M.A. Van Hove, W.H. Weinberg, and C.M. Chan. *Low Energy Electron Diffraction.* Springer Verlag, Heidelberg, Berlin, New York, 1986.

[17] L.J. Clarke. *Surface Crystallography: An Introduction to Low Energy Electron Diffraction.* John Wiley, New York, 1985.

[18] M.A. Van Hove, R.J. Koestner, and G.A. Somorjai. *Phys. Rev. Lett.* **50** (1983) 903.

[19] C.M. Mate and G.A. Somorjai. *Surf. Sci.* **160** (1985) 542.

[20] C.M. Mate, B.E. Bent, and G.A. Somorjai. *J. Electron Specrosc. Related Phenomena* **39** (1986) 205.

[21] C.M. Mate, C.-T. Kao, B.E. Bent, and G.A. Somorjai. *Surf. Sci.* **197** (1988) 183.

[22] G.S. Blackman, C.-T. Kao, B.E. Bent, C.M. Mate, M.A. Van Hove, and G.A. Somorjai. *Surf.Sci.,* in press.

[23] C.-T. Kao, C.M. Mate, G.S. Blackman, B.E. Bent, M.A. Van Hove, and G.A. Somorjai. *J. Vac. Sci. Technol. A* **6** (1988) 786.

[24] G.C. Bond. *Heterogeneous Catalysis: Principles and Applications.* Clarendon Press, Oxford, 1987.

[25] J.M. Thomas and W.J. Thomas. *Introduction to the Principles of Heterogeneous Catalysis.* Academic Press, New York, 1966.

[26] F.C. Tompkins. *Chemisorption of Gas on Metals.* Academic Press, London, 1978.

[27] A.M. Wodtke and Y.T. Lee. *J. Phys. Chem.* **89** (1985) 4744.

[28] W.T. McGown, C. Kemball, and D.A. Whan. *J. Catalysis* **51** (1978) 173.

[29] J.M. Moses, A.H. Weiss, K. Matusek, and L. Guczi. *J. Catalysis* **86** (1984) 417.

[30] D.P. Woodruff and T.A. Delchar. *Modern Techniques of Surface Science.* Cambridge University Press, Cambridge, 1986.

[31] J.E. Crowell. PhD thesis, University of California, Berkeley, 1984.

[32] C.M. Mate. PhD thesis, University of California, Berkeley, 1986.

[33] R.J. Koestner, M.A. Van Hove, and G.A. Somorjai. *Surf. Sci.* **121** (1982) 321.

[34] R.C. Yeats. PhD thesis, University of California, Berkeley, 1985.

[35] R.G. Musket, W. Mclean, C.A. Colmenares, D.M. Makowiecki, and W.J. Siekhaus. *Appl. Surf. Sci.* **10** (1982) 143.

[36] R.J. Baird, R.C. Ku, and P. Wynblatt. *Surf. Sci.* **97** (1980) 346.

[37] S. Semancik, G.L. Haller, and J.T. Yates, Jr. *Appl. Surf. Sci.* **10** (1982) 133.

[38] D.G. Castner, B.A. Sexton, and G.A. Somorjai. *Surf. Sci.* **71** (1978) 519.

[39] L. Dubois. *J. Chem. Phys.* **77** (1982) 5228.

[40] L.J. Richter, B.A. Gurney, and W. Ho. *J. Chem. Phys.* **86** (1987) 477.

[41] L. de Broglie. *C. R. Acad. Sci.* **177** (1923) 517.

[42] L.V. Azaroff. *Elements of X-Ray Crystallography.* McGraw-Hill, New York, 1968.

[43] C.J. Davisson and L.H. Germer. *Nature* **119** (1927) 558.

[44] D.F. Ogletree. PhD thesis, Unversity of California, Berkeley, 1986.

[45] D.F. Ogletree, G.A. Somorjai, and J.E. Katz. *Rev. Sci. Instrum.* **57** (1986) 3012.

[46] G. Wedler. *Chemisorption : An Experimental Approach*, chapter 5. Butterworths, London, Boston, 1970.

[47] R.L. Park and M.G. Lagally, editors. *Solid State Physics: Surfaces.* Volume 22 of *Methods of Experimental Physics*, Academic Press, New York, 1987.

[48] D. Edwards, Jr. *Surf. Sci.* **54** (1976) 1.

[49] C.M. Chan, R. Aris, and W.H. Weinberg. *Appl. Surf. Sci.* **1** (1978) 360.

[50] P. Skinner, M.W. Howard, J.A. Oxton, S.F.A. Kettle, D.B. Powell, and N. Sheppard. *J. Chem. Soc. Faraday Trans.* **77** (1981) 1203.

[51] B.E. Bent, Mate. C.M., C-T. Kao, A.J. Slavin, and G.A. Somorjai. *J. Phys. Chem.* **92** (1988) 4720.

[52] R.M. Badger. *J. Chem. Phys.* **2** (1934) 128.

[53] A.A. Zavitsas. *J. Phys. Chem.* **91** (1987) 5573.

[54] R. Eischens, W.A. Pliskin, and S.A. Francis. *J. Chem. Phys.* **22** (1954) 1786.

[55] M.L. Hair. *Infrared Spectroscopy in Surface Chemistry.* Dekker, New York, 1967.

[56] J.T. Yates, Jr. and T.E. Madey. *Vibrational Spectroscopy of Molecules on Surfaces.* Plenum, New York, 1987.

[57] R.K. Chang and T.E. Furtak, editors. *Surface Enhanced Raman Scattering.* Plenum, New York, 1981.

[58] Y. Chabal. *Surface Sci. Report* **8** (1988) 211.

[59] F. Hoffman. *Surface Sci. Report* **3** (1983) 107.

[60] I.J. Malik, S.B. Brubaker, M.E. Mohsin, and M. Trenary. *J. Chem. Phys.* **87** (1987) 5554.

[61] X.D. Zhu, H. Suhr, and Y.R. Shen. *Chem. Phys. Lett.* **133** (1987) 189.

[62] P. Guyot-Sionnest, J.H. Hunt, and Y.R. Shen. *Phys. Rev. Lett.* **59** (1987) 1597.

[63] J.H. Hunt, P. Guyot-Sionnest, and Y.R. Shen. *Chem. Phys. Lett.* **133** (1987) 189.

[64] R. Superfine, P. Guyot-Sionnest, J.H. Hunt, C.-T. Kao, and Y.R. Shen. *Surf. Sci. Lett.* **200** (1988) 445.

[65] T. Wolfram, editor. *Inelastic Electron Tunneling Spectroscopy.* Volume 4 of *Springer Series in Solid State Sciences*, Springer-Verlag, Berlin, 1978.

[66] G. Binnig, H. Rohrer, Ch. Gerber, and E. Weibel. *Phys. Rev. Lett.* **49** (1982) 597.

[67] R.V. Coleman, B. Drake, P.K. Hansma, and G. Slough. *Phys. Rev. Lett.* **55** (1985) 394.

[68] B.T.M. Willis, editor. *Chemical Applications of Thermal Neutron Scattering.* Oxford University Press, Oxford, 1973.

[69] S. Chiang, R.G. Tobin, and P.L. Richards. *Phys. Rev. Lett.* **49** (1984) 648.

[70] M.J.D. Low and G.A. Parodi. *Applied Spectrosc.* **34** (1980) 76.

[71] F. Trager, H. Coufal, and T.J. Chuang. *Phys. Rev. Lett.* **49** (1982) 1720.

[72] L. Rothberg. *J. Phys. Chem.* **91** (1987) 3467.

[73] F.M. Probst and T.C. Piper. *J. Vac. Sci. Technol.* **4** (1967) 53.

[74] H. Ibach, editor. *Electron Spectroscopy for Surface Analysis.* Volume 4 of *Topics in Current Physics*, Springer-Verlag, Berlin, 1977.

[75] Ph. Avouris and J.E. Demuth. *Ann. Rev. Phys. Chem.* **35** (1984) 49.

[76] N.J. DiNardo, J.E. Demuth, and Ph. Avouris. *Phys. Rev. B* **27** (1983) 5832.

[77] E.B. Wilson, J.C. Decius, and P.C. Cross. *Molecular Vibrations: The Theory of Infrared and Raman Vibrational Spectra.* McGraw-Hill, New York, 1955.

[78] D.C. Harris and M.D. Bertolucci. *Symmetry and Spectroscopy: An Introduction to Vibrational and Electronic Spectroscopy.* Oxford University, New York, 1978.

[79] Demuth J.E. *Surf. Sci.* **80** (1979) 367.

[80] Demuth J.E. *Surf. Sci.* **93** (1980) 282.

[81] L.L. Kesmodel, L.H. Dubois, and G.A. Somorjai. *Chem. Phys. Lett.* **56** (1978) 267.

[82] L.L. Kesmodel, L.H. Dubois, and G.A. Somorjai. *J. Chem. Phys.* **70** (1979) 2180.

[83] P.W. Sutton and L.F. Dahl. *J. Am. Chem. Soc.* **89** (1967) 261.

[84] G.A. Somorjai and J. Carrazza. *Ind. Eng. Chem. Fundam.* **25** (1986) 67.

[85] S.M. Davis, F. Zaera, and G.A. Somorjai. *J. Am. Chem. Soc.* **104** (1982) 7453.

[86] S.M. Davis, F. Zaera, and G.A. Somorjai. *J. Catalysis* **85** (1984) 206.

[87] J.A. Gates and L.L. Kesmodel. *Surf. Sci.* **124** (1983) 68.

[88] L.L. Kesmodel, G.D. Waddill, and J.A. Gate. *Surf. Sci.* **138** (1984) 4466.

[89] E.M. Stuve and R.J. Madix. *J. Phys. Chem.* **89** (1985) 105.

[90] L.L. Kesmodel. *Phys. Rev. Lett.* **53** (1984) 1001.

[91] G.D. Waddill and L.L. Kesmodel. *Phys. Rev. B* **31** (1984) 4940.

[92] L.H. Dubois, D.G. Castner, and G.A. Somorjai. *J. Chem. Phys.* **72** (1980) 5234.

[93] R.J. Koestner, M.A. Van Hove, and G.A. Somorjai. *Surf. Sci.* **121** (1982) 321.

[94] B.E. Koel, B.E. Bent, and G.A. Somorjai. *Surf. Sci.* **146** (1984) 211.

[95] B.E. Koel, J.E. Crowell, C.M. Mate, and G.A. Somorjai. *J. Phys. Chem.* **88** (1984) 1988.

[96] B.E. Koel, B.E. Crowell, B.E. Bent, C.M. Mate, and G.A. Somorjai. *J. Phys. Chem.* **90** (1986) 2949.

[97] Ts.S. Marinova and K.L. Kostov. *Surf. Sci.* **181** (1987) 573.

[98] S. Lehwald, H. Ibach, and J.E. Demuth. *Surf. Sci.* **78** (1978) 577.

[99] J.C. Bertolini and J. Rousseau. *Surf. Sci.* **83** (1979) 531.

[100] J.E. Demuth and H. Ibach. *Surf. Sci.* **85** (1979) 365.

[101] S. Lehwald and H. Ibach. *Surf. Sci.* **89** (1979) 425.

[102] H. Ibach and S. Lehwald. *J. Vac. Sci. Tchnol.* **18** (1981) 625.

[103] B.J. Bandy, M.E. Chesters, M.E. Pemble, G.S. McDougall, and N. Sheppard. *Surf. Sci.* **139** (1984) 87.

[104] J.A. Stroscio, S.R. Bare, and W. Ho. *Surf. Sci.* **148** (1984) 499.

[105] N.J. DiNardo, J.E. Demuth, and Ph. Avouris. *J. Vac. Sci. Technol. A* **1** (1983) 1244.

[106] J.A. Gate and L.L. Kesmodel. *J. Chem. Phys.* **76** (1982) 4218.

[107] J.A. Gates and L.L. Kesmodel. *Surf. Sci.* **124** (1983) 68.

[108] L.L. Kesmodel, G.D. Waddill, and J.A. Gates. *Surf. Sci.* **138** (1984) 464.

[109] L.L. Kesmodel. *J. Chem. Phys.* **79** (1983) 4646.

[110] H. Ibach, H. Hopster, and B. Sexton. *J. Appl. Phys.* **14** (1977) 21.

[111] H. Ibach and S. Lehwald. *J. Vac. Sci. Technol.* **15** (1978) 407.

[112] G.H. Hatzikos and R.I. Masel. *Surf. Sci.* **185** (1987) 479.

[113] N.R. Avery. *J. Am. Chem. Soc.* **107** (1985) 6711.

[114] E.M. Stuve, R.J. Madix, and B.A. Sexton. *Surf. Sci.* **123** (1982) 491.

[115] U. Seip, M.-C. Tsai, J. Kuppers, and G. Ertl. *Surf. Sci.* **147** (1984) 65.

[116] W. Erley, A.M. Baro, and H. Ibach. *Surf. Sci.* **120** (1982) 273.

[117] J.E. Parmeter, M.M. Hills, and W.H. Weinberg. *J. Am. Chem. Soc.* **108** (1986) 3563.

[118] J. Bertolini, B. Tardy, R. Dueros, and C.R. Acad. *Acad. Sci. Paris* **298** (1984) 107.

[119] C. Backx, B. Feuerbacher, B. Fitton, and R.F. Willis. *Surf. Sci.* **63** (1977) 193.

[120] J.C. Hamilton, N. Swanson, B.J. Waclawski, and R.J. Celotta. *J. Chem. Phys.* **74** (1981) 4156.

[121] C. Backx and R.F. Willis. *Chem. Phys. Lett.* **53** (1978) 471.

[122] L.H. Dubois, D.G. Castner, and G.A. Somorjai. *J. Chem. Phys.* **72** (1980) 5234.

[123] J. Yoshinobu, H. Tsuda, M. Onchi, and M. Mashijima. *Chem. Phys. Lett.* **130** (1986) 170.

[124] M.J.S. Dewer. *Bull. Soc. Chim. Fr.* **18** (1951) 79.

[125] J. Chatt and L.A. Duncanson. *J. Chem. Soc.* (1953) 2939.

[126] N. Sheppard. *J. Electron Spectrosc. Related Phenom.* **38** (1986) 175.

[127] G. Gervasio, R. Rossetti, and P.L. Stangettini. *Organomet.* **4** (1985) 1612.

[128] P.F. Heveldt, B.F.G. Johnson, J. Lewis, P.R. Raithby, and G.M. Sheldrick. *J. Chem. Soc. Chem. Commun.* (1978) 340.

[129] T. Shimanouchi. *Tables of Molecular Vibrational Frequencies, Consolidated Vol I.* NSRDS-NBS, 1972.

[130] Y. Iwashita, F. Tamura, and A. Nakamura. *Inorg. Chem.* **4** (1969) 79.

[131] Y. Iwashita. *Inorg. Chem.* **9** (1970) 1178.

[132] C.E. Anson, B.T. Keiller, I.A. Oxton, D.B. Powell, and N. Sheppard. *J. Chem. Soc. Chem. Comm.* (1983) 470.

[133] A.J. Slavin, B.E. Bent, C.-T. Kao, and G.A. Somorjai. *Surf. Sci.* **202** (1988) 388.

[134] L.H. Dubois. *J. Chem. Phys.* **77** (1982) 5228.

[135] B.A. Gurney and W. Ho. *J. Chem. Phys.* **87** (1987) 1376.

[136] J.A. Stroscio, S.R. Bare, and W. Ho. *Surf. Sci.* **148** (1984) 499.

[137] M.M. Hills, J.E. Parmeter, C.B. Mullins, and W.H. Weinberg. *J. Am. Chem. Soc.* **108** (1986) 3554.

[138] B.E. Bent, C.M. Mate, J.E. Crowell, B.E. Koel, and G.A. Somorjai. *J. Phys. Chem.* **91** (1987) 1493.

[139] J. Evans and G.S. McNutly. *J. Chem. Soc. Dalton Trans.* (1984) 79.

[140] A.J. Carty, S.A. MacLaughlin, and N.J. Taylor. *J. Am. Chem. Soc.* **103** (1981) 2456.

[141] G. Casalone, M.G. Cattania, and M. Simmonetta. *Surf. Sci.* **103** (1981) .

[142] J.A. Gates and L.L. Kesmodel. *Surf. Sci. Lett.* **120** (1982) .

[143] L.H. Dubois, D.G. Castner, and G.A. Somorjai. *J. Chem. Phys.* **72** (1980) 5234.

[144] H. Steininger, H. Ibach, and S. Lehwald. *Surf. Sci.* **117** (1982) 685.

[145] Hills. M.M., J.E. Parmeter, C.B. Mullins, and W.H. Weiberg. *J. Am. Chem. Soc.* **108** (1986) 3554.

[146] P Skinner, M.W. Howard, I.A. Oxton, S.F.A. Kettle, D.B. Powell, and N. Sheppard. *J. Chem. Phys., Faraday, Trans.* **77** (1981) 1203.

[147] Sheppard. N. private communications.

[148] B.E. Koel, B.E. Bent, and G.A. Somorjai. *Surf. Sci.* **146** (1984) 211.

[149] M.B. Lee, Q.Y. Yang, S.L. Tang, and S.T. Ceyer. *J. Phys. Chem.* **85** (1986) 1693.

[150] J. Evans and G.S. McNulty. *J. Chem. Soc., Dalton Trans.* (1983) 639.

[151] J.R. Durig, A.E. Sloan, and J.D. Witt. *J. Phys. Chem.* **76** (1972) 3591.

[152] L.L. Kesmodel, L.H. Dubois, and G.A. Somorjai. *J. Chem. Phys.* **70** (1979) 2180.

[153] R.J. Koestner, M.A. Van Hove, and G.A. Somorjai. *Surf. Sci.* **121** (1982) 321.

[154] Slavin A.L., B.E. Bent, C.-T. Kao, and G.A. Somorjai. to be published.

[155] J.E. Parmeter, M.M. Hills, and W.H. Weinberg. *J. Am. Chem. Soc.* **109** (1987) 72.

[156] J. Evans and G.S. McNulty. *J. Chem. Soc., Dalton Trans.* (1983) 639.

[157] A.M. Baro and H. Ibach. *J. Chem. Phys.* **74** (1981) 4194.

[158] J.E. Demuth and H. Ibach. *J. Chem. Phys.* **78** (1978) 1238.

[159] Y. Kim, H.C. Peebles, and J.M. White. *Surf. Sci.* **114** (1982) 363.

[160] S. Hengrasmee, P.R. Waston, D.C. Frost, and K.A.R. Mitchell. *Surf. Sci.* **87** (1979) .

[161] P. Avouris and J.E. Demuth. *J. Chem. Phys.* **75** (1981) 4783.

[162] J.A. Horsley, J. Stohr, A.P. Hitchcock, D.C. Newbury, and F. Sette. *J. Chem. Phys.* **83** (1985) 6099.

[163] M.A. Van Hove, R.F. Lin, and G.A. Somorjai. *J. Am. Chem. Soc.* **108** (1986) 2532.

[164] R.F. Lin, G.S. Blackman, M.A. Van Hove, and G.A. Somorjai. *Acta Crystallogr. B* **43** (1987) 368.

[165] D.F. Ogletree, M.A. Van Hove, and G.A. Somorjai. *Surf. Sci.* **183** (1987) 1.

[166] H. Jobic, B. Tardy, and J.C. Bertolini. *J Electron Spectrosc. Relat. Phenom.* **38** (1986) 55.

[167] I.E. Idrissi-Rachidi, C. Minot, M.A. Van Hove, and G.A. Somorjai. *Surf. Sci.,* in press.

[168] E.L. Garfunkel, C. Minot, A. Gavezzotti, and M. Simmonetta. *Surf. Sci.* **167** (1986) 177.

[169] H. Ohtani. *Phys. Rev. Lett.,* in press.

[170] M. Neumann, J.U. Mack, E. Bertel, and F.P. Netzer. *Surf. Sci.* **155** (1985) 629.

[171] E. Bertel, G. Rosina, and F.P. Netzer. *Surf. Sci.* **172** (1986) .

[172] W.L. Parker, R.M. Hexter, and A.R. Siedle. *J. Am. Chem. Soc.* **107** (1985) 4584.

[173] J.C. Bertolini and J. Rousseau. *Surf. Sci.* **89** (1979) 467.

[174] G.D. Waddill and L.L. Kesmodel. *Phys. Rev. B* **31** (1985) 4940.

[175] J.C. Bertolini, J. Massardier, and G. Dalmai-Imelik. *J. Chem. Soc. Faraday Trans.* **74** (1978) 1720.

[176] J.C. Bertolini, J. Massardier, and B. Tardy. *J. Chim. Phys.* **78** (1981) 939.

[177] B. Tardy and J.C. Bertolini. *J. Chim. Phys.* **82** (1985) 407.

[178] G.D. Waddill and L.L. Kesmodel. *Phys. Rev. B* **32** (1985) 2107.

[179] M. Surman, S.R. Bare, P. Hofmann, and D.A. King. *Surf. Sci.* **126** (1983) 349.

[180] B. Tardy, J.C. Bertolini, and R. Ducros. *Bull. Soc. Chim. Fr.* **3** (1985) 313.

[181] P. Jakob and D. Menzel. *Surf. Sci.* **201** (1988) 503.

[182] N. Sheppard. *Ann. Rev. Phys. Chem.* **39** (1988) 589.

[183] H.F. Efner, D.E. Tevault, W.B. Fox, and R.R. Smardzewski. *J. Organomet. Chem.* **146** (1978) 45.

[184] H. Ohtani, M.A. Van Hove, and G.A. Somorjai. *J. Phys. Chem.* **92** (1988) 3974.

[185] J. Somers, M.E. Bridge, D.R. Lloyd, and T. McCabe. to be published.

[186] J.U. Mack, E. Bertel, and F.P. Netzer. *Surf. Sci.* **159** (1985) 265.

[187] F.P. Netzer, H.H. Graen, H. Kuhlenbeck, and M. Neumann. *Chem. Phys. Lett.* **133** (1987) 49.

[188] W.F. Egelhoff. *Chemical Physics of Solid Surfaces and Heterogeneous Catalysis*, chapter 9. Volume 4, Elsevier, Amsterdam, 1982.

[189] T.W. Root, L.D. Schmidt, and G.B. Fisher. *Surf. Sci.* **150** (1985) 173.

[190] G.A. Papapolymerou and L.D. Scgmidt. *Langmuir* **1** (1985) 488.

[191] R.E. Hendershot and R.S. Hansen. *J. Catalysis* **98** (1986) 150.

[192] F.A. Cotton and G. Wilkinson. *Advanced Inorganic Chemistry.* Wiley, New York, 3 edition.

[193] S.-S. Sung, R. Hoffmann, and P.A. Thiel. *J. Phys. Chem.* **90** (1986) 1380.

[194] C.C. Su and J.W. Faller. *J. Organomet. Chem.* **84** (1975) 53.

[195] JANAF. *Thermochemical Tables.* Volume 37 of *Natl. Stand. Ref. Data Ser.*, Natl. Bur. Stand., 2 edition, 1971.

[196] J.B. Benziger. *Appl. Surf. Sci.* **6** (1980) 105.

[197] L. A. DeLouise and N. Winograd. *Surf. Sci.* **159** (1985) 199.

[198] R.I. Masel. *Catal. Rev.-Sci. Eng.* **28** (1986) 335.

[199] S. Lehwald, J.T. Yates, Jr., and H. Ibach. *Proceedings of the Fourth International Conference on Solid Surfaces*, page 221. Institute of Physics and Physical Society, London, 1980.

[200] G. Pirug, H.P. Bonzel, H. Hopster, and H. Ibach. *J. Chem. Phys.* **71** (1979) 593.

[201] D.J. Castner, B.A. Sexton, and G.A. Somorjai. *Surf. Sci.* **71** (1978) 519.

[202] T.W. Root, L.D. Schmidt, and G.B. Fisher. *Surf. Sci.* **134** (1983) 30.

[203] T.W. Root, G.B. Fisher, and L.D. Schmidt. *J. Chem. Phys.* **85** (1986) 4679.

[204] M.A. Van Hove, Koestner R.J., J.C. Frost, and G.A. Somorjai. *Surf. Sci.* **129** (1983) 482.

[205] C.E. Dinerman and G.E. Ewing. *J. Chem. Phys.* **53** (1970) 626.

[206] M.E. Bartram, R.G. Windham, and B.E. Koel. *Surf. Sci.* **184** (1987) 57.

[207] N.R. Avery. *Surf. Sci.* **131** (1983) 501.

[208] U. Schwalke and W.H. Weinberg. *J. Vac. Sci. Technol. A* **5** (1987) 459.

[209] K. Nakamoto. *Infrared and Raman Spectra of Inorganic and Coordination Compounds.* Wiley, New York, 1977.

[210] R.B. King and M.B. Bisnette. *J. Am. Chem. Soc.* **85** (1963) 2527.

[211] R.C. Elder, F.A. Cotton, and R.A. Schunn. *J. Am. Chem. Soc.* **89** (1967) 3645.

[212] J. Muller and S. Schmidt. *J. Organometa. Chem.* **97** (1975) .

[213] M.A. Van Hove, R.F. Lin, and G.A. Somorjai. *Phys. Rev. Lett.* **51** (1983) 778.

[214] M.A. Van Hove and S.Y. Tong. *Surface Crystallography by LEED.* Springer Verlag, Heidelberg, Berlin, New York, 1979.

[215] Pauling L. *The Nature of Chemical Bond.* Cornell University Press, 1960.

[216] R.J. Koestner, M.A. Van Hove, and G.A. Somorjai. *Surf. Sci.* **107** (1981) 439.

[217] F. Solymosi and J. Sarkany. *Appl. Surf. Sci.* **3** (1979) 68.

[218] H. Conrad, G. Ertl, J. Kuppers, and E.E. Latta. *Surf. Sci.* **65** (1977) 235.

[219] J.P. Collman and L.S. Hegedus. *Principles and Applications of Organotransition Metal Chemistry.* University Science Books, Mill Valley, 1980.

[220] I. Harrison, C.-T. Kao, and G.A. Somorjai. to be published.

[221] S.W. Jorgensen, N.D.S. Channing, and R.J. Madix. *Surf. Sci.* **179** (1987) 322.

[222] H. Ibach and S. Lehwald. *Surf. Sci.* **76** (1978) 1.

[223] B.A. Gland, J.B. Sexton. *Surf. Sci.* **94** (1980) 355.

[224] B.E. Hayden. *Surf. Sci* **131** (1983) 419.

[225] J.S. Villarrubia and W. Ho. *J. Chem. Phys.* **87** (1987) 750.

[226] L.H. Dubois, P.K. Hansma, and G.A. Somorjai. *J. Catalysis* **65** (1980) 318.

[227] P.A. Thiel, W.H. Weinberg, and J.T. Yates, Jr. *Chem. Phys. Lett.* **67** (1979) 403.

[228] P.A. Thiel, W.H. Weinberg, and J.T. Yates, Jr. *J. Chem. Phys.* **71** (1979) 1643.

[229] H. Conrad, R. Scala, W. Stenzel, and R. Unwin. *Surf. Sci.* **1** (1984) 145.

[230] W.F. Banholzer and R.I. Masel. *Surf. Sci.* **137** (1984) 339.

[231] E.G. Seebauer, A.C.F. Kong, and L.D. Schmidt. *J. Vac. Sci. Technol. A* **5** (1987) 464.

[232] A.M. Bradshaw and F.M. Hoffmann. *Surf. Sci.* **72** (1978) 513.

[233] H. Ohtani, M.A. Van Hove, and G.A. Somorjai. *Surf. Sci.* **187** (1987) 372.

[234] H.A.C.M. Hendrickx, A.M.E. Winkelman, and B.E. Nieuwenhuys. *Appl. Surf. Sci.* **27** (1987) 458.

[235] W.F. Banholzer, Y.O. Park, K.M. Mak, and R.I. Masel. *Surf. Sci.* **128** (1985) 176.

[236] J.M. Gohndrone, Y.O. Park, and R.I. Masel. *J. Catalysis* **95** (1985) 244.

[237] E. Pelach, R.E. Viturro, and M. Folman. *Surf. Sci.* **161** (1985) 553.

[238] C. Klauber and B.G. Baker. *Appl. Surf. Sci.* **22**.

[239] S. Tatarenko, M. Alnot, and R. Ducros. *Surf. Sci.* **163** (1985) 249.

[240] C.-T. Kao, G.S. Blackman, M.A. Van Hove, C.M. Chan, and G.A. Somorjai. *J. Phys. Chem.,* submitted.

[241] C.-T. Kao, G.S. Blackman, and G.A. Somorjai. to be published.

[242] R. Levis, N. Winograd, and L.D. Delouise. *J. Am. Chem. Soc.* **109** (1987) 6873.

[243] R.J. Koestner, M.A. Van Hove, and G.A. Somorjai. *J. Phys. Chem.* 87 (1983) 203.

[244] J. Muller and S. Schmidt. *J. Organomet. Chem.* **97** (1975) .

[245] A. Kubat-Matin, A.D. Rae, and L.F. Dahl. *Organometallics* **4** (1985) 2221.

[246] P.A. Dimas, R.J. Lawson, and J.R. Shapley. *Inorg. Chem.* **20** (1981) 281.

[247] T.W. Root, G.B. Fisher, and L.D. Schmidt. *J. Chem. Phys.* **85** (1986) 4687.

[248] L. Bugyi and F. Solymosi. *Surf. Sci.* **188** (1987) 475.

[249] J.E. Crowell and G.A. Somorjai. *Appl. Surf. Sci.* **19** (1984) 73.

[250] J.R. MacDonald and C.A. Barlow, Jr. *J. Chem. Phys.* **39** (1963) 412.

[251] J.R. MacDonald and C.A. Barlow, Jr. *J. Chem. Phys.* **44** (1966) 202.

[252] M.A. Van Hove, R.J Koestner, and G.A. Somorjai. *Phys. Rev. Lett.* **50** (1983) 903.

[253] A. Berko and F. Solymosi. *Surf. Sci.* **187** (1987) 359.

[254] H.W.K. Tom, C.M. Mate, X.D. Zhu, J.E. Crowell, Y.R. Shen, and G.A. Somorjai. *Surf. Sci.* **172** (1986) 466.

[255] B.E. Koel, J.E. Crowell, C.M. Mate, and G.A. Somorjai. *J. Phys. Chem.* **88** (1984) 1988.

[256] E.V. Albano. *Appl. Surf. Sci.* **14** (1982) 183.

[257] C.W. Bauschlicher, Jr. *Chem. Phys. Lett.* **118** (1985) 307.

[258] W. Muller and P. Bagus. *J. Electron Spectrosc. Related Phenomena* **30** (1983) 59.

[259] P.S. Bagus, C.J. Nelin, W. Muller, M.R. Philpott, and H. Seki. *Phys. Rev. Lett.* **58** (1987) 559.

[260] K. Kunimatsu, H. Seki, W.G. Golden, and M.R. Philpott. *Langmuir* **1** (1985) 245.

[261] D.K. Lambert. *Phys. Rev. Lett.* **50** (1983) 2106.

[262] D.K. Lambert. *J. Vac. Sci. Technol. B* **3** (1985) 1479.

[263] R.A. DePaola, J. Hrbek, and F.M. Hoffmann. *J. Chem. Phys.* **82** (1985) 2484.

[264] M.E. Dry, T. Shinsles, L.J. Boshoff, and G.J. Oosthuizen. *J. Catal.* **15** (1969) 190.

[265] E.L. Garfunkel, J.E. Crowell, and G.A. Somorjai. *J. Phys. Chem.* **86** (1982) 310.

[266] J. Lee, C.P. Hanrahan, J. Arias, R.M. Matin, and H. Matiu. *Phys. Rev. Lett.* **51** (1983) 1803.

[267] D.L. Fehrs and R.E. Stichney. *Surf. Sci.* **24** (1971) 309.

[268] D. Lackey, M. Surman, S. Jacobs, S. Grider, and D.A. King. *Surf. Sci.* **152**.

[269] W. Eberhardt, F.M. Hoffmann, R. Depsola, D. Heskett, I. Strathy, E.W. Plummer, and H.R. Moser. *Phys. Rev. Lett.* **54** (1985) 1856.

[270] D. Heskett, E.W. Plummer, R.A. dePaola, and W. Eberhardt. *Phys. Rev. B* **33** (1986) 5171.

[271] J. Benziger and R.J. Madix. *Surf. Sci.* **94** (1980) 119.

[272] C. Somerton, C.F. McConville, D.P. Woodruff, D.E. Grider, and N.V. Richardson. *Surf. Sci.* **138** (1984) 31.

[273] U.A. Shushunov. *Chem. Abstr.* **44** (1950) 2833.

[274] M.A. Van Hove, R.F. Lin, and G.A. Somorjai. *J. Am. Chem. Soc.* **108** (1986) 2532.

[275] J.K. Norskov, S. Holloway, and N.D. Lang. *J. Vac. Sci. Technol. A* **3** (1985) 1668.

[276] N.D. Lang, S. Holloway, and J.K. Norskov. *Surf. Sci.* **150** (1985) 24.

[277] A. Gavezzotte, M. Simonetta, M.A. Van Hove, and G.A. Somorjai. *Surf. Sci.* **154** (1985) 109.

[278] R. West, D. Eggerding, J. Perkins, D. Handy, and E.C. Tuazon. *J. Am. Chem. Soc.* **101** (1979) 1710.

[279] B.E. Bent and G.A. Somorjai. *Progress in Colloid and Polymer Science* **70** (1985) 38.

[280] P.S. Bratterman. *Metal Carbonyl Spectra.* Academic Press, London, 1975.

[281] S.F.A. Kettle. *Top. Curr. Chem.* **71** (1977) 149.

[282] S.C. Avanzino, A.A. Bakke, H.-W. Chen, C.J. Donahue, W.L. Jolly, T.H. Lee, and A.J. Ricco. *Inorg. Chem.* **19** (1980) 1931.

[283] W.L. Jolly. *Top. Curr. Chem.* **71** (1977) 149.

[284] H. Ohtani, M.A. Van Hove, and G.A. Somorjai. *J. Phys. Chem.,* in press.

[285] H. Ohtani, C.M. Mate, M.A. Van Hove, and G.A. Somorjai. *Appl. Surf. Sci.,* in press.

[286] C.-T. Kao, B.E. Bent, and G.A. Somorjai. to be published.

[287] L.J. Whitman and W. Ho. *J. Chem. Phys.* **83** (1985) 4808.

[288] L. Westerlund, L. Jonsson, and S. Andersson. *Surf. Sci.* **187** (1987) .

[289] J.L. Gland and G.A. Somorjai. *Surf. Sci.* **38** (1973) 157.

[290] F.P. Netzer and J.U. Mack. *J. Chem. Phys.* **79** (1983) 1017.

[291] J.E. Demuth and D.E. Eastman. *Phys. Rev. Lett.* **32** (1974) 1123.

[292] B.E. Nieuwenhuys. *Surf. Sci.* **105** (1981) 505.

LAWRENCE BERKELEY LABORATORY
CENTER FOR ADVANCED MATERIALS
1 CYCLOTRON ROAD
BERKELEY, CALIFORNIA 94720